Boston University

OpenBU **http://open.bu.edu**

Mechanical Engineering ENG: Mechanical Engineering: Theses & Dissertations

2002

HEATING IN VASCULAR TISSUE AND FLOW-THROUGH TISSUE PHANTOMS INDUCED BY FOCUSED ULTRASOUND

https://hdl.handle.net/2144/1375

Boston University

BOSTON UNIVERSITY

COLLEGE OF ENGINEERING

Dissertation

HEATING IN VASCULAR TISSUE AND FLOW-THROUGH TISSUE PHANTOMS INDUCED BY FOCUSED ULTRASOUND

by

JINLAN HUANG

B.S., Nanjing University, 1992
M.S., Nanjing University, 1995

Submitted in partial fulfillment of the

requirements for the degree of

Doctor of Philosophy

2002

Approved by

First Reader

_____

Ronald A. Roy, Ph.D.
Associate Professor of Aerospace and Mechanical Engineering

Second Reader

_____

R. Glynn Holt, Ph.D.
Assistant Professor of Aerospace and Mechanical Engineering

Third Reader

_____

Don Wroblewski, Ph.D.
Associate Professor of Aerospace and Mechanical Engineering

Fourth Reader

_____

Kullervo Hynynen, Ph.D.
Professor of Radiology, Harvard Medical School

Acknowledgements

I would like to take this opportunity to express my deep gratitude to all those who have assisted me in one way or the other with my Ph.D. studies. Most importantly, I would like to thank my husband, Mingxiang, for his patient love and unwavering support. Without him, this would not have been possible.

To my research and dissertation advisor, Dr. Ronald A. Roy, I am deeply indebted. I am so grateful for his continual support, guidance, and encouragement. Without his tremendous help over the years, my work would not have been nearly as productive or fulfilling. I also wish to sincerely thank Dr. Glynn Holt, who gave his stimulating suggestions particularly in the experimental aspect of my work. My appreciation also goes to Dr. Donald Wroblewski, who provided constructive comments on my work with his great patience and pedagogical skills. A special acknowledgement is forwarded to the Director of Therapeutic Ultrasound Laboratory, Harvard Medical School, Dr. Kullervo Hynynen, for being a committee member and offering very valuable comments and suggestions.

It has been very rewarding for me to meet Dr. Robin Cleveland, who helped me a lot with modeling and simulation issues. Thanks are also due to Dr. Ali Nadim for his insightful discussion on numerical modeling on acoustic streaming.

Many of my fellow graduate students in the PACLAB have been giving me great support. I want to thank Dr. Preston Wilson, Dr. Sebastien Manneville, Dr. Patrick Edson, Charles Thomas, Ryan McCormick, Xinmai Yang, Li Liu, Lei Sui and Eun-Joo

Park for their help and friendship through both good and bad times. In particular, I thank Dr. Ibrahim Hallaj for his contributions in the FDTD code development, Charles Thomas and Ryan McCormick for reading the dissertation draft and providing the language refinement, and Xinmai Yang for helping the measurement of harmonic generation in tissue phantom.

The funding for this research was generously provided by the Defense Advanced Research Projects Agency, the U. S. Army, and the Center for Subsurface Sensing and Imaging Systems.

HEATING IN VASCULAR TISSUE AND FLOW-THROUGH TISSUE PHANTOMS INDUCED BY FOCUSED ULTRASOUND

(Order No.)

JINLAN HUANG

Boston University, College of Engineering, 2002

Major Professor: Ronald A. Roy, Associate Professor
of Aerospace and Mechanical Engineering

ABSTRACT

High intensity focused ultrasound (HIFU) can be used to control bleeding, both from individual blood vessels as well as from gross damage to the capillary bed. This process, called acoustic hemostasis, is being studied in the hope that such a method would ultimately provide a lifesaving treatment during the so-called "golden hour", a brief grace period after a severe trauma in which prompt therapy can save the life of an injured person. Thermal effects play a major role in occlusion of small vessels and also appear to contribute to the sealing of punctures in major blood vessels. However, aggressive ultrasound-induced tissue heating can also impact healthy tissue and can lead to deleterious mechanical bioeffects. Moreover, the presence of vascularity can limit one’s ability to elevate the temperature of blood vessel walls owing to convective heat transport.

In an effort to better understand the heating process in tissues with vascular structure we have developed a numerical simulation that couples models for ultrasound propagation, acoustic streaming, ultrasound heating and blood cooling in Newtonian

viscous media. The 3-D simulation allows for the study of complicated biological structures and insonation geometries. We have also undertaken a series of *in vitro* experiments, in non-uniform flow-through tissue phantoms, designed to provide a ground truth verification of the model predictions. The calculated and measured results were compared over a range of values for insonation pressure, insonation time, and flow rate; we show good agreement between predictions and measurements.

We then conducted a series of simulations that address two limiting problems of interest: hemostasis in small and large vessels. We employed realistic human tissue properties and considered more complex geometries. Results show that the heating pattern in and around a blood vessel is different for different vessel sizes, flow rates and for varying beam orientations relative to the flow axis. Complete occlusion and wall-puncture sealing are both possible depending on the exposure conditions. These results concur with prior clinical observations and may prove useful for planning of a more effective procedure in HIFU treatments.

Contents

List of Tables

List of Figures

Chapter 1

Introduction

1.1 Historical Background

The application of high intensity ultrasound to problems in medicine dates back to the 1920s and 1930s, when investigators created excitement by reports of physical, chemical and biological effects that could be produced by ultrasound at intensities up to several hundred watts per cm^2 [1-4]. All the early investigations of the medical uses of ultrasound utilized plane waves until Lynn *et al.* made an attempt to increase the local intensity by bringing the sound beam to a focus [5]. Two years later, Lynn and Putnam used this technique in an initial study in which focused ultrasound was applied to the brains of dogs, cats and monkeys [6]. They reported that "At the will of the operator, reversible, partially reversible and irreversible disabilities could be produced". This technique was later modified and further developed by the Fry brothers to destroy tissue in the central nervous system [7, 8]. In a detailed review article, Fry described both structural and functional changes produced by exposure of the central nervous system to focused ultrasound [9].

During the same general period, Hueter [10], and Lele and coworkers [11, 12] were investigating the production of focal lesions and other effects in laboratory animals

and plastic models from exposure of repeated pulses of focused ultrasound. Their objective was to find optimum values for the ultrasound frequency, the focal intensity, the duty factor and other characteristics of the ultrasound field. Since then, many studies have been made of the various physical mechanisms governing ultrasound interaction with tissue. Extensive reviews on this topic have been given by several authors including Wells [13], Driller and Lizzi [14], ter Haar [15] and Nyborg [16] (a summary discussion follows below). Briefly stated, high intensity ultrasound exposure can induce bioeffects in soft tissue by means of both thermal and mechanical mechanisms. Thermal mechanism is simply the bulk heating of tissue due to viscous absorption of the acoustic energy. Mechanical mechanisms include the various manifestations of acoustic cavitation, and other mechanical effects such as acoustic streaming and radiation pressure.

In the meanwhile, the therapeutic use of “high intensity focused ultrasound” (HIFU) has been extensively investigated. The clinical applications generally fall into two categories, namely “ultrasound hyperthermia” and “focused ultrasound surgery” (FUS). Which category a given HIFU exposure falls into depends on the dosage parameters (*i.e.*, field intensity and exposure time) employed during treatment [45]. Generally, during hyperthermia applications, tissues are exposed to ultrasound for long periods (from 10 to 60 minutes) at lower intensity levels, such that the irradiated tissue temperature is elevated and maintained at 41-45°C during the therapy. The biological change thus induced can be reversible. In contrast, focused ultrasound surgery utilizes intense, relatively short bursts (0.1-30 seconds) to induce irreversible changes in the focal tissue volume. The tissue temperature in the focal zone can reach 70-90°C within a few

seconds. At these high temperatures, protein denaturation occurs, which results in tissue necrosis in a very short time. The damaged tissue volume is commonly known as a "lesion". This technique is also known as ultrasound ablation.

Research into the application of HIFU for tissue ablation has been conducted in a number of clinical fields, including neurosurgery, ophthalmology, urology and oncology [17, 18]. Surgical treatments have been applied to destroy tissue volumes in the brain (Warwick and Pond [19]; Fry *et al*. [20]), to treat eye disorders (Lizzi *et al.* [21-23]; Coleman *et al*. [24-26]), to cure the disease of the inner ear (Angell [27]; Sorensen and Andersen [28]), and to damage soft tissue tumors in breast (Hynynen *et al*. [29, 30]), kidney (Vallancien *et al*. [31]; ter Haar *et al*. [32]), liver (ter Haar *et al*. [32]), prostate (ter Haar *et al*. [32]; Bihrle *et al*. [33]; Madersbacher *et al.* [34]; Gelet *et al*. [35]; Chapelon *et al*. [36]) and bladder (Vallancien *et al*. [37]). HIFU has also been used to occlude blood flow within vessels (Delon-Martin *et al*. [38]; Hynynen *et al*. [39, 40]; ter Haar *et al*. [41]; Rivens *et al*. [42]) and show great potential to arrest bleeding (Vaezy *et al*. [43, 44]). [We will discuss the application of HIFU to bleeding control (*i.e.* acoustic hemostasis) in greater detail later in this chapter.] Early equipment was heavy and cumbersome, and imaging techniques were inadequate either to ensure accurate pretreatment targeting of lesions in a living patient or to be capable of providing good treatment follow-up. However, there has been tremendous progress made in ultrasound transducer technology and imaging modalities during the last 10 years [45]. These new R&D efforts have enhanced the capabilities of ultrasound therapy and there is a resurgence of interest in the clinical application of this technique.

The most recent studies of HIFU as a means of medical therapy are largely motivated by what are potentially substantial advantages as compared to conventional surgery. By focusing high power ultrasound beams at a distance from the source, total necrosis of tissues lying within the focal volume may be achieved with minimal damage to structures lying elsewhere in the path of the beam. This technique has clear advantages over conventional forms of surgery in that it can be used to target tissues lying at depth without the need for conventional surgical intervention. HIFU technology thus offers a non-invasive surgical alternative which, when coupled with the modern imaging techniques such as diagnostic ultrasound imaging [46-48] or magnetic resonance imaging (MRI) [49, 50], makes clinical, bloodless, noninvasive treatment of deep target volumes possible.

1.2 HIFU Damage Mechanisms

Common clinical applications of HIFU involve the destruction of a volume of tissue for therapeutic effect. The physical mechanisms leading to damage depend on several factors, including tissue physiology, tissue rheology, and ultrasound exposure parameters. The conventional categorization of mechanisms is into those that are thermal in origin, those that arise from cavitation effects, and a third class that is neither thermal nor cavitational in origin (*e.g.*, acoustic streaming, radiation stress) [15]. These mechanisms may be modeled separately, but in practice are difficult to isolate when biological effects are studied. In the paragraphs that follow we discuss in brief the

physics of the various HIFU-related bioeffects, and then cast this knowledge in the context of effects that may be observed in biological tissues.

When an ultrasound beam passes through a volume of tissue it creates local, periodic perturbations in density, pressure, and temperature and induces small-scale displacements. The energy of the ultrasound beam is attenuated by two main mechanisms: absorption and scattering. Regions of differing acoustic impedance within the tissue reflect the sound beam to varying extents, and scatter energy out of the primary beam to surrounding volumes. Some of the primary acoustic field is absorbed locally by the tissue and then turned into heat; thus, a temperature elevation results. The magnitude of the temperature increase is a function of the physical properties of the medium (*e.g.*, acoustic absorption, density, specific heat), properties of the focused ultrasound device (*e.g.*, beam geometry), and the frequency and time-averaged acoustic intensity of the acoustic field [51, 52]. The actual temperature rises that may be obtained also depend on the conduction and convection properties of the tissue involved. Blood perfusion, for example, plays an important role in determining the final temperature that is achieved, and this may depend on both the temperature and the exposure time [53]. This temperature rise, when sufficiently high, can denature tissue – useful for "cooking" cancer cells as a way to kill them – or even vaporizes tissue by the boiling of its constituent water. These can cause irreversible damage to the tissue, an effect described loosely as tissue necrosis [18]. Microscopy of the focused lesions shows "island" and "moat" structures [19] similar to those seen when a fine heated wire is embedded in tissue [54]. The center of the lesion (the "island") contains coagulated, necrosed tissue

that takes up stain readily. Surrounding this region is a border of cells that takes up stain less than normal cells (the “moat”). Various papers have reported the threshold of necrosis by using an acoustic intensity threshold [55-59] or temperature threshold [60] criterion. However, Damianou and Hynynen pointed out that the intensity or temperature threshold might not be the best quantity to define the formation of lesions [61]. Because the effect of temperature elevation in tissue depends on both the temperature and the duration of the exposure, the development of a lesion due to thermal damage can be defined best by a thermal dose criterion which links the temperature achieved and the time of exposure in a nonlinear fashion. Studies by Meshorer *et al*. [62], Horst [63], Lyons *et al*. [64], Borrelli *et al*. [65], and Jansen and Haverman [66] show that the threshold thermal dosage reference at 43ºC is between 50 and 240 min. Based on the evaluation of the 240-min thermal does boundary, Damianou and Hynynen conducted a parametric study to investigate the effect of various physical parameters on the size and shape of the lesions, and they reported that the threshold intensity for 1- and 5-s sonications to be about 1000 and 400 W/cm^2, respectively [61].

Sound absorption results in the deposition of heat and the transfer of momentum to the tissue. As a sinusoidal ultrasonic wave propagates, a small steady force is generated within the medium in the direction of propagation. This effect arises because the speed of sound increases with pressure; therefore, the pressure maxima of the wave travel faster than the pressure minima. The resultant distortion of the ultrasonic pressure waveform generates harmonics, including a steady pressure component, similar to a “DC” level, termed the “radiation pressure” [67]. In several situations, this steady

pressure can result in a net force on tissue, thereby inducing steady mechanical stresses. For example, reflection causes a pressure difference that produces a net force on the reflecting interface, called the acoustic radiation force; attenuation in a fluid causes a gradient in the pressure and results in fluid flow, known as acoustic streaming. Radiation pressure thus exerts a force on liquid drops, small particles, boundaries or any other inhomogeneities within a field and may cause them to move. Local differences in radiation pressure will cause variations in force, and where one object is subject to these variations along its length, this may give rise to a torque, or to translational movement [68]. The fluid velocities induced by unidirectional acoustic streaming are spatially non-uniform, and velocity gradients are thus set up within the field. Objects within the field are therefore subject to shear stresses. If the fluid is near a rigid boundary, a non-slip condition may exist that means the velocity is zero at the boundary, and so velocity gradients tend to be highest in that region. High shear stresses have been implicated to be sufficient to cause biological damage and the effect is stronger at higher intensities and frequencies [69, 70].

When the acoustic intensity is increased, other effects can occur as well. The process of initiating acoustic cavitation occurs when the tensile acoustic stress reaches the nucleation threshold in which the tension serves to “tear” the tissue or liquid apart, the cavity so formed filling with vapor and/or any gasses that are dissolved within the liquid [71, 72]. The nucleation threshold pressure depends on the tensile strength of the fluid and any impurities and inhomogeneities in the liquid serve to reduce this pressure. Once created, the sound field drives the bubble into radial and shape oscillations. A bubble can

experience either violent nonlinear or gentle linear oscillations, depending on the bubble size, the rheology of the surrounding medium, and the acoustic pressure amplitude [73]. A newly formed bubble within a relatively low amplitude acoustic field possesses a resonant frequency that can be quite distinct from the applied frequency. It experiences small amplitude volume pulsations that are spherically symmetric in shape, and linear. Bubble oscillations at moderate amplitudes are potentially nonlinear and may persist for several acoustic cycles; this behavior is referred to as stable or noninertial cavitation [74]. The dynamics of noninertial cavitaion are dominated by the compressibility of the gas in the cavity. Under this circumstance the bubble scatters and emits sound at the same frequency as the driving field. As the bubble grows *via* rectified diffusion [75, 76] toward its resonance radius or, as the amplitude of the applied sound field increases, the volumetric changes in the bubble evolve to more complex functions of time within an acoustic cycle, and the acoustic emissions include the superharmonics of the applied signal. Eventually, the once stably oscillating bubble grows unstably and collapses violently. This is generally referred to as transient or inertial cavitation [74] because the dynamics of the collapse is dominated by the inertia of the inrushing fluid. The transition from stable cavitation to transient cavitation occurs at the transient cavitation threshold pressure, a well defined pressure that depends on several factors, including the acoustic frequency, the bubble equilibrium size, and the media viscosity [74]. Associated with inertial cavitation are broad-band acoustic emissions and even shock wave formation, high localized temperature generation [theoretical predictions 1000-20000 K (Flynn [77]; Apfel [78]), and the formation of hydrodynamic jets if the bubble is near an interface.

This high-energy event can generate a wide range of potentially destructive effects such as erosion, cell disruption, *etc.* [74]. In addition, cavitating bubbles may compress their contents adiabatically, resulting in a dramatic heating of the bubble's contents, the dissociation of chemical species, and the subsequent of production of free radicals [79, 80]. Free radicals within biological tissue can create significant biological damage by inducing deleterious chemical reactions with carbohydrates, nucleic acids, lipids, and proteins [81]. The presence of bubbles in a sound field also engenders forces acting between them, known as Bjerknes forces [74]. Furthermore, the acoustic forcing allows a pulsating bubble to create vorticity and hence a viscous boundary layer within the liquid adjacent to its surface, known as microstreaming [82, 83]. The shear induced in this layer can stress materials and boundaries in proximity to the bubble. Thus, cavitation produces mechanical damage directly and also induces chemical-based damage.

Since Fry *et al*. reported on cavitation effects in frogs [84], several authors have reported evidence of cavitation activity *in vivo* (Lehmann and Herrich [85]; Fry *et al*. [55, 86]; Lele [87, 88]; Frizzell [58, 59]; Hynynen [89]), and related biological effects such as nerve paralysis [55] and bubble-enhanced tissue hyperthermia [88, 89]. The use of focused ultrasound to destroy parts of the central nervous system for therapeutic purposes revealed that for time durations less than 40 ms, intensities above 2000 W/cm^2 at the frequencies of 1 and 3 MHz (with higher values at 3 MHz) were required to cause cavitation in cat's brain *in vivo* (Fry *et al*. [55]). Lele observed a lower intensity of 1000-1500 W/cm^2 at 2.7 MHz to be the threshold for transient cavitation in cat's brain *in vivo* and in calf liver *in vitro* [87, 88]. Their measurements were made for 0.2- and 0.3-second

cw insonation times. Later Frizzell reported the threshold dosages for high intensity focal lesion production at 3 MHz for exposure durations from 0.003-35 second in the cat liver *in vivo*, and concluded that a transient cavitation mechanism of damage became dominant at intensities above 2500 W/cm^2 [59]. Hynynen, in a study of the threshold for the transient cavitation in dog's thigh muscle *in vivo*, reported that the measured cavitation pressure amplitude threshold depends almost linearly on frequency with a slope of about 5.3 MPa/MHz [89]. Measurements were made between 0.246 and 1.68 MHz for a 1-second cw insonation duration.

In summary, potential ultrasound damage mechanisms include thermal effects [54, 90], mechanical interactions (cavitation and other mechanical forces) [55, 86, 89, 90] as well as chemical reactions/accelerations. Thermal or cavitational effects that occur in tissues during sonication have been found to depend nonlinearly on the applied acoustic intensity, ultrasound frequency, exposure duration, tissue type and location [61]. The lesions created by cavitation in the tissue were found to occur at higher applied intensities and shorter durations than those for creating thermally induced lesions [58, 59]. This suggests that at the low intensities and long time durations of exposure the lesion is produced by a thermal mechanism, and at the highest intensities and shortest time durations, cavitation is the mechanism responsible for the sometimes randomly appearing lesions.

On histology, lesions resulting from exposures well above the threshold for thermal necrosis are commonly found to contain holes or "implosion cysts" [91]. These holes are apparently caused either by cavitation or by boiling of tissue water, but their

precise origin is still unclear [18]. Cavitation is usually considered something to be avoided (except in cases such as lithotripsy) because of the seaming inability to control the formation of lesions in the presence of bubble activity. It has been shown that a cavitating bubble, once generated, can cause significant mechanical damage to tissue in a region outside the treatment area, or excessive damage within the treatment area [88, 92].

Since thermal mechanisms are much more predictable and better understood than cavitation, tissue heating has been the mechanism of choice for most ultrasound surgery studies. However, observations of enhanced heat deposition in the presence of cavitation activity have received more and more attention. Several researchers have reported increased temperature responses in tissue or tissue mimicking material beyond what can be attributed to absorption of the primary acoustic field and concluded the enhanced heating was due to the occurrence of cavitation activity [88, 89, 93]. Another attractive feature of cavitation comes from the idea that the gas bubbles produced may act as scatterers that allow the lesion's position to be readily seen in an ultrasonic image [94].

1.3 The Role of Blood Flow and Perfusion

In spite of the possibilities afforded by the exploitation of mechanical bioeffects, the preferred modality for HIFU-based FUS and hyperthermia therapy continues to be bulk heating due to sound absorption. The effectiveness of HIFU treatment thus depends on the ability to both raise the temperature of the tissue and maintain that temperature level for a sufficient period of time. Uniform temperature distributions are also crucial during HIFU exposure. The inhomogeneity introduced by blood perfusion and blood

circulation in large blood vessels presents a significant problem, because the tissue temperature in their vicinity may be lowered due to convective cooling. Many authors have reported on the cooling effects caused by blood flows in heated tissues during HIFU treatments [95-101]. The effects of blood flow on the temperature distribution in the treated volume during uniform heating of tissues have been calculated using a mathematical model by Patterson and Strang [95]. The results showed that blood flow increased the insonation time required to produce a certain temperature rise. The effect of the blood perfusion rate on the temperature distribution during scanned, focused ultrasound hyperthermia has been investigated experimentally using a dog kidney model by Hynynen *et al*. [96]. They found that the blood perfusion rate of the heated tissue significantly modified the temperature distribution. The plateau temperatures achieved in the kidney without flow were about five times higher than those with full flow for the same applied acoustic power. Creeze and Lagendijk investigated the impact of large vessels during hyperthermia [99]. They found that the vessel wall temperature determines the minimum tumor temperature near a large vessel. In their studies a number of factors influencing the vessel wall temperature were considered – effective tissue conductivity, flow type, vessel size, entrance effects and counter-current flow. In some specific cases, especially when tissue perfusion is high, the vessel wall temperature may reach therapeutic levels when the mean blood temperature is still low.

The usual way to mediate these temperature variations is to monitor the temperature invasively and then adjust the spatial ultrasound power deposition pattern accordingly [102]. An alternative method is to perform the treatment in a very short

period of time and at sufficiently high acoustic intensities to achieve an equivalent thermal dose [100, 103, 104]. A drawback to this approach is that one runs the risk of exceeding the tissue cavitation threshold. In either case, timely and accurate monitoring and feedback control systems are required for the safe and effective treatment of highly vascularized tissues. A number of commercial ultrasound hyperthermia systems are available or currently under development which allow for a higher degree of spatial and dynamic control of the heating [105]. The advantages of these systems include a favorable range of energy penetration characteristics in soft tissue and the ability to shape the energy deposition patterns. Heating systems have been developed for interstitial, intracavitary, or external approaches that utilize features such as multiple transducer arrays, phased arrays, focused beams, mechanical and/or electrical scanning, dynamic frequency control and transducers of various shapes and sizes [105].

1.4 HIFU Hemostasis and Other Effects

Other adverse effects associated with the presence of blood vessels in a HIFU treatment region include hemorrhage caused by rupture of capillary vessels [55, 87] and small vessel occlusion after ultrasound exposure [106]. These may cause serious problems if the ruptured or occluded vessels service a significant tissue volume. On the other hand, vessel occlusion can be thought of as being an advantageous feature of the acoustic lesions created by HIFU in vascular rich tissue such as liver in that they are effectively self-cauterized after treatment. Lesion tissue shows coagulative necrosis, with little or no flow of blood from the healthy normal region to the affected tissue [91, 107].

It has been observed that rapid heating created by HIFU has successfully stopped blood flow *in vivo*. Delon-Martin *et al*. [38] occluded exposed rat femoral veins using a sequence of several three-second bursts. Two days after exposure the blood vessels remained occluded by large blood clots. Hynynen *et al*. [39] occluded blood flow in rabbit femoral arteries with ultrasound by creating a transient mechanical constriction of the blood vessel. They did this by inducing cavitation in and around the arteries. In a follow-up study [40] they showed that the combination of an initial cavitating pulse of ultrasound followed by rapid heating induced by ultrasound in the same area occluded the renal artery of rabbits *in vivo*, all done noninvasively using MRI-guided focused ultrasound. More recently, ter Haar *et al*. [41, 42] have also applied focused ultrasound to occlude intact blood vessels *in vivo*. The specific clinical application they have had in mind is the treatment of "feto-fetal transfusion syndrome" by occluding the placental shunt vessels responsible for the vascular imbalance in twins sharing a placenta.

These observations suggest another important application of HIFU: a process called acoustic hemostasis. The application of HIFU to control bleeding has been explored more recently in the hope that it would ultimately provide a lifesaving treatment during the so-called "golden hour", a brief grace period after a severe trauma injury during which prompt intervention can save the life of an injured person (in most cases, loss of life within the golden hour is traced to exsanguination) [43, 44]. A series of studies in animals by Vaezy and coworkers at the University of Washington demonstrated the potential of HIFU in producing *in vivo* hemostasis in submerged samples such as cut liver [108], spleen [109], as well as in punctured blood vessels [110].

Different biological mechanisms have been identified as being responsible for hemostasis in different tissues. For example, the collapse of small blood vessels appeared to cause hemostasis in bleeding liver tissue while the fusion of the breached vascular walls was observed to result in hemostasis of punctured and lacerated blood vessels [43]. Temperature measurements performed during HIFU treatments and the histological results showed that thermal effects could play a major role in the structural modification of tissue components and may thus be responsible for the occlusion of small vessels. Numerical simulations support this interpretation and showed that for the high-gain transducers used for acoustic hemostasis, nonlinear propagation in tissue led to a significant enhancement of heat generation [111]. Bulk heating due to sound absorption also appears to contribute to the sealing of the puncture holes at major blood vessels. Vaezy *et al.*'s *in vivo* experiments show that HIFU has the potential to induce hemostasis of punctured blood vessels, without complete blockage of the vessel that may lead to ischemic problems [110].

Another potentially important physical effect of HIFU is acoustic streaming and radiation stress, as we discussed in the HIFU damage mechanisms. Acoustic streaming not only imparts shear stress within the flow and on the vessel wall, it also could serve to change both the mean blood flow velocity and the velocity profile, and thus alter the heat deposition and blood cooling behavior during hemostasis application. For example, in an attempt to occlude a small blood vessel, better heat deposition may be achieved by applying HIFU in an opposite direction to that of the blood flow. This may result in a reduction in the mean blood flow velocity during insonation and thus minimize the

convective cooling effect. In efforts to seal punctured vessels, streaming may serve to clear the outward flowing blood away from the site. This will help create an acoustically "clear" pathway for acoustic energy to enter the wound, thereby facilitating the sealing of vessel wall. Since radiation pressure is a steady stress imparted on interfaces and scattering sites, it exerts a force on small particles in suspension. In addition to this "primary" radiation stress, particles in suspension can experience secondary Bjerknes stresses that can lead to agglomeration. It is conceivable that blood cells could be "pinned against" the vessel wall by these acoustic radiation stresses, thereby greatly enhancing the heating within this captive population. Cavitation and subsequent tissue emulsification may also be useful for hemostasis by providing a mechanism for wound sealing and accelerated scab formation for a specific set of acoustic parameters [43], although the role of cavitation in acoustic hemostasis, and whether its presence is desirable are still uncertain.

1.5 Motivation and Focus of Our Work

Until now, hemostasis studies have been limited primarily to animal experiments. A systematic study is needed to determine the optimal acoustic parameters such as acoustic frequency, pulse duration, acoustic intensity, *etc*., for the application of therapeutic ultrasound that would induce acoustic hemostasis at discrete breaches in the vascular system, or over extended volumes within major internal organs. As part of the hemostasis project team at the University of Washington, our research effort at Boston University focuses on the underlying physical processes of acoustic hemostasis (we are

not focused on associated biological and chemical processes). In an effort to better understand the heating process in tissues involving blood vessels we have developed theoretical models coupling ultrasound propagation, heating and blood cooling which take into account the effect of acoustic streaming. We have also undertaken a series of *in vitro* experiments in non-uniform flow-through tissue phantoms. The experiments are designed to provide a ground truth verification of the model predictions. The studies include (a) predicting and measuring temperature fields as a function of acoustic pressure, insonation time and flow rate, (b) investigating the effects on the flow due to nonlinear effects of ultrasound, and (c) investigating different insonation geometries including on-axis and off-axis. In fact, the long-term objective of the hemostasis project is to develop a medical device that would have the broad capabilities of (a) using scanning ultrasound to identify internal bleeding and hemorrhaging, (b) using Doppler ultrasound to locate specific breaches in the vascular system, both from damaged vessels and gross damage to the capillary bed, and (c) using therapeutic ultrasound (HIFU) to treat the damaged region and to induce immediate hemostasis. By developing a better understanding of the physical processes behind acoustic hemostasis, we couple our research to the University of Washington's clinical efforts, hopefully leading to the development of instruments for promoting acoustic hemostasis that may one day work on the battlefield and in our civilian hospitals.

The models for ultrasound propagation and heating in tissue and blood as well as streaming in blood due to the direct absorption of the incident ultrasound are presented in Chapter 2. The result is a numerical model that allows us to predict the space- and time-

dependent temperature field resulting from HIFU insonation of media with arbitrary variability and with prescribed convective flow. The *in vitro* experiments described in Chapter 3 provide a means to quantitatively verify the model. The calculated and measured results are examined over a range of values for insonation pressure, insonation time, and flow rate in Chapter 4; we show good agreement between predictions and measurements. This allows us to use the numerical model to conduct broader simulations in Chapter 5, simulations that employ more complex geometries and consider realistic human tissue properties. A summary of results and concluding remarks are presented in Chapter 6, along with proposals for future work.

We should mention in closing that, in most cases, cavitation is not induced in human tissues by HIFU application because the cavitation threshold pressure is relatively high *in vivo*. Unfortunately, it is much easier to cavitate in a tissue-mimicking material due to the presence of physical inhomogeneities that act as cavitation nuclei. A previous study has shown a direct correlation between the onset of "enhanced" heating and the onset of observed cavitation activity [112]. In that study, a sudden acceleration in the temperature rise was observed to be accompanied by a sudden increase in the output of the passive cavitation detector. By monitoring the temporal behavior of temperature rise we are able to detect, and thus avoid, cavitation during our experiments.

Chapter 2

HIFU-Induced Heating in Vascular Tissues

Since the primary mechanism of lesion damage during HIFU is thermal in nature, to characterize lesion formation accurate thermal models are needed that calculate the transient temperature distributions reached during insonation. This chapter is devoted to a review of existing thermal models for temperature prediction during focused ultrasound exposure, specifically those including vascular structures. Important factors that have been found to prominently affect the heating of tissue in models are discussed. Our goal is to develop a relatively complete model that captures all the important factors within the framework of our *in vitro* experimental investigation, and then apply that model to more realistic cases. A full 3-D numerical simulation is implemented that allows for the study of complicated biological structures and insonation geometries. Some preliminary results are also presented for a qualitative look at the numerical simulation based on our model.

2.1 General Considerations and Reviews

In this section, we will discuss those important factors involved in the heating of tissue with vascular structure during exposure to HIFU. We begin by first providing a brief review of existing thermal models for temperature prediction during focused ultrasound exposure.

2.1.1 Direct Linear Heating Due to Sound Absorption

The temperature elevation in a region subjected to an acoustic disturbance is a direct result of acoustic power absorption in the region of interest. In early attempts to relate the temperature change in tissue to energy deposition from an incident ultrasound field, Fry *et al*. developed a thermal model concerned exclusively with the effects of ultrasound, ignoring heat conduction and various biological effects [113, 114]. The temperature change in a non-conducting medium used by Fry *et al*. is

$$\rho C \frac{\partial T}{\partial t} = q, \tag{2.1}$$

where ρ and C are the density and specific heat of the medium, and q is the energy deposition per unit time and volume due to the absorption of ultrasound, which is approximated by Fry *et al*. as

$$q = 2\alpha I_0, \tag{2.2}$$

where α is the acoustic absorption coefficient and I_0 is the spatial-peak, time-averaged acoustic intensity at the focus of the acoustic source. Equation 2.2 assumes a mono-frequency, locally plane wave at the focus. Equation 2.1 coupled with Eq. 2.2 is readily solved to predict the temperature at the focus as a function of time during insonation:

$$T_h(t) = \frac{2\alpha I_0}{\rho C} t, \quad t < t_i, \tag{2.3}$$

where T_h is the temperature during heating, and t_i is the insonation time. Equation 2.3 represents the linear rate of heating that is characteristic of short insonation times. This result is only valid when conduction in the tissue is not a factor, *i.e.*, for insonation times that are much less than the thermal diffusion time.

2.1.2 The Role of Heat Conduction

For insonation times that are comparable to or larger than the thermal diffusion time, heat conduction from or to the surrounding regions due to temperature gradients has to be taken into account to predict the rate of heating during insonation. It is also required to describe the subsequent temperature decay (or the rate of cooling) after the sound is turned off. Therefore, knowledge of the ultrasound intensity distribution in space is necessary to find the temperature distribution so that conduction effects can be accurately modeled. Lele [11] extended Fry *et al.*'s work to include the effects of heat conduction and he observed that, for focused beams with numerical apertures (the ratio of focal length to transducer diameter) greater than unity, the focal intensity falloff in the radial direction is many times greater than the rate of intensity fall off in the axis of insonation. To study situations involving a wide range of insonation and material geometries, Parker also include the effects of heat conduction in one dimension during insonation (heating), and heat conduction in one and two dimensions after insonation (cooling) [115, 116]. We will describe in the following the model Parker used to show the effect of heat conduction. A conduction term is thus added into Eq. 2.1:

$$\rho C \frac{\partial T}{\partial t} = \mathrm{K}\nabla^2 T + q, \tag{2.4}$$

where K is the thermal conductivity of the medium. Parker assumed that the focal region of highest intensity has cylindrical symmetry and is thin with respect to the axial (z) direction. In addition, a Gaussian radial (r) profile is assumed for the acoustic intensity within this focal region:

$$I(r) = I_0 e^{-r^2/b}, \tag{2.5}$$

where *b* is a measure of the Gaussian variance of the intensity field. The intensity distribution is assumed to have no variation in the axial direction, which precludes any heat transfer in the *z* direction.

Parker started out by evaluating Eq. 2.4 for an infinitely long, instantaneous line source extending along the *z* axis. He derived the temperature history at any distance *r* following a short pulse of duration Δt and assuming the radial intensity profile given by Eq. 2.5:

$$T_h(r,t) = \frac{2\alpha I_0 \Delta t}{\rho C\left[1+\left(4\kappa t/b\right)\right]} e^{-r^2/\left(4\kappa t+b\right)}, \tag{2.6}$$

where $\kappa = \dfrac{\mathrm{K}}{\rho C}$ is the thermal diffusivity. If the intensity on axis is maintained at a constant value of I_0 for long durations, the temperature can be expressed as the convolution of the impulse response of the system, Eq. 2.6, with a step input:

$$T_h(r,t) = \int_0^t \frac{2\alpha I(r)}{\rho C\left[1+\left(4\kappa t/b\right)\right]} d\tau. \tag{2.7}$$

Equation 2.7 is readily solved for the temperature on axis, *r=0*:

$$T_h(0,t) = \frac{2\alpha I_0}{\rho C}\left(\frac{b}{4\kappa}\right)\ln\left(1+\frac{4\kappa t}{b}\right), \tag{2.8}$$

which for $4\kappa t/b << 1$ reduces to Fry *et al.*'s result.

Given the initial condition determined by Eq. 2.7 at the end of insonation, the temperature decay can be determined from Eq. 2.4, including the effects of conduction,

but absent any source term. Parker derived the solution for post-insonation cooling, as a function of radial distance and time, when considering one dimensional conduction only:

$$T_c(r,t) = \frac{T_{\max}}{(4\kappa/b)t+1} e^{-r^2/(4\kappa t+b)}, \tag{2.9}$$

where T_c is the temperature during cooling, time is referenced from the end of insonation, and $T_{\max}$ is the peak temperature at the end of insonation as determined by Eq. 2.7. Parker subsequently incorporated the effects of axial conduction, the result of which is the following equation for the temperature decay after insonation:

$$T_c(r,z,t) = \frac{T_{\max}}{(4\kappa/b)t+1} e^{-r^2/(4\kappa t+b)} erf\left(\frac{z}{4\kappa t}\right). \tag{2.10}$$

Equations 2.8 and 2.9 have been shown by Parker to provide suitable estimates given the assumptions specified in the derivations. However, a more complete model which includes 3-D conduction and a more accurate representation of the source and material geometry is required to predict heating and cooling rates in human tissue or tissue phantoms with complicated geometries. In this case, an analytical solution is not available, numerical simulations are instead required for a more complete formulation of Eq. 2.4.

2.1.3 The Effect of Nonlinear Propagation

Another effect to consider is enhanced heating due to nonlinearity. When ultrasonic transducers are driven to produce high focal intensities the sound wave, in many cases, propagates in a nonlinear fashion (Muir and Carstensen [117]; Carstensen *et al*. [118]). Due to the increase in the speed of sound with pressure, the pressure maximum

of a finite amplitude wave travels faster than the pressure minimum. This causes a distortion of the waveform and generation of harmonics of the source frequency. The absorption coefficient of the human tissue is proportional to f^n, where f is the frequency and n is about 1.1 (Duck [119]). Therefore, the higher harmonics are absorbed more readily than the source frequency, resulting in increased absorption of the nonlinear wave. The appearance of higher harmonics also has an effect on the spatial distribution of the acoustic field because the harmonics are focused to a tighter degree than the fundamental frequency. The increased absorption will augment the heating rate of the tissue and the narrowing of the ultrasonic spatial profile will more tightly constrain the initial temperature boundaries compared to the predictions of linear theory (Goss and Fry [120]; Swindell [121]; Hynynen [122]; Bacon and Carstensen [123]; Curra *et al*. [111]).

2.1.4 The Role of Blood Cooling

Biological structures also play an important role and need to be taken into account for accurate predictions. The presence of macroscopic structural variations and fluid transport pathways makes for an inhomogeneous medium for both acoustic wave propagation and heat transfer. For example, blood is a poor absorber of ultrasound; the HIFU induced temperature rise in it is prone to be much smaller than that in the highly absorptive tissue. It thus can present an excellent heat sink for surrounding tissue. Moreover, blood flow can convect heat away and serve to counteract any ultrasound-induced rise in tissue temperature. Work from the field of hyperthermia has shown that blood flow cooling can be divided into two modes: the first being the highly localized

cooling by individual large vessels traversing heated volumes, and the second, microvascular cooling that from capillary vessels that encompass larger tissue scales. The contribution of thermally significant vessels (r>~0.2mm) clearly should be treated individually, however the large number and the architectural and dimensional variety of smaller sized vessels make it impractical to account for their individual contribution to heat transfer processes in the tissue. Instead, only the collective behavior of the small structures is taken into consideration in a statistical manner. Simply put, the thermal characteristics of a large number of small vessels are spatially averaged so that a single parameter describes the ability for capillary flow to remove thermal energy from this region (Chen and Holmes [124]; Baish [125]; Nyborg [126]).

Work has been dedicated to the incorporation of large vessel effects in bioheat transfer formulations (Roemer [98]; Mooibroek and Lagendijk [206]; Chen and Roemer [207]; Moros *et al*. [208]; Kolios *et al*. [101]; Curra *et al*. [111]). The localized cooling by thermally significant vessels can usually be adequately modeled by a forced convection term in the regions of blood flow [208, 101, 111]:

$$\rho_b C_b \frac{\partial T}{\partial t} = \mathrm{K}_b \nabla^2 T - \rho_b C_b (\vec{u} \cdot \nabla T) + q, \tag{2.11}$$

where the subscript *b* refers to blood domain. Compared to Eq. 2.4, the added second term on the right hand side of Eq. 2.11 is the advective term that models heat transport due to the mass transport of blood with velocity $\vec{u}$.

The contributions of the many smaller sized vessels are averaged in order to predict a local average temperature. Two such models have been used in hyperthermia treatment planning: the Pennes bioheat transfer equation (BHTE) (Pennes, [127]) and the

scalar effective thermal conductivity equation (ETCE) (Weinbaum *et al.* [128]; Lagendijk [129]). The BHTE assumes that blood reaches the capillaries at the temperature of the supply vessels and thermally equilibrates with the surroundings instantaneously. The blood exits the veins at the local average temperature. Microvascular flow thus acts as a heat sink in this model. The ETCE model assumes that blood equilibration occurs at higher levels of the circulation, and that the collective effect of these vessels can be modeled as an enhanced conductivity of tissue. A review of exiting models can be found in Arkin *et al*. [130]. Recent experimental data supports both models mentioned (Crezee and Lagendijk [131]; Moros *et al*. [132]). However, a study by Kolios *et al*. showed that the BHTE predictions agreed with published experimental lesion data, while the ETCE did not predict tissue lesioning for high values of perfusion [101].

The widely used Pennes bioheat transfer equation is a relatively simple modification of the ordinary heat conduction equation and has been shown to be fairly accurate under many circumstances (Damianou *et al*. [133]; Sorrentino [134]; Wissler [135]). In Pennes's model, the temperature field in the perfused tissue domain can be expressed as:

$$\rho_t C_t \frac{\partial T}{\partial t} = \mathrm{K}_t \nabla^2 T - w_b C_b (T - T_\infty) + q, \tag{2.12}$$

where the subscripts *t* and *b* refer to the tissue and blood domain, and T_∞ is the temperature at large distances from the focus. The second term on the right hand side of Eq. 2.12 is responsible for blood perfusion losses with w_b being the perfusion rate.

2.1.5 The Role of Acoustic Streaming

When ultrasound is propagating in an absorbing fluid, bulk movement of the medium is induced within the beam as a by-product of sound absorption. The flow velocity scales roughly with the sound intensity, and time-independent current of fluid circulates globally when constrained to occur in a confined space (Eckart [136]). Such macroscopic fluid movement is called acoustic streaming. The generation mechanism for acoustic streaming is, loosely speaking, a radiation pressure gradient induced by the absorption of the sound wave as it propagates through the medium [137].

Therefore, acoustic streaming will be induced in the blood domain when a HIFU beam propagates through it. Acoustic streaming alters the blood flow characteristics and hence will change the temperature distribution as well. These effects could be prominent especially when the acoustic intensity is high and the mean flow velocity is small. To provide accurate predictions, this nonlinear effect of ultrasound need also be considered.

2.1.6 Literature Reviews

Although there have been numerous methods implemented for modeling thermal diffusion effects during exposure to HIFU, most have limited themselves to representing simple situations for which analytical solutions exist and the use of cylindrical geometries suffice. Pond [54] developed a simple analytical model that broke down the heating volume into a series of cylinders that he used as elemental heat sources. Robinson and Lele [138] also chose a uniform, cylindrical heat deposition pattern and produced analytical expressions for the temperature distributions surrounding the primary heated

regions as a function of time. Carstensen *et al*. [118, 139, 140] have modeled both focused and unfocused ultrasound heat deposition using analytical expressions, which incorporated nonlinear effects. Hynynen [89, 122] also included nonlinear effects in a study of single-exposure heating. There have also been important contributions by Nyborg [141, 142], Beissner [143], Cavicchi and O'Brien [144], and Mair *et al*. [145] concerning the proper computation of heat generation during ultrasound exposure. Lizzi *et al*. [146, 147] developed both analytical and numerical solutions to the bioheat equation using several simplifications, especially with regard to the treatment of glaucoma and various ocular conditions. Hill *et al*. [148] developed a general analytical model for lesion formation based on a Gaussian approximation to the beam shape. Wu and Du [149, 150] have also developed an analytical expression for temperature rise assuming a Gaussian beam approximation.

There are numerous recent implementations of numerical algorithms that modeled heating in tissue using the bioheat equation that are of particular interest. In the first, Kolios *et al*. [101] utilized a finite difference approach to solve the basic equations of heat transfer in perfused tissues in 2-D cylindrical coordinates. Both the effects of regional cooling by the microvasculature and of localized cooling due to thermally significant vessels are investigated. Second, by Curra *et al*. [111] also employed a 2-D finite difference implementation to investigate the importance of nonlinear effects on the space and time properties of wave propagation and heat generation in perfused liver models when a blood vessel also might be present. Fan and Hynynen [209-211] have developed a 3-D numerical model using finite difference technique to solve the bioheat

transfer equation; they used their model to investigate the noninvasive surgery of a tumor by focused transducers and phased arrays employing multiple sonications. Two other numerical simulations of the bioheat equation have also been reported. Wan *et al.* [151] employed a 3-D finite difference implementation using matrix relaxation methods to investigate critical parameters governing the performance of their phased-array system. Meaney *et al*. [152] chose to implement a 3-D finite-element representation of the bioheat equation in which the heat deposition patterns were computed assuming a linear propagation model. More recently, Krasovitski and Kimmel [212] presented a 3-D simulation of the temperature field in and around a blood vessel for a simplified geometry.

2.2 Our Theoretical Model

In our study, we implement a nonlinear 2-D model of acoustic wave propagation that captures not only the focal intensity but also its spatial distribution as well. A 3-D model for both heating (in the presence of blood flow) and acoustic streaming is developed so that off axis insonation could be investigated and any beam and vessel orientation is allowed. The acoustic streaming field is coupled to the bioheat equation to take into account this nonlinear effect of ultrasound, which has never been reported in the previously reviewed literature.

2.2.1 Sound Propagation Model

Our acoustic propagation model is based on an inhomogeneous wave equation that is derived from the basic equations of fluid mechanics and thermodynamics for a

thermoviscous fluid, keeping terms up to second order, thus is appropriate for the propagation of finite amplitude sound in inhomogeneous biological tissue (Hallaj [153]). The wave equation is related to the Westervelt equation [154], with the addition of the loss term. The equation accounts for the combined effects of diffraction, absorption, inhomogeneity, and nonlinearity. This second-order wave equation describing the acoustic pressure in terms of space, time and the fluid's material properties can be written as follows:

$$\left(\nabla^2 - \frac{1}{c^2}\frac{\partial^2}{\partial t^2}\right)p - \frac{1}{\rho}\nabla p \cdot \nabla \rho + \frac{\delta}{c^4}\frac{\partial^3 p}{\partial t^3} + \frac{\beta}{\rho c^4}\frac{\partial^2 p^2}{\partial t^2} = 0, \tag{2.13}$$

where c is the local sound speed, ρ is the local density, δ is the local acoustic diffusivity, and $\beta = 1+B/2A$ is the local coefficient of nonlinearity with B/A being the nonlinear parameter of the medium [155]. The first term in the left hand side of Eq. 2.13 is the D'Alembertian present in all wave equations which describes the propagation of a wave in time and space, the second term accounts for the ambient inhomogeneity in the medium's density and is zero for a homogeneous medium, the third term is the loss term due to the viscosity of the fluid, the standard acoustic absorption coefficient α is related to the acoustic diffusivity by $\alpha = \frac{\delta\omega^2}{2c^3}$ with ω being the angular frequency [154], and the last term captures the nonlinearity during propagation. Our time domain simulation assumes a classical thermoviscous medium in which the absorption increases as the frequency squared, though for tissues the power law for absorption is closer to $f^{1.1}$. This might introduce error in the case of strongly nonlinear propagation waves. However, the current model allows for detailed investigation of spatial and temporal characteristics of

the energy deposition and heating in an arbitrary medium using either pulsed or continuous ultrasound.

It is important to note that the accurate representation of a sound beam in a medium with 3-D variability requires a 3-D propagation model. Although such a model can be numerically implemented in principle, the execution time required for our simulations is prohibitive. We have chosen to assume a 2-D sound field for purpose of modeling the experiments and carrying forth additional simulations. This assumption is supported by two facts. First, the HIFU source we use in experiments is an axially symmetrical transducer. Second, the variability in the acoustic impedance of various structures in tissue is small (bone and lung being notable exceptions). Thus, the impact that these inhomogeneities will have on the sound beam will, in many cases, also be small. *We therefore assume a priori that the sound beam generated by our HIFU transducer will continue to be 2-D axisymmetric throughout its propagation path*. This assumption is supported in the experiments because we purposely chose materials for constructing simulated blood vessels (both the vessel wall and the blood mimicking fluid itself) that are approximately impedance matched to the surrounding tissue phantom material. A 2-D representation is thereby adequate to compute the acoustic pressure and intensity fields while significantly reducing the computational requirements.

For an axisymmetric sound beam that propagates in the positive z direction, Eq. 2.13 can be cast in a cylindrical coordinates, with the nonlinear term expanded into two terms and the loss term represented using the absorption coefficient, as follows,

$$\frac{\partial^2 p}{\partial r^2}+\frac{1}{r}\frac{\partial p}{\partial r}+\frac{\partial^2 p}{\partial z^2}-\frac{1}{c^2}\frac{\partial^2 p}{\partial t^2}-\frac{1}{\rho}\left(\frac{\partial p}{\partial r}\frac{\partial \rho}{\partial r}+\frac{\partial p}{\partial z}\frac{\partial \rho}{\partial z}\right)+\frac{2\alpha}{c\omega^2}\frac{\partial^3 p}{\partial t^3}+\frac{2\beta}{\rho c^4}\left[p\frac{\partial^2 p}{\partial t^2}+\left(\frac{\partial p}{\partial t}\right)^2\right]=0. \quad (2.14)$$

In order to couple the pressure field model to the temperature field model (described below) we need to quantify the thermal energy deposition associated with the absorption of the ultrasonic wave. To do this we employ the following expression from Pierce [156] for the spatially-dependent ultrasonic power deposition per unit volume:

$$q = 2\alpha_{ABS} I = \frac{2\alpha_{ABS}}{\omega^2 \rho c}\left\langle\left(\frac{\partial p}{\partial t}\right)^2\right\rangle, \quad (2.15)$$

where α_{ABS} refers to the local absorption coefficient of the medium, I is the local acoustic intensity, and the brackets denote time average over one acoustic cycle.

2.2.2 Temperature Field Model

We choose the widely used Pennes bioheat transfer equation to model the temperature field. Equation 2.11 is used to simulate the temperature rise in blood domain, and Eq. 2.12 in tissue domain. The two equations are rewritten here for convenience:

$$\rho_t C_t \frac{\partial T}{\partial t} = \mathrm{K}_t \nabla^2 T - w_b C_b (T - T_\infty) + q \qquad (\textit{tissue domain}), \quad (2.16)$$

and

$$\rho_b C_b \frac{\partial T}{\partial t} = \mathrm{K}_b \nabla^2 T - \rho_b C_b (\vec{u} \cdot \nabla T) + q \qquad (\textit{blood domain}), \quad (2.17)$$

where ρ, C, and K are the density, specific heat and thermal conductivity with the subscripts t and b referring to tissue and blood domain, T_∞ refers to the temperature at large distances from the focus. The first term in the right sides of Eq. 2.16 and 2.17 accounts for heat diffusion, the second term of Eq. 2.16 is responsible for blood perfusion

losses with w_b being the perfusion rate, and the second term in Eq. 2.17 captures the advection of heat created by the flow of blood with velocity $\vec{u}$. The term q in both equations is the rate of ultrasonic energy deposition per unit volume defined by Eq. 2.15.

In the blood domain, the flow velocity consists of the sum of two components: the first is the flow profile before HIFU is turned on which is usually assumed to be a parabolic profile as in laminar Pouiseille flow, the second is the imposed flow profile due to acoustic streaming. Thus, the blood flow velocity can be written as:

$$\vec{u} = \vec{u}_{ext} + \vec{u}_{str} = 2U_0\left[1-\left(\frac{r}{r_0}\right)^2\right] + \vec{u}_{str}, \tag{2.18}$$

where $\vec{u}_{ext}$ represents the parabolic Pouiseille flow and $\vec{u}_{str}$ is the acoustic streaming, U_0 is the average velocity of the Pouiseille flow, r is the distance to the flow axis, and r_0 is the radius of the vessel.

2.2.3 Acoustic Streaming Model

There is a considerable body of literature that develops the theoretical basis of acoustic streaming. The fluid motion is described by the continuity and Navier-Stokes equations applied to a viscous incompressible fluid [157]. The driving force of the streaming derives from the acoustic field, is manifested as a momentum transfer from sound waves to fluid motion, and is spatially distributed in the beam. The first theoretical analysis of the time-independent flow circulation associated with high intensity ultrasound beams in an absorbing fluid seems to have been given by Eckart [136], who solved the nonlinear equations of motion in a viscous fluid to a second order

approximation, the oscillatory solution of the linearized equations being taken as a first approximation. Contributions by several authors followed Eckart's pioneering work. Excellent reviews are given by Nyborg [82, 158], Beyer [159], Rudenko and Soluyan [157], and Lighthill [160].

The early theoretical analyses were mainly concerned with plane continuous waves and the solutions of acoustic streaming were based on a second-order approximation. In this approximation, the flow pattern is independent of the first-order acoustic velocity amplitude A, and the streaming speed is proportional to A^2. It was recognized by early investigators that these features apply only when the amplitude and the associated streaming speeds are relatively low [158]. In cases when the second-order velocity is not small compared to the first-order velocity, or the Reynolds number is high, the nonlinear term should be included [159, 160]. Parabolic approximations of nonlinear streaming equations for flows produced by directional sound beams are given by Gusev and Rudenko [161]. More recently, Tjøtta *et al.* [162] pointed out that the hydrodynamic nonlinearity term (convective term) in the Navier-Stokes equation plays an essential role on the generation of acoustic streaming in the beam, in particular, from a strongly focusing source. Others who have dealt with theory for acoustic streaming at higher speeds, especially in applications to focused ultrasound beams, include Wu and Du [163], Mitome [164], Kamakura *et al.* [165], Hamilton *et al.* [166] and Shi *et al.* [167].

The results of an experimental investigation of the mean streaming motions induced by focused ultrasound beams were reported by Starritt *et al.* [168]. They measured the velocity of acoustic streaming in water generated by commercial medical

equipment, and observed that the highest velocity is 14 *cm/s* in the pulsed Doppler mode operation. They also observed that when conditions are such that a propagating wave undergoes nonlinear distortion, the speed of acoustic streaming can be greatly increased. In order to theoretically explain the above experimental results, Wu and Du [163] investigated the streaming velocity along the beam induced by a CW and tone bursts from planar and focusing sources with a Gaussian pressure distribution including acoustic nonlinearity. They employed the method of successive approximations to derive the solution of the Navier-Stokes equation. Using almost the same source parameters as the Starritt *et al*. experiment, they calculated on-axis velocity profiles under steady-state conditions. Unfortunately, their computed results did not agree closely with the experiment. Kamakura *et al*. [165] pointed out that this was because their second-order approximation neglected the hydrodynamic nonlinearity term in the Navier-Stokes equation, which plays an essential role on the generation of acoustic streaming from a strongly focusing source.

Kamakura *et al.* [165, 169] conducted both theoretical and experimental investigations of acoustic streaming generated by focused beams. Good agreement was reported for both the buildup characteristics of the streaming velocity at different observation points and streaming velocity profiles along and across sound beams as a function of time. In their theoretical analysis, axisymmetric nonlinear flow equations for a viscous incompressible fluid were transformed into the vorticity transport and Poisson's equations. They were numerically solved via a finite difference method imposing appropriate initial and boundary conditions. Their studies showed that the velocity slope

changed abruptly around the focus, thus the hydrodynamic nonlinearity cannot be excluded from a theoretical prediction of the streaming. Comparison with linear flow theory revealed that the nonlinearity reduces the streaming velocity in the focal and prefocal region, whereas it tends to accelerate the flow in the postfocal region.

In the previously mentioned theoretical models for describing acoustic streaming, the mean mass-flow velocity, rather than the mean value of the Eulerian velocity, is usually used in the governing equations because its velocity field is solenoidal to a second-order approximation. For a beam of sound, the difference between these two mean motions is roughly given by $\left(\rho_0 c_0^{\,2}\right)^{-1}\vec{I}$ [160]. Here, $\vec{I}$ is the acoustic intensity vector, ρ_0 and c_0 are the ambient density and sound speed, respectively. In general this difference is small enough compared with the observed streaming effect, and it has therefore been discarded in previous theories.

Like the theoretical model proposed by Kamakura *et al.*, we begin with the continuity equation and the Navier-Stokes equation in a viscous incompressible fluid, which are described in the flowing forms:

$$\nabla \cdot \vec{U} = 0, \tag{2.19}$$

$$\frac{\partial \vec{U}}{\partial t} + \left(\vec{U} \cdot \nabla\right)\vec{U} - \frac{\mu}{\rho_0}\nabla^2 \vec{U} = -\frac{1}{\rho_0}\nabla P + \frac{1}{\rho_0}\vec{F}, \tag{2.20}$$

where $\vec{U}$ is the streaming velocity, P is the pressure, μ is the shear viscosity of the medium, ρ_0 and c_0 are the ambient density and sound speed, respectively. The second term in Eq. 2.20 is the convective term which captures hydrodynamic nonlinearity, the third term accounts for viscous stress, and the forth term captures the stress due to

pressure variance in the fluid. $\vec{F}$ in the last term is the force acting on the fluid by the presence of sound, and to a second approximation can be written as [158]

$$\vec{F} = -\rho_0 \left\langle (\vec{u}_1 \cdot \nabla)\vec{u}_1 + \vec{u}_1(\nabla \cdot \vec{u}_1) \right\rangle, \tag{2.21}$$

where $\vec{u}_1$ is the first order approximation for the acoustic particle velocity. The brackets indicate an average over time, whose interval is much shorter than the transient time of streaming and much longer than the acoustic period.

Since our acoustic model gives the space- and time-dependent pressure field, we would like to cast Eq. 2.21 in terms of acoustic pressure rather than particle velocity. Moreover, other approximations can be employed in order to obtain a simpler expression. The axial component of the acoustic particle velocity in an ultrasonic beam is generally much larger than the radial component. This fact also holds true for the driving force of acoustic streaming. If we neglect the radial component of acoustic particle motion, then the force in the acoustic axis direction can be written as follows (taking *z* as the axis of the beam),

$$F_z = -\rho_0 \left\langle 2u_{1z} \frac{\partial u_{1z}}{\partial z} \right\rangle = -\rho_0 \left\langle \frac{\partial u_{1z}^{\,2}}{\partial z} \right\rangle = -\rho_0 \frac{\partial}{\partial z} \left\langle u_{1z}^{\,2} \right\rangle. \tag{2.22}$$

Using a linear impedance relation between the sound pressure and the particle velocity, $p_1 = \rho_0 c_0 u_1$, where p_1 is the first order approximation for the acoustic pressure, Eq. 2.22 can be rewritten as

$$\begin{aligned} F_z &= -\frac{1}{\rho_0 c_0^{\,2}} \frac{\partial}{\partial z} \left\langle p_1^{\,2} \right\rangle = -\frac{1}{c_0} \frac{\partial I}{\partial z} = \frac{2\alpha_{ABS}}{c_0} I, \\ I &= \frac{1}{\rho_0 c_0} \left\langle p_1^{\,2} \right\rangle = \frac{1}{\omega^2 \rho_0 c_0} \left\langle \left(\frac{\partial p_1}{\partial t} \right)^2 \right\rangle, \end{aligned} \tag{2.23}$$

where I is the intensity in the direction of propagation, and $\frac{\partial I}{\partial z} = -2\alpha_{ABS} I$ for a linear approximation, where α_{ABS} is the pressure absorption coefficient of the medium.

2.3 Numerical Implementation

In this section we will present a numerical solution to the model equations described above. Determining the temperature rise due to acoustic absorption is a two-step process, as outlined briefly as follows:

(1) Solve for the steady-state pressure in the tissue and blood domain (Eq. 2.14) based on the known parameters for the acoustic source, the propagation geometry, and material properties. The ultrasonic power deposition per unit volume q and the driving force for acoustic streaming $\vec{F}$ can then be calculated based on Eq. 2.15 and Eq. 2.23.

(2) Incorporate the driving force $\vec{F}$ in the flow equations 2.19 and 2.20 to solve for the spatial- and time-dependent acoustic streaming generated in blood domain. The power deposition q and the instantaneous acoustic streaming velocity field are then fed into the bioheat equations 2.16 and 2.17 for temperature field computation.

A finite-difference-time-domain (FDTD) simulation is implemented to calculate the acoustic pressure, the acoustic streaming and the temperature. The FDTD method relies on discrete differences in place of partial derivatives in the model equations by dividing the spatial and time domains into discrete spatial grid points and discrete time steps [170, 171]. The particular implementation chosen here is an explicit method where

only known values from past time steps are required. The important aspects of the implementation at each step will be described below.

2.3.1 Pressure Field Calculation

Equation 2.14 used to solve for the pressure in the tissue or tissue phantom is presented in 2-D cylindrical coordinate, with the acoustic axis of the source transducer as the *z* (axial) axis. Radial (*r*) position is measured from the axis. The implementation of the numerical solution is based directly on the code developed previously by Hallaj [153]. The desired solution domain, in time and space, is divided into a discrete grid where $p_{i,j}^{n}$ represents the pressure, $p(z_i, r_j, t_n)$, at location indices (*i*, *j*) and time step *n*. The mapping to spatial location and time from these indices is

$$z_i = (i-1)dz, \quad r_j = (j-1)dr, \quad t_n = (n-1)dt, \tag{2.24}$$

where *dz*, *dr*, and *dt* represent the space between grid points and time steps respectively. The differential equations used for Eq. 2.14 are second order accurate in space and time:

$$
\begin{aligned}
&\frac{\partial \rho}{\partial r} = \frac{1}{2dr}\left(\rho^{n}_{i,j+1} - \rho^{n}_{i,j-1}\right),\\
&\frac{\partial \rho}{\partial z} = \frac{1}{2dz}\left(\rho^{n}_{i+1,j} - \rho^{n}_{i-1,j}\right),\\
&\frac{\partial p}{\partial r} = \frac{1}{2dr}\left(p^{n}_{i,j+1} - p^{n}_{i,j-1}\right),\\
&\frac{\partial^2 p}{\partial r^2} = \frac{1}{dr^2}\left(p^{n}_{i,j+1} - 2p^{n}_{i,j} + p^{n}_{i,j-1}\right),\\
&\frac{\partial p}{\partial r} = \frac{1}{2dr}\left(p^{n}_{i,j+1} - p^{n}_{i,j-1}\right),\\
&\frac{\partial^2 p}{\partial z^2} = \frac{1}{dz^2}\left(p^{n}_{i+1,j} - 2p^{n}_{i,j} + p^{n}_{i-1,j}\right),\\
&\frac{\partial p}{\partial t} = \frac{1}{2dt}\left(3p^{n}_{i,j} - 4p^{n-1}_{i,j} + p^{n-2}_{i,j}\right),\\
&\frac{\partial^2 p}{\partial t^2} = \frac{1}{dt^2}\left(p^{n+1}_{i,j} - 2p^{n}_{i,j} + p^{n-1}_{i,j}\right), \quad \text{"}\textit{centered}\text{"}\ \textit{formulation}\\
&\frac{\partial^2 p}{\partial t^2} = \frac{1}{dt^2}\left(2p^{n}_{i,j} - 5p^{n-1}_{i,j} + 4p^{n-2}_{i,j} - p^{n-3}_{i,j}\right), \quad \text{"}\textit{backward}\text{"}\ \textit{formulation}\\
&\frac{\partial^3 p}{\partial t^3} = \frac{1}{2dt^3}\left(6p^{n}_{i,j} - 23p^{n-1}_{i,j} + 34p^{n-2}_{i,j} - 24p^{n-3}_{i,j} + 8p^{n-4}_{i,j} - p^{n-5}_{i,j}\right),
\end{aligned}
\tag{2.25}
$$

Two formulations for the second time derivative are shown. For the explicit method only one unknown term, representing the future pressure value is permissible. With several time derivatives in the equation, one must be chosen to contain this reference to the future value. The second time derivative in the D'Alembertian in the wave equation is chosen because the numerical solution was found to behave best in the original implementation (Hallaj [153]).

Solution domain

Figure 2.1 shows a typical example of the geometry of spatial domain for the simulations presented in this dissertation. It represents a slice along the axial and radial

axes. The curve in the figure indicates the location of the source transducer face. In this case, it simulates the HIFU transducer we use in the experiments, which has an aperture of 3.5 cm in radius and a focal length of 6.264 cm. The source pressure values are specified along this curve as a function of time. The shaded region represents the location of tissue or tissue phantom (the blood and vessel may be present in the tissue, which are not shown here), and the remaining portion of the domain is water.

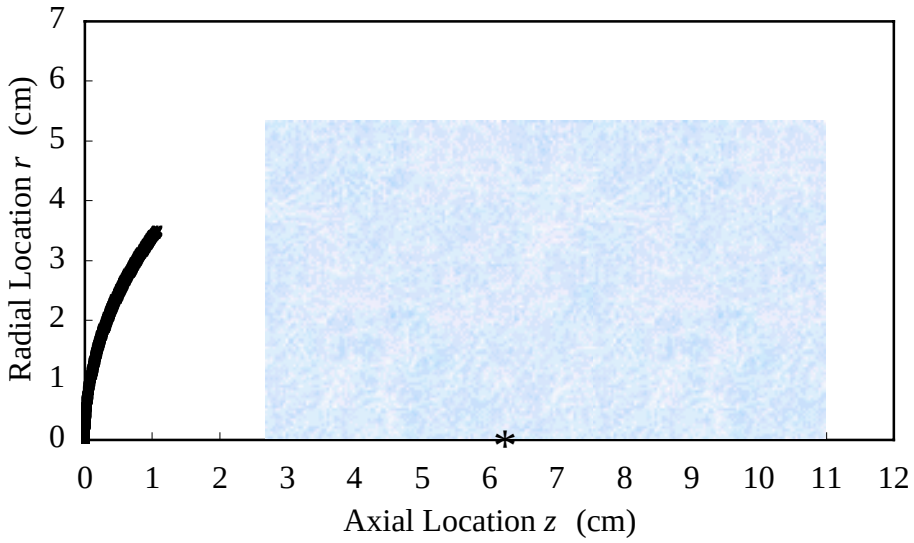

Figure 2.1: A typical example of the geometry of the 2-D FDTD pressure solution domain.

In general, the solution spatial domain should be large enough to include all the variations in the path of wave propagation so that the reflections from any real boundary are taken into account. The reflections from the edges of the computational domain, however, should be prevented or minimized because this is an artifact introduced by numerical simulation that is confined in a limited space. Appropriate boundary conditions will be applied at the computational edges, which will be described in detail below.

It may be necessary to solve the problem for two time domains: (1) short pulses where the transient response is desired or (2) long insonation times where a steady-state pressure field is reached long before the full insonation time expires. The pressure solution will reach steady-state at approximately the time it takes for the wave to propagate to the farthest distance from the source transducer in the solution domain. We will see that in most of our simulations, the pressure solution reaches steady-state in 100 acoustic cycles for a frequency of 1 MHz. This is much smaller than the insonation times we use (1 s or 10^6 cycles, and longer). To conserve time and computing resources, we will only calculate a solution for a fraction of the insonation time necessary to reach steady-state.

Spatial and time grids

Accurate FDTD modeling of wave propagation requires sufficient resolution in space and time with respect to the relevant length and time scales, where the resolution is defined by the separation of the grid points and the time steps. An accurate representation of a sinusoidal waveform generally requires a minimum of 10-12 spatial points per wavelength. For a source frequency of 1 MHz that does not see substantial harmonic generation during propagation, and a speed of sound on the order of 1600 m/s for the tissue or tissue phantom (the wavelength is thus about 1.6 mm), we will be using a grid separation of 0.1 mm. The maximum time step where the stability of the solution is assured is, in general, a function of the spatial grid separation and the speed of sound for wave propagation. For an absorbing wave equation, a simple expression for the

maximum stable time step is not available. However, prior consideration of the stability of this solution has demonstrated that for our grid separation and material properties, a time step of 1×10^{-8} s is sufficient (Hallaj, [153]).

Initial and boundary conditions

The initial condition in all simulations is a pressure value of zero everywhere. This is not required, however; by recalling variables, a simulation could be resumed from past results. An absorbing boundary condition (ABC) is imposed at the edges of the computational domain (except the axis of symmetry) to prevent or to minimize reflections from the edges of the domain (Mur [172]). By doing so the simulations approximate the behavior of waves in infinite media. Low order ABC's are relatively easy to implement. We employ Mur's well known method that applies a radiation condition

$$\frac{\partial p}{\partial x}-\frac{1}{c}\frac{\partial p}{\partial t}=0, \tag{2.26}$$

where x represents r or z in their respective propagation directions. This radiation-condition ABC's is applied along all the edges except at the symmetric axis (r=0), where a symmetric boundary condition is used:

$$\frac{\partial p}{\partial r}=0. \tag{2.27}$$

The intensity distribution

From Eqs. 2.15 and 2.23 we can see that both the spatially-dependent ultrasonic power deposition per unit volume q and the driving force for acoustic streaming in the acoustic axis direction F_z are related to the time-averaged acoustic intensity I. The last 10 acoustic cycles of the pressure simulation are taken as a reasonable basis for determining the intensity. The discrete form we use to calculate the intensity is

$$I_{i,j} = \frac{1}{\rho_{i,j} c_{i,j} \omega^2} \left(\frac{1}{2dt} \right)^2 \sum_{n=1}^{N} \left(3p_{i,j}^{n} - 4p_{i,j}^{n-1} + p_{i,j}^{n-2} \right)^2, \tag{2.28}$$

where N is the number of time steps averaged.

2.3.2 Acoustic Streaming Calculation

The flow equations 2.19 and 2.20 are also solved using the same FDTD approach as in pressure field simulation with the exception that the acoustic streaming simulation is cast in full 3-D Cartesian coordinates in the blood domain. As sketched in Fig. 2.2, the z axis is set to be parallel to the axis of the vessel, and x and y axes orthogonal to the vessel axis. The desired solution domain, in time and space, is divided into a discrete grid where $\vec{U}_{i,j,k}^{n}$ represents the streaming velocity, $\vec{U}(x_i, y_j, z_k, t_n)$, at location indices ($i$, j, k) and time step n. The mapping to spatial location and time from these indices is

$$x_i = (i-1)dx, \quad y_j = (j-1)dy, \quad z_k = (k-1)dz, \quad t_n = (n-1)dt, \tag{2.29}$$

where dx, dy, dz, and dt represent the space between grid points and time steps respectively.

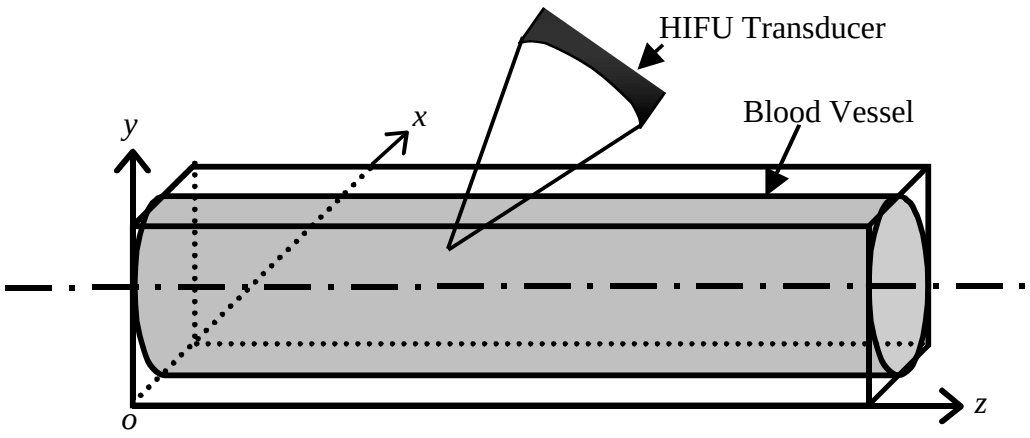

Figure 2.2: The geometry of the 3-D FDTD acoustic streaming solution domain.

For convenience, Eq. 2.20 is rewritten here as follows:

$$\frac{\partial \vec{U}}{\partial t} = N\left(\vec{U},\vec{F}\right) - \frac{1}{\rho_0}\nabla P,$$
$$N\left(\vec{U},\vec{F}\right) = -\left(\vec{U}\cdot\nabla\right)\vec{U} + \frac{\mu}{\rho_0}\nabla^2\vec{U} + \frac{1}{\rho_0}\vec{F}. \tag{2.30}$$

Since the two unknowns $\vec{U}$ and P are coupled in Eq. 2.30, an intermediate variable $\vec{U}^*$ is introduced at each time step to facilitate the numerical procedure:

$$\frac{\vec{U}^* - \vec{U}^n}{dt} = N\left(\vec{U}^n,\vec{F}^n\right), \tag{2.31}$$

$$\frac{\vec{U}^{n+1} - \vec{U}^*}{dt} = -\frac{1}{\rho_0}\nabla P^{n+1}, \tag{2.32}$$

Note that the addition of Eqs. 2.31 and 2.32 goes back to Eq. 2.30, with the first time derivative of $\vec{U}$ represented by the difference equation. Apply a divergence manipulation on both sides of Eq. 2.32, we get

$$\nabla^2 P^{n+1} = \frac{\rho_0}{dt}\left(\nabla\cdot\vec{U}^* - \nabla\cdot\vec{U}^{n+1}\right). \tag{2.33}$$

The condition of continuity (Eq. 2.19) requires that

$$\nabla \cdot \vec{U}^{n+1} = 0. \tag{2.34}$$

Equation 2.33 is thus written as

$$\nabla^2 P^{n+1} = \frac{\rho_0}{dt} \nabla \cdot \vec{U}^{*}. \tag{2.35}$$

Therefore, $\vec{U}$ and P are uncoupled such that Eq. 2.31 is solved first to get $\vec{U}^{*}$, Eq. 2.35 is solved secondly to get P^{n+1}, and finally Eq. 2.32 is solved which gives the result for $\vec{U}^{n+1}$.

The iteration method of SOR (successive over-relaxation) is used to solve the pressure field (Eq. 2.35) at each time step. This method is helpful for solving large-scaled linear algebraic equation as fast as possible [173].

The difference equations used for Eqs. 2.31, 2.32 and 2.35 are second order accurate in space and time:

$$\begin{aligned}
\frac{\partial \mathrm{X}}{\partial x} &= \frac{1}{2dx}\left(\mathrm{X}_{i+1,j,k} - \mathrm{X}_{i-1,j,k}\right), \\
\frac{\partial^2 \mathrm{X}}{\partial x^2} &= \frac{1}{dx^2}\left(\mathrm{X}_{i+1,j,k} - 2\mathrm{X}_{i,j,k} + \mathrm{X}_{i-1,j,k}\right), \\
\frac{\partial \mathrm{X}}{\partial y} &= \frac{1}{2dy}\left(\mathrm{X}_{i,j+1,k} - \mathrm{X}_{i,j-1,k}\right), \\
\frac{\partial^2 \mathrm{X}}{\partial y^2} &= \frac{1}{dy^2}\left(\mathrm{X}_{i,j+1,k} - 2\mathrm{X}_{i,j,k} + \mathrm{X}_{i,j-1,k}\right), \\
\frac{\partial \mathrm{X}}{\partial z} &= \frac{1}{2dz}\left(\mathrm{X}_{i,j,k+1} - \mathrm{X}_{i,j,k-1}\right), \\
\frac{\partial^2 \mathrm{X}}{\partial z^2} &= \frac{1}{dz^2}\left(\mathrm{X}_{i,j,k+1} - 2\mathrm{X}_{i,j,k} + \mathrm{X}_{i,j,k-1}\right),
\end{aligned} \tag{2.36}$$

where X represents P^{n+1}, or the *x*, *y*, *z* components of $\vec{U}^{n}$ and $\vec{U}^{*}$.

Spatial and time grids

In most of our simulations, the vessel size is of the order of 1 mm. To adequately represent the flow pattern, fine spatial discretization is necessary in the transverse direction to the vessel axis, *i.e.*, in the *x* and *y* direction. We thus maintain *dx* and *dy* to be 0.1 mm, the same spatial discretization as in the pressure field calculation. The spatial discretization in the vessel axis direction, *dz*, is chosen to be 0.2 mm for a slower velocity gradient in this direction. As compared to the pressure solution, the relatively slow rate of change of the streaming response with respect to the acoustic frequency means that the resolution in time may be reduced by orders of magnitude. We have found that, a time step of 0.5 ms is sufficient for stability and accuracy.

Initial and boundary conditions

We consider acoustic streaming to be a perturbation to the main flow of blood circulation in a vessel, and thus it can be treated separately. As soon as ultrasound is radiated into the fluid, the driving force is instantaneously generated in the beam, and acoustic streaming begins from velocity zero. We can therefore state the initial conditions

$$\vec{U} = 0 \qquad at \quad t = 0. \tag{2.37}$$

Because of viscosity, the streaming velocity must vanish everywhere on the inner surface of the vessel, a non-slip boundary condition is applied at the vessel wall:

$$\vec{U} = 0 \qquad at \quad vessel\ wall. \tag{2.38}$$

A continuous boundary condition is imposed at the inlet and outlet of the computational domain. By doing so the simulations approximate the behavior of flows in a tube with open ends:

$$\hat{n} \cdot \nabla \vec{U} = 0 \qquad \textit{at} \quad \textit{inlet and outlet,} \tag{2.39}$$

where $\hat{n}$ is the unit vector in the direction of inlet/outlet.

The 3-D driving force

As shown in Eq. 2.23, the spatially-dependent driving force for acoustic streaming in the acoustic axis direction is proportional to the time-averaged acoustic intensity *I*. Since the pressure solution is in 2-D cylindrical coordinate and the acoustic streaming is in 3-D Cartesian coordinate, we need to map the intensity from 2-D to 3-D.

For convenience, the acoustic intensity in 2-D is represented here as $I_{2d}(r_{2d}, z_{2d})$, where r_{2d}, and z_{2d} are the coordinates in the pressure simulation. The acoustic intensity in 3-D is represented as $I_{3d}(x,y,z)$, where *x*, *y*, and *z* are the coordinates in the 3-D Cartesian coordinate. The 3-D simulation allows for any insonation geometry (as shown in Fig. 2.2). For the acoustic axis in the direction (n_{ax}, n_{ay}, n_{az}) and the focus at the location (x_f, y_f, z_f) in the 3-D Cartesian coordinate, the mapping of intensity from 2-D to 3-D is as follows:

$$I_{3d}(x,y,z) = I_{2d}(h(x,y,z), l_f \pm l(x,y,z)), \tag{2.40}$$

where *h(x,y,z)* is the distance from *(x,y,z)* to the acoustic axis, *l(x,y,z)* is the distance from *(x,y,z)* to the focal plane, and l_f is the focal length. If *(x,y,z)* is further away from the

source relative to the focus, a "+" sign is chosen. On the other hand, if *(x,y,z)* is closer to the source compared to the focus, a "-" is used. The formulations used to calculate *h(x,y,z)* and *l(x,y,z)* are listed below:

$$h(x,y,z)=\sqrt{(x-x_p)^2+(y-y_p)^2+(z-z_p)^2}, \tag{2.41}$$

$$x_p=\frac{1}{r_p}\left[\left(n_{ay}^2+n_{az}^2\right)x_f+n_{ax}^2x+n_{ax}n_{ay}(y-y_f)+n_{ax}n_{az}(z-z_f)\right],$$

$$y_p=\frac{1}{r_p}\left[\left(n_{ax}^2+n_{az}^2\right)y_f+n_{ay}^2y+n_{ax}n_{ay}(x-x_f)+n_{ay}n_{az}(z-z_f)\right],$$

$$z_p=\frac{1}{r_p}\left[\left(n_{ax}^2+n_{ay}^2\right)z_f+n_{az}^2z+n_{ax}n_{az}(x-x_f)+n_{ay}n_{az}(y-y_f)\right],$$

$$r_p=n_{ax}^2+n_{ay}^2+n_{az}^2,$$

and

$$l(x,y,z)=\frac{\left|n_{ax}(x-x_f)+n_{ay}(y-y_f)+n_{az}(z-z_f)\right|}{\sqrt{n_{ax}^2+n_{ay}^2+n_{az}^2}}. \tag{2.42}$$

Therefore, the driving force for acoustic streaming can be represented as

$$F_x(x,y,z)=\frac{n_{ax}}{\sqrt{n_{ax}^2+n_{ay}^2+n_{az}^2}}\frac{2\alpha_b}{c_b}I_{3d}(x,y,z),$$

$$F_y(x,y,z)=\frac{n_{ay}}{\sqrt{n_{ax}^2+n_{ay}^2+n_{az}^2}}\frac{2\alpha_b}{c_b}I_{3d}(x,y,z),$$

$$F_z(x,y,z)=\frac{n_{az}}{\sqrt{n_{ax}^2+n_{ay}^2+n_{az}^2}}\frac{2\alpha_b}{c_b}I_{3d}(x,y,z), \tag{2.43}$$

where $F_x, F_y,$ and F_z are the force components in the *x*, *y*, and *z* direction, and α_b and c_b are the acoustic absorption coefficient and the sound speed of the blood, respectively.

2.3.3 Temperature Field Calculation

The numerical implementation of the bioheat equation is analogous to the acoustic streaming solution using FDTD approach in full 3-D Cartesian coordinates. Again, the *z* axis is set to be parallel to the axis of the vessel, and *x* and *y* axes orthogonal to the vessel axis, as shown in Fig. 2.3. The solution domain is limited to the region of the tissue or tissue phantom. The simulation allows for any insonation geometry.

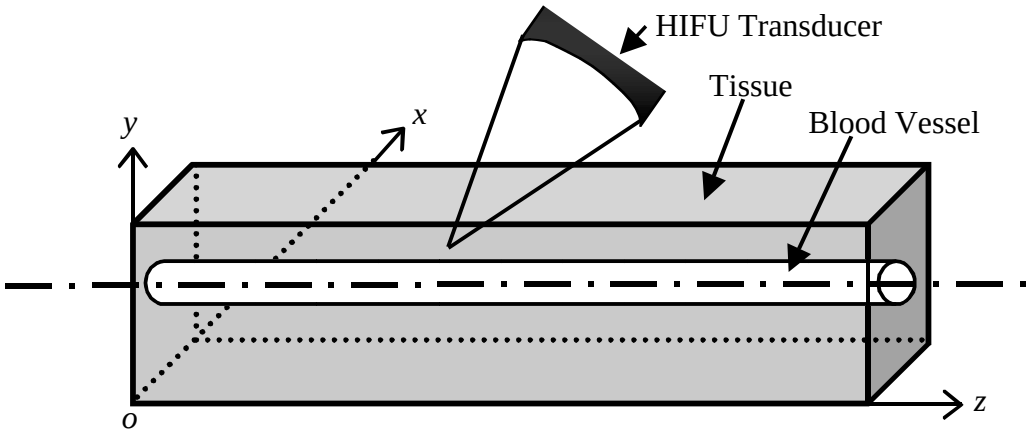

Figure 2.3: The geometry of the 3-D FDTD temperature solution domain.

We should mention here that it is not necessary that the vessel axis be in the *z* direction as we sketched in Fig. 2.3. Since our simulation is in 3-D, the calculation allows for any vessel orientation. Although only one vessel is shown in Fig. 2.3, this is not necessary either. In fact, our 3-D model allows for an arbitrary number of vessels to be present in the calculation domain. Of course, calculations with more vessels will require simultaneously solving the acoustic streaming in each vessel domain, and thus will substantially increase the computational time. To save the computational resources, we

only include one vessel in each simulation. This is deemed adequate for us to study the effect of blood flow cooling (including the acoustic streaming) on tissue heating during HIFU exposure. For the one-vessel configuration, it is most convenient to set the vessel axis in the *z* direction.

The discretized partial derivatives in space used for Eqs. 2.16, and 2.17 are the same as those for the acoustic streaming, as represented in Eq. 2.36. For $\partial T/\partial t$, a centered difference is used to determine the next temperature value in time:

$$\frac{\partial T}{\partial t} = \frac{1}{2dt}\left(T_{i,j,k}^{n+1} - T_{i,j,k}^{n-1}\right). \tag{2.44}$$

Spatial and time grids

For the same reason as that we described earlier, we maintain the same spatial discretization in the temperature calculation as that in the acoustic streaming solution, *i.e.*, $dx=dy$=0.1 mm, dz=0.2 mm. The maximum time step required for the stability of the solution is a function of the spatial grid separation and the maximum flow rate present in the blood domain. A simple expression for the maximum stable time step is, again, not available. However, for a fixed spatial grid separation, the maximum stable time step will decrease as the maximum flow rate increases. Therefore, to assure stable solution and to save the computational resource, we will scale the time step in the temperature calculation to accommodate the maximum flow rate present in the blood domain. The resulting time step used in each simulation will be specified when the results are presented.

Initial and boundary conditions

The initial condition is simply the ambient temperature T_∞ at every point for simulations of experiments performed using the tissue phantom, or 37°C for simulations using real human tissue properties. Usually, there is a large reservoir of water surrounding the tissue or tissue phantom, which serves as an excellent constant-temperature boundary condition. However, this isothermal condition cannot be applied at the flow outlet because the high flow rate will convect heat to that region quickly so that there is not enough time for the heat to diffuse into the surrounding medium. Therefore, a continuous boundary condition is applied at the boundary surface containing the flow outlet, and an isothermal boundary condition is applied at all other computational boundaries.

The 3-D ultrasonic power deposition

Analogous to the driving force for the acoustic streaming, the spatially-dependent ultrasonic power deposition per unit volume, q, is proportional to the time-averaged intensity I (Eq. 2.15). Since the temperature field is also simulated in 3-D Cartesian coordinates, a 3-D intensity field representation converted from 2-D solution (Eqs. 2.40-2.42) is needed to calculate the 3-D ultrasonic power deposition, which is as follows:

$$q(x,y,z) = 2\alpha(x,y,z)I_{3d}(x,y,z), \tag{2.45}$$

where $\alpha(x, y, z)$ is the local acoustic absorption coefficient at (x, y, z).

In summary, the numerical approach involves several smaller steps, which are depicted in Fig. 2.4. Another issue we should mention here, one that relates to the time

steps used in the acoustic streaming and the temperature field calculations. Although both the acoustic streaming field and the temperature field are solved simultaneously, the time steps used for these two calculations are not necessarily the same. As we discussed in Section 2.3.2, the maximum time step required for the stability of the temperature field solution will decrease when the maximum flow rate increases. As a result, a much smaller time step is required for the temperature solution than that for the acoustic streaming solution in case of high flow rate present in the blood domain. To save the computational time while assuring accuracy, different time steps are chosen for the two calculations. For example, if the time steps used for temperature and acoustic streaming calculations are dt_T and dt_U, respectively, they usually have a relation as $dt_U = N dt_T$, where N is an integer larger than 1.

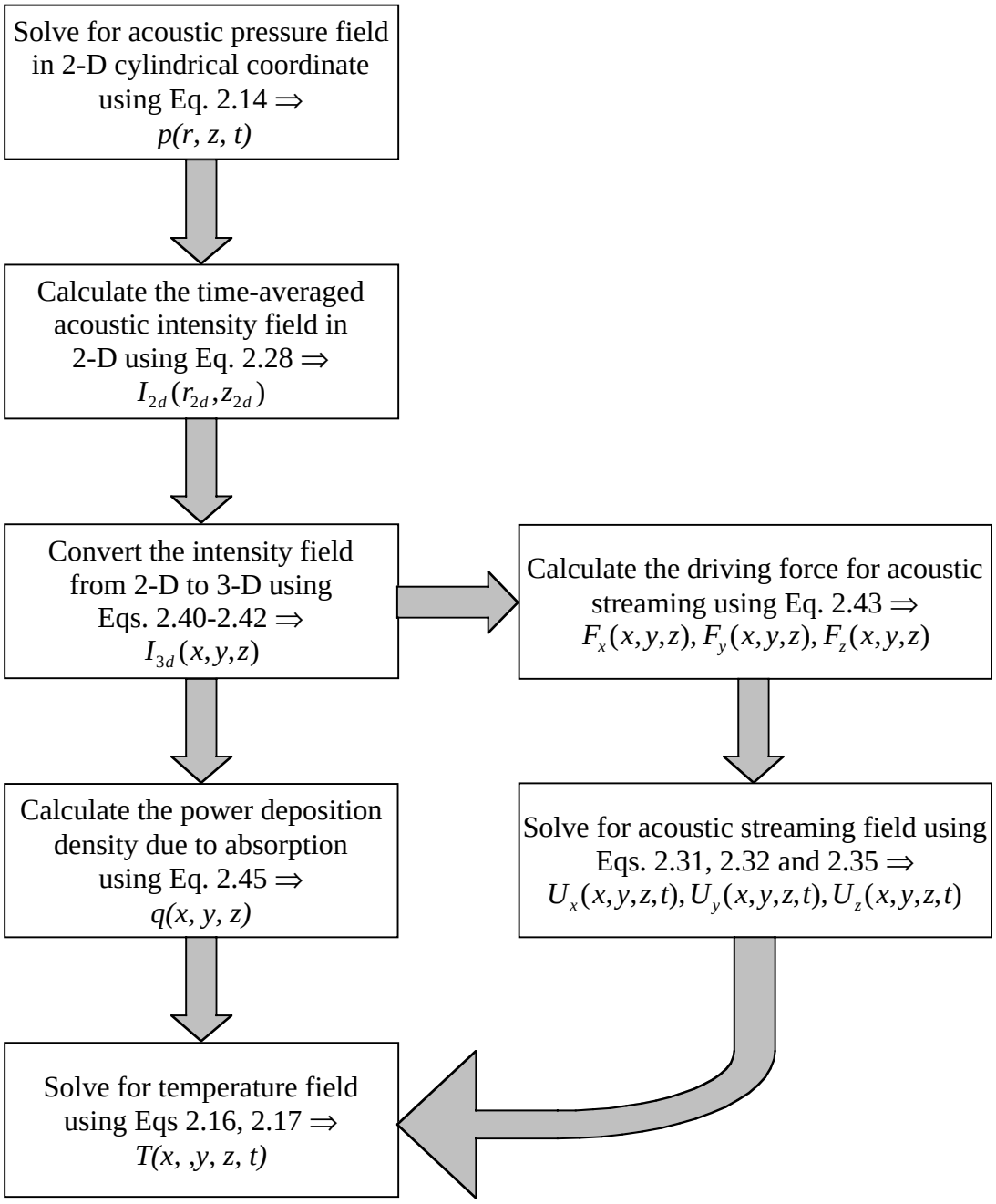

Figure 2.4: General flow of the calculations presented in this dissertation.

2.3.4 Example of Model Predictions

In this section we take a qualitative look at the acoustic intensity field generated by a HIFU source and the resulting temperature field predicted by our model. The example presented here is a tissue phantom insonated by our HIFU source at 1 MHz for 1 second (as sketched in Fig. 2.1). Table 2.1 lists the tissue phantom properties used by the model. These values are consistent with measurements of the tissue phantom materials used in Chapter 3.

Property	Tissue Phantom	Water
Density (kg/m^3)	1044	998
Sound Speed (m/s)	1568	1483
Attenuation ($Np/m/MHz$)	8.55	0.025
Specific Heat ($J/kg\cdot^0C$)	3710	N/a
Thermal Conductivity ($W/m\cdot^0C$)	0.59	N/a

Table 2.1: Material properties used in the example of model predictions. The properties of water are required to calculate the pressure.

Figure 2.5 shows a plot of the acoustic intensity as a function of radial and axial location for a peak negative pressure amplitude of 1.11 MPa at the focus. The intensity is plotted in *log* scale (*10logI*) for better visualization. The axial location is with respect to the phantom not the transducer. The radial location is with respect to the acoustic axis of the source. The solution is calculated in the half-radial domain as indicated previously. This half solution is mirrored in the plot to better illustrate the complete field.

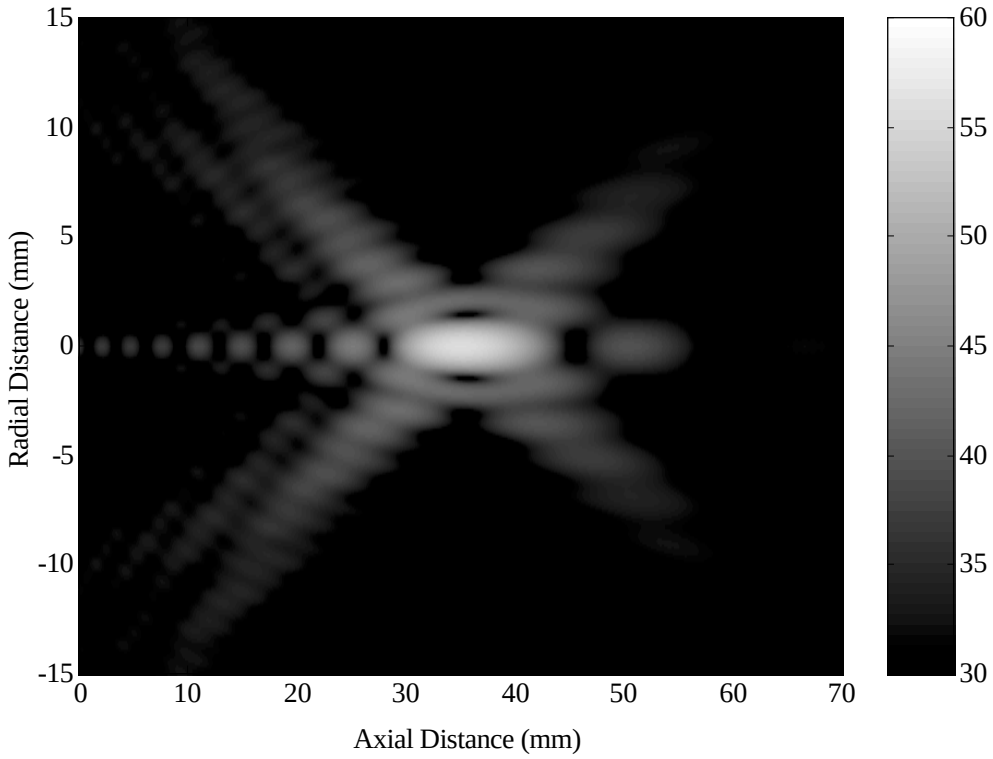

Figure 2.5: Acoustic intensity (in *log* scale) as a function of axial and radial location for FDTD solution to the wave equation. The peak negative pressure at the focus is 1.11 MPa.

The high intensity region is cigar shaped, lying along the beam axis. The side lobes can be explained by a well-known diffraction phenomenon [174, 175]. The pressure generated by a focusing source is the addition of two components. The first one is a purely spherical component while the second one has its origin in the diffraction from the circular edge of the source. Side lobes appear at those locations where the diffracted waves issued from each portion of the edge are in phase and they coherently add to form the second component. The second component therefore interferes significantly with the first component, producing oscillations with periodic pressure zeros. At locations where the second component is composed of diffracted waves adding incoherently, the second

component loses its importance and the first component plays the main role. In that case the phase anomaly is similar to that of a purely spherical wave.

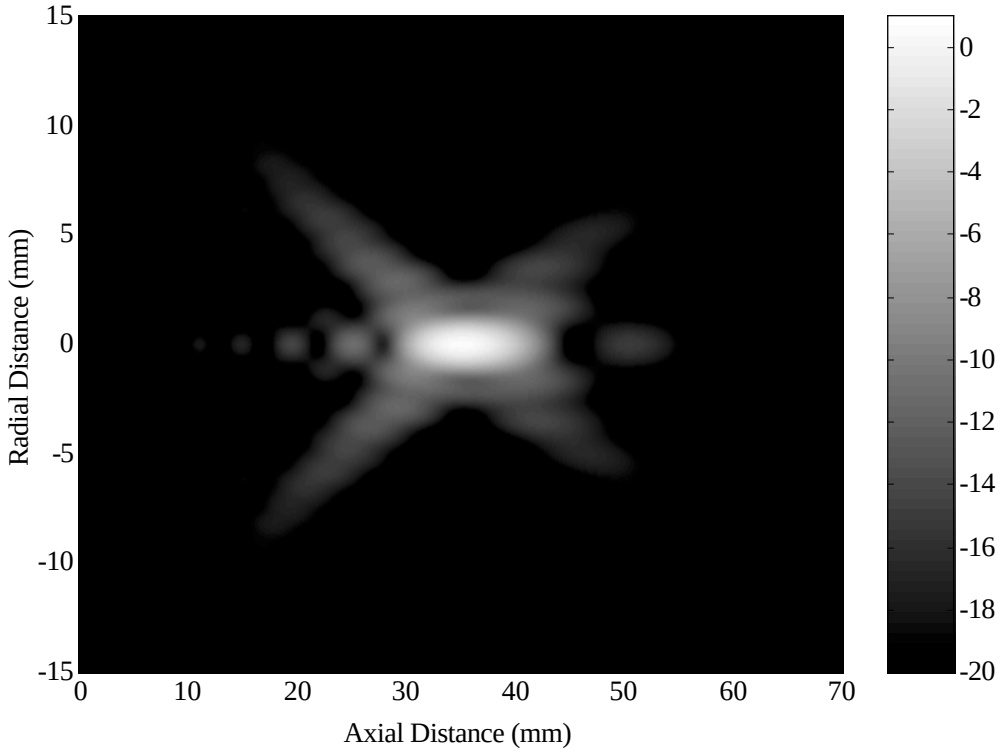

Figure 2.6: Temperature change (in *log* scale) as a function of axial and radial location for FDTD solution to the bioheat equation. The peak negative pressure at the focus is 1.11 MPa.

Figure 2.6 shows a plot of the resulting temperature change in the tissue phantom at the end of 1-second insonation as a function of radial distance off-axis and axial distance in the phantom. The temperature is also plotted in *log* scale (*10logT*). The side lobes in the intensity field are mitigated in the temperature response due to the smoothing effect of conduction. In general, our model suggests the temperature change should be nearly proportional to the intensity.

2.4 Summary

In this chapter we discussed the heating of tissue with vascular structure due to HIFU exposure. A 3-D numerical simulation of the bioheat equation (in both the tissue and blood domain) has been developed, with a 2-D nonlinear acoustic propagation model and a 3-D acoustic streaming model. In the following chapter we will describe the experiments that are designed to test this model. The experimental results and their comparison with the numerical simulations will be presented in Chapter 4.

Chapter 3

Experimental System and Approach

The experiments performed as part of this dissertation were motivated by the goal to verify the models we developed in Chapter 2. An apparatus was developed that could measure the acoustically induced temperature rise in a flow-through tissue-mimicking phantom with varying flow size and flow rate. As we know, the difficulties of *in vivo* studies arise from the complexity of the medium, and thus the uncertainty of the mechanisms governing the biological effect. It is also difficult to perform *in situ* measurement noninvasively *in vivo*. Consequently, we employ *in vitro* experiments that admit the precise control of various acoustic parameters and quantify the extent of the effect. This may eventually allow us to identify and rank-order the candidate physical mechanisms in terms of relative importance, and determine if and when it is possible to manipulate the acoustic field to enhance the coagulating action. Therefore, an important attribute of our experimental arrangement will be the ability to measure and to control the insonification parameters and physical properties of the medium.

A schematic of the measurement apparatus is shown in Fig. 3.1. The acoustic source and tissue phantom are immersed in filtered, deionized, and degassed water contained in a 58-cm long, 43-cm wide and 46-cm high acrylic tank, which is open to the atmosphere. A function generator generates the source waveforms. The generator output

is amplified and routed to the focused HIFU transducer. A three-dimensional computer-controlled positioning system is used to move the transducer along the beam axis and in both orthogonal directions. We have an axially symmetric tissue phantom setup in which the flow is in a straight "vessel" which is aligned collinearly with the acoustic axis or radially displaced from the axis of the beam of sound. The flow is created by gravity feed, and a flow control and monitor system is used to vary and stabilize the flow rate. We have thermocouples that can monitor the temperature in the flow (central focus, upstream and downstream, and near wall) and in the outer "tissue" (near wall and further away). We also have a calibrated needle hydrophone embedded in the phantom for *in situ* pressure measurements and position calibration. The hydrophone voltage is sampled using a digital oscilloscope. The function generator, the oscilloscope and the processed thermocouple output are connected to a computer so that we can control the source level, capture the *in situ* pressure, and monitor the temperature field using LabVIEW.

The apparatus can be conveniently divided into five primary components: (1) sound generation, (2) flow generation, (3) flow-through tissue phantom, (4) temperature measurement, and (5) pressure calibration. Detailed descriptions of all components are provided in subsequent sections. Measurement systems and approaches for determining the thermal and acoustic properties of tissue and blood mimicking material are also described in this chapter.

At this point it is important that we stress that, although we would like to employ materials and experimental arrangements that closely simulate biological media, that is, in fact, a secondary consideration. Our primary goal is to validate our numerical models.

Therefore, we choose experimental arrangements that facilitate precise measurements and unambiguous comparison with model predictions.

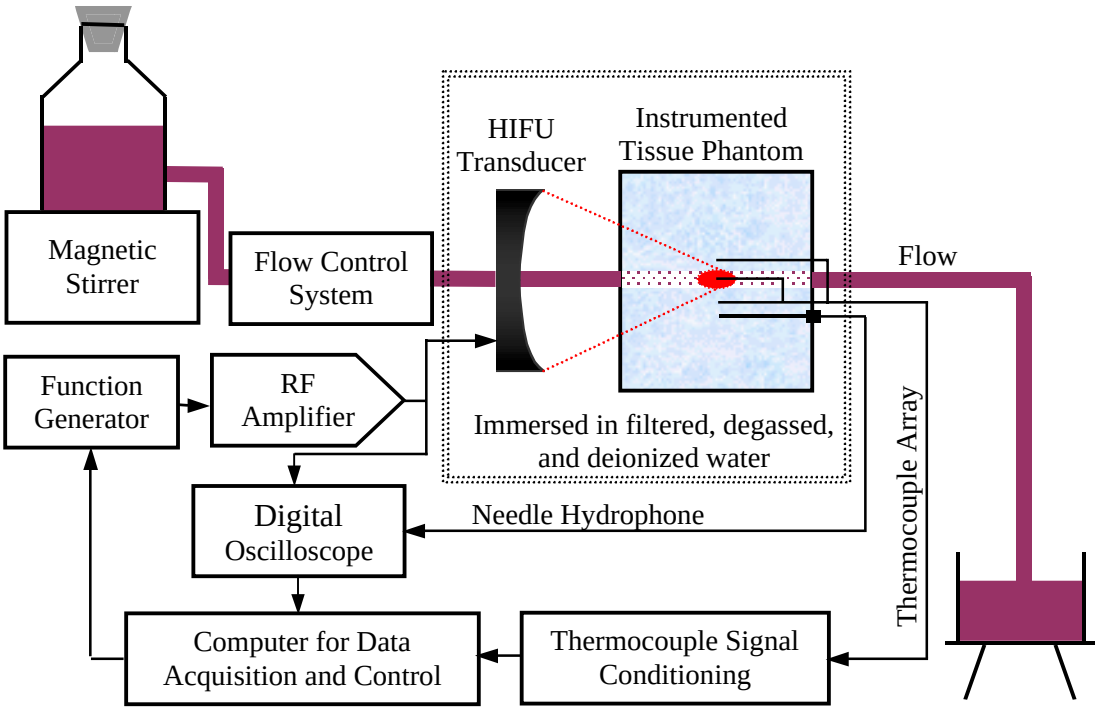

Figure 3.1: Schematic diagram of the apparatus. The HIFU transducer has a hole in the center through which we feed the simulated vascular flow.

3.1 Acoustic Generation System

Our acoustic sources include two single-element, spherically focused, piezoceramic transducers (Sonic Concepts, Woodinville, WA), one (Model H-102) with a hole of diameter 20.0 mm in the center, and the other one (Model H-101) without a hole. A photo of the transducers is shown in Figure 3.2. The H-102 is suitable for on-axis or off-axis parallel insonation (flow axis is parallel to acoustic axis) in flow-through

phantom experiments. Both transducers have a focal length of 62.64 mm, an aperture of 70.0 mm and a center frequency of 1.1 MHz.

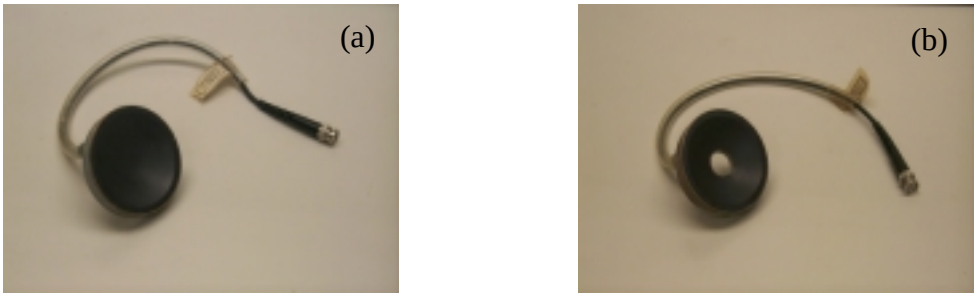

Figure 3.2: Sonic Concepts HIFU transducers: (a) Model H-101; (b) Model H-102.

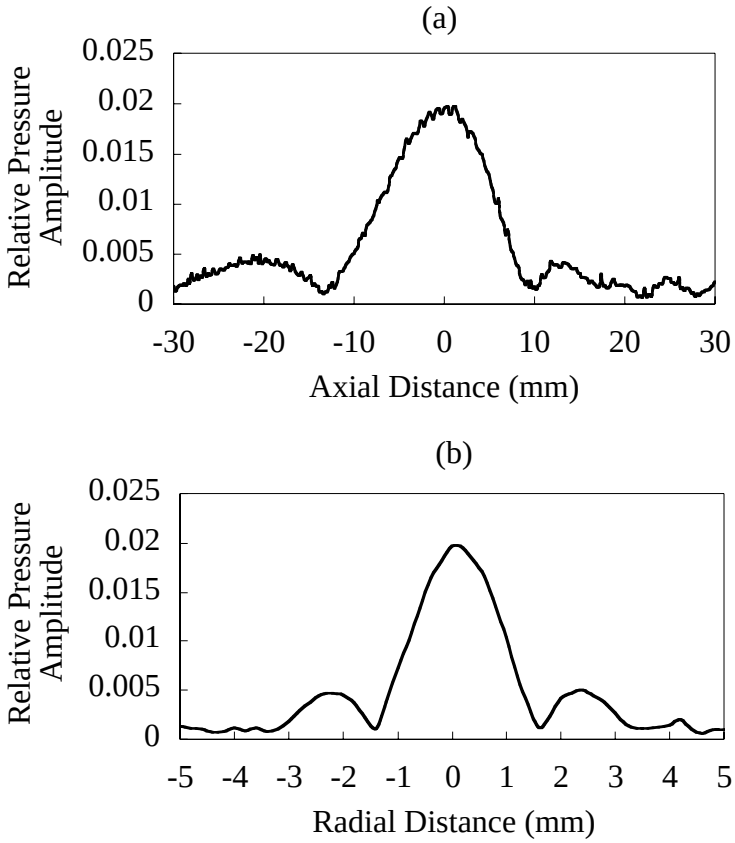

Figure 3.3: The HIFU beam of H-102: (a) axial beam pressure profile; (b) radial beam pressure profile in the focal plane.

In most of our experiments the transducer is driven at 1 MHz using a continuous sinusoidal voltage produced from a function generator (33120A, Hewlett Packard) and passed through a RF amplifier (A-500, 60 dB fixed gain, Electronic Navigation Industries, Rochester, NY). The acoustic pressure field from the system is characterized in water using a calibrated PVDF membrane hydrophone (Model 804, 0.6 mm active element, Perceptron, Hatboro, PA, calibrated by the National Physical Laboratory in the U.K.). A beam plot is shown in Fig. 3.3. The high intensity region is cigar shaped, lying along the beam axis, and is about 15 mm long in the axial direction and 1.5 mm in diameter in the transverse direction.

3.2 The Instrumented Tissue Phantom

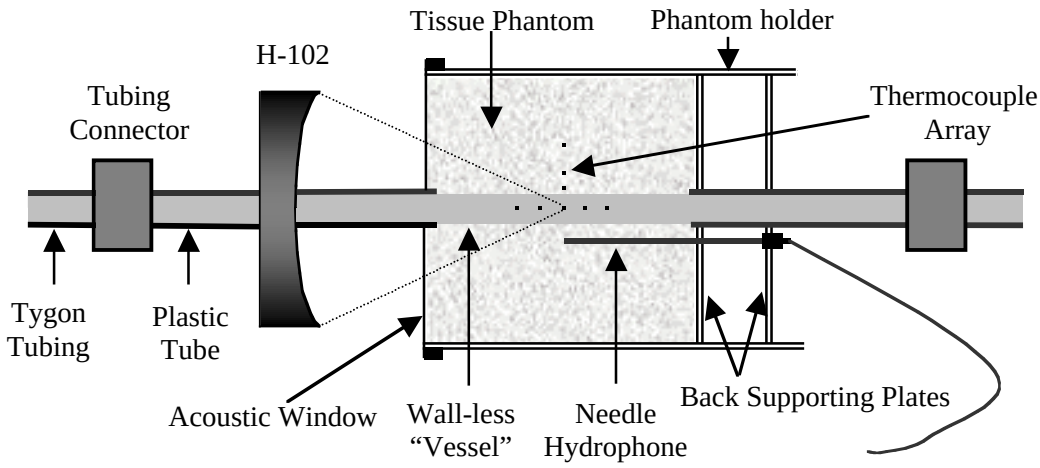

Figure 3.4: Schematic diagram of the instrumented tissue phantom.

Figure 3.4 is a detailed diagram of the instrumented flow-through tissue phantom configured for an on-axis insonation. All is submerged in deionized and degassed water. The phantom is fixed in space and the transducer can be moved both axially and laterally. The extent of lateral motion is limited by the size of the "vessel" and the diameter of the hole in the center of the H-102 transducer. This axially symmetric phantom is 10.72 cm in diameter and 8 cm in length, in which the flow is in a "vessel" along the acoustic axis. The phantom holder is made from a cast acrylic tube with inner diameter of 10.72 cm. The "vessel" in the phantom is wall-less except at a small region at the two ends. The "blood" simulant flows through rigid plastic tubes (cellulose acetate propionate, wall thickness 0.6 mm) with an inner diameter that is the same as that of the "vessel" before and after it enters the phantom. The plastic tubes are connected to Tygon tubing with the same inner diameter, which are connected to the flow generation system. Thermocouples (see Section 3.4) are built into the flow and embedded in the outer "tissue". A needle hydrophone is built into the outer "tissue" close to the flow, with its tip at the focal plane. The two back plates are to support the plastic tube and the needle hydrophone. There are two holes in the second plate for the water to enter and fill between the two plates. An acoustic window (transparency film) is placed in the front surface of the tissue phantom to secure the phantom and the front plastic tube.

To facilitate distribution of thermocouple arrays in the flow, we fabricate wall-less single "vessel" flow-through phantoms using two identical hemi-cylinders as molds. To do this, we cast the phantom hemi-cylinders, build in thermocouples, and clamp the two halves together. Each hemi-cylinder is cast with a hemi-cylindrical trough along the

surface (see Fig. 3.5). When the two halves are clamped together, what results is a circular channel that acts as a wall–less vessel running along the axis of the cylinder.

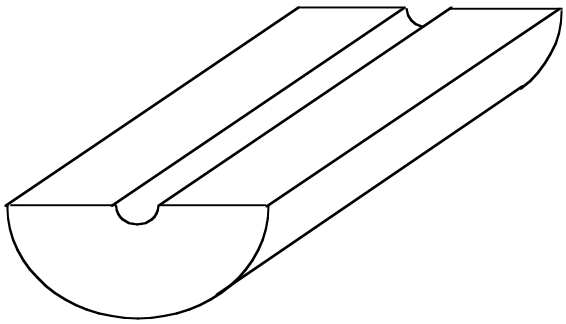

Figure 3.5: Oblique view of one of the cast hemi-cylindrical phantom segments showing the flow channel. The diameter of the hemi-cylinder is 10.72 cm and its length is 8 cm.

3.2.1 Tissue-Mimicking Material

We have two recipes for making tissue-mimicking materials that simulate both the acoustical properties and thermal properties of human tissue. The first is an agar-based graphite phantom and the second is an acrylamide gel. Most of our experiments are conducted on agar-based graphite phantoms because they are easily made and their properties are relatively easily controlled. Although no experimental data using the acrylamide gel will be presented, the recipe and its properties will still be described here as a source for future investigation. In fact, acrylamide gel is ideal for flow visualization since it is optically clear. This attractive feature is also the initial reason we developed this recipe.

Agar-based phantom

The agar-based phantom material is a mixture of water, agar, graphite powder (acts as a scatterer), methyl paraben (acts as a preservative), and 1-propanol (acts as sound speed tuning). The specific quantities of each component depend on the desired properties of the resulting phantom. To create the phantom mixture, water is first heated to a minimum of 85°C. Then agar and methyl paraben are added one at a time and mixed well at this temperature. As the mixture cools, the graphite powder is added at about 80°C, and then 1-propanol is added at about 70°C. The well-mixed liquid may then be degassed by exposure to a vacuum if desired. The mixture should remain in a thermal bath (about 70°C) to maintain a liquid state while degassing. The degassed mixture is finally poured into the mold with the thermocouples and hydrophone already in position. It is then covered and left to sit for at least half a day to cool and gel. The phantom should be isolated from air before and after solidification (to avoid drying and in-gassing). Therefore, molds must be designed to be airtight for the purpose of casting and storage. Alternatively the phantoms may be stored in degassed water.

Table 3.1 lists the recipe for the agar phantoms used in this research. Table 3.2 specifies the measured phantom properties using techniques described in Section 3.6. The corresponding values for human soft tissue are also listed for reference [176].

The most appealing feature of the agar-based phantoms is that the critical acoustical properties of the phantoms (sound speed and attenuation) can easily be varied by altering the phantom recipe and can be controlled independently. The sound speed can be changed by varying the percentage of 1-propanol, the attenuation can be reduced by

using less graphite powder, and both have a nearly linear dependence on the weight percentage [177]. For example, the attenuation is reduced by approximately 50% if only half the amount of graphite powder is used [178]. However, because this kind of phantom is black and totally optically opaque, it causes difficulties in flow phantom fabrication and more importantly, is not suitable for flow visualization.

Component	Amount
Water	600 ml
Agar	18 g
Methyl Paraben	0.75 g
Graphite	54 g
1-propanol	50 ml

Table 3.1: Agar-based tissue phantom recipe.

Property	Agar Phantom	Human Tissue [176]
Density (kg/m^3)	1045	1000-1100
Sound Speed (m/s)	1551	1450-1640
Attenuation ($Np/m/MHz$)	10.17	4.03-17.27
Specific Heat ($J/kg\cdot^0C$)	3710	3600-3890
Thermal Conductivity ($W/m\cdot^0C$)	0.59	0.45-0.56

Table 3.2: Measured acoustic and thermal properties of agar phantom and human tissue.

Acrylamide gel

Acrylamide gel is an optically transparent tissue-mimicking material that is ideal for flow visualization. It is formed by co-polymerization of acrylamide and bis-acrylamide (N,N-methylene-bis-acrylamide) [179]. Polymerization is initiated by TEMED (tetramethylethylenediamine) and ammonium persulfate. In our recipe, 5 ml 30% acrylamide stock solution (mix 29.2 g acrylamide powder and 0.8 g bis-acrylamide, increase sample volume to 100 ml with purified water), 8.4 ml purified water, and 1.5 ml 10X phosphate buffered saline (PBS, mix 8.76 g $NaCl$, 2.41 g Na_2HPO_4 and 0.41 g $NaH_2PO_4 \cdot H_2O$, increase sample volume to 95 ml with purified water, adjust to pH 7.4 with 6 M $NaOH$ solution, make to final volume of 100 ml, filter with 0.2 μm filter) are mixed and degassed for 15 min under vacuum. Then 75 μl ammonium persulfate solution is added (made fresh, 20 mg ammonium persulfate plus 100 μl water) followed by 10 μl TEMED. The solution is capped and mixed well. The mixture is poured into a mold and left to sit for 2 hours to ensure the reaction is sufficiently complete. The density of the gel thus prepared is approximately 1030 kg/m^3, and the sound speed is about 1534 m/s. The attenuation is generally too low (below 0.1 dB/cm/MHz) to simulate that of human tissue. Such low attenuation also makes it easier to induce shock formation in the propagating pressure waves. The attenuation might be increased by substituting the water component with a more absorptive liquid such as glycerin (sound speed 1920 m/s, attenuation 0.23 dB/cm at 1 MHz and 21.7 °C). The transparency of acrylamide gel is very attractive for future research work, especially for those involving flow visualization.

3.2.2 Blood-Mimicking Fluid

Several factors influence our choice of flow medium. For starters we seek to match the acoustical and thermal properties of blood. This includes matching the acoustic impedance, absorption coefficient and scattering effect. Human blood is composed of a liquid called plasma in which are suspended red blood cells (RBCs), white blood cells, and platelets. The scattering of ultrasound by blood presumably is due to RBCs [180]. People have reported different flow model designs using artificial particles suspended in a liquid and showed results that are consistent with those seen *in vivo* [181]. The viscosity, and therefore the absorption, of the aqueous suspensions can be increased to a value approaching those of whole blood by adding glycerin to the water [182-184]. In order to mimic the scattering of ultrasonic pressure waves by blood, it seems appropriate to choose particles having a mean volume roughly equal to RBCs, and to ensure that the size distribution is approximately the same. The viscosity of human blood lies in the range of 3 to 4 cP at 37°C [181]. The RBC is an elastic, non-nucleated biconcave disk with an average diameter of 7 μm, an average thickness of 2 μm [180], and an average volume of 87 μm^3 [180, 181].

We have been using two different suspensions to mimic human blood throughout the experiments. The first blood mimicking fluid (BMF1) employs a suspension of cellulose powder (MN301, Matherey and Nagel, Duren, Germany) in a glycerin/water mixture. This cellulose powder has particle sizes of 2-20 μm, the same as those used by Newhouse *et al.* [185], and Petrick *et al.* [182]. They both suggested a powder concentration of about 0.8 g/L for Doppler ultrasound studies. The suspension containing

0.8 g/L in a glycerin/water mixture of ratio 9:10 at room temperature has the same dynamic viscosity (4 cP) as whole blood at body temperature [182]. The advantage of this suspension is that cellulose powder is water wettable, and no surfactant is thus needed. Therefore, this suspension is easy to prepare and degas. Because cellulose powder is heavier than glycerin/water mixture, the particles can aggregate and settle very quickly. Consequently, the suspension needs to be continuously mixed by magnetic stirring. However, stirring is impractical in the flow, especially in the tested area. Eventually the particles will collect on the bottom of the tubular "vessel", and the flow properties will thus be changed. This can become a big problem, especially when the original vessel size is small and the flow rate is slow.

Using a concentric cylinder viscometer (LV2000, Cannon Instrument Company, State College, PA) and our sound speed/attenuation measurement system (see Section 3.6) we determined an optimal recipe, which is given in Table 3.3. The measured properties of the cellulose-based blood mimicking fluid are shown in Table 3.4. The corresponding values for human whole blood are also listed for reference [176].

Component	Composition (in mass %)
Water	54.90
Glycerin	41.58
Cellulose Powder	3.52

Table 3.3: Recipe for BMF1.

Property	BMF1	Whole Blood [176]
Density (kg/m^3)	1108	1052-1064
Sound Speed (m/s)	1704	1540-1590
Attenuation ($Np/m/MHz$)	1.32	1.32-1.84
Specific Heat ($J/kg\cdot^0C$)	3450	3600-3840
Thermal Conductivity ($W/m\cdot^0C$)	0.45	0.48-0.53
Viscosity ($kg/s\cdot m$)	0.0037	0.0035-0.0045

Table 3.4: Measured acoustic and thermal properties of BMF1.

To help avoid the problem with particle settling, a second blood mimicking fluid (BMF2) is used. This recipe has been extensively used as a flow Doppler test phantom [186, 187]. Orgasol particles (Orgasol 2001 UD NAT, Atofina Chemicals Inc., Philadelphia, PA) are employed in this recipe. They have very fine size (5 μm) and a nominal density close to that of water (1030 kg/m^3). The particles are suspended in the glycerol/water mixture. The amount of the glycerol is adapted in order to maintain the density of the fluid at the same value as that of the Orgasol particles, thus ensuring neutral buoyancy of the particles. Dextran (Sigma D-4876) is added to adjust the viscosity. Unlike cellulose powder, Orgasol particles are not water wettable, and thus a surfactant needs to be used (Synperonic N, Trademark of ICI, PLC, BDH Laboratory Supplies, Poole, England). Finally, sodium azide (Sigma S-8032) is added as a preservative. The presence of a surfactant requires a longer time to degas the suspension. Although settling is not a problem here, particle aggregation still can occur. A stirrer is still needed to ensure uniform particle dispersion and stable acoustic scattering level. The

recipe for this blood mimicking fluid is given in Table 3.5, and its measured physical properties are listed in Table 3.6.

Component	Composition (in mass %)
Water	84.02
Glycerin	9.62
Dextran	3.36
Orgasol	1.82
Synperonic N surfactant	0.9
Sodium Azide	0.29

Table 3.5: Recipe for BMF2.

Property	BMF2	Whole Blood [176]
Density (kg/m^3)	1036	1052-1064
Sound Speed (m/s)	1549	1540-1590
Attenuation ($Np/m/MHz$)	0.46	1.32-1.84
Specific Heat ($J/kg\cdot^0C$)	3930	3600-3840
Thermal Conductivity ($W/m\cdot^0C$)	0.57	0.48-0.53
Viscosity (kg/s·m)	0.0042	0.0035-0.0045

Table 3.6: Measured acoustic and thermal properties of BMF2.

3.2.3 Vessel Wall Mimicking – "Wall-less"

In vivo, the acoustic impedance of the vessel wall and blood are nearly identical [181], and consequently an ideal vessel-mimicking material would be one whose acoustic impedance is close to that of the fluid suspension to assure little distortion and attenuation of the incident and scattered waves. Latex and silicone rubbers can have acoustic impedances close to human vessels and so have been used by many researchers. However, rubber tubing has a very high acoustic attenuation compared to tissue and therefore can introduce significant thermal artifacts.

Our initial idea for experiments with a flow-through phantom was to use Tygon tubing to mimic a "blood vessel". Fully aware of the thermal artifacts that Tygon tubing might introduce due to its high acoustic absorption compared to tissue, we did simple and explicit experiments to see how significant this artifact could be. In the first experiment, only the H-102 transducer and one thermocouple were immersed in deionized and degassed water. The thermocouple was positioned on the acoustic axis and moved along the axis to effect a change in the relative position of the acoustic focus and the thermocouple. The on-axis temperature profiles on the focal plane and off the focal plane are shown in Fig. 3.6(a). In this free-water, no-tubing situation, the temperature rise occurred promptly and lasted for the duration of the acoustic insonation. As we will discuss in detail later, since the absorption coefficient of water is so small that the heating of water can be neglected, the sharp temperature rise we observed in Fig. 3.6(a) is mainly due to the viscous heating in the boundary layer of the thermocouple, the so-called thermocouple artifact (see Section 3.4).

We then added Tygon tubing with 1/8” ID and 1/16” wall thickness to the arrangement. Similarly, the tubing was submerged in de-ionized, degassed water along with the H-102 transducer. Two thermocouples were inserted in the flow, one (TC1) on the flow axis, and the other one (TC2) against the tubing wall (see Fig. 3.6(b)). The source level was kept the same as that in the no-tubing situation so the pressure at the focus in this with-tubing situation was reduced from 1.77 MPa (no tubing) to 1.01 MPa due to the tubing's absorption and scattering effect. A second peak, delayed in time, was obvious in the TC1 temperature profiles. The first peak at TC1 was due to the thermocouple artifact as we just mentioned. The delay in the second peak showed evidence of thermal conduction. The highly absorptive Tygon tubing could absorb acoustic energy much better than water such that the resultant temperature gradient caused the transfer of heat from the tubing wall to the flow center by conduction, which resulted in the second peak (and time delay) in TC1. There was no second peak or time delay in the TC2 temperature profiles since TC2 was connected directly to the “vessel” wall. The temperature rise at TC2 was a direct response of the tubing being heated. The peak temperature rise at TC2 could equal that at TC1 even when the focus was positioned right on top of TC1. These results demonstrate that Tygon tubing can introduce a significant thermal artifact due to its excessively high absorption coefficient.

To avoid the problems associated with vessel wall attenuation and impedance mismatches, some researchers have employed wall-less vessel phantoms [188]. This is exactly the way we chose to build our flow-through phantoms, using the mold arrangement shown in Fig. 3.5.

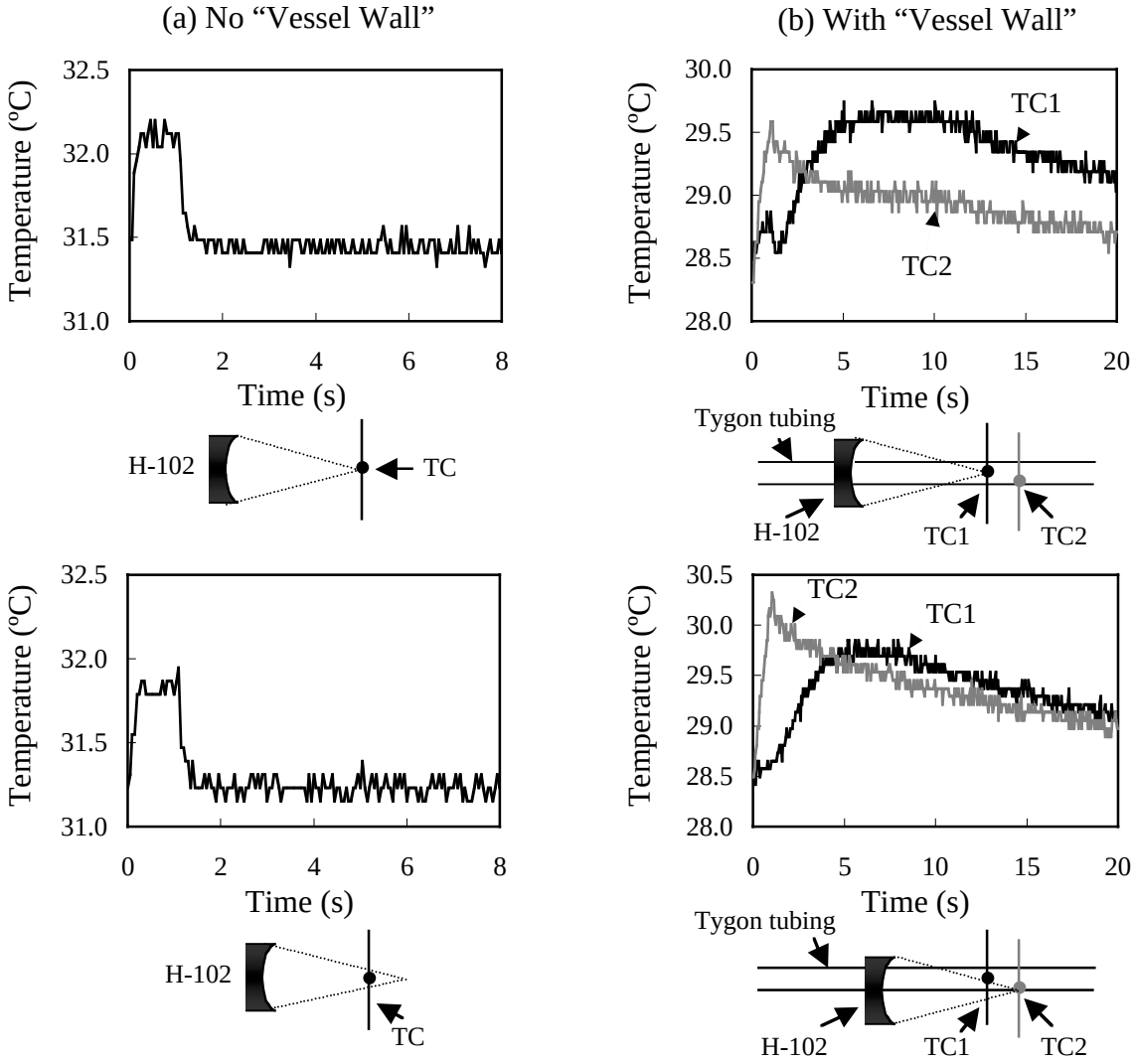

Figure 3.6: The experimental results showing the artifact induced by using high absorptive material to simulate a blood vessel wall (1 second insonation): (a) No "vessel wall", focus pressure 1.77 MPa; (b) With "vessel wall", focus pressure 1.01 MPa.

3.3 Flow Generation System

The human circulatory system is a very complex system. Blood vessel diameters can range from 0.005 mm (capillaries) up to 25 mm (ascending aorta), and the mean flow velocity can vary from 0.05 cm/s to above 50 cm/s [189]. Table 3.7 lists a selection of typical blood vessel parameters for the human circulatory system [99]. The specified velocity is the temporal mean velocity averaged over the cardiac cycle, unless otherwise stated. The focus of our experimental study is to investigate the effect of a single large "blood vessel" (diameter greater than 2 mm) in a tissue phantom with varying flow rate and vessel size and to use the measured results to validate the model described in Chapter 2.

Vessel Type	Diameter (mm)	Velocity (cm/s)
Ascending aorta	25	22
Descending aorta	16-20	27 (peak)
Internal carotid artery	4	50
Femoral artery	5	26
Renal artery	4	50
Large arteries	2-6	20-50 (peak)
Capillaries	0.005-0.01	0.05-0.1
Large veins	5-10	15-20
Venae cavae	20	11-16

Table 3.7: A selection of human blood vessel parameters [99].

The smooth laminar flow through the phantom is driven by gravity from the upper reservoir to the lower reservoir, as shown in Fig. 3.1. The flow velocity is controlled and

monitored by a flow–control system (Model: 32916-32, Cole-Parmer), which allows a flow rate from 0 to 500 ml/min and allows for a maximum particulate size of 50 μm. The flow velocities can be calibrated by measuring the rate that the blood mimicking fluid is collected in the lower reservoir. Material collected in the lower reservoir is returned to the upper reservoir by a peristaltic pump (Masterflex L/S™, Model 7552-02, Cole-Parmer Instrument Company, Vernon Hills, IL).

To ensure a laminar flow in the test volume, the Reynolds number, Re_D, based on the tube diameter should be much less than 2300 [190]. The Reynolds number is given by $\mathrm{Re}_D = UD/\nu$, where U is the spatial mean velocity, D is the diameter of the tube and ν is the kinematic viscosity of the fluid. Furthermore, the flow-control system should be installed sufficiently far upstream from the phantom to ensure that the flow is fully developed before it enters the test region. Thus the tube length between the flow control system and the entrance of the tissue phantom should exceed the so-called flow entrance length L, which can be determined by the following formula [190],

$$\frac{\mathrm{L}}{\mathrm{D}} = 0.06\,\mathrm{Re}_{\mathrm{D}}\,. \tag{3.1}$$

The laminar flow distribution in the fully developed region of the tube flow is known as Hagen-Poiseuille flow and can be written in cylindrical coordinates as,

$$u(r) = 2U\left[1-\left(\frac{r}{r_0}\right)^2\right], \tag{3.2}$$

where $u(r)$ is the velocity at r ($r=0$ is the flow axis), and r_0 is the radius of the tube. This is the flow model used in the simulations described in Chapter 4.

3.4 Temperature Measurement

Thermocouples (Type E, bare junction, 125 μm diameter, response time less than 40 ms, Omega Engineering Inc., Stamford, CT) are built into the phantom and the flow channel to monitor the temperature field. The thermocouple outputs are connected to an electronically compensated isothermal terminal block (TBX-1328, National Instruments, Austin, TX) and the terminal block outputs are connected to a signal-conditioning module (SCXI-1120, National Instruments, Austin, TX) with eight isolated input channels. The thermocouple voltages are low pass filtered (BW=10 kHz) and amplified with a gain of 1000, and the outputs are connected to the analog inputs of a multifunction input/output (MIO) data acquisition board (AT-MIO-16E-1, 12-bit resolution, 1.25 MS/s maximum sampling rate, National Instruments, Austin, TX) installed in a standard PC computer. The signals are sampled at 1 KHz, converted from voltage to temperature, and saved on disk for off-line processing.

Figure 3.7 is an example of a typical *in situ* temperature measurement. The thermocouple is in the tissue phantom (no "vessel") and positioned at the center of the primary acoustic pressure lobe of the source transducer. Temperature is plotted as a function of time for an insonation duration of 1 second, a source frequency of 1 MHz, and with a peak negative acoustic pressure of 1.55 MPa. Figure 3.7(a) is the plot of the raw data without any averaging or other post-processing. The high frequency noise seen in Fig. 3.7(a) is not characteristic of *in situ* temperature responses. It is the direct result of electrical noise in the temperature measurement system. A substantial portion of this high frequency noise can be removed, with little or no effect on the relatively slowly changing

temperature response, by applying a simple moving-average filter. Figure 3.7(b) shows the filtered temperature values using a 20-point moving average filter. The results show the classical heating/cooling curves and exhibits with good reproducibility (standard deviation within 0.1°C). Unless otherwise specified, the remainder of the temperature data presented in this dissertation will be processed using this moving-average technique.

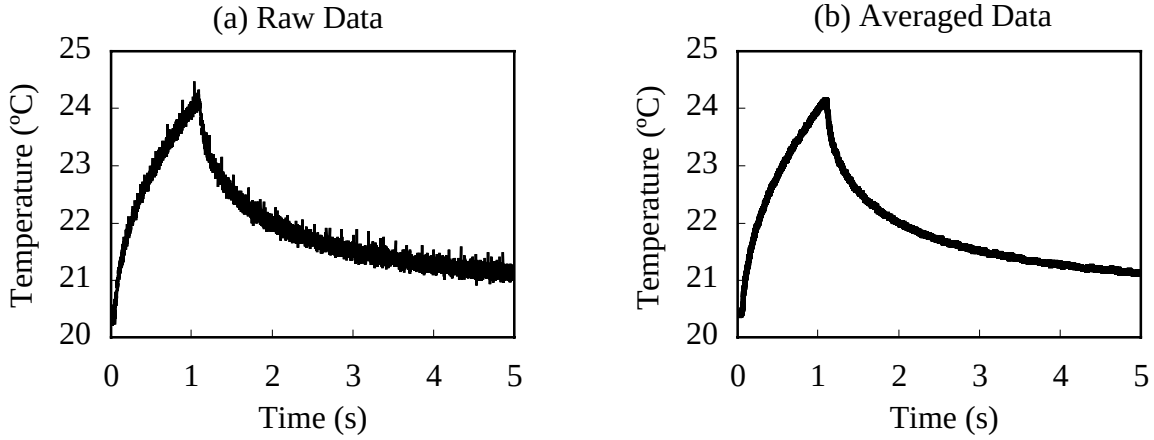

Figure 3.7: A typical plot of measured temperature *vs.* time in the degassed agar phantom: 1 MHz, 1.55 MPa peak pressure, 1.0 sec insonation: (a) raw data; (b) filtered with 20 point moving average.

Thermocouple artifact

The temperature measurement artifacts caused by using thermocouple probes were first reported and discussed by the Fry brothers [191, 192]. The phenomenon that they termed viscous heating results from the relative shearing motion of the surrounding medium with respect to the surface of the probe; this shearing motion is constrained to a boundary layer and serves to heat the probe surface. This translates into thermocouple temperatures that are higher than the temperature of the surrounding tissue. Due to the

sharp temperature gradients generated by this interaction, the resulting temperature elevation reaches steady state very soon after the sound field has been switched on, after which point the probe tracks the temperature changes in the medium. The thermocouple also returns to the temperature of the medium rapidly after the sound field is switched off. The effect of viscous heating on absorption measurements was later analyzed by Goss *et al*. [193]. It was also shown by Hynynen *et al*. [194] that this enhanced heating generation could be an important factor impacting ultrasound hyperthermia measurements when focused beams are used.

Another type of artifact caused by a temperature-sensing probe is ultrasonic beam distortion resulting from scattering from the probe. In addition to changing the profile of the beam, this can cause increased power density around the probe and, again, artificially high temperature readings. In an experimental evaluation of the aforementioned problems, Hynynen and Edwards [195] reported that probes with diameters equal to or greater than half of the square root of the sonic wavelength (λ) tend to scatter the waves, and thus distort the field significantly. Smaller probes with diameter less than about $\sqrt{\lambda}/5$ had a measurable effect which was very local, and therefore will probably not have a significant impact on the overall temperature distribution. Nevertheless, a viscous heating artifact was found even with the smallest probes and its magnitude depended on the probe size, material, structure, orientation, and the acoustic frequency.

The thermocouples we use in our experiments are 125 μm in diameter, which is only half of $\sqrt{\lambda}/5$, with $\lambda \approx 1.5$ mm at frequency of 1 MHz. Therefore, we do not observe significant beam distortion caused by the presence of thermocouples. However,

we do observe the viscous heating artifact. Recall that Fig. 3.6 showed evidence of such an artifact. Figure 3.8 shows a second example of this artifact, this time using a high acoustic pressure amplitude. In this simple experiment, the HIFU beam insonates the thermocouple junction immersed in pure water, with the thermocouple wires oriented transverse to the direction of sound propagation. The temperature curves show a rapid heating and cooling when the sound is switched on and off. Since the absorption coefficient of water is so small that temperature rise caused by bulk heating of water can be neglected, the temperature change we see here is mainly due to the thermocouple artifact.

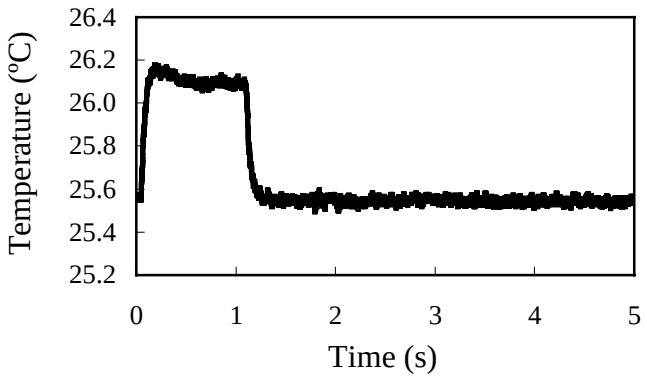

Figure 3.8: An example of thermocouple (TC) artifact in water (1 second insonation, negative peak pressure 2.36 MPa, TC at focus).

Fully aware of this thermocouple artifact, we have developed an *ad hoc* experimental method to correct it, one that can be used for the temperature measurements in both the tissue phantom and the blood mimicking fluid. As we discussed before, the temperature rise measured by a thermocouple comes from two sources: 1. bulk heating

due to the absorption of acoustic energy, which is related to the acoustic absorption coefficient of the medium; 2. enhanced viscous heating due to the presence of the thermocouple. Using our acoustic property measurement system (described below) to determine the attenuation coefficient of the tissue phantom and blood mimicking fluid, we learned that acoustic attenuation in our phantoms occurs mainly because of the presence of particles. The agar phantom without graphite powder and the blood mimicking fluid before adding any particles ("plasma") both have attenuation coefficients that are too small to be measured. Adding particles can subsequently increase the attenuation coefficient of both of these non-particulate media.

This view is supported by Wu *et al.*'s [196] investigation of the microscopic mechanisms governing the attenuation of compressional ultrasonic waves in tissue-mimicking materials. They reported that most of the acoustic power loss due to the presence of graphite powder in an agar phantom is due to mode conversion. Acoustic mode conversion occurs at the particle surface where acoustic shear waves are excited at the expense of compressional wave energy, and are subsequently converted into internal energy within a few micrometers due to the extremely high shear wave absorption coefficients in liquids or gel-type suspending media. According to their calculation, over 90% of the attenuation coefficient of the agar phantom we use comes from acoustic mode conversion, and only 0.01% is contributed by acoustic scattering. Thus, absorption dominates attenuation. We therefore conclude that the absorption of our tissue phantom is mainly due to the presence of the particles. This assumption also applies to the blood mimicking material. This leads to a reasonable conclusion that the absorption coefficients

of the non-graphite agar phantom and the particle-free “plasma” are small enough to be neglected. Consequently the temperature rise we observe in both non-particle media is mainly due to the thermocouple artifact.

We therefore have a means for measuring the thermocouple artifact as a function of insonation pressure and subsequently correcting our data to account for the presence of this artifactual heating. Implicit in this process is the further assumption that the artifact generated in the non-graphite agar phantom or “plasma” is the same as that in the tissue phantom and blood mimicking fluid. This is tantamount to assuming that the viscosity of the media is not altered by the addition of particles. This was easily verified by measuring the viscosity of the fluid with and without particles; no significant change was observed.

In summary, the thermocouple artifact can be directly measured using a non-graphite agar phantom and particle-free “plasma”. We have measured the artifact as a function of pressure level, insonation time and relative location of the thermocouple to the acoustic focus. The data is stored and used to correct the temperature measurements obtained in the subsequent parametric study described in Chapter 4.

3.5 Acoustic Pressure Calibration

The acoustic pressure field inside the flow phantoms can be determined by two methods: 1. *In situ* measurement of the pressure using a calibrated hydrophone, the size of which should be small enough that the acoustic field inside the phantom is not affected; 2. FDTD calculation for the acoustic pressure in the phantom, based on the known physical properties of the medium and the transducer calibration in water. A

needle hydrophone (Dapco NP-4, 1.0 mm active element, 0.54 ± 0.03 V/MPa sensitivity, Branford, CT) is embedded in the tissue phantom, which allows us to determine the *in situ* geometric characteristics of the focal region and the level of focal pressure. It is also one method of accurately positioning the thermocouples with respect to the acoustic axis and the focal plane of the source transducer. The focus of the source can be readily determined by moving the transducer until the maximum acoustic pressure amplitude is measured with the hydrophone. Since the location of the hydrophone relative to the thermocouples is determined at the time they are affixed to the mold, the position of the thermocouples with respect to the focus is thus established. Placing a hydrophone in a phantom also permits us to verify our propagation model by comparison to the measurement of the absolute, *in situ* pressure amplitude at the focus. Both methods will thus be used, and we will present the comparison in the next chapter.

Ideally, the hydrophone would posses a perfectly flat frequency response above 1 MHz. This would capture the fundamental frequency and harmonics above the source frequency resulting from nonlinear effects that may develop during propagation of the incident field. Unfortunately, the response of the needle hydrophone is not “flat” as a function of frequency but rather posses some resonance peaks between 700 kHz and 2 MHz. It is also difficult to obtain the complete spatial pressure distribution by using only one hydrophone fixed in the tissue phantom. To overcome these deficiencies, we take advantage of the FDTD solution for the acoustic pressure field in the phantom, as discussed in Chapter 2. The numerical solution also provides us with far more complete information on the spatial pressure and intensity distribution than we can hope to obtain

using the needle probe embedded in the phantom. It is this numerically computed pressure field that we use in the thermal model developed in Chapter 2.

To perform the FDTD calculation for the acoustic pressure in the phantom, acoustic properties such as density, sound speed and attenuation must be specified for all the media involved. We will describe the acoustic property measurement system in detail in the next section in this chapter. Furthermore, the acoustic pressure at the surface of the transducer is also needed in order to run the simulation. We are unable to measure directly the pressure at the transducer surface with the equipment available. The most conveniently measurable quantities are the voltage to the source transducer and the focal pressure using a calibrated hydrophone in water. With this information, we need to determine the relationship between the voltage to the transducer and the pressure at the face of the source. This is the so-called source pressure calibration.

The source pressure calibration can be accomplished by comparing precise experimental and numerical results in pure water. A calibrated PVDF membrane hydrophone (Model 804, 0.6 mm active element, Perceptron, Hatboro, PA, calibrated by the National Physical Laboratory) is used to measure the acoustic pressure at the focus. Thus, a relationship between the peak voltage to the transducer and the peak acoustic pressure at the focus is experimentally established. From the FDTD simulations the linear relationship between the transducer pressure and the focal pressure can be determined (this is often called the focusing gain). By comparing the measured focal pressures with predicted values from the FDTD solution representing the same conditions, we can determine the linear relationship between the peak voltage to the transducer and the peak

pressure at the source. This relationship will be valid so long as nonlinearity does not begin to manifest itself in the propagating acoustic wave as the source voltage is increased.

Figure 3.9 shows the measured focal pressure (peak negative pressure P_f^{pk-}) as a function of voltage to the transducer H-102 (peak negative voltage, V_m^{pk-}), and the computed focal pressure (peak negative pressure P_f^{pk-}) as a function of the source pressure (P_s^{pk-}). All measurements and simulations were performed in pure water at 17.9°C. The signal is a sinusoidal tone burst with 10 cycles at 1 MHz central frequency. The hydrophone voltage was sampled at frequency of 100 MHz using a digital oscilloscope (9304AM, LeCroy Corp., Chestnut Ridge, NY) and coherently time-averaged over 300 waveforms. From Fig. 3.9 we can obtain the following linear relationship between the source pressure and voltage to transducer H-102 (in pure water at 17.9°C): $P_s^{pk-} = 0.00297 V_m^{pk-}$.

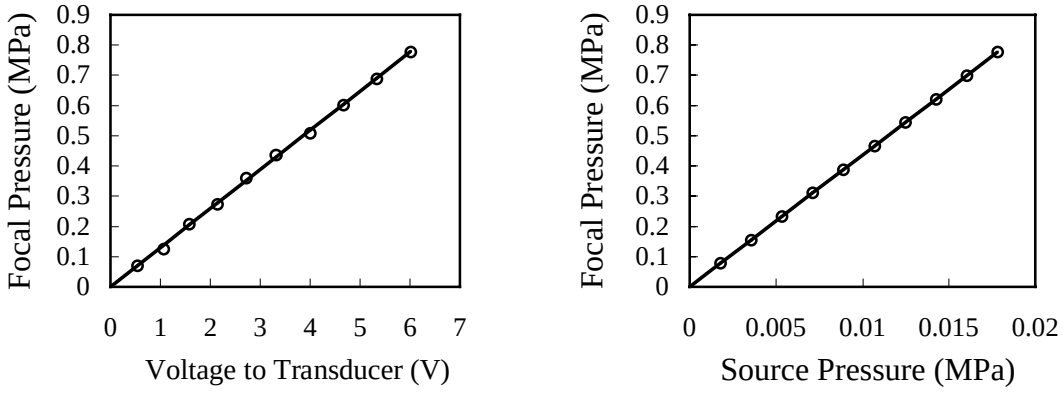

Figure 3.9: Peak negative acoustic pressure at the focus of the source transducer H-102: (a) measured as a function of peak negative voltage to transducer; and (b) the pressure at the face of the source transducer (numerical simulations).

3.6 Property Measurement

We need to know both the thermal and acoustical properties of the various media (including tissue-mimicking material and blood-mimicking material) to ensure that they are at least comparable to real tissue and blood characteristics, and also to establish that these properties remain stable during the course of the study. Those values are also required to run our theoretical simulations in which all the model parameters will be obtained by independent measurements. All properties are assumed to be independent of any temperature changes, which is consistent with experimental observations made over the limited temperature changes encountered in this study.

The specific heat measurement is conducted using adiabatic calorimetry. The thermal conductivity is measured using the steady-state longitudinal heat flow method. The acoustic properties (sound speed and attenuation) are measured using a pulse-transmission technique in the near field of a piston source. These measurements are all outlined below.

3.6.1 Thermal Property Measurement

The thermal properties we need to know for simulations are heat capacity and thermal conductivity. The specific heat of the sample is measured using adiabatic calorimetry at room temperature. The calorimeter is made with a Styrofoam cup surrounded by PVC pipe and employing a Styrofoam cap, as shown in Fig. 3.10. A sample of known mass m_s is heated to a temperature T_s and then is dropped into the calorimeter that contains a known amount of water of mass m_w with initial temperature

T_w. The temperature of the mixture is then monitored by a thermocouple of type identical to that we described in temperature measurement section. We allow the output of the thermocouple to stabilize before we record the highest reading, T_f. We can then calculate the specific heat of the sample using the formula [197]:

$$C_s = \frac{C_w m_w (T_f - T_w)}{m_s (T_s - T_f)}, \tag{3.3}$$

where C_s and C_w are the specific heats of the sample and of water respectively.

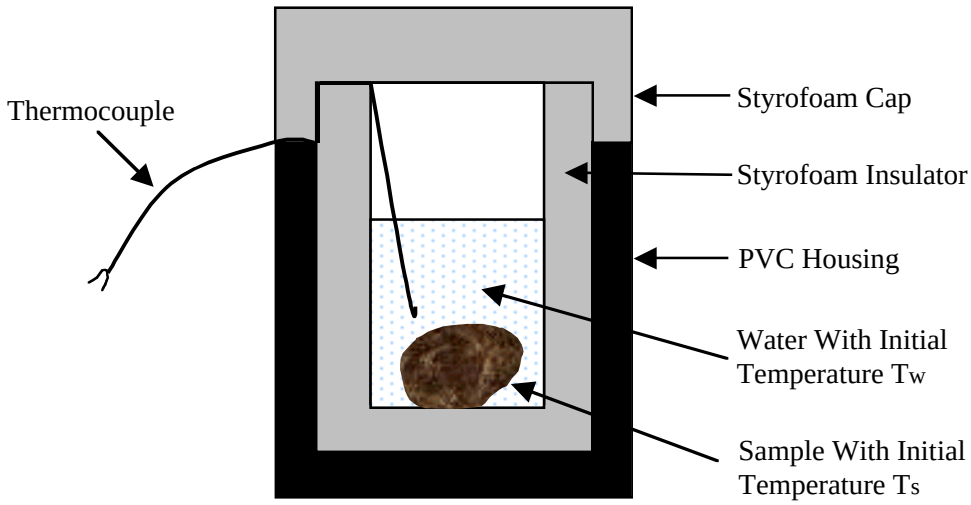

Figure 3.10: Scheme of calorimeter.

The thermal conductivity is measured using a steady-state longitudinal heat flow method. The experimental arrangement is designed so that the flow of thermal energy is only in the axial direction of a rod (or disk) specimen. Radial heat transfer is prevented or minimized by using an insulating boundary. In our measurement, a sample disk is sandwiched between two identical standards with the same diameter as the sample. The bottom surface of the lower standard disk is maintained at a certain temperature, which is

controlled by a thermostatic bath, and the top surface of the upper standard disk is kept at zero degrees using ice water. The disks are shielded with a thick layer of Styrofoam and sponge. As sketched in Fig. 3.11, the temperatures at all the interfaces are recorded until steady state is reached.

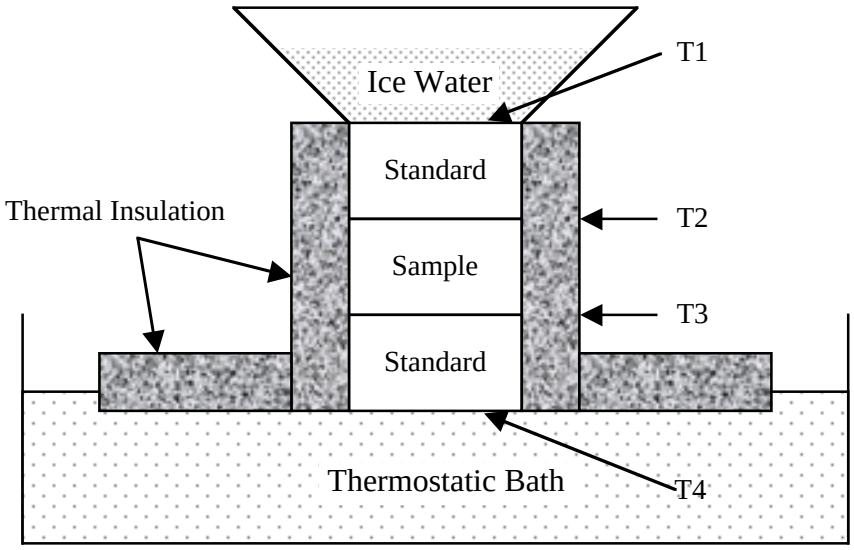

Figure 3.11: Scheme of thermal conductivity measurement.

Suppose the thermal conductivity of the standard and sample are K_d and K_s, the thickness of the standard and sample disks are h_d and h_s, and the temperatures at the four interfaces from top to bottom are T_1, T_2, T_3 and T_4, respectively. Then at steady state, the heat flux through the top standard disk will be the same as that through the sample [197]:

$$\mathrm{K}_d \frac{\Delta T_d}{h_d} = \mathrm{K}_s \frac{\Delta T_s}{h_s}, \tag{3.4}$$

where $\Delta T_d = T_2 - T_1$, and $\Delta T_s = T_3 - T_2$. By using the above equation, we can then obtain the thermal conductivity of the sample.

The standard we currently use is Delrin (Natural color, Small Parts Inc., Miami Lakes, FL), which has a thermal conductivity of 0.389 $W/m \cdot K$. The interface temperatures are recorded using type E thermocouples.

3.6.2 Acoustic Property Measurement

There have been a great many methods devised for making measurements of sound speed and attenuation in a variety of media, and reviews of measurement methods have been given by various authors including McSkimin [198], Dunn *et al*. [199] and Papadakis [200]. The pulse transmission method is popular because it is straightforward and simple to implement. However, difficulties still arise because of the large number of possible sources of error, including diffraction loss, distance measurement, and alignment of transmitting and receiving transducers. Failure to apply corrections will lead to large errors and uncertainties; this has resulted in considerable variations in published data. Recent study by Madsen *et al*. [201] compared measurements made by 10 laboratories of ultrasonic propagation speeds, attenuation coefficients and backscatter coefficients in identical tissue-mimicking material samples produced at the University of Wisconsin. The major conclusion from this study is that uniformity does not exist among laboratories in terms of determination of fundamental ultrasonic properties in tissue-like media. A primary complicating effect is the diffraction of transducers used, which contributes an additional amplitude loss. Although diffraction loss has been addressed by many authors, no simple guidelines are available that detail how to do the corrections. During our effort to obtain accurate values of the acoustic properties of the tissue-mimicking material (gel)

and the blood-mimicking material (liquid) with ready availability, we have developed simple, convenient ways to obtain diffraction corrections in the attenuation measurement.

The apparatus is devised to be suitable for measuring both the sound speed and attenuation. As illustrated in Fig. 3.12, two identical piston transducers (V305-SU, Panametrics Inc., Waltham, MA) of central frequency 2.25 MHz, and effective aperture diameter of 1.905 cm (0.75"), are used, one as the transmitter and the other as the receiver. The two transducers are both baffled with 10.16 cm (4") by 11.43 cm (4.5") stainless steel plates. Another identical stainless steel plate (back plate) is connected at a fixed distance relative to the plate containing the transmitter (front plate) with two 15.24 cm (6") long stainless steel rods. The plate housing the receiver (central plate) is a mobile plate that sits between the two other fixed plates and slides on the two supporting rods using precision thrust bearings. The sample is sandwiched between the front plate and the moving plate, with the rods supporting the sample from below. The moving plate can be fixed in any place along the rods with four collars on both sides. Thus, a sample of varying size can be held securely while maintaining parallel measurement faces. The sample can also be a liquid that will fill the tank, which is just big enough for the whole setup to sit in (16 cm $\times$ 11 cm $\times$ 12 cm). This avoids the problem that very large sample volumes present. Moreover, the use of a small tank permits us to submerge the entire apparatus in a constant temperature bath for thermal control. For each measurement, a 10-cycle pulse of central frequency 1 MHz is transmitted through a piece of sample of known thickness, and received by the second transducer.

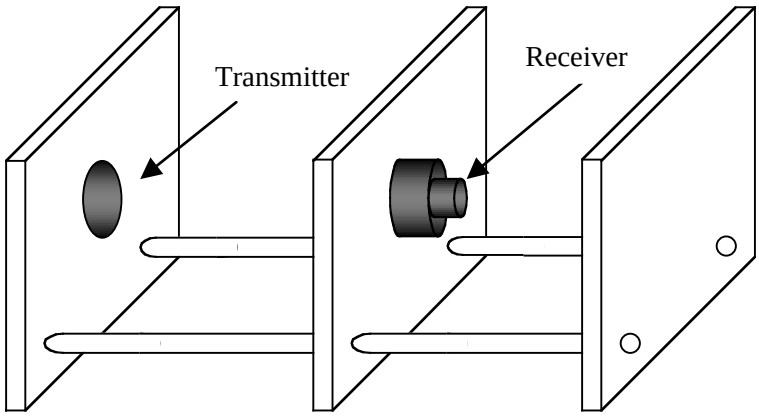

Figure 3.12: Apparatus for the measurement of sound speed and attenuation.

Sound speed measurement

Sound speed is determined using a through-transmission technique, where the speed is calculated by the ratio of the known source/receiver distance (Δd) and the time of flight (Δt) of the acoustic pulse traveling that distance. A digital caliper can conveniently and accurately measure the distance. The time of flight can be obtained directly from the digital oscilloscope using the time cursor by measuring the time difference between the first zero crossings of the input waveform to the transmitting transducer and the output waveform from the receiving transducer. This can also be determined by computing the cross correlation of the transmitted and received signals, but the signal to noise ratio of the data was deemed large enough to justify the use of the simpler and more convenient cursor method. However, it is important to note that the Δt measurements will include electronic time delays, although small, these will result in an upward bias to Δt and a downward bias to the sound speed.

To alleviate this problem, we can employ either a relative or an absolute measurement scheme. For the relative method, only one sample with thickness Δd is needed. The time of flight of the acoustic pulse in the sample is measured along with the time of flight through an identical thickness of water from which the sound speed is calculated with the following relationship:

$$c_s = \frac{c_w t_w}{t_s}, \tag{3.5}$$

where c_w and c_s are the sound speeds of water and the sample, t_w and t_s are the measured sound propagation times of flight in the water and in the sample, respectively. This relative measurement requires the information on the sound speed of water, which can be obtained by measuring the temperature of the water using a thermocouple, and using the following formula [202]:

$$\begin{aligned} c_w(T) = {} & 0.314643091\times10^{-8}\mathrm{T}^5 - 0.147800417\times10^{-5}\mathrm{T}^4 + 0.334198834\times10^{-3}\mathrm{T}^3 \\ & - 0.0580852166\mathrm{T}^2 + 5.03711129\mathrm{T} + 1402.38754, \end{aligned} \tag{3.6}$$

where T is in degrees Celsius.

We could also use an absolute method to measure sound speed, in which two samples with different thickness ($d_{s1}, d_{s2}, d_{s2} > d_{s1}$) are required without any reference to water or other medium. If the times of flight in d_{s1} and d_{s2} are t_{s1} and t_{s2}, respectively, the sound speed of the sample can be calculated by:

$$c_s = \frac{d_{s2} - d_{s1}}{t_{s2} - t_{s1}}. \tag{3.7}$$

The absolute measurement is suitable for determining the sound speed of a liquid when the tank is filled up with the sample. No measurement in the water path is

necessary. Unless otherwise stated, we have used the absolute method to measure the sound speed of the tissue phantom and the blood mimicking fluid.

Attenuation measurement

The voltage signal from the receiving transducer is proportional to the spatially averaged pressure over the receiving aperture, and the peak amplitude (or the Temporal-Peak-Spatially-Averaged-Pressure (p_{TPSA}) varies with distance due to both attenuation and diffraction. To obtain the attenuation coefficient of a medium, a relative method can be employed which usually uses water as a reference and is essentially a substitution method. This requires that the efficiency of the transmitter does not change with the impedance of the medium. However, we find that this is not true with our transducer. Therefore, to obtain attenuation we employ the absolute method that needs two samples with different thickness (d_{s1}, d_{s2}, $d_{s2} > d_{s1}$); we use the same two samples employed in the sound speed absolute measurement. A 10-cycle burst with desired central frequency is transmitted through the two samples sequentially. The signal from the receiver is coherently averaged over 500 waveforms and the peak amplitude is recorded as V_{s1} (at d_{s1}) and V_{s2} (at d_{s2}). Assuming *d* is the geometrical separation of the transmitter and the receiver, and V_0 is the amplitude of the signal at *d=0*, then the amplitudes of the received signal V_{s1} (at d_{s1}) and V_{s2} (at d_{s2}) are

$$V_{s1} = V_0 D_1 e^{-\alpha d_{s1}}$$
$$V_{s2} = V_0 D_2 e^{-\alpha d_{s2}}, \qquad (3.8)$$

where α is the attenuation coefficient of the sample, and D_{s1} and D_{s2} account for the diffraction loss in the sample through distances d_{s1} and d_{s2}. By knowing V_{s1}, V_{s2}, d_{s1} and d_{s2}, α can be calculated as

$$\alpha = \frac{1}{d_{s2} - d_{s1}} \ln\left(\frac{D_{s2}}{D_{s1}} \cdot \frac{V_{s1}}{V_{s2}}\right). \tag{3.9}$$

The diffraction loss D is not only dependent on the traveling distance d but also a function of the Rayleigh distance of the transmitting piston $X_{ray} = \frac{1}{2}ka^2 = \frac{1}{2}\frac{\omega}{c}a^2$, where $\omega = 2\pi f$ is the acoustic frequency, c is the sound speed of the medium and a is the effective radiation radius of the transmitter piston. Figure 3.13 shows how the diffraction loss changes with distance in media with different sound speeds at 1 MHz frequency. The p_{TPSA} decreases more quickly due to diffraction in the higher sound speed medium. However, the two curves overlap if plotted in distances normalized by respective Rayleigh distances, as shown in Fig. 3.14. The curves in Figs. 3.13 and 3.14 are the calculated results based on an analytical solution by Liauh [203].

This means that the diffraction loss *vs.* normalized distance is independent of the propagation medium, which gives us a way to measure the diffraction loss in the lossy sample. The sample sound speed is first measured by the absolute method described above and is denoted by c_s. The thickness of the sample is d_s and the equivalent propagation distance in pure water, d_w, which has the same diffraction loss as that in the sample can be calculated by:

$$\frac{d_s}{X_{ray-s}} = \frac{d_w}{X_{ray-w}}, \tag{3.10}$$

where $X_{ray-s} = \frac{1}{2} k_s a^2 = \frac{1}{2} \frac{\omega}{c_s} a^2, \quad X_{ray-w} = \frac{1}{2} k_w a^2 = \frac{1}{2} \frac{\omega}{c_w} a^2$ are the Rayleigh distances in the sample and water, respectively. Since the attenuation in water is small enough to be neglected, the decrease of the amplitude with distance in water can be considered to be due only to diffraction.

Therefore, to obtain the ratio of $\frac{D_{s2}}{D_{s1}}$ in Eq. 3.9, the equivalent propagation distances in pure water, d_{w1} and d_{w2}, are calculated based on Eq. 3.10. With the central plate moved to d_{w1} and d_{w2}, and measuring the amplitudes of the received signals V_{w1} and V_{w2}, the diffraction loss in the sample can be calculated using the following formula:

$$\frac{D_{s2}}{D_{s1}} = \frac{V_{w2}}{V_{w1}}. \qquad (3.11)$$

In summary, the experimental systems and methods described in this chapter are intended to enhance our understanding of the physical mechanisms involved in HIFU-induced heating in vascularized human tissues, and to verify the theoretical model we developed in Chapter 2. All the experimental results will be compared to the FDTD numerical simulations, which will be presented in the next chapter. Both the thermal and acoustic properties of the media involved are independently measured with the methods described above.

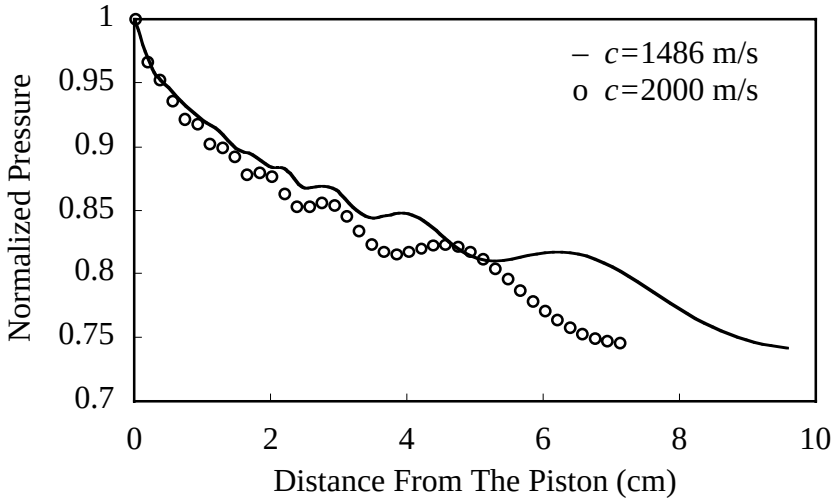

Figure 3.13: Computed p_{TPSA} decreases with the distance to the transmitting piston due to diffraction in two media with different sound speeds (solid line: c=1486 m/s, circle: c=2000 m/s). Calculated from the solution in Liauh [203].

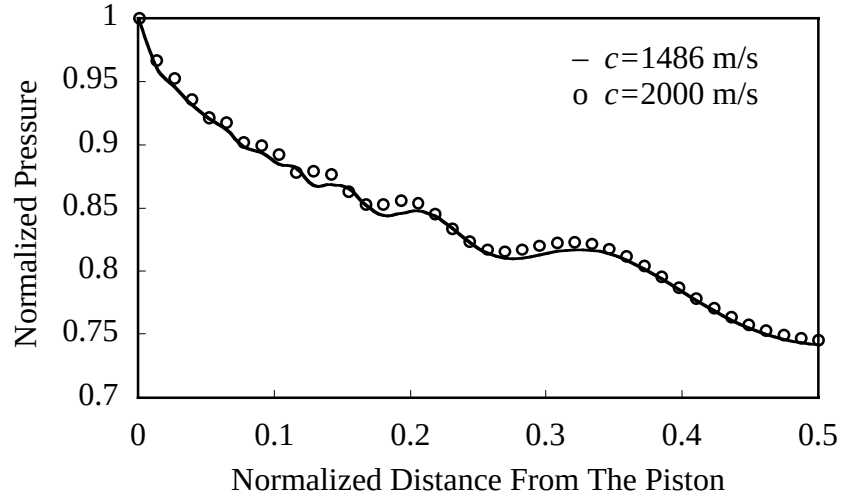

Figure 3.14: Computed p_{TPSA} decreases with the normalized distance to the transmitting piston due to diffraction in two media with different sound speeds (solid line: c=1486 m/s, circle: c=2000 m/s). Calculated from the solution in Liauh [203].

Chapter 4

Experimental Results and Comparison with Numerical Simulations

In this chapter we present the results of each suite of experiments run in our instrumented tissue phantoms employing both vessel-free and flow-through configurations. The objective is to generate experimental data for comparison with model predictions. The experimental parameters are all independently measured. In order to facilitate this process, we limit ourselves to relatively simple insonation configurations. More complex (*i.e.* biologically relevant) exposure conditions are explored via model simulations in Chapter 5.

4.1 Pressure Field Generated by HIFU Transducers

The first thing we need to verify is that our sound propagation model accurately predicts the spatial pressure (or intensity) distribution generated by HIFU transducers. Pressure is the most conveniently measurable quantity and thus will be used for comparison. As described in Section 3.5, it is difficult to obtain the complete spatial pressure distribution by using only one hydrophone fixed in the tissue phantom. This can be achieved, however, in pure water. With the hydrophone fixed in place, we moved the transducer to effect a spatial scanning of the pressure field. The measured pressure

profiles are compared with the predictions in this section. Results for both HIFU transducers, H-101 and H-102, are presented.

Figures 4.1-4.4 show computed and measured results obtained in water at 30˚C, for the H-101 and H-102 sound sources. The pressures shown are all peak negative quantities that have been normalized to the spatial maximum value present at the focal point. The focal peak negative pressures for H-101 and H-102 are 0.24 and 0.40 MPa, respectively. Figures 4.1 and 4.3 are contour plots of the pressure as a function of axial and radial distance from the focal spot (r, z = 0, 0). Figures 4.2 and 4.4 show the pressure profiles along acoustic axis and as a function of the radial distance from the acoustic axis (in the focal plane); solid lines and open circles correspond to predictions and measurements respectively. Except maybe for the peripheral regions of the field (where the measurement signal to noise ratio is poor) we see that our model is able to predict all the detail structure and good agreement is found in the focal region and along the side lobes (in the focal plane) for both transducers. Since power deposition is quadratic in the pressure, it is in the high-pressure regions in and near the focus where all the significant heating will take place.

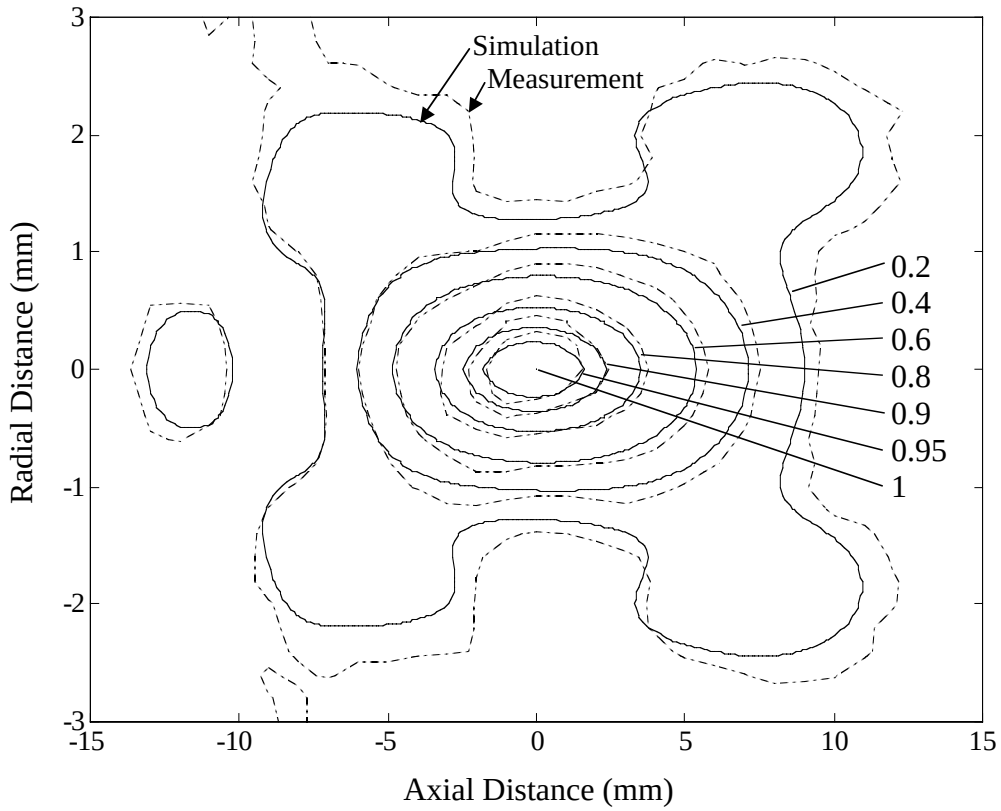

Figure 4.1: Contour plot of pressure field of H-101 in pure water (30º) as a function of axial and radial distances. The contours correspond to the peak negative pressure normalized by the spatial peak negative pressure at the focus, 0.24 MPa. The solid and dotted lines represent simulation and measurement respectively.

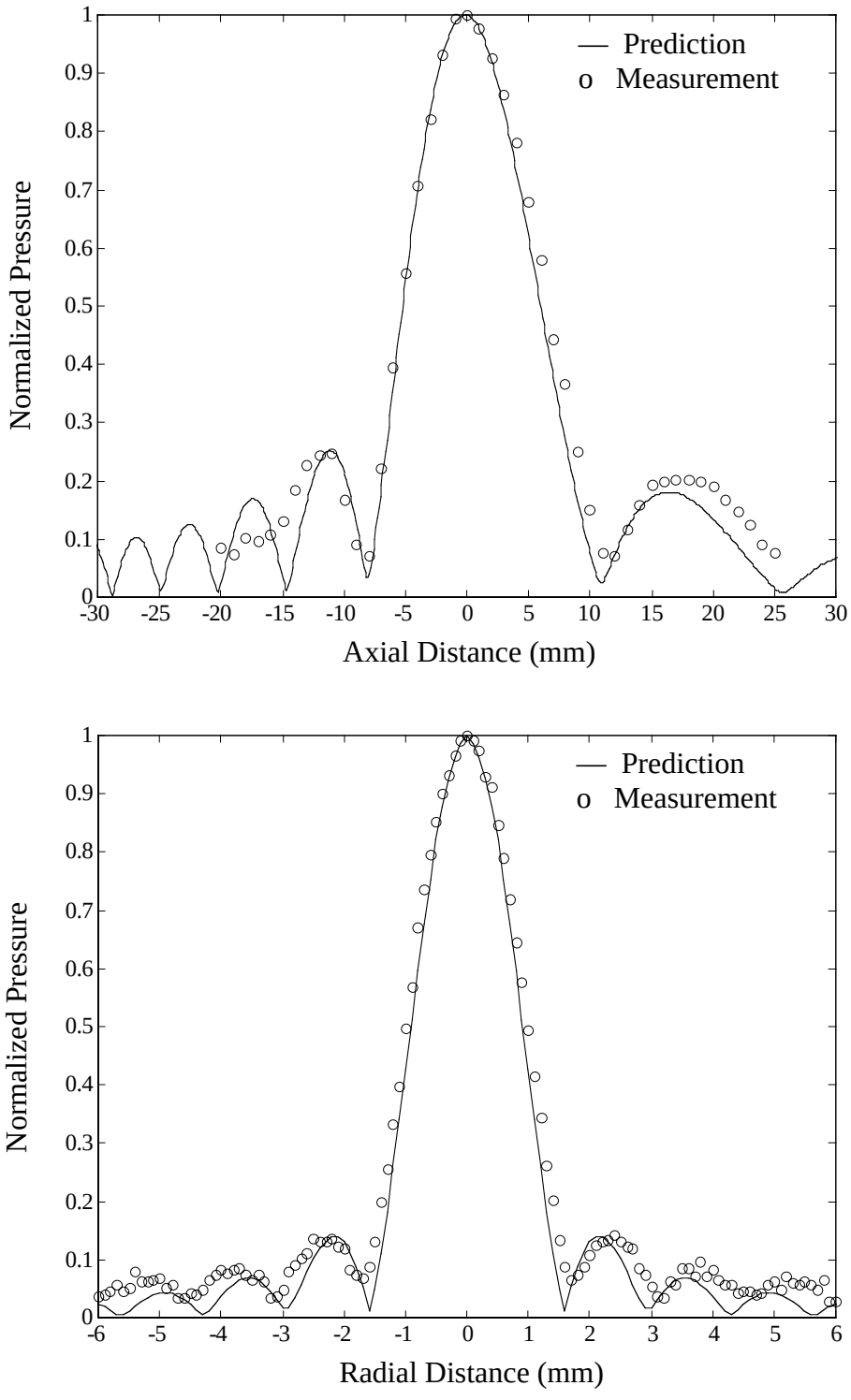

Figure 4.2: H-101 pressure profiles along acoustic axis and in focal plane.

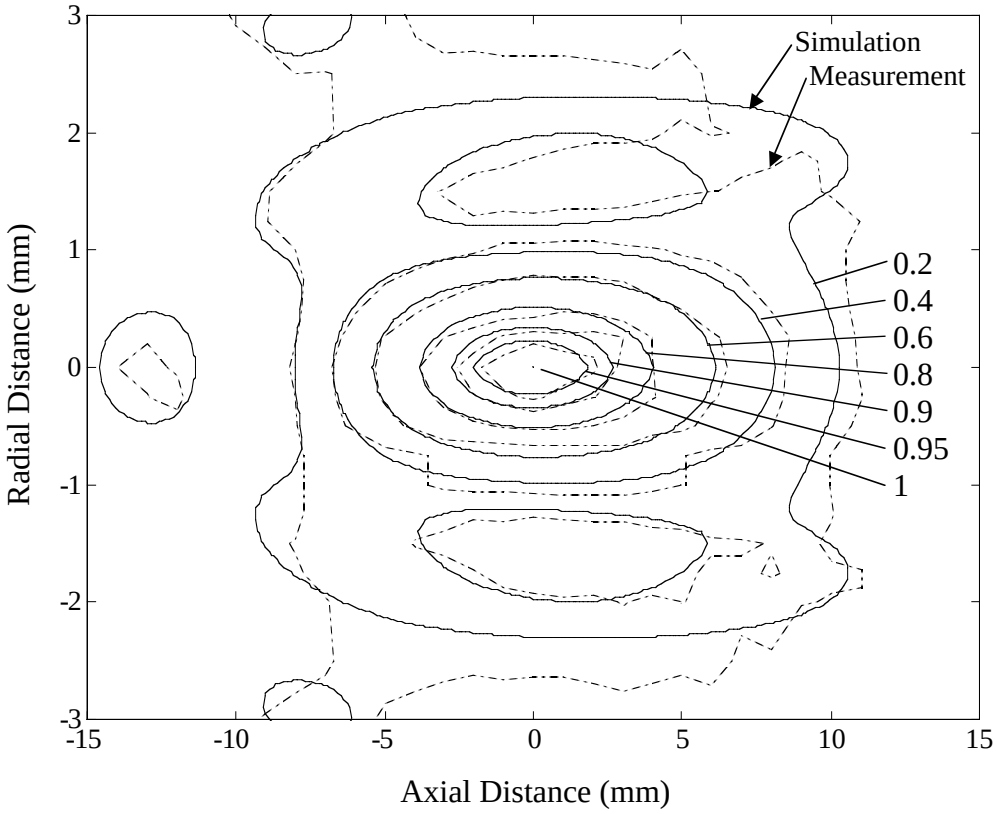

Figure 4.3: Contour plot of pressure field of H-102 in pure water (30º) as a function of axial and radial distances. The contours correspond to the peak negative pressure normalized by the spatial peak negative pressure at the focus, 0.40 MPa. The solid and dotted lines represent simulation and measurement respectively.

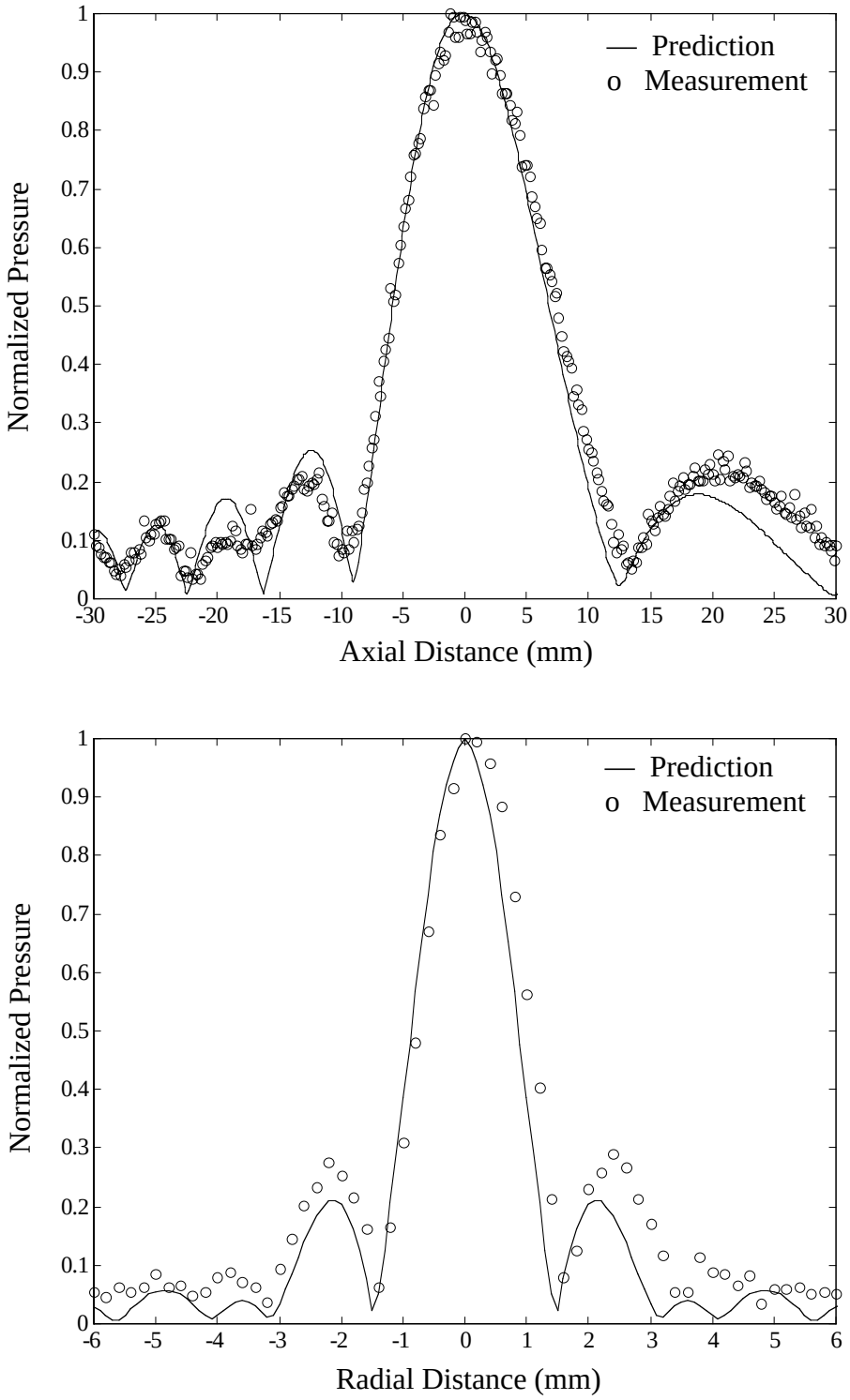

Figure 4.4: H-102 pressure profiles along acoustic axis and in focal plane.

4.2 Heating in Uniform Tissue Phantoms

Uniform phantoms that are void of vascular structure provide a relatively simple means to experimentally study heating in the absence of convective heat transfer. They also give us a way to check the method we use to correct for the thermocouple artifact, as described in Section 3.4. In addition, knowledge of phantom material's cavitation threshold pressure obtained from this simple geometry will serve to guide our flow-through tissue phantom experiment since we want to avoid cavitation throughout the experiments. Figure 4.5 shows a scheme of this non-flow configuration. The HIFU transducer employed is Model H-102. The phantom size is 53.6 mm in radius and 80.5 mm in length. The insonation duration is 1 second at a source frequency of 1 MHz. One thermocouple (TC1) is positioned at the focus, and the other one (TC2) is located in the focal plane, 0.5 mm off acoustic axis. The needle hydrophone is imbedded in the phantom and its tip is located in the focal plane and displaced 6 mm off axis as shown. The physical properties for this particular phantom are listed in Table 4.1, along with the values for surrounding water.

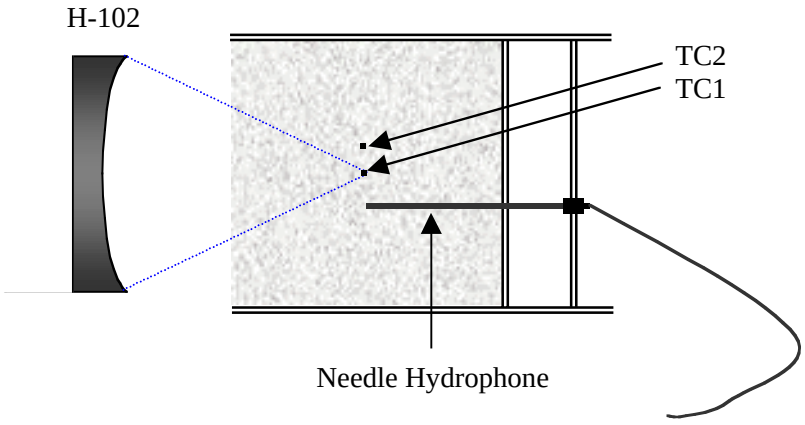

Figure 4.5: Scheme of non-flow uniform configuration.

Physical Property	Tissue Phantom	Water
Density (kg/m^3)	1044	998
Sound Speed (m/s)	1568	1483
Attenuation ($Np/m/MHz$)	8.55	0.025
Specific Heat ($J/kg\cdot^0C$)	3710	N/a
Thermal Conductivity ($W/m\cdot^0C$)	0.59	N/a

Table 4.1: Physical properties of the non-flow uniform tissue phantom.

4.2.1 Pressure Amplitude at the Focus in Phantom

We have shown in Section 4.1 that our acoustic model can accurately predict the spatial pressure distribution in water. Although this whole field comparison cannot be done in phantom, we can compare predicted and measured (*in situ*) pressure amplitudes at the focus. This comparison provides us another way to verify our acoustic model. Figure 4.6 shows the measured (circles) and predicted (solid line) peak negative pressure at the focus as a function of source pressure (peak negative value). The source pressure (*i.e.* the pressure at the face of the transducer) was obtained from the acoustic pressure calibration method described in Section 3.5 and the measured focal pressures are the average of two measurements obtained on subsequent days using the calibrated needle hydrophone. (The largest measured deviation in repeated pressure measurements was 1.4%.) The predicted pressures were calculated using our 2-D FDTD sound propagation code based on the known source pressure and the independently measured physical properties of the phantom material and the surrounding water. We show pretty good

agreement between the measured and predicted values; all deviations are less than 5% (0.4 dB).

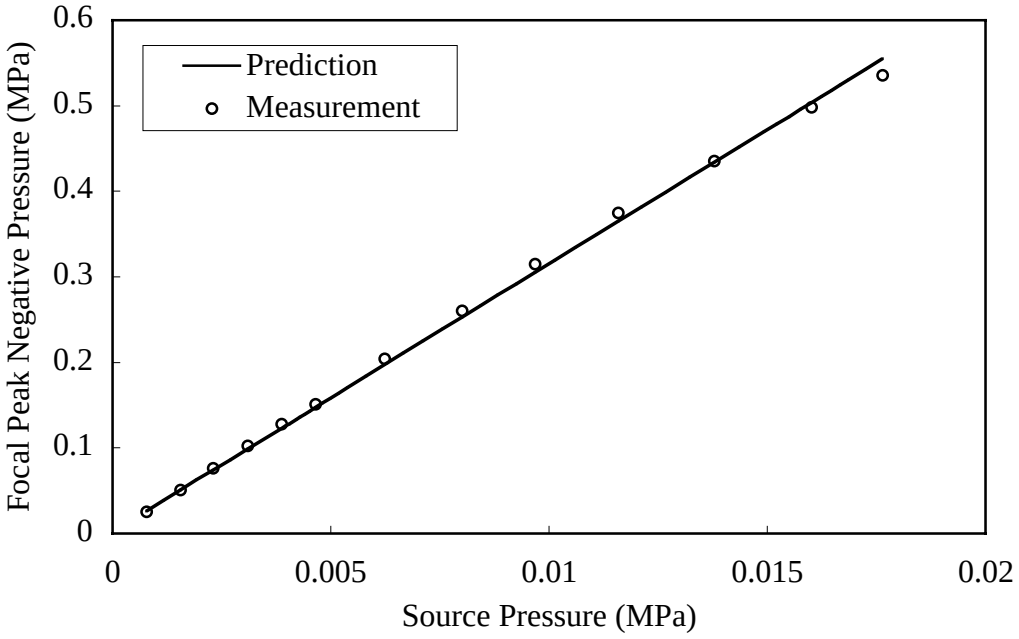

Figure 4.6: Comparison of the measured (circles) and predicted (solid line) peak negative pressure at the focus in phantom as a function of source pressure (peak negative value). The measurement precision is estimated to be better than 1.5% and is too small to display on this scale.

4.2.2 Heating and Cooling Curves

Figure 4.7 shows a typical temperature response as a function of time as measured by TC1 at the focus and as predicted by our numerical model. The peak negative pressure at the focus is 1.11 MPa. Temperature has been normalized to the peak temperature so as to provide a qualitative look at the shapes of the curves.

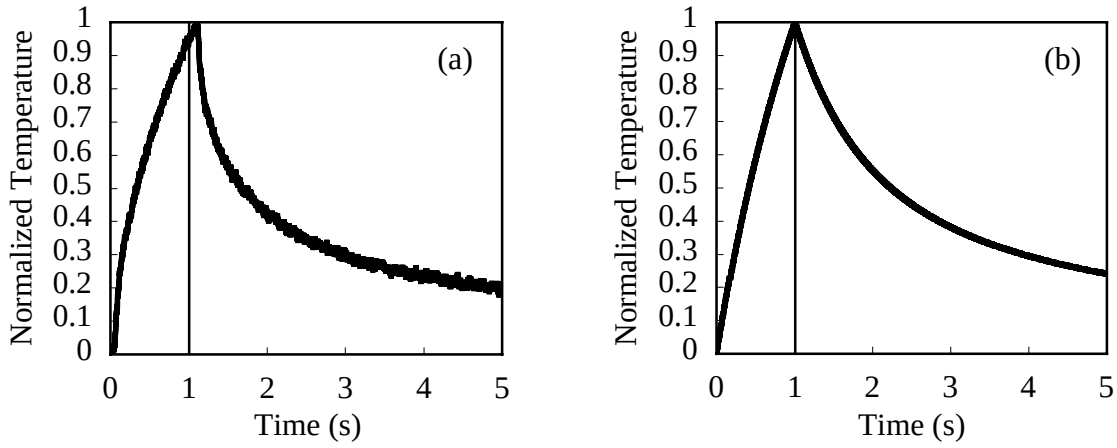

Figure 4.7: Typical temperature response at the focus in tissue phantom as a function of time: (a) as measured by the thermocouple; (b) as predicted by our numerical model. The sound field is activated at time zero and turned off after one second.

There are obvious discrepancies between the measured and predicted curves. For starters, the measurements show a faster than predicted heating rate immediately after the HIFU source is switched on. Also, the measured curve exhibits continued heating for a very short time after the HIFU source is turned off and a faster cooling rate than the predicted curve. These differences are attributed to the presence of the thermocouple. The instant the sound field is switched on, viscous heating in a boundary layer adjacent to the thermocouple surface results from the relative movement of the surrounding medium and the thermocouple probe. This leads to a rapid temperature rise at the probe surface. Once the temperature rise due to viscous heating reaches steady state, the thermocouple subsequently tracks the temperature changes in the medium. Finally, the phantom material has a large heat capacity relative to the thermocouple; thus, when the sound field is turned off, the surface temperature of the sensor quickly equilibrates with its surroundings. It is important to note that this rapid heating and cooling is limited to the

thermocouple surface; it is not duplicated in the bulk of the medium. This phenomenon is commonly known as the “thermocouple artifact” (see Section 3.4).

The interpretation of Fig. 4.7 is complicated somewhat by the fact that both the thermocouple artifact and conventional bulk heating are present at the same time. In an attempt to quantify the contribution of artifactual thermocouple heating, we insonated an agar phantom that was prepared without graphite. The attenuation coefficient for this material was only 0.03 dB/cm at 1 MHz, therefore the relative contribution of the artifact is greatly increased. Temperature versus time measurements made in this material make it possible to estimate the extent of the enhanced heating and to subsequently correct for it. Moreover, the exclusion of graphite from the phantom recipe does not alter the shear viscosity of the medium. Thus, for a given acoustic pressure amplitude, the magnitude of the artifactual heating in the two phantoms should be the same.

Figure 4.8 shows the resulting temperature response curve as a function of time for the pressure amplitude of 1.11 MPa at the focus. The curve shows the characteristic sharp temperature rise immediately after the sound field is switched on, continued heating for a very short time after the HIFU source is turned off and finally, rapid cooling. The temperature rise due to bulk heating is only about 0.05ºC (obtained from theory). Therefore, what we measured is essentially the artifact. From this plot we see that, for a pressure amplitude of 1.11 MPa, the artifact consists of 0.6˚C of rapid heating followed by 0.6˚C of equally rapid cooling. In the case of heating in absorptive medium, the artifact appears to be additive to bulk heating, thus, we can correct for it in an *ad hoc* manner by either subtracting the small temperature elevation from the measured data, or

adding it to simulation. Unless otherwise stated, we chose the latter when doing all comparisons between measurement and theory.

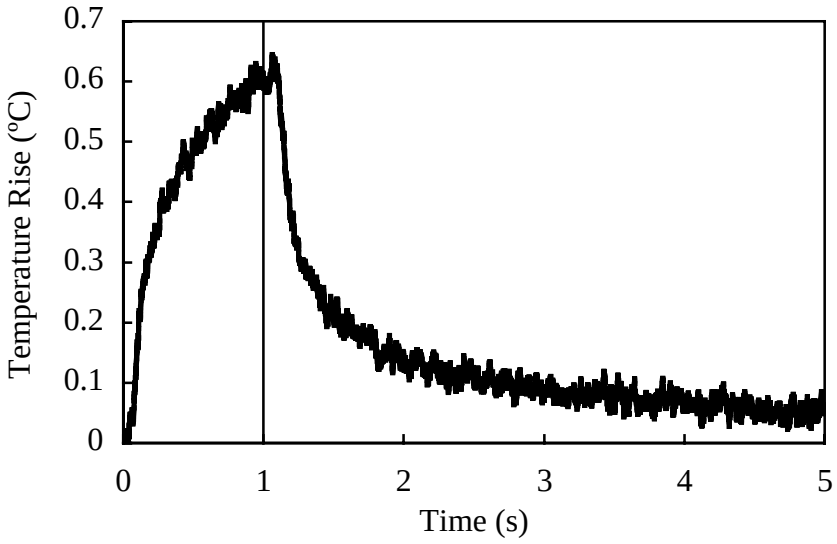

Figure 4.8: Typical temperature response as a function of time due to thermocouple artifact measured in non-graphite agar phantom. The thermocouple is located at the focus of the source (TC1 in Fig. 4.5) and the pressure amplitude is 1.11 MPa.

To illustrate the effectiveness of this procedure, we returned to the agar+graphite phantom and measured the temperature profile, as shown in Fig. 4.9, curve (a). This was obtained using TC1 and a peak negative pressure at the focus is 1.11 MPa. Curve (c) is the calculated temperature profile; the poor agreement between measurement and theory is evident. Next, we measured the thermocouple artifact in the graphite-free phantom at this same pressure amplitude; this is given by curve (d). Finally, we correct the calculation by simply adding (c) and (d), yielding curve (b). We can see that after including the thermocouple artifact, the simulated result agrees well with the

measurement not only with regards to the maximum temperature rise but also in terms of the overall shape of the curve.

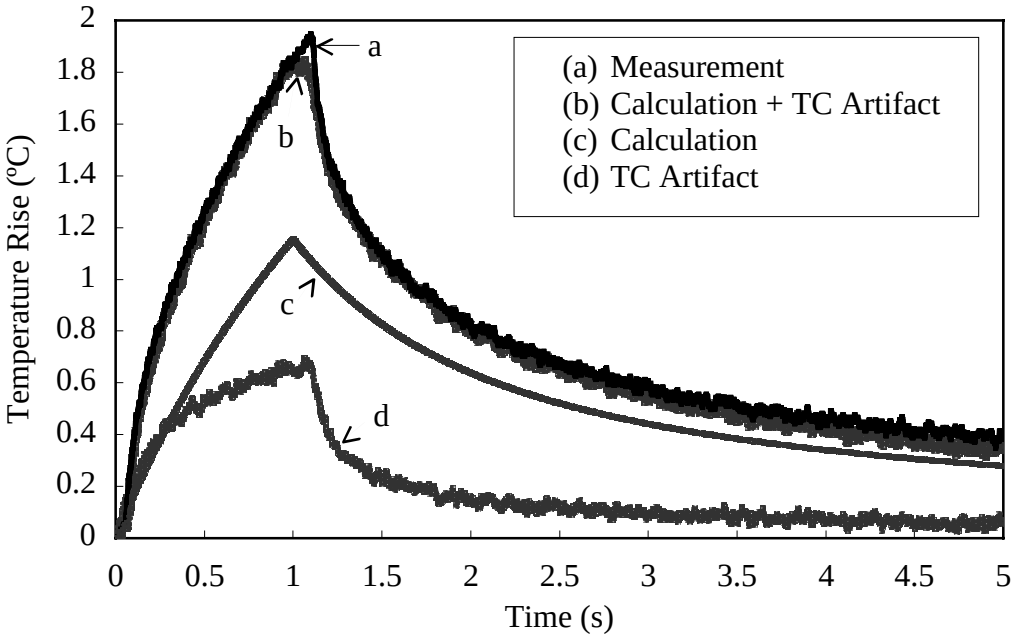

Figure 4.9: Comparison between the measured and simulated temperature response at TC1 (at the acoustic focus) in the graphite agar phantom. The peak negative pressure at the focus is 1.11 MPa.

For the same focal pressure, we compare the measured and simulated temperature response as a function of time at TC2, which is located in the focal plane, 0.5 mm off acoustic axis. A representative result is shown in Fig. 4.10. Again, good agreement is found between prediction (corrected for the thermocouple artifact) and measurement. This level of quantitative agreement was found in all the experiments run in the uniform agar + graphite phantom provided the thermocouple artifact was accounted for and there was no evidence of cavitation enhanced heating.

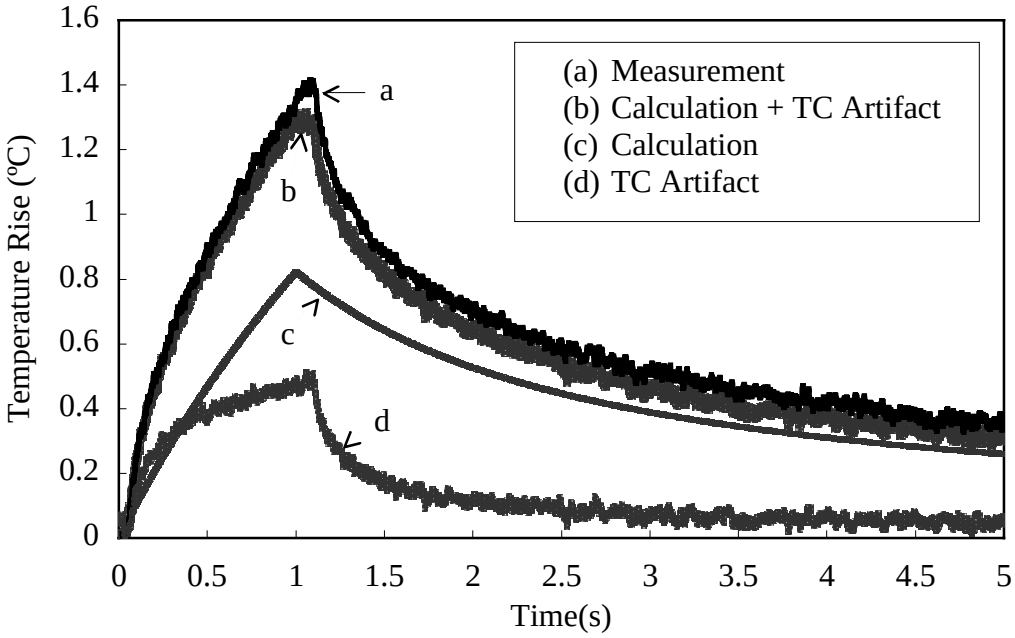

Figure 4.10: Comparison between the measured and simulated temperature response as a function of time at TC2, which is in the focal plane, 0.5 mm off acoustic axis. The peak negative pressure at the focus is 1.11 MPa.

4.2.3 Peak Temperature Rise Versus Pressure

Figure 4.11 is a plot of the measured and predicted peak temperature rise at TC1 and TC2 due to acoustic absorption as a function of peak negative acoustic pressure amplitude at the focus. Each data point is the average of five sequential measurements, minus the thermocouple artifact. The phantom is allowed to cool completely between measurements and the error bars indicate the maximum deviation from the mean. We report only those results obtained in the absence of any enhanced heating due to cavitation. The small differences between measured results and numerical predictions are due to approximations in the model, uncertainties in the measurement of medium

properties, and uncertainties in the estimated pressure level, thermocouple position, *etc*. (see Appendix A). Note also the quadratic dependence between the temperature rise and the acoustic pressure, consistent with the notion that any temperature rise associated with visco-thermal absorption will scale with the acoustic intensity, as predicted by Eq. 2.3. The quantitative agreement between measurement and model within the estimated uncertainty (see Appendix A) further serves to validate the accuracy of the coupled acoustic and thermal models described in Chapter 2.

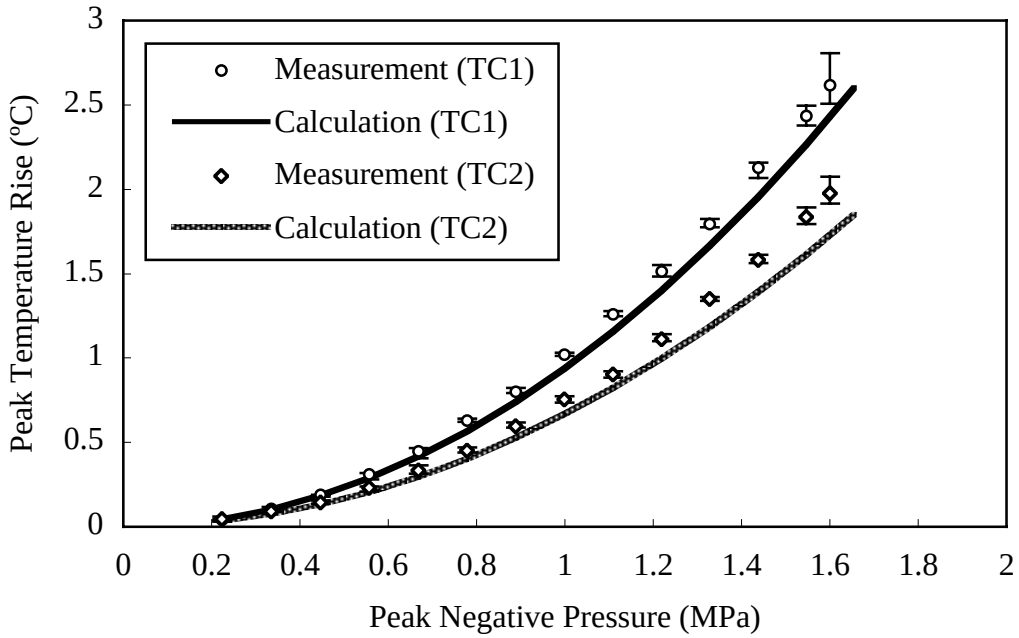

Figure 4.11: Measured and Predicted peak temperature rise at TC1 and TC2 due to acoustic absorption as a function of the peak negative acoustic pressure amplitude at the focus. Each point is an average of 5 measurements and the error bars are the maximum deviation from the mean.

4.2.4 Determination of the Cavitation Threshold Pressure

As we described in Section 1.2, a traditional definition for the cavitation threshold pressure can be summarized as the minimum pressure amplitude required to initiate or nucleate cavitation activity. Since the occurrence of any cavitation-related enhanced heating effect can be related to the indicators of cavitation activity [93, 205], and since a direct temperature measurement is the most obvious detection mechanism for the enhanced heating effect, an analysis of the temperature measurements can establish the threshold pressure for cavitation. There are two methods to determine cavitation threshold pressure based on temperature measurements. The first one is by observing the rate of heating from the temperature response curve with time. Figure 4.12 (a) for a peak negative acoustic pressure amplitude of 1.60 MPa, shows a typical temperature response obtained in the absence of cavitation. In Fig. 4.12 (b) we present the heating curve obtained at 1.66 MPa; note the pronounced “kink” in the curve at approximately the 600 msec mark. This indicates the onset of the enhanced heating effect due to cavitation activity, and 1.66 MPa is the apparent threshold for this effect in this phantom, given a 1 second insonation duration. (Since cavitation nucleation is a statistical process, one might measure a lower threshold if one is willing to wait longer.) In Fig. 4.12 (c), the pressure amplitude at the focus has been increased to 1.76 MPa, the threshold pressure has been exceeded, and the cavitation activity and thus the enhanced heating effect occur nearly instantaneously.

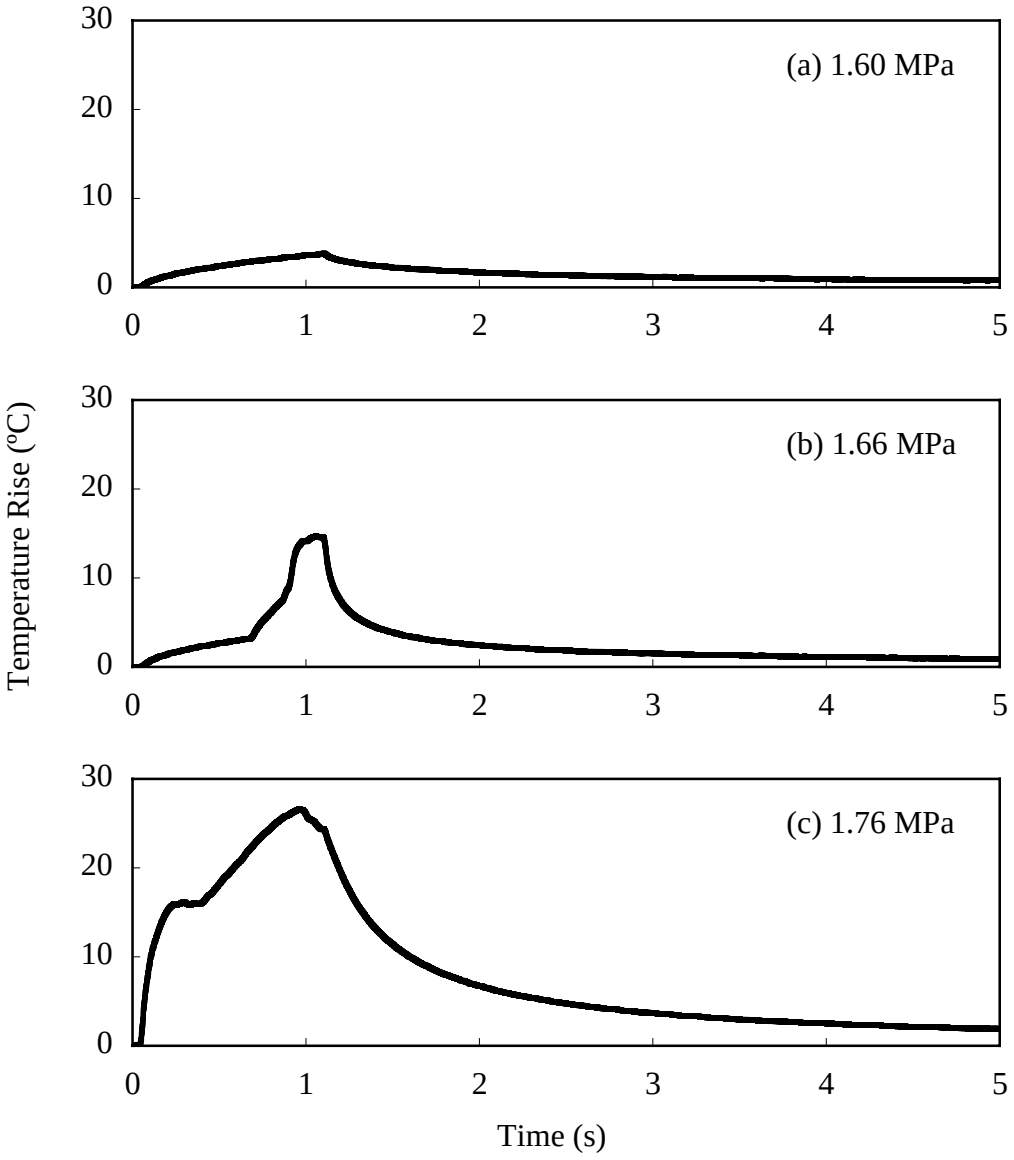

Figure 4.12: Temperature response as a function of time for three measurements by TC1 below, at, and above the cavitation threshold pressure.

Another way to determine the cavitation threshold pressure based on temperature measurements is to consider the dependence of peak temperature rise with pressure. Figure 4.13 is the extension of the results given in Fig. 4.11 up to pressures above cavitation threshold pressure; note the peak temperature rise after the measurement at 1.6 MPa. As indicated earlier, the model described in Chapter 2 predicts a peak temperature that is nearly proportional to the acoustic pressure squared. The changes in Fig. 4.8 are consistent with these predictions up to and including 1.6 MPa. However, above this pressure, the peak temperature output is substantially larger than expected and the scatter in subsequent measurements increases dramatically. It is known that this dramatic increase in the magnitude and variability of the temperature response is associated with the onset of acoustic cavitation [93, 205]. Therefore, 1.66 MPa is the apparent threshold for this effect in this phantom. Figure 4.13 not only serves to further demonstrated the excellent agreement between theory and measurement for sub-threshold pressures, it also emphasizes the fact that the model provided in Chapter 2 is incapable of making even approximate predictions once bubbles are present. Indeed, once the cavitation threshold is exceeded, it appears that the heating process is dominated by bubble-related effects [205].

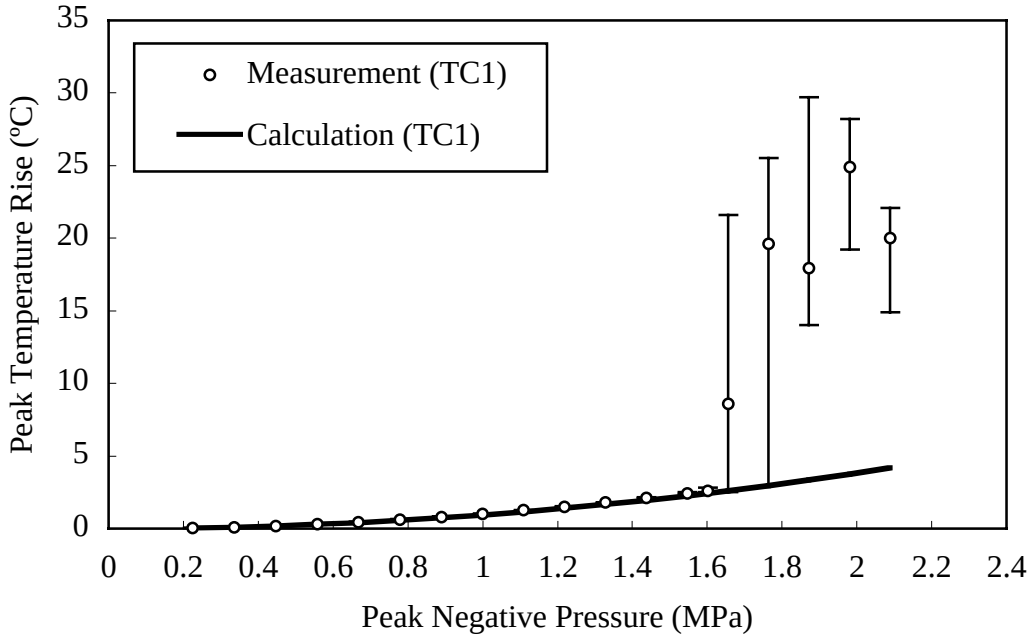

Figure 4.13: Measured and Predicted peak temperature rise at TC1 as a function of peak negative acoustic pressure amplitude at the focus. The dramatic increase in the peak temperature rise at 1.66 MPa indicates the onset of cavitation activity. Each point is an average of 5 measurements and the error bars are the maximum deviation from the mean.

4.3 Heating in Flow-Through Tissue Phantoms

In this section we present the experimental results obtained in single vessel flow-through tissue phantoms. A scheme of this flow phantom configuration is shown in Fig. 3.4, which is repeated here for convenience (Fig. 4.14). This is a good model to experimentally study the heating of the "blood" and the "vessel wall", the convective cooling effect, and the impact of acoustic streaming. It thus provides a simple and effective way to verify our numerical transport models in a vascularized tissue phantom. Validation of the acoustic streaming model presents a challenge, for we do not have the ability to quantitatively measure the streaming field. Fortunately, Kamakura *et al*. [165, 169] have conducted both theoretical and experimental investigations of acoustic

streaming generated by focused beams, and showed good agreements between measurements and predictions. Their 2-D study provides us a way to verify our 3-D numerical model by reproducing their calculations using their published parameters. Results from this comparison will be presented in Section 4.3.1. The experimental results on heating in the "blood" will then be reported and compared with model predictions in Section 4.3.2. Both the experimental and simulated results on the heating at the "vessel" wall will be presented in Section 4.3.3 and 4.3.4. Two vessel sizes are employed; one has a diameter of 6.35 mm, and the other one of 2.5 mm. The entire manifold of results will be summarized and discussed at the end of this chapter.

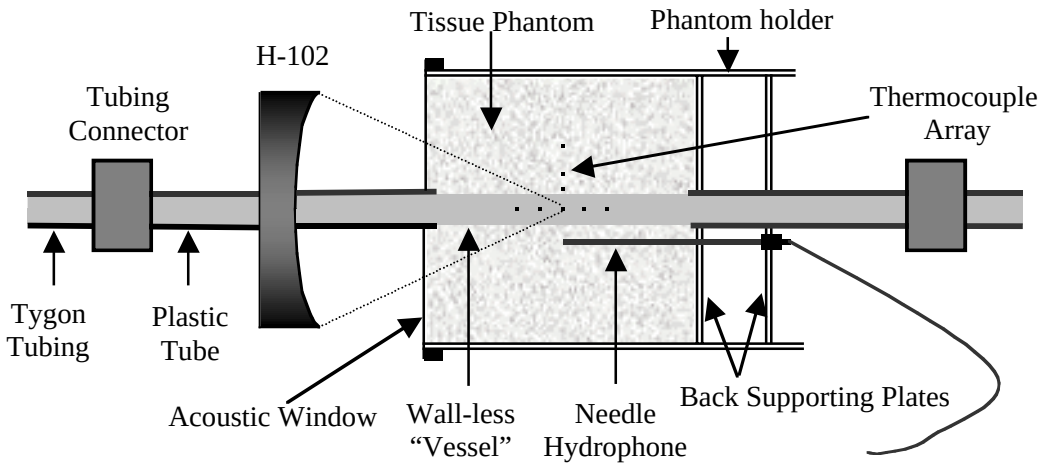

Figure 4.14: Schematic diagram of the instrumented flow-through tissue phantom.

4.3.1 Verification of Acoustic Streaming Code

Kamakura *et al*. [165] investigated acoustic streaming induced in water inside a rigid closed tube insonified axially by focused Gaussian beams. The end wall opposite the source is an absorbing boundary and the tube radius is larger than the source radius.

The tube is 2 cm in radius and 20 cm in length. Their sound source model is a 5 MHz ultrasonic radiator with Gaussian amplitude profiles in both the axial and radial direction. The radius and focal length are 1 and 5 cm, respectively. Figure 4.15 shows their computation region for axisymmetric acoustic streaming.

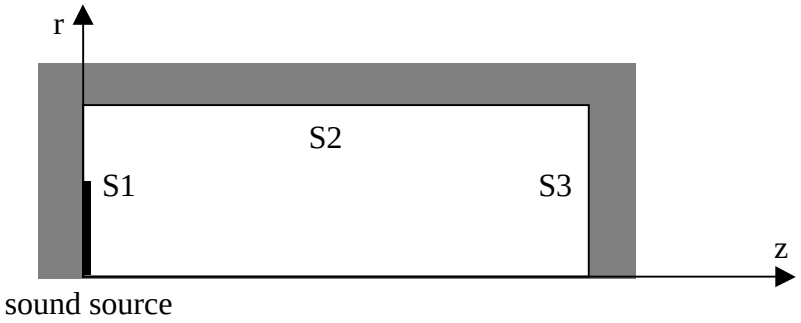

Figure 4.15: Computation region for axisymmetric acoustic streaming in water in a closed tube.

The model equations they use to describe for cylindrically symmetric flow are the continuity equation and the Navier-Stokes equation in a viscous incompressible fluid in 2-D cylindrical coordinates:

$$\frac{\partial U_z}{\partial z}+\frac{1}{r}\frac{\partial}{\partial r}(rU_r)=0, \tag{4.1}$$

$$\frac{\partial U_r}{\partial t}+U_r\frac{\partial U_r}{\partial r}+U_z\frac{\partial U_r}{\partial z}=F_r-\frac{1}{\rho_0}\frac{\partial P}{\partial r}+\nu\left[\frac{\partial^2 U_r}{\partial z^2}+\frac{\partial}{\partial r}\left(\frac{1}{r}\frac{\partial}{\partial r}(rU_r)\right)\right], \tag{4.2}$$

$$\frac{\partial U_z}{\partial t}+U_r\frac{\partial U_z}{\partial r}+U_z\frac{\partial U_z}{\partial z}=F_z-\frac{1}{\rho_0}\frac{\partial P}{\partial z}+\nu\left[\frac{\partial^2 U_z}{\partial z^2}+\frac{1}{r}\frac{\partial}{\partial r}\left(r\frac{\partial U_z}{\partial r}\right)\right], \tag{4.3}$$

where U_r and U_z are the radial and axial components of streaming velocity, P is the pressure, $\nu=\eta/\rho_0$ is the kinematic viscosity, η is the shear viscosity, ρ_0 is the density, and F_r, F_z are the radial and axial components of the external driving force.

Because of viscosity, the streaming velocity must vanish everywhere on the inner surface of the tube:

$$U_r, U_z = 0 \quad on\ S1, S2, and\ S3. \tag{4.4}$$

The other boundary conditions follow from the axisymmetry assumption:

$$U_r = 0, \quad \frac{\partial U_z}{\partial r} = 0 \quad on\ the\ axis. \tag{4.5}$$

The initial conditions are

$$U_r, U_z = 0 \quad in\ the\ space\ at\ t = 0. \tag{4.6}$$

Kamakura *et al*. employ the parabolic approximation to analyze the ultrasound beams. Within this approximation, the complex pressure $\tilde{p}$ for a Gaussian source with focal length *d* and on-source pressure amplitude p_0 can be represented in 2-D cylindrical coordinates as

$$\tilde{p} = p_0 \frac{1}{1-(1+jG^{-1})z/d} \exp\left[-\left(\frac{r}{a}\right)^2 \frac{1-jG}{1-(1+jG^{-1})z/d} - (\alpha + jk)z\right], \tag{4.7}$$

where $G = R_a/d$, $R_a = ka^2/2$ is the Rayleigh distance for planar piston source, *a* is the radius of the sound source, *k* is the wave number, and α is the sound absorption coefficient of water. The driving force for acoustic streaming is written as

$$\begin{aligned} F_z &= \frac{\alpha}{(\rho_0 c_0)^2} |\tilde{p}|^2, \\ F_r &= \frac{2\alpha r}{(\rho_0 c_0)^2 ka^2} \frac{z/R_a - G(1-z/d)}{(1-z/d)^2 + (z/R_a)^2} |\tilde{p}|^2, \end{aligned} \tag{4.8}$$

where

$$|\tilde{p}|^2 = p_0^2 \frac{1}{(1-z/d)^2 + (z/R_a)^2} \exp\left[-2\left(\frac{r}{a}\right)^2 \frac{1}{(1-z/d)^2 + (z/R_a)^2} - 2\alpha z\right], \tag{4.9}$$

and c_0 is the sound speed of water.

Table 4.2 lists the values for the parameters used in Kamakura *et al.*'s calculation; we employ these same values used in our 3-D numerical simulation.

Parameter	Value
a	1 cm
d	5 cm
f	5 MHz
ρ_0	998 kg/m^3
c_0	1483 m/s
α	0.63 Np/m
G	21.2
p_0	30 kPa

Table 4.2: Values for the parameters used in the streaming calculation.

Below we present results predicted by Kamakura *et al.*'s 2-D model and our 3-D model side by side to make the comparison and demonstrate the performance of our model. All the plots can be found in Kamakura *et al.*'s paper [165].

Buildup profiles of the streaming on the axis are given in Fig. 4.16. Five observation points are 4, 5, 6, 8, and 10 cm from the source. As can clearly be seen, the buildup characteristics of axial streaming predicted by our 3-D model agree well with Kamakura *et al.*'s 2-D model, except that our model predicts slightly higher peak velocities. This discrepancy is mainly attributed to the boundary conditions we incorporate into the pressure calculations; the pressure should be continuous at the tube

wall. However, it is not easy to define a continuous boundary condition along a curved surface in 3-D Cartesian coordinates. Thus we simply assume a squared tube with the same inner diameter for pressure calculation. This "looser" boundary can result in a higher streaming velocity along the axis. We should mention that it is much easier to set a zero boundary condition at the curved surface. Therefore we *do* apply a non-slip velocity boundary condition at the wall of the circular tube.

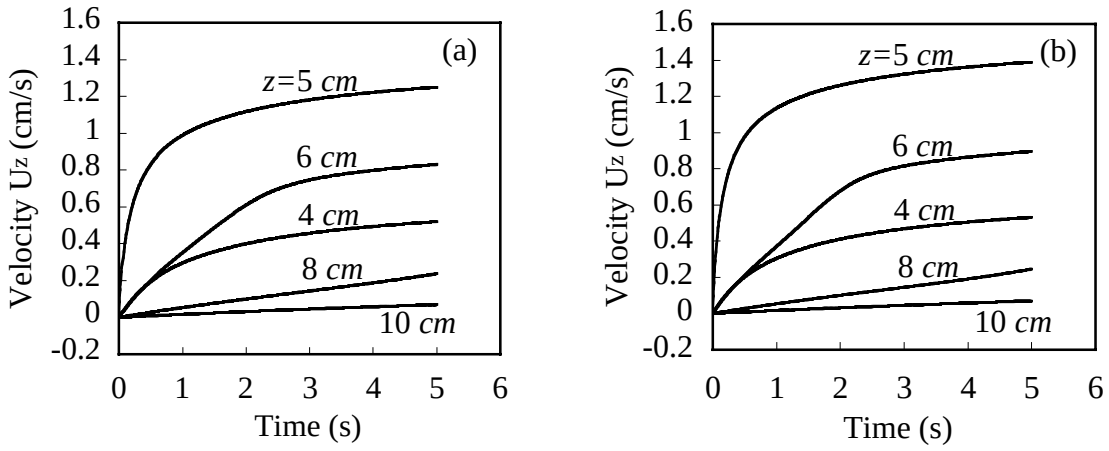

Figure 4.16: Buildup characteristics of axial streaming for p_0=30 kPa predicted by (a) Kamakura *et al.*'s 2-D model and (b) our 3-D model.

Figure 4.17 shows the axial velocity distribution at different times from 0.1 to 5 seconds. No significant streaming is found close to the source. However, near the focus the velocity reaches the maximum value. Strictly speaking, the maximum-velocity point is located somewhat outside of the focus. The streaming profiles in the postfocal region change due to mass flow out of the focal region. Again, the axial streaming velocity profiles predicted by our 3-D model agree well with those by Kamakura *et al.*'s 2-D model except that the overall levels are slightly higher.

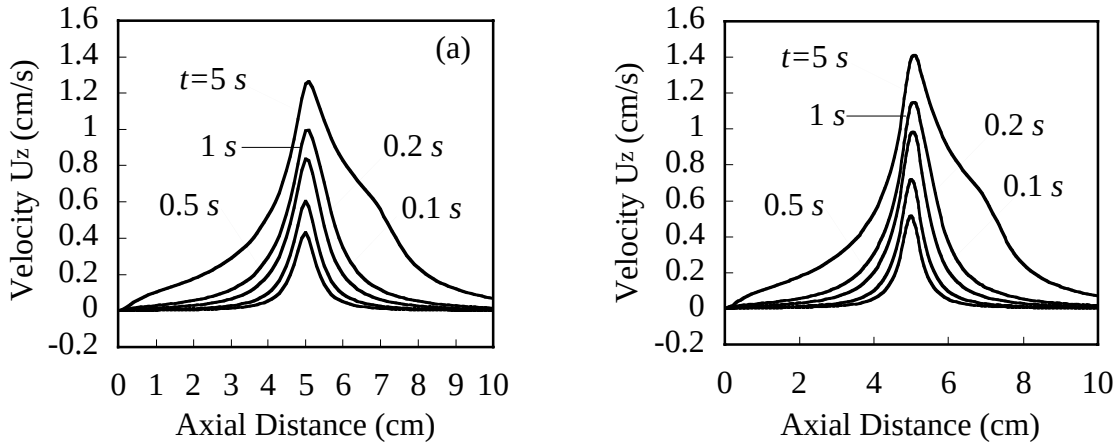

Figure 4.17: Axial streaming velocity profiles at different times between 0.1 and 5 sec for p_0=30 kPa predicted by (a) Kamakura *et al.*'s 2-D model and (b) our 3-D model.

Radial distributions of the velocity at 5 sec are given in Fig. 4.18 in three planes perpendicular to the axis. Streaming profiles in the focal plane are narrowest. The velocities decrease gradually with the radial distance and change direction around 6 mm from the axis. Reverse streaming outside that point is quite slow. Good agreement between the 2-D and 3-D simulations is also found in this plot.

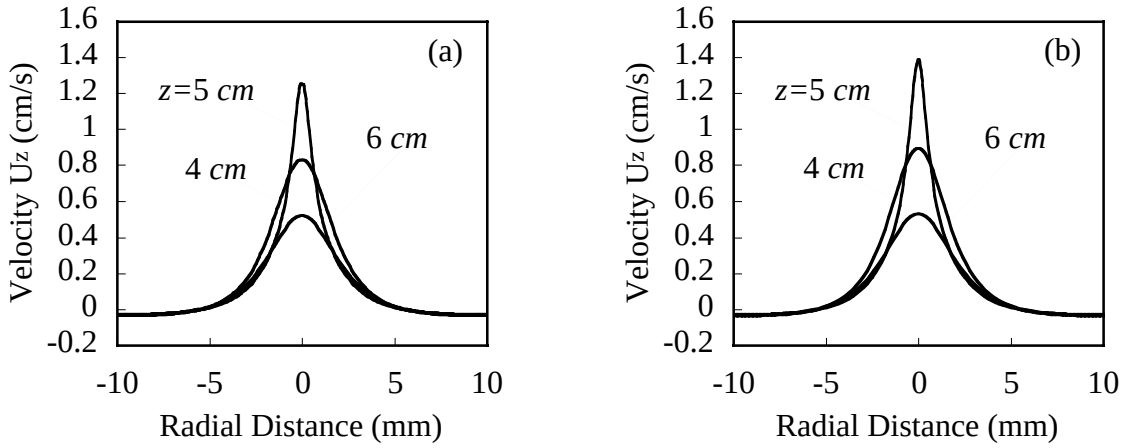

Figure 4.18: Streaming velocity profiles at 5 sec in three planes perpendicular to the axis for p_0=30 kPa predicted by (a) Kamakura *et al.*'s 2-D model and (b) our 3-D model.

Streaming velocity profiles in the focal plane at different times are shown in Fig. 4.19. All velocities are normalized by their value on the axis. As time goes on, the streaming profile tends to broaden, as expected, and there continues to be good agreement between the prediction of our 3-D model and the published results of Kamakura *et al*.

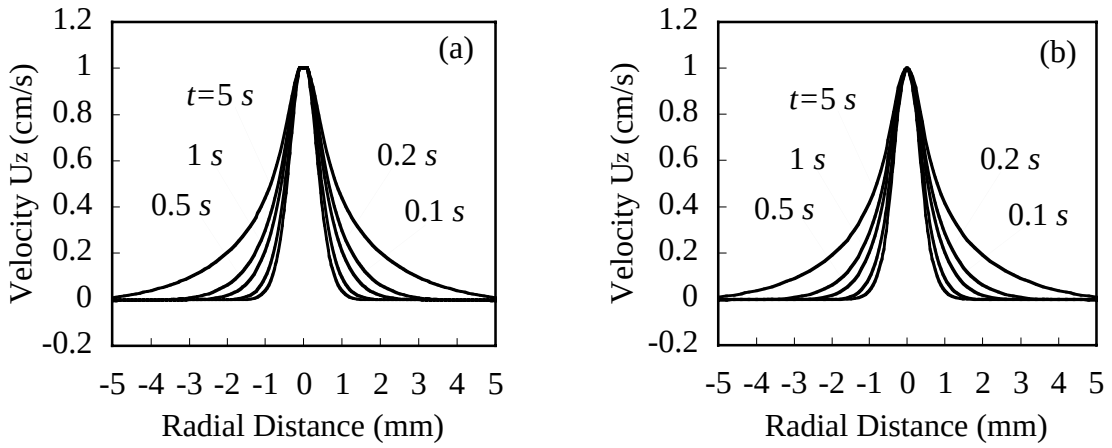

Figure 4.19: Changes in the focal-plane streaming velocity profiles with time for p_0=30 kPa predicted by (a) Kamakura *et al.*'s 2-D model (b) our 3-D model.

In summary, Kamakura *et al.*'s work provides a convenient means to assess the performance of our 3-D numerical acoustic streaming model. We have been able to reproduce their published results, except for a slight difference in overall velocity levels that we attribute to an approximation that we employ when imposing the boundary conditions. This general agreement confirms the validity of our 3-D numerical solution for the acoustic streaming field. We now feel confident that we can apply this model to the simulation of acoustic streaming fields induced in both real and artificial blood vessels by HIFU and the study of streaming effects on heating in highly vascularized tissues. In closing, it is important to note that our streaming model assumes a uniform

Newtonian fluid. Blood, whether real or simulated using the recipe described in Chapter 3, is neither uniform nor Newtonian. The validity of this widely employed approximation is not well understood and lies beyond the scope of this work.

4.3.2 Heating at the "Blood"

As we mentioned before, the acoustic absorption coefficient of the blood mimicking material (also true for the real human whole blood) is very small and so is the temperature rise in the "blood", especially for our *in vitro* experiments in which the highest pressure is kept below the cavitation threshold and is thus relatively low. As was the case in the uniform tissue phantom, the temperature rise measured in "blood" is the addition of the bulk heating of the "blood" and the thermocouple artifact. When there is an applied external flow or acoustic streaming is not negligible, the temperature rise in blood is usually too small to be detected and the measured temperature rise is dominated by thermocouple artifact.

To study the heating of "blood" by HIFU exposure, we use the first of the two recipes for blood mimicking fluid (BMF1) described in Section 3.2.2 because the acoustic absorption coefficient of BMF1 is larger than BMF2. This will result in a more readily detectable temperature rise for the same acoustic pressure amplitude. To quantity the thermocouple artifact in "blood" and check if it is appropriate to assume that the attenuation coefficient of "blood" is dominated by absorption coefficient, we conducted a simple experiment, shown in Fig. 4.20. HIFU transducer H-102 and the container filled with "blood" (or "plasma") are immersed in deionized and degassed water. HIFU beams travel from water to "blood" through an acoustic window (Tegaderm™, 3M Health Care,

St. Paul, MN). A thermocouple is inserted in the 'blood" to monitor the temperature rise. A calibrated needle hydrophone is also embedded in the "blood" for *in situ* pressure measurement and position calibration. An acoustic streaming barrier (Tegaderm™, 3M Health Care, St. Paul, MN) is placed between the acoustic window and the thermocouple (about 1 mm to the thermocouple) to block or minimize acoustic streaming. This arrangement permits us to exclusively study the temperature rise in the "blood" or "plasma" due to acoustic absorption and thermocouple artifact. The container is first filled with (non-absorbing) "plasma", and the temperature rise is measured as a function of pressure, insonation time and relative location of the thermocouple to the acoustic focus. This yields the thermocouple artifact. The data is stored and used later to correct for the temperature measurements obtained in "blood". The container is then filled with "blood", and all the measurements in "plasma" are repeated and the temperature rises are recorded.

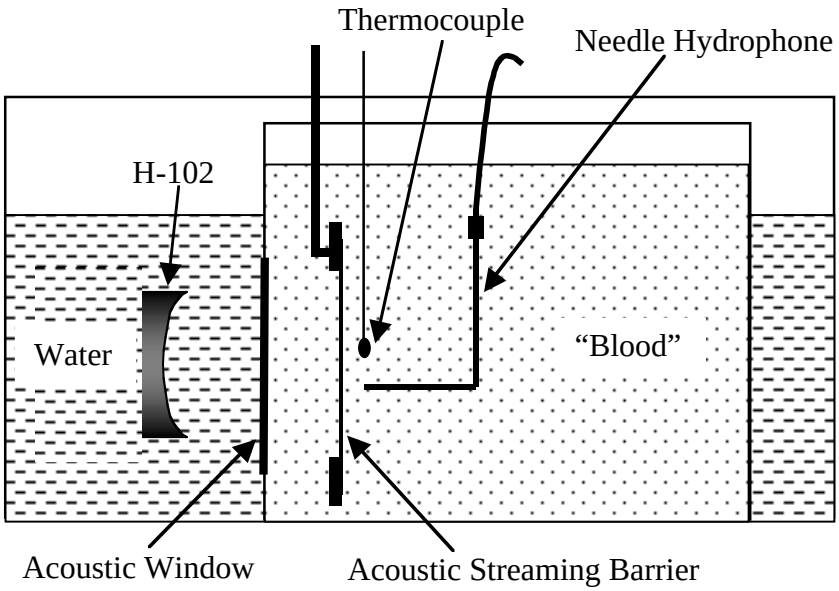

Figure 4.20: A schematic of thermocouple artifact measurement in "blood".

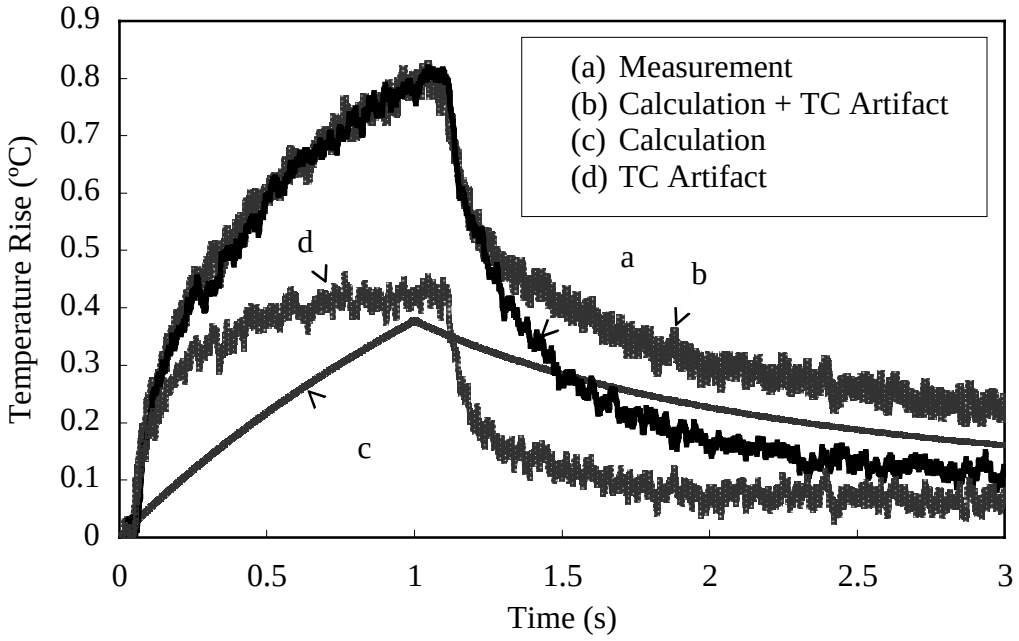

Figure 4.21: Comparison between the measured and simulated temperature response in "blood" as a function of time at the focus for 1 second insonation. The peak negative pressure at the focus is 1.52 MPa.

Figure 4.21 is a comparison between the measured and simulated temperature response in "blood" as a function of time at the focus for 1-second insonation times. The peak negative pressure at the focus is 1.52 MPa. We can see that after including the thermocouple artifact, the simulated peak temperature rise and the heating rate agree well with the measurement. However, the measured curve shows a faster cooling rate compared to prediction. It is still unclear to us what causes this. A possible reason is that the acoustic streaming is not totally blocked by the Tegaderm window. Since the visco-thermal absorption coefficient of "blood" is higher than that of "plasma", the acoustic streaming velocity induced in "blood' is larger than that in "plasma". Therefore, a stronger cooling effect may occur for HIFU exposure in "blood". Nevertheless, good agreement is still found between the measured and predicted temperature rise as a

function of pressure within the estimated uncertainty (see Appendix A), which is shown in Fig. 4.22. Each data point is the average of five sequential measurements, minus the thermocouple artifact. The medium is allowed to cool completely between measurements and the error bars indicate the maximum deviation from the mean. Results are based only on those measurements where enhanced heating due to cavitation is not detected.

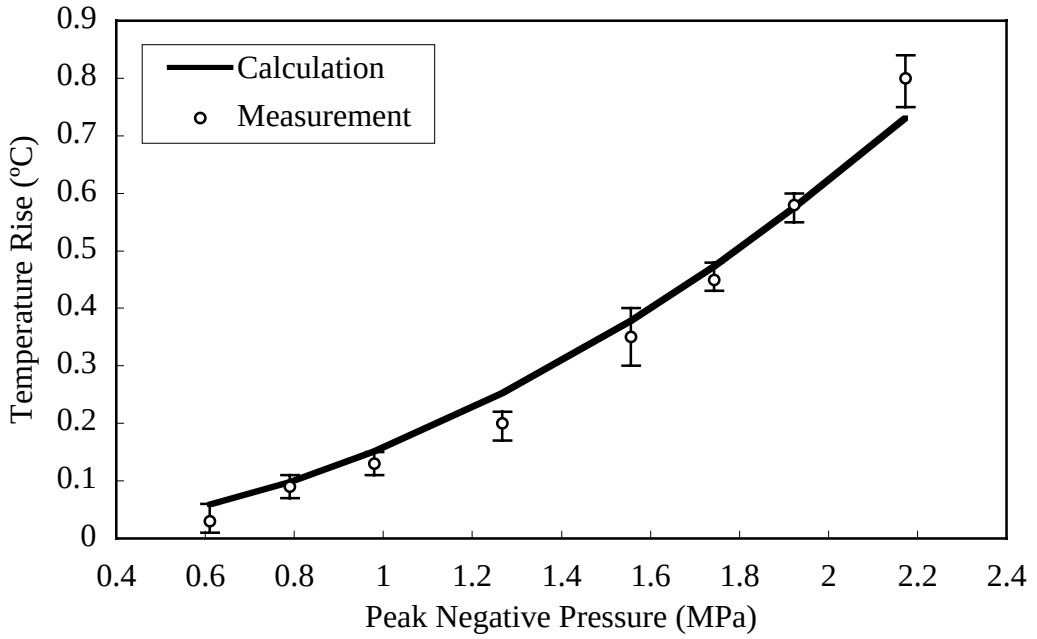

Figure 4.22: Measured and Predicted peak temperature rise in “blood” due to absorption as a function of peak negative acoustic pressure amplitude at the focus for 1 second insonation. Each point is an average of 5 measurements and the error bars are the maximum deviation from the mean.

Good agreement in Fig. 4.22 assures us that it is appropriate to assume that the attenuation coefficient of the blood mimicking fluid is dominated by the absorption coefficient, and we can use the temperature rise measured in “plasma” to correct for the thermocouple artifact measured in “blood”.

Property	Tissue Phantom	BMF1	Water
Density (kg/m^3)	1003	1108	998
Sound Speed (m/s)	1585	1704	1510
Attenuation ($Np/m/MHz$)	5.39	1.32	0.025
Specific Heat ($J/kg\cdot^0C$)	3710	3450	N/a
Thermal Conductivity ($W/m\cdot^0C$)	0.59	0.45	N/a
Viscosity (kg/s·m)	N/a	0.0037	N/a

Table 4.3: Physical properties of the relatively large "vessel" size flow-through tissue phantom with BMF1.

We now present the results of heating at the flow center in the flow-through tissue phantom experiment (Fig. 4.14) with the blood stimulant BMF1. The "vessel" size is 6.35 mm in diameter. The focus is positioned dead on the thermocouple that is at the flow center and 35 mm from the surface of the phantom. The physical properties for this relatively large "vessel" size flow-through tissue phantom are listed in Table 4.3, along with the values for surrounding water. The spatial grids used for the FDTD simulations are: $dx=dy$=0.1 mm, dz=0.2 mm and the time steps used for temperature field and acoustic streaming simulations are both 0.2 ms.

Figure 4.23 shows a comparison between the measured and simulated temperature response at the focus and flow center as a function of time for a 1-second insonation duration. The peak negative pressure is 1.52 MPa and there is no externally applied flow. We can see that the thermocouple artifact dominates the measured temperature rise, which is about four times greater than the temperature rise due to bulk heating in the

presence of acoustic streaming. After corrected for the thermocouple artifact, the predicted peak temperature rise agrees well with the measured value.

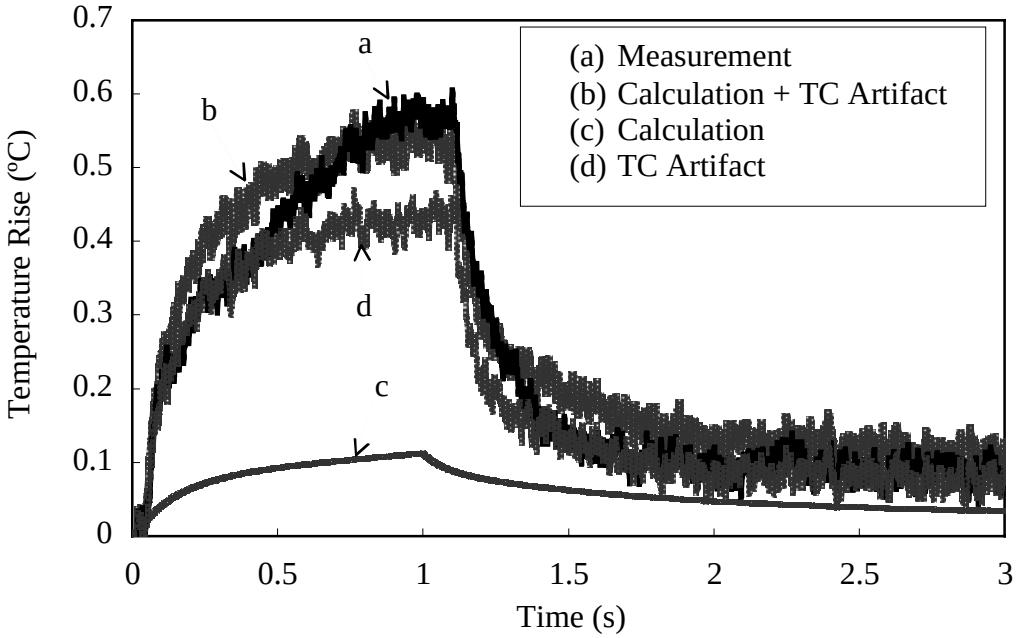

Figure 4.23: Comparison between the measured and simulated temperature response in "blood" as a function of time at the focus and flow center for a 1-second insonation. The peak negative pressure at the focus is 1.52 MPa.

This simulation includes the effect of acoustic streaming induced by HIFU propagation. Although there is no externally applied flow, the maximum flow velocity at the focus can still reach as high as 4.93 cm/*s* for a pressure amplitude of 1.52 MPa and 1 second insonation. The calculated streaming profile around the focal region is given in Fig. 4.24. For this axisymmetric case, streaming is illustrated only in the half-space. The direction of the arrow indicates the direction of the velocity, and the size of the arrow denotes the magnitude of the velocity. The plot shows a local circulation around the focus where the maximum velocity is found in post-focal region. Figure 4.25 shows the

temporal buildup of the acoustic streaming at the focus. The streaming velocity in the focus rises very rapidly and reaches near steady-state after only 0.2 seconds. The streaming declines equally fast after HIFU is turned off. Acoustic streaming present during HIFU insonation leads to significant cooling at the focus. To show how the acoustic streaming affects the heating, we performed a calculation of the temperature rise at the focus and in flow center when the acoustic streaming is neglected, shown in Fig. 4.26. The result shows a predicted temperature that substantially exceeds the measured value; a significant over estimation of the heating of the “blood” ensues when acoustic streaming is neglected.

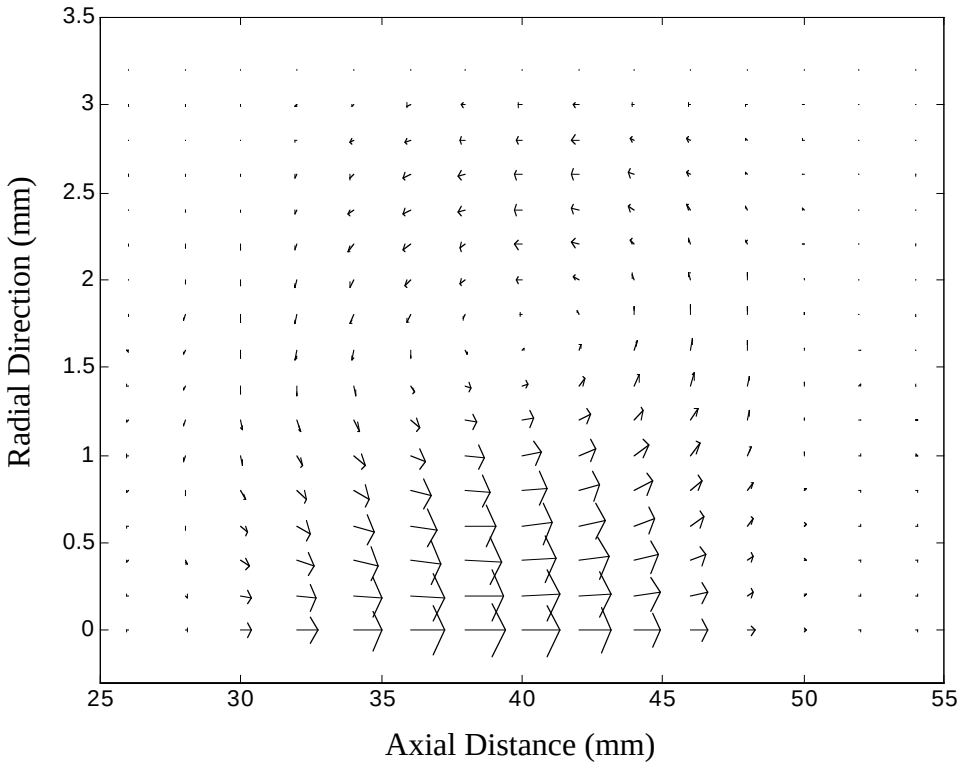

Figure 4.24: Simulated streaming profile around focal region. Axial distances are measured from the surface of the tissue phantom. Focal plane is at 35 mm. The length of the arrow denotes flow speed.

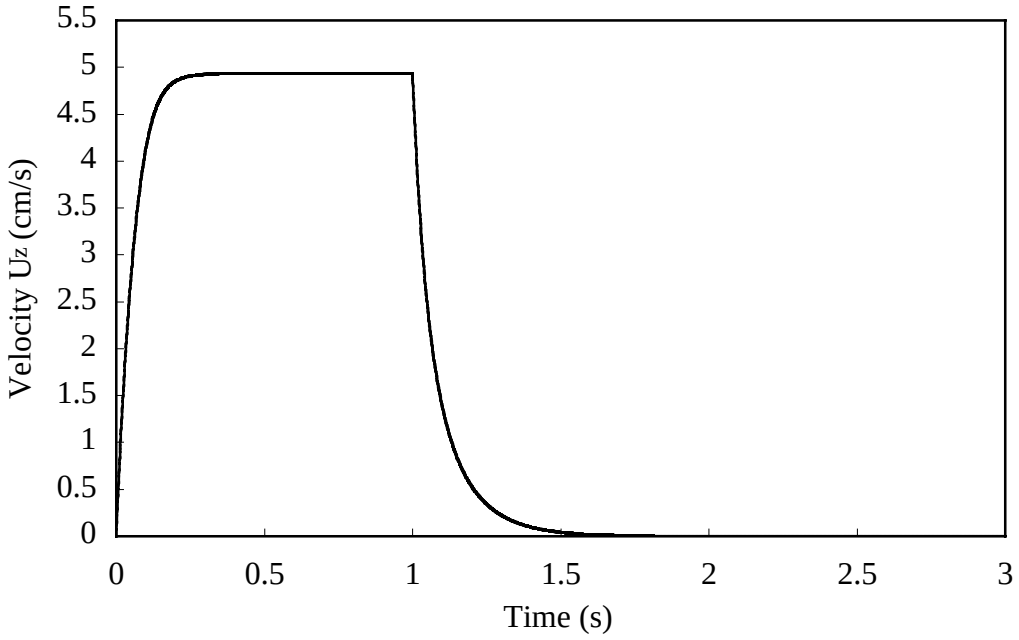

Figure 4.25: Buildup characteristics of acoustic streaming at the focus and along the flow center in the flow-through tissue phantom for 1 second insonation. The "vessel" is 6.35 mm in diameter, and the "blood" is BMF1. The peak negative pressure is 1.52 MPa.

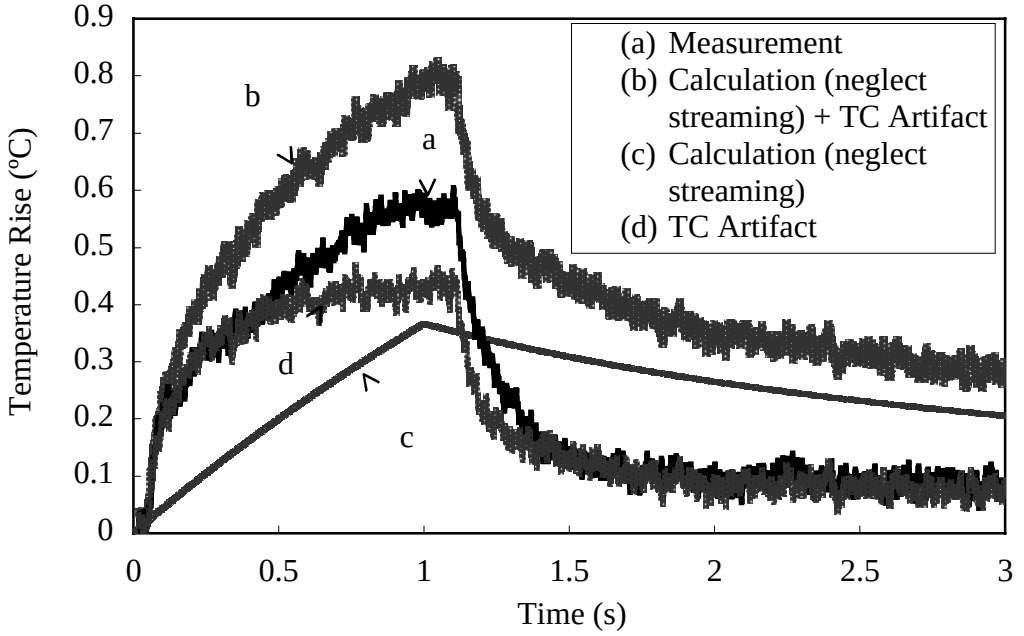

Figure 4.26: Comparison between the measured and simulated temperature response in "blood" as a function of time at the focus and flow center for 1 second insonation when acoustic streaming is neglected. The peak negative pressure at the focus is 1.52 MPa.

In this section we have shown that our model can accurately predict the temperature rise in flow center. BMF1 provides a good test fluid for verifying our thermal model for predicting the heating in the "blood" phase because it has a relatively high acoustic absorption coefficient (close to that of human whole blood) so that a more detectable temperature change can be produced. However, its propensity to settle out complicates long duration experiments. Slow-flow experiments with smaller "vessels" are also problematic for this same reason. We therefore switched to BMF2 as blood simulant for all subsequent experiments. BMF2 has an absorption coefficient of only 0.04 dB/cm at 1 MHz, which results in a much smaller temperature rise than measured in BMF1 provided that the other conditions are kept same. However, since the heating in "blood" is generally much smaller than heating in tissue phantom for our experimental conditions (*i.e.* no cavitation), this will not result in misleading results, particularly since for the focus of the next stage of the study will be the heating at or near the "vessel" wall. Moreover, the objective of the laboratory experiments is to verify the model. And thus can be done even if the absorption coefficient of the blood simulant is less than that encountered *in vivo*.

4.3.3 Heating at the "Vessel" Wall

In this section we will present the results of heating at or near the "vessel" wall in the presence of an applied external flow. The focus of the HIFU beam is positioned at TC2, which is 0.4 mm to the vessel wall, as shown in Fig. 4.27. The blood simulant is BMF2, and the "vessel" size is 2.6 mm in diameter. There are five thermocouples embedded in both the flow and the tissue phantom. TC1, TC4 and TC5 are positioned in

the vessel, spaced 5 mm apart in the axial direction. TC1, TC2 and TC3 are on a plane perpendicular to the flow axis and 35 mm from the front surface of the tissue phantom. TC2 and TC3 are embedded in the phantom, and their distances to the "vessel" wall are 0.4 and 2.3 mm, respectively. The physical properties for this relatively smaller "vessel" size flow-through tissue phantom are listed in Table 4.4, along with the values for surrounding water. The spatial grids used for the FDTD simulations are: $dx=dy$=0.1 mm, dz=0.2 mm and the time steps used for temperature field and acoustic streaming simulations are both 0.5 ms.

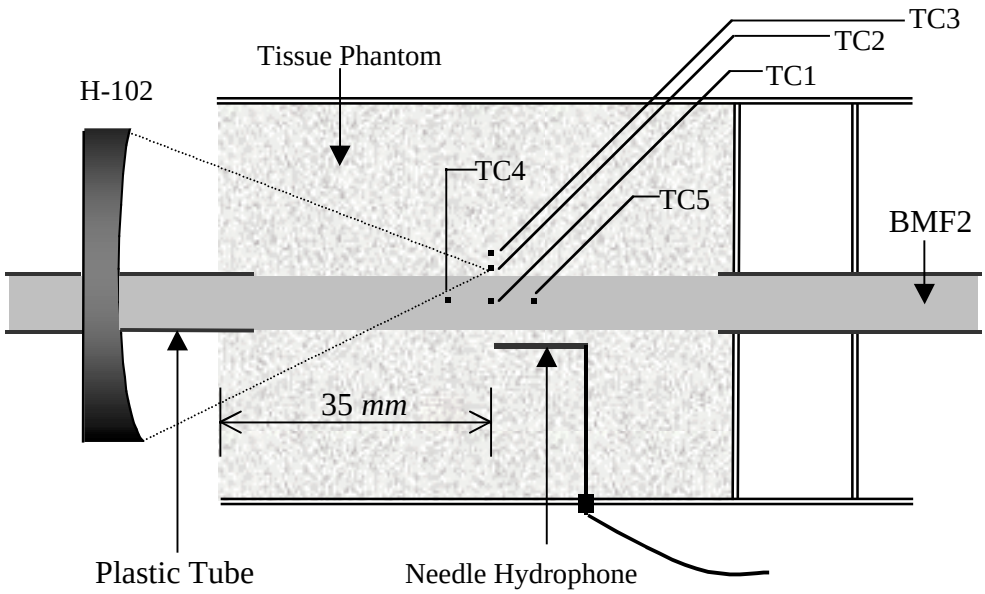

Figure 4.27: Schematic diagram of the instrumented flow-through tissue phantom: heating at "vessel" wall. The "vessel" size is 2.6 mm in diameter. Note that the acoustic focus is no longer positioned in the center of the flow, but rather is now pointed in the tissue phantom and close to the "vessel" wall.

Property	Tissue Phantom	BMF2	Water
Density (kg/m^3)	1045	1036	998
Sound Speed (m/s)	1551	1549	1488
Attenuation ($Np/m/MHz$)	10.17	0.46	0.025
Specific Heat ($J/kg\cdot^0C$)	3710	3930	N/a
Thermal Conductivity ($W/m\cdot^0C$)	0.59	0.57	N/a
Viscosity (kg/s·m)	N/a	0.0042	N/a

Table 4.4: Physical properties of the relatively smaller "vessel" size flow-through tissue phantom with BMF2.

As described in Section 3.2, to facilitate the deployment of the thermocouple arrays in the flow, we fabricated wall-less, single-"vessel" flow-through phantoms using two identical hemi-cylinders as molds. To do this, we cast the phantom hemi-cylinders, build in thermocouples, and clamp the two halves together. We find that when the two halves are clamped together, the hydrophone and the thermocouples in the phantom will be still in place. However, the positions of the thermocouples in the flow will usually change from their original locations. To accurately re-locate these thermocouples, we scan the focus of the transducer around each thermocouple using short insonations and record the position where maximum temperature rise is measured. By doing this we can find the position of each thermocouple relative to the hydrophone, and then its distance to the flow axis or "vessel" wall can be obtained. Using this method, we find that TC1, TC4 and TC5 are all above the flow axis. TC1 and TC4 are 0.8 mm to the "vessel" wall, and TC5 is 0.4 mm to the "vessel" wall.

Another issue to consider is the task of registering the experimental and computational coordinate systems. This was done by comparing the pressure waveform measured *in situ* with the computed waveform at the estimated location of the hydrophone. The computational coordinates were then translated slightly (typically ± 0.3 mm) to minimize this error and registration was achieved.

Heating at the Focus (TC2)

We will first present the results at the focus (TC2) for different pressures, insonation times and flow rates. A parabolic Pouiseille flow profile is assumed for the external applied flow in the test region, as described in Section 3.3. Figure 4.28 shows the temporal temperature response at TC2 for insonation times of 1, 3 and 5 seconds and for a peak negative pressure of 1.45 MPa. The left column (a) are the results for no external applied flow, and the right column (b) are the results for with external applied flow having spatially averaged velocity of 1.87 cm/s. Dark solid lines are the measurements, and light dashed lines are the prediction obtained using our 2-D pressure model coupled with our 3-D thermal model. The predictions demonstrate good agreement with the measurements. Figure 4.28 also shows an increasing flow cooling effect on the heating at the "vessel" wall with insonation time. To better illustrate this effect, Fig. 4.28 is re-plotted in Fig. 4.29 with only the experimental results shown. Dark solid lines are the results when there is no external applied flow, and light dashed lines are the results for with external applied flow of spatially averaged velocity 1.87 cm/s. The flow cooling effect is more notable for longer insonation times (*e.g.* 5 seconds). The flow not only

reduces the maximum temperature reached during HIFU exposure, but also decelerates the heating during insonation and expedites the cooling after HIFU is turned off.

The comparison of measured and predicted peak temperature rise at the focus as a function of pressure with varying flow speed for a 5-second insonation time is given in Fig. 4.30. Each data point is the average of five sequential measurements, minus the thermocouple artifact. The phantom is allowed to cool completely between measurements and the error bars indicate the maximum deviation from the mean. Good agreement is found for mean flow velocity of 0, 0.67 and 1.87 cm/s within the estimated uncertainties in temperature measurement and model prediction (see Appendix A).

Figure 4.31 is a plot of measured peak temperature rise at the focus as a function of spatially averaged flow velocity for a 5-second insonation time. Again, each data point is the average of five sequential measurements, minus the thermocouple artifact. The error bars indicate the maximum deviation from the mean. Results for six different pressures are shown. The trends are all consistent with the physical picture of a heated region being cooled by convective heat transfer.

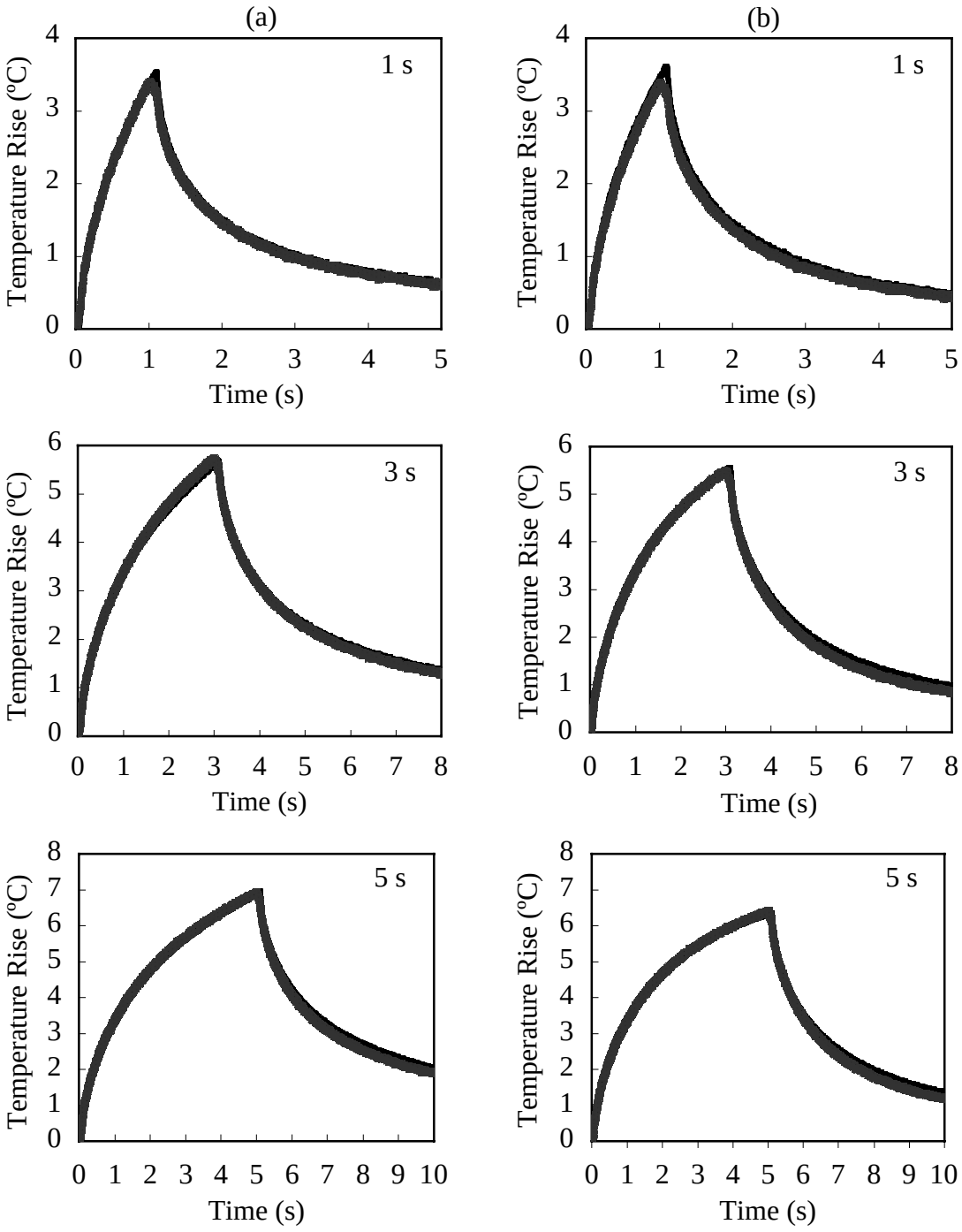

Figure 4.28: Comparison of measured and predicted temperature rise versus time at the focus (TC2) for insonation times of 1, 3 and 5 seconds, and an spatially averaged external applied flow velocity of (a) 0 and (b) 1.87 cm/s. The peak negative pressure at the focus is 1.45 MPa. Dark solid line - measurement, light dashed line - prediction.

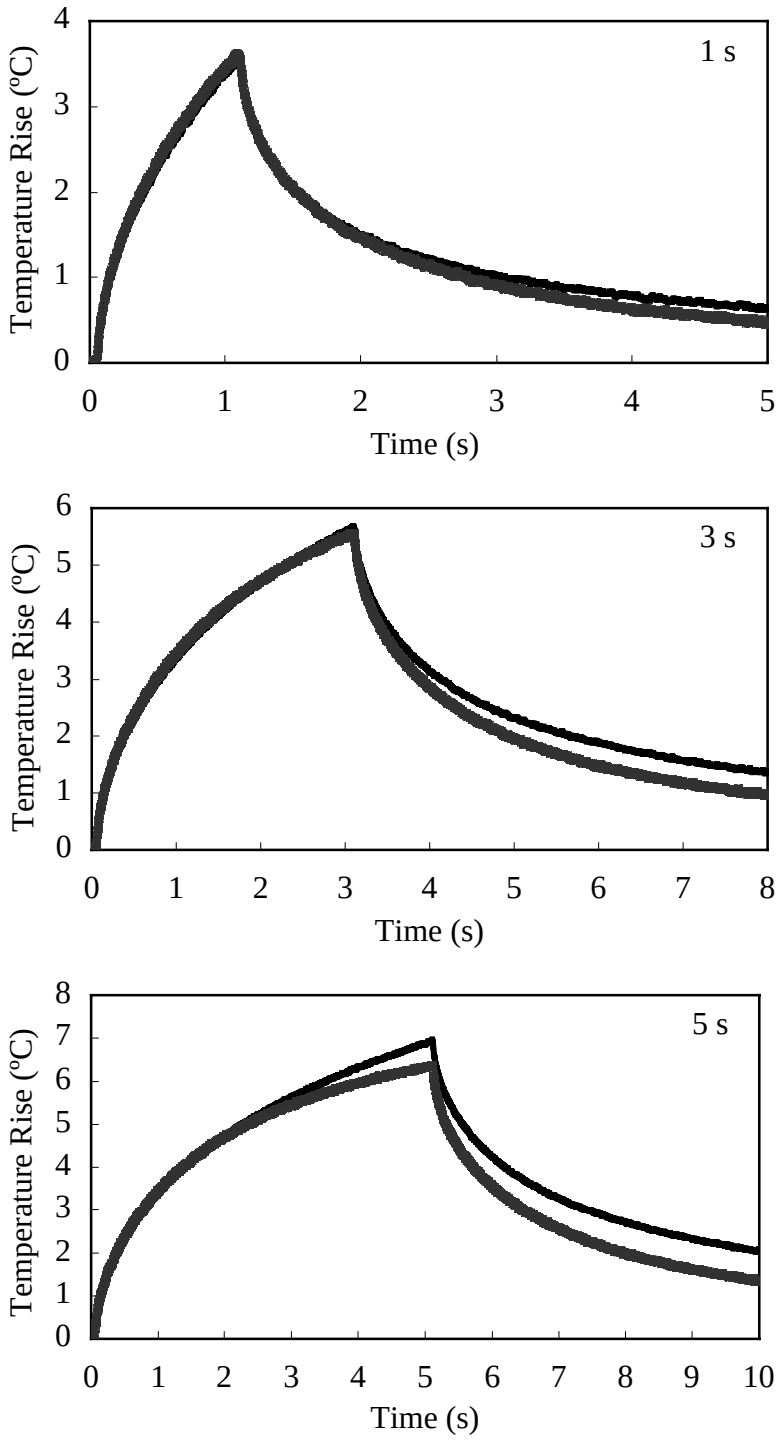

Figure 4.29: Experimental data showing increasing flow cooling effect on heating close to the "vessel" wall (TC2) with insonation time for a peak negative pressure of 1.45 MPa. Dark solid line – no external applied flow; light dashed line – external applied mean flow velocity 1.87 cm/s.

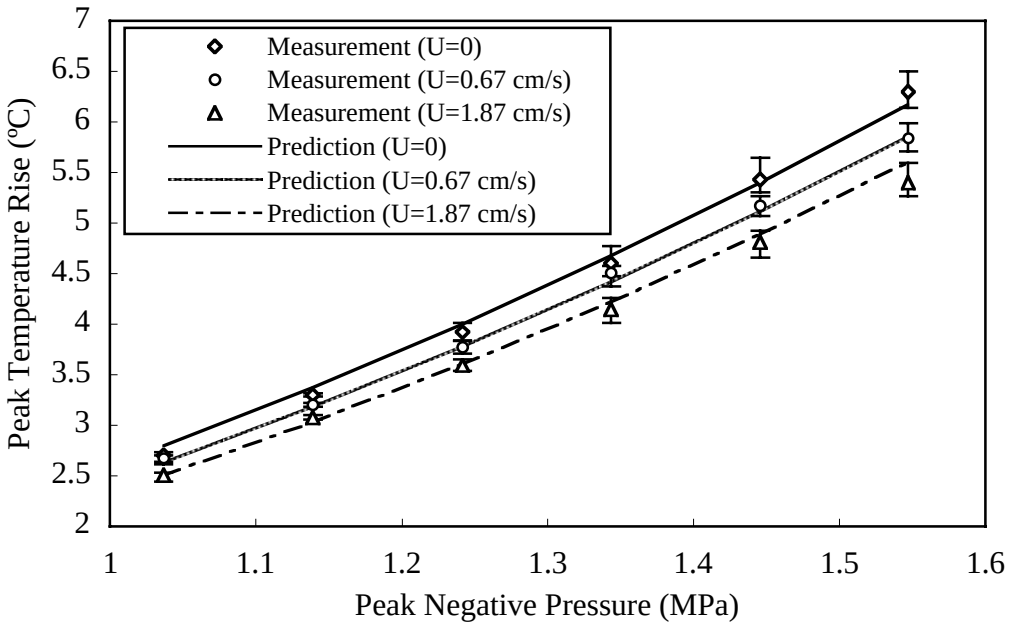

Figure 4.30: Comparison of the measured and predicted peak temperature rise at the focus (positioned in phantom and close to the vessel wall) as a function of pressure for varying external applied flow speeds. The insonation time is 5 seconds. Each point is an average of 5 measurements and the error bars are the maximum deviation from the mean.

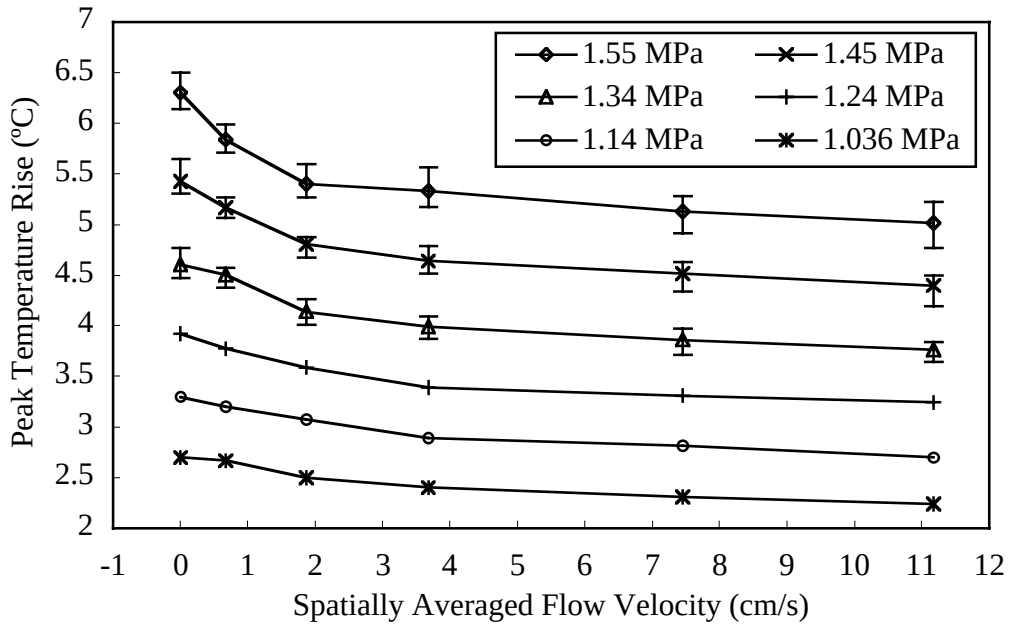

Figure 4.31: Measured peak temperature rise at the focus (positioned in the phantom and close to the vessel wall) as a function of spatially averaged flow velocity for a 5-second insonation time. Results are for six different peak negative pressures and each point is an average of 5 measurements and the error bars are the maximum deviation from the mean.

Heating at Other Sites

We have shown that our model can accurately predict the heating at the acoustic focus (TC2) for a variety of acoustic pressures, flow speeds, and insonation times. We now focus our attention on measurements obtained at the other thermocouple sites in an attempt to further test the validity of our numerical model. The acoustic focus is still positioned at TC2 (see Fig. 4.27).

Comparison between the measured and predicted temperature response as a function of time for TC1 and TC3 and for insonation times of 1, 3, and 5 seconds are given in Figs. 4.32 and 4.33. The peak negative pressure is 1.45 MPa at the focus. The left column are the results for no external applied flow, and the right column are the results for a mean flow speed of 1.87 cm/s. Figure 4.32 shows a much smaller temperature rise at TC1 when there is an applied external flow, which indicates substantial cooling by convective flow in “blood”. The measured temperature rise in this case is mainly due to thermocouple artifact. However, no significant cooling effect is found at TC3 because TC3 is in tissue phantom and is relatively far away from the flow. Good agreement is found between measurements and predictions for both TC1 and TC3.

Figure 4.34 and 4.35 are the obtained results for the TC4 and TC5 thermocouples. Good agreement between theory and experiment is shown for the no external flow condition. However, the measured data do not match well with simulations when there is an applied external flow. TC4 shows a somewhat smaller measured temperature rise than predicted, however, even the predicted rise is quite small and it is not clear how well we can resolve these small temperature rises given the precision of the thermocouple and the

electrical noise floor within the system. In any case, the temperature rise due to bulk heating at TC4 is so small that it can be neglected; the thermocouple artifact, however small in this case, dominates. Figure 4.35(b) for TC5 shows what appears to be a series of abnormal measured temperature profiles, particularly after the external flow is activated. The measured temperature rise during insonation is much smaller than prediction, and an abrupt temperature elevation occurs after HIFU is turned off. We can come up with no viable physical explanation for this peculiar behavior. The fact that there appears to be a transient jump in the temperature coincident with the shutting down of the acoustic field is quite suspicious, and suggests the possibility that TC5 may have been malfunctioning, particularly given the forces exerted upon it by the flow. These thermocouples are very delicate and it is quite plausible that TC5 may have been damaged in the process of measurement. The fact that this is the only thermocouple that failed to generate data in agreement with the model predictions further supports this hypothesis. Nevertheless, this is merely a plausibility argument and it is conceivable that the results in Fig. 4.35 (b) could be real. If so, its explanation eludes us and we leave the resolution of this issue to future work.

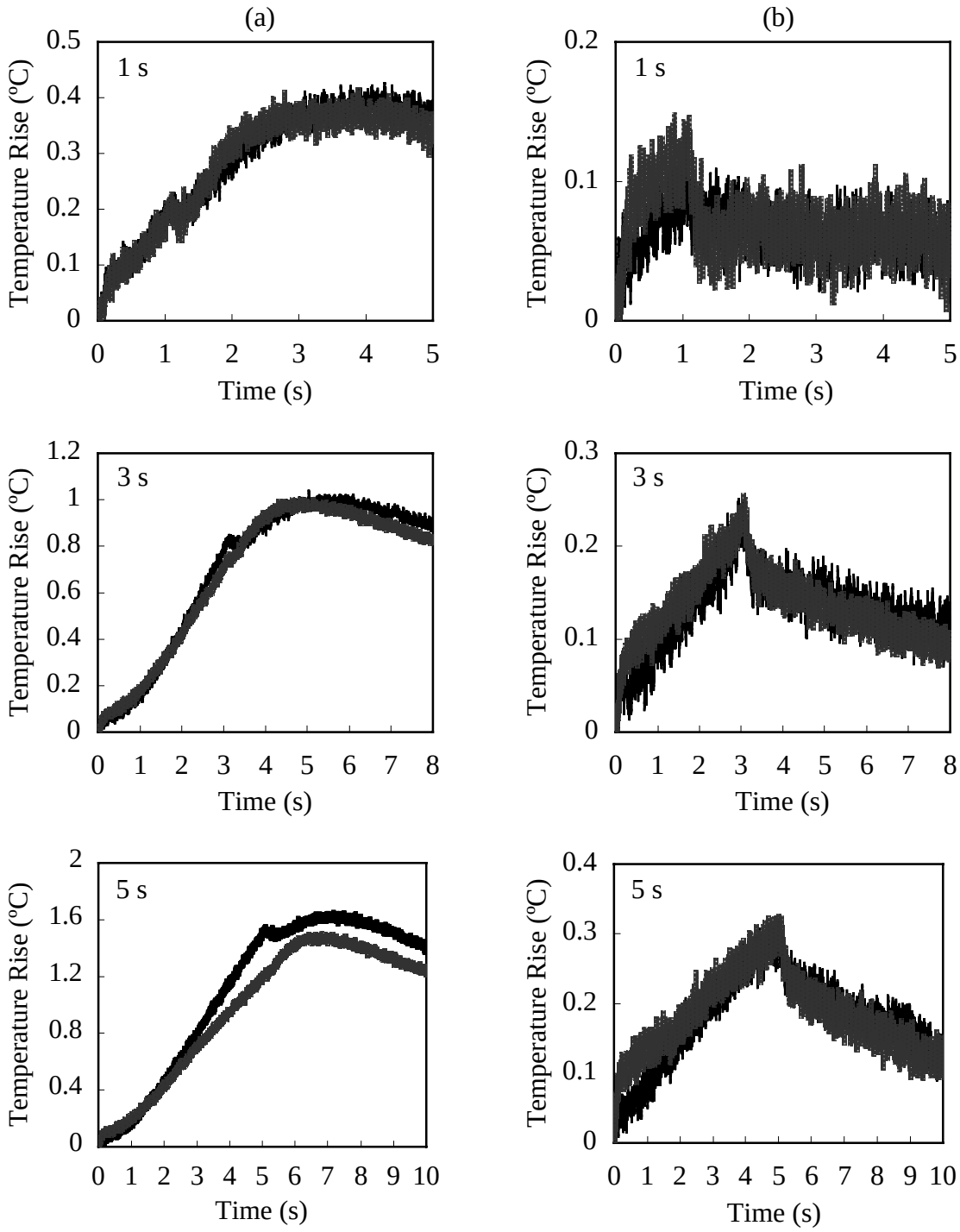

Figure 4.32: Comparison of the measured and predicted temperature rise versus time at TC1 for insonation times of 1, 3 and 5 seconds, and an averaged external applied flow speed of (a) 0 and (b) 1.87 cm/s. The peak negative pressure at the focus is 1.45 MPa. Dark solid line - measurement, light dashed line - prediction.

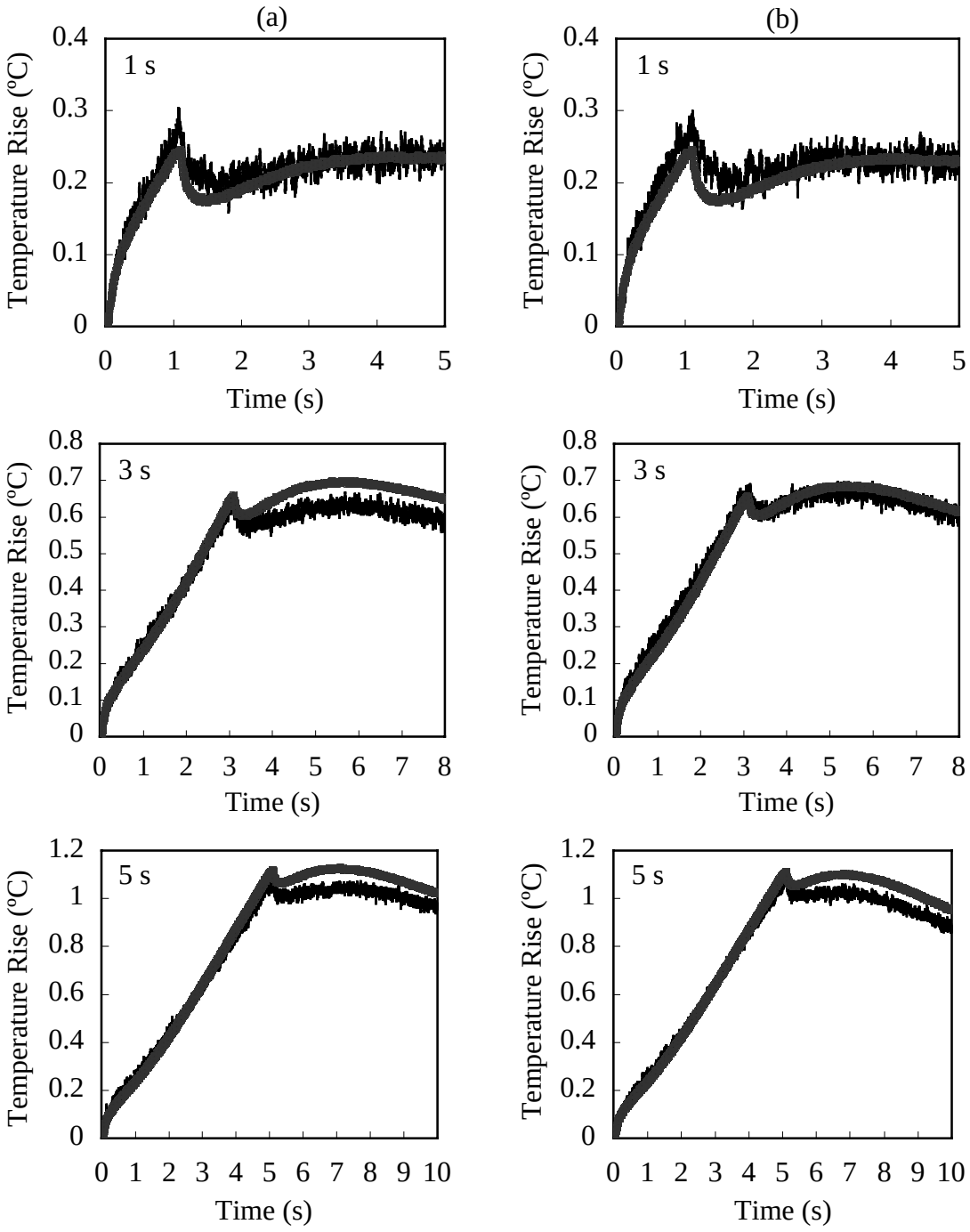

Figure 4.33: Comparison of the measured and predicted temperature rise versus time at TC3 for insonation times of 1, 3 and 5 seconds, and an averaged external applied flow speed of (a) 0 and (b) 1.87 cm/s. The peak negative pressure at the focus is 1.45 MPa. Dark solid line - measurement, light dashed line - prediction.

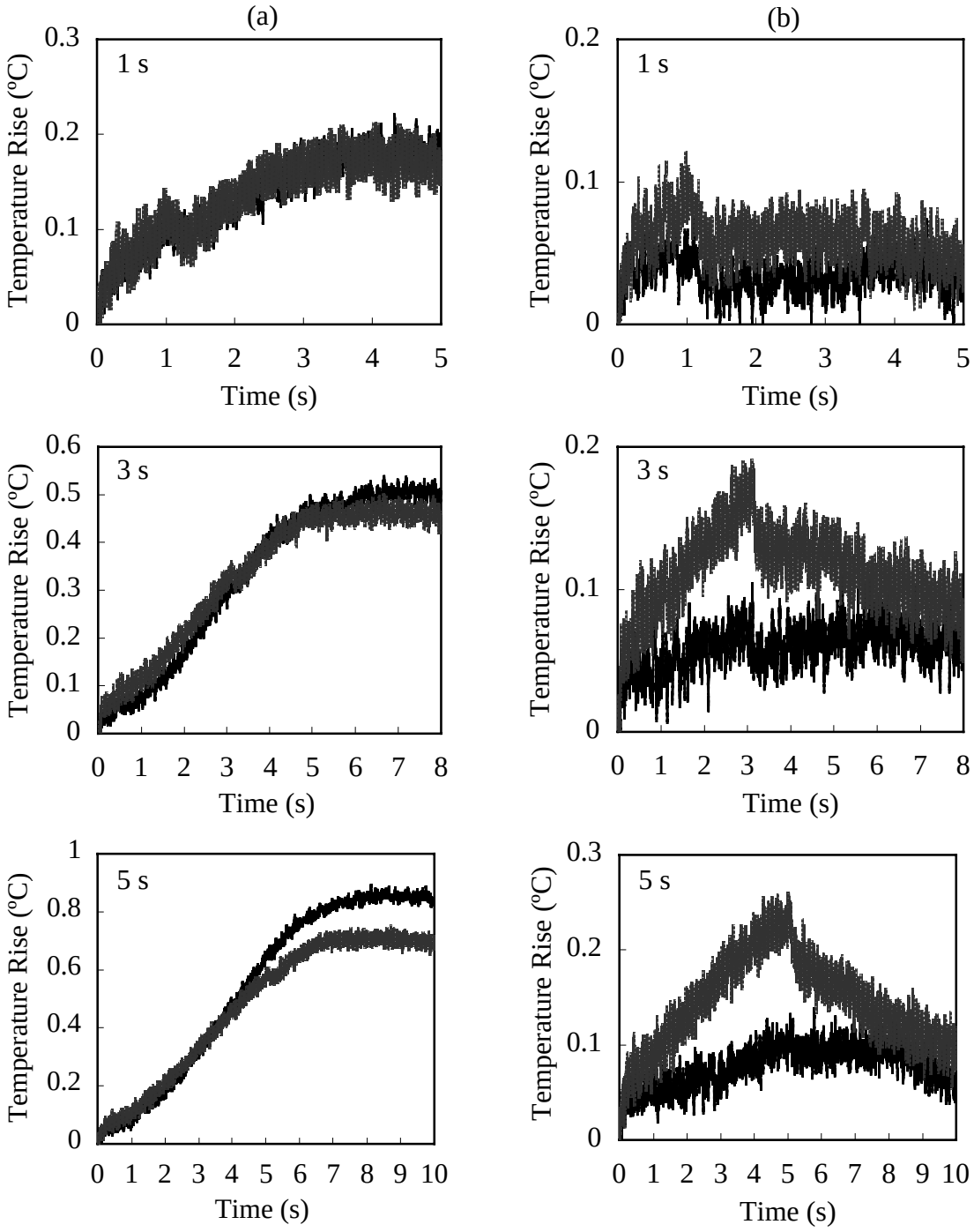

Figure 4.34: Comparison of the measured and predicted temperature rise versus time at TC4 for insonation times of 1, 3 and 5 seconds, and an averaged external applied flow speed of (a) 0 and (b) 1.87 cm/s. The peak negative pressure at the focus is 1.45 MPa. Dark solid line - measurement, light dashed line - prediction.

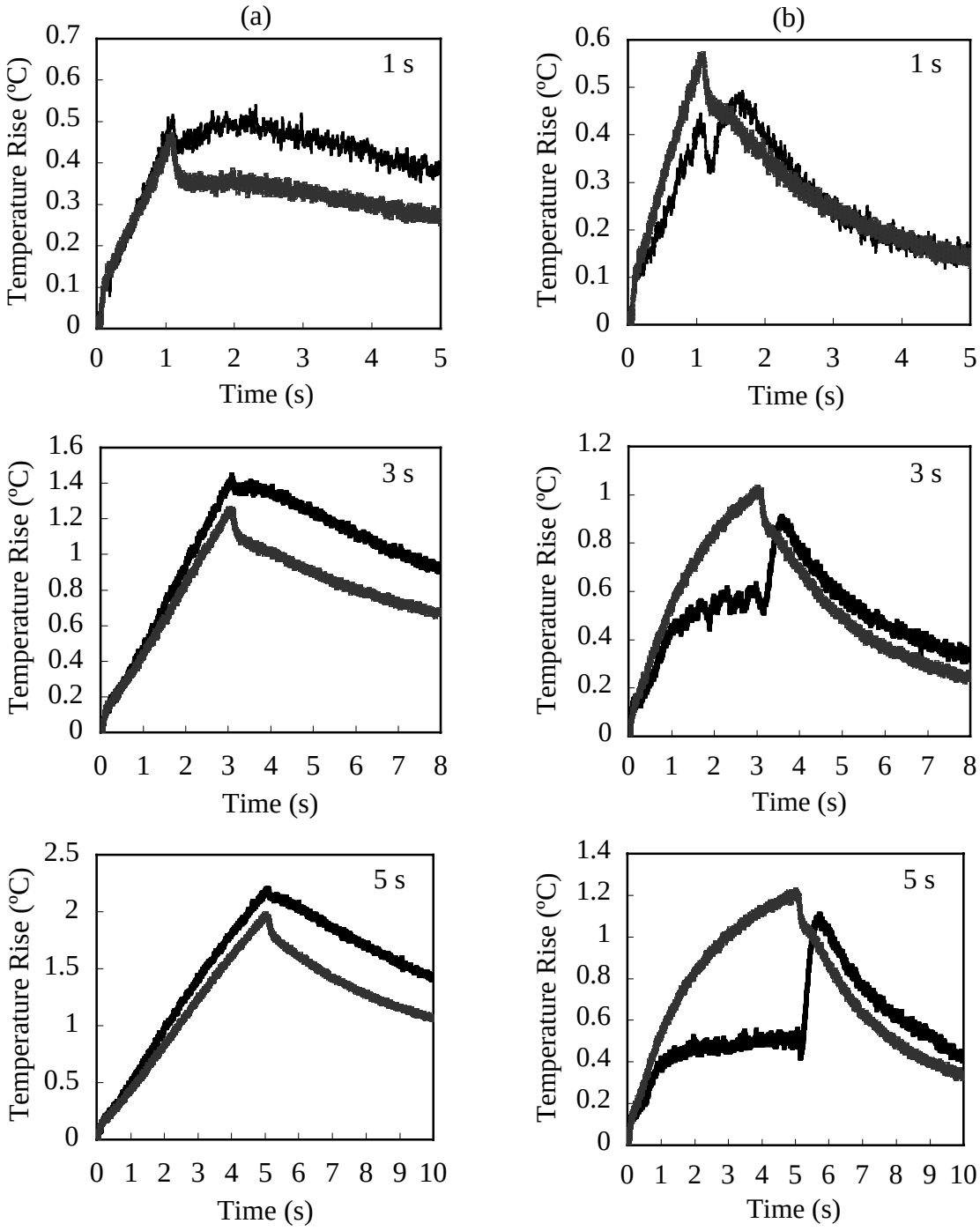

Figure 4.35: Comparison of the measured and predicted temperature rise versus time at TC5 for insonation times of 1, 3 and 5 seconds, and an averaged external applied flow rate of (a) 0 and (b) 1.87 cm/s. The peak negative pressure at the focus is 1.45 MPa. Dark solid line - measurement, light dashed line - prediction.

A closer look at the temperature field

Instead of focusing on specific test points, we now present simulation results that give a more complete picture of what the streaming and temperature fields look like. This is one of the most powerful and attractive features of numerical simulation. Because the tissue phantom and the HIFU transducer have been arranged in such a way that they are symmetric in *x* direction, all the results will be plotted only in the *yz* plane (see Fig. 2.3). To present the results in a clearer way, the solution domain is sketched in Fig. 4.36, showing the coordinates of the focus, the flow axis, and the vessel wall. The HIFU beam is propagating in the *z* direction, the acoustic axis is at y = 11.7 mm, and the focal plane is located at z = 35 mm.

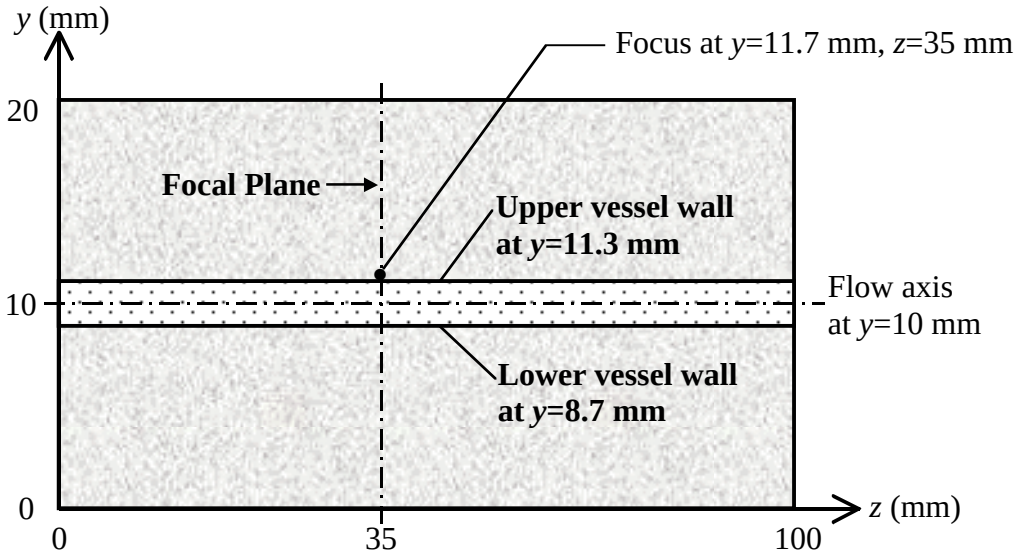

Figure 4.36: The computational domain in *yz* plane for simulations of heating in relatively smaller "vessel" size (2.6 mm in diameter) flow-through tissue phantom. The focus is just outside the vessel and 0.4 mm to the vessel wall.

Figure 4.37 is a plot of the steady state streaming profile inside the “vessel” that is just below the focal spot. The plot shows the expected local circulation pattern around beneath the focal spot. The streaming vanishes at the vessel wall (y = 8.7 mm and 11.3 mm).

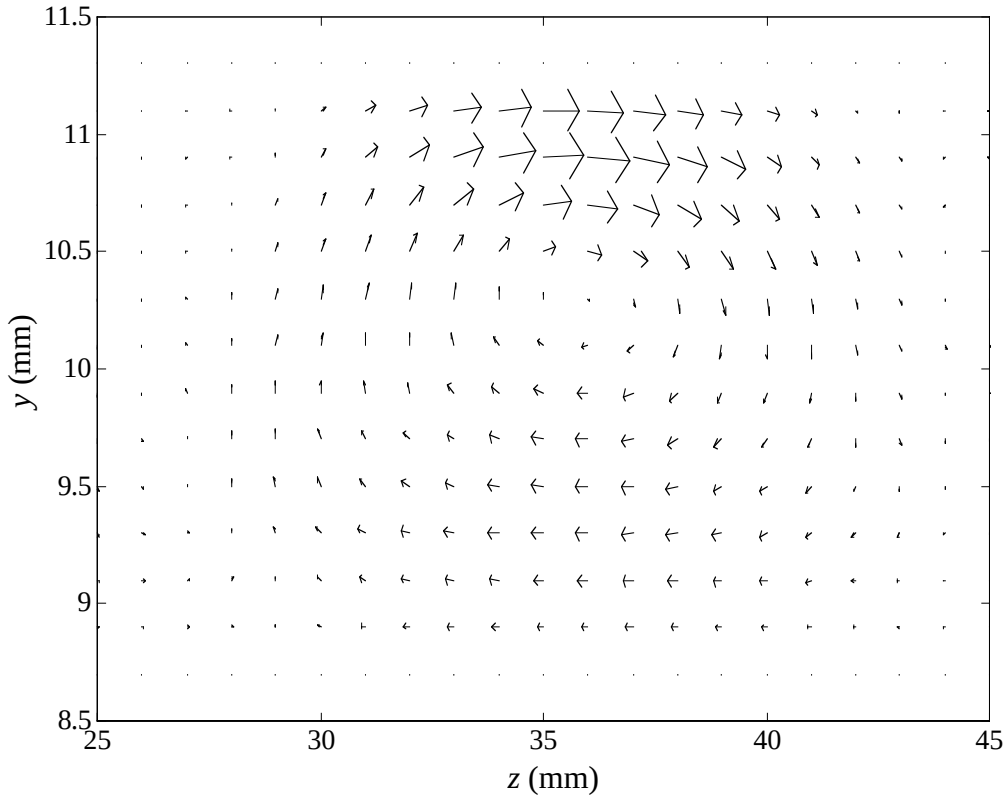

Figure 4.37: Simulated steady state streaming profile inside the “vessel” that is just below the focal spot. The Peak negative pressure is 1.45 MPa at the focus (35 cm axial & 11.7 mm radial). The vessel walls are at the radial locations 8.7 mm and 11.3 mm.

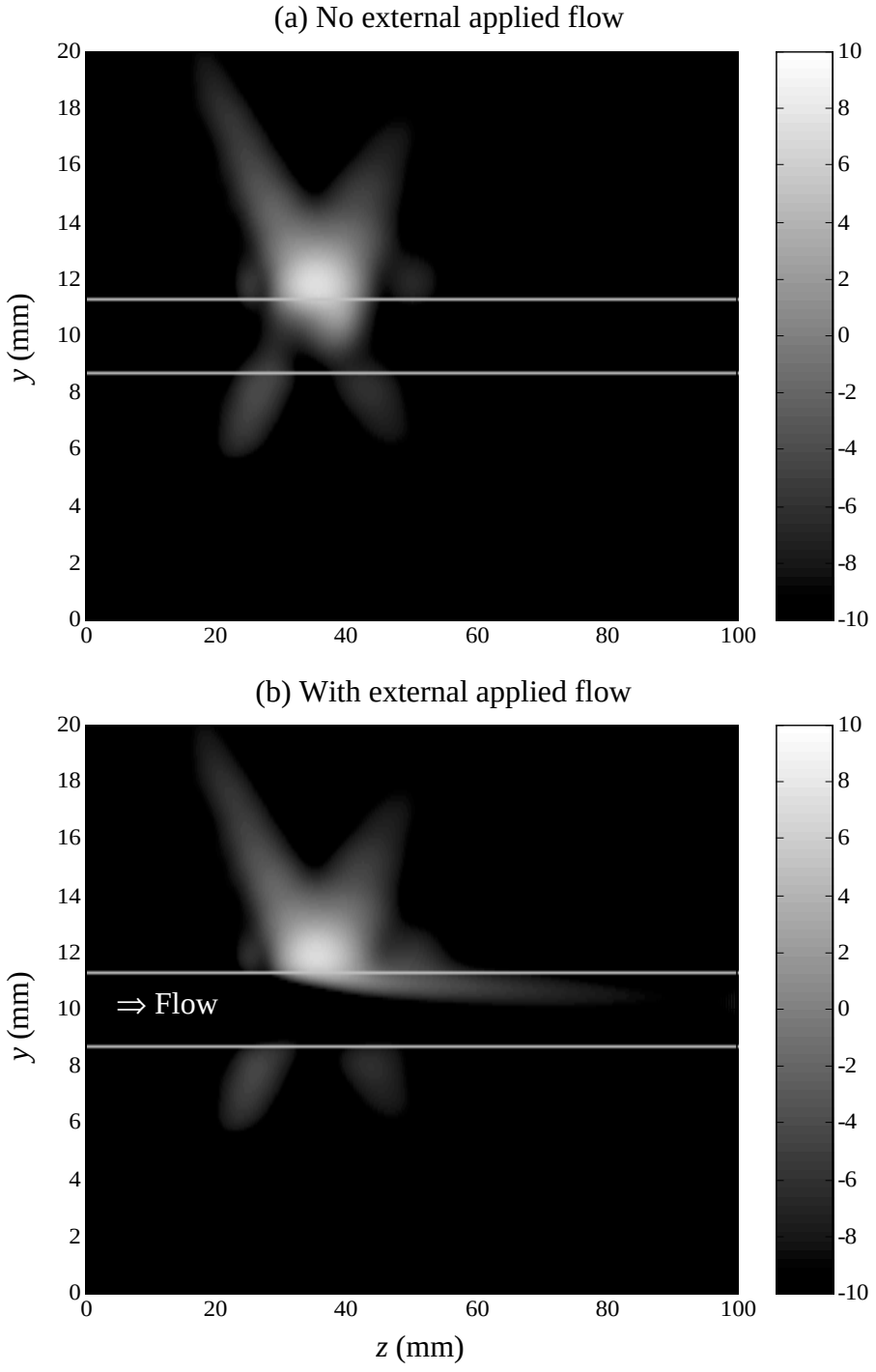

Figure 4.38: Temperature field in the *yz* plane after a 5-second insonation for a peak negative pressure of 1.45 MPa. The two bright lines indicate the region of flow. Temperature is plotted on a *log* scale (*10logT*).

Figure 4.38 is a plot of temperature distribution in the *yz* plane after a 5-second insonation for a peak negative pressure of 1.45 MPa. The two white lines indicate the vessel walls. Temperature is plotted in *log* scale (*10logT*) for better visualization. Figure 4.38(a) is the temperature field when there is no external applied flow, and (b) when there is an external applied flow with mean flow velocity of 1.87 cm/s. The plot shows obvious convective cooling effects in the "blood" region. Diffraction side lobes in the intensity field produce the lobes in the temperature field. The computed intensity field, also plotted in the same *log* scale, is given in Fig. 4.39 for reference.

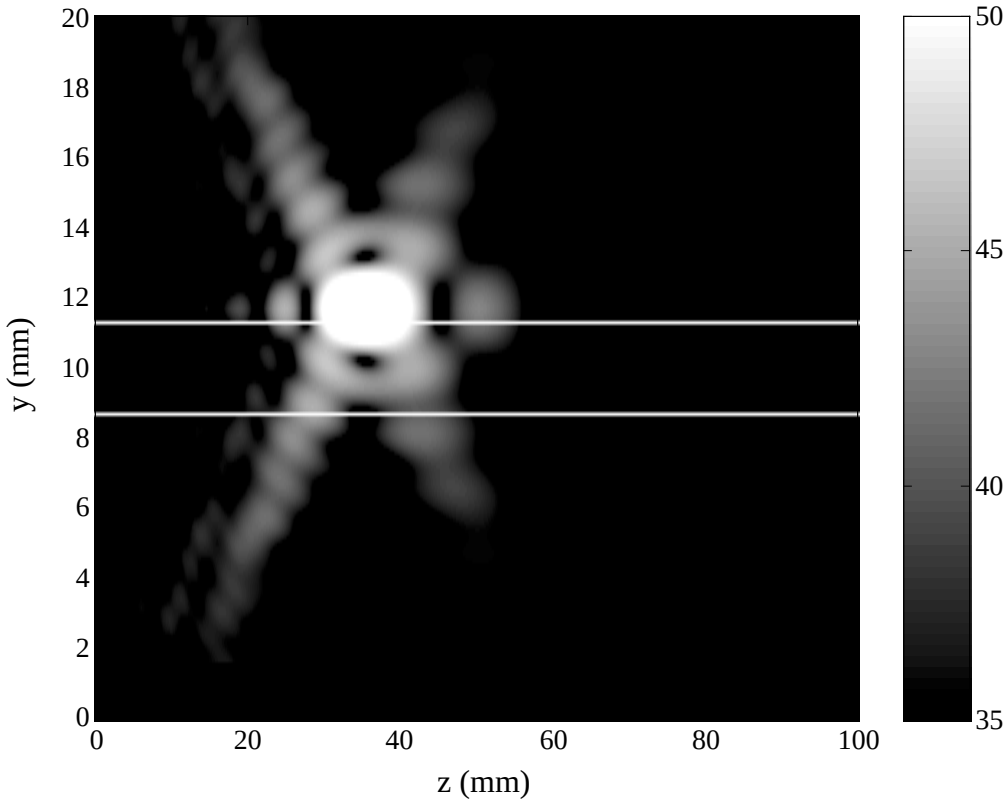

Figure 4.39: Acoustic intensity field in the *yz* plane for a peak negative pressure of 1.45 MPa. The two bright lines indicate the region of flow. Intensity is plotted in *log* scale (*10logI*).

4.4 Summary of Results

We have been able to show in this chapter that our model accurately predicts the temperature change due to HIFU exposure in a uniform tissue phantom, in blood mimicking fluid, and in a flow-through tissue phantom. The simulation includes the effects of acoustic streaming and an *ad hoc* thermocouple artifact correction is employed. Good agreement between experimental data and model predictions are found for a range of acoustic pressures, insonation times and flow conditions. Care is taken to avoid cavitation, for once bubbles are produced the temperature field cannot be predicted on the basis of simple conventional visco-thermal absorption due to the introduction of heating mechanisms unique to bubbles. The results also show that acoustic streaming may play an important role, especially for the heating at the "blood" region when there is no external applied flow or when the flow rate is relatively small. The flow promotes a cooling effect on the heating at and near the "vessel" wall, while no significant cooling is found for heating in the tissue region removed from the vessel.

So, in conclusion, we have developed a powerful computational tool for predicting HIFU-generated temperature fields in vascularized tissues and validated that code through direct quantitative comparison with *in vitro* measurements. Although the pressure code is 2-D, the temperature and streaming codes are 3-D and are able to handle rather complex geometries. So long as the tissue structures do not present significant impedance mismatches that can alter the sound field, we will assume for the purpose of subsequent simulations that all tissue inhomogeneity is weak and that pressure calculations can be run in 2-D. (This is essentially a Born approximation.) The 2-D

pressure field and the assumed vascular flow field are then coupled to the 3-D temperature/streaming code to come up with a 3-D solution to the temperature field in space and time. This allows us to study the heating pattern for a host of complex geometries, provided there are no strong scatterers (such as bone and lung) near the region of interest. In the next chapter, we will apply the model to simulate heating in real tissue with macrovascular structure. The study will be focused on two very simple questions. Given a single vessel in tissue (i) what is the best way to occlude a smaller vessel and (ii) what is the best way to seal a puncture at the vessel wall?

Chapter 5

Simulation of Heating in and Around Human Blood Vessels

In this chapter we present results of temperature field simulations in and around a "virtual" blood vessel when it is sonicated by a HIFU beam. These simulations employ known human tissue properties and consider more complex geometries (*e.g.*, a realistic vessel wall is included; the beam axis can be positioned at any angle relative to the flow axis). The objective of the studies is to investigate two important scenarios in HIFU hemostasis: the occlusion of a "small" blood vessel and the sealing of a puncture in the wall of a "large" vessel. As discussed in Section 1.4, it has been shown that HIFU is capable of causing vessel occlusion when applied to small intact arteries and veins either near the skin surface or within deep tissue [38-42]. Occlusion of small blood vessels near the skin surface plays a role in both therapeutic (*e.g.*, treatment of skin cancer) and cosmetic (*e.g.*, treatment of port-wine stains) applications [7, 148]. Deeper blood occlusion is useful for treating arteriovenous malformations in different parts of the body; for controlling abdominal, peritoneal and pelvic hemorrhage; and also for treating of some tumors with identifiable blood supply [40]. It has also been shown that HIFU can be used to arrest bleeding in larger blood vessels by providing a seal for the puncture hole while leaving the vessel patent [110]. Such vascular injury can result from civilian or military trauma, as well as a number of medical and surgical procedures. The injury may

lead to ischemia or, more frequently, to hemorrhagic complications. Trials in animals have shown that HIFU may provide a method for achieving hemostasis rapidly and in an extracorporeal manner, suitable for treatments of patients at the scene of an injury.

For both applications, an ultrasonic transducer is placed on the skin and the focal zone is made to coincide with the blood vessel. With the aid of a suitable imaging technique, a desired insonation angle (the angle between the acoustic axis and the flow axis) could, in principle, be achieved to attain maximal efficiency. In reality such control may not be possible, either because the transducer operates within a confined space or simply because the blood vessel is too small (or the flow velocity is too low) to be detected by a convenient imaging modality. Even under these circumstances, knowing the differences associated with different insonation geometries and vessel sizes will help to guide the clinician in selecting the best combination of acoustic parameters to do a given job. Clearly, such a parametric study could require a considerable number of time consuming and computationally expensive simulations. For the purposes of this thesis, we limit ourselves to the two simple scenarios indicated above, and consider primarily the effect of insonation geometry.

So, the question is, does an optimum insonation geometry exist and, if so, does this optimal geometry apply to more than one scenario? To answer these questions (in a limited sense) a comparison of simulated temperature distributions in and around a blood vessel is needed for different insonation geometries and for different blood vessel sizes. This comparison will also provide insight on how to induce hemostasis while minimizing collateral thermal damage to surrounding tissue.

We should mention here that the purpose of the study in this chapter is not to evaluate if a temperature rise is enough to induce hemostasis or not. Instead, the objective is to compare the heating pattern for different insonation geometries under different scenarios, which may be used for planning of a more effective procedure in HIFU treatments.

5.1 Simulation Conditions

The simulation requires input parameters in order to run. These parameters include the acoustical and thermal properties of the media (tissue, vessel, blood) and the characteristics of the simulated HIFU source. These properties are described in this section.

5.1.1 Media Properties

Table 5.1 lists all the acoustic and thermal properties used in the simulations in this chapter. These numbers correspond to human tissues and are drawn from the published literature [119]. The properties of water are also listed, which we employ in the pressure field calculation.

Property	Tissue	Vessel	Blood	Water
Density (kg/m^3)	1060	1060	1060	998
Sound Speed (m/s)	1584	1584	1584	1524
Attenuation ($Np/m/MHz$)	7.00	3.45	1.73	0.025
Nonlinear parameter *B/A*	7.0	7.0	7.0	5.0
Specific Heat ($J/kg\cdot^0C$)	3840	3840	3840	N/a
Thermal Conductivity ($W/m\cdot^0C$)	0.53	0.53	0.53	N/a
Viscosity ($kg/s\cdot m$)	N/a	N/a	0.004	N/a
Perfusion Rate ($kg/m^3\cdot s$)	20	N/a	N/a	N/a

Table 5.1: Media properties used in the simulations in this chapter [119].

5.1.2 Simulated Blood Vessels

The reported diameters of the blood vessels that have been successfully occluded are less than 0.7 mm, and the diameters of the punctured blood vessels that have been sealed are 2-10 mm. Table 5.2 lists the characteristics of the simulated blood vessels used in our simulations. These numbers are consistent with published values for typical blood vessel sizes, wall thicknesses and mean flow velocities for human arterial and venous systems [99, 204, see also Appendix B]. The upper limit of the mean flow velocity corresponds to that of arterial system, and the lower limit to that of venous system.

Blood vessel	Internal diameter (mm)	Wall thickness (mm)	Mean flow velocity (mm/s)
BV1	0.6	0.3	5-60
BV2	2.0	0.6	10-100

Table 5.2: Characteristics of the simulated blood vessels.

5.1.3 Characteristics of the Simulated HIFU Source

The simulated HIFU source for the studies in this chapter is a single-element, spherically focused transducer with an aperture of 70 mm. The radius of the curvature is 50 mm. The transducer is operated at 1 MHz, and the intensity at the focus is kept at 335 W/cm^2 for all simulations. The transducer's characteristics and operating parameters are listed in Table 5.3. This intensity level is well below the *in vivo* cavitation threshold that has been reported in literature (see Section 1.2). The computed spatial intensity profile as a function of axial and radial distance is plotted in Figs. 5.1 and 5.2.

Operating frequency (MHz)	Radius of curvature (mm)	Aperture diameter (mm)	Half-maximum beam width and length (mm)	Intensity at focus (W/cm^2)	Peak positive pressure at focus (MPa)	Peak negative pressure at focus (MPa)
1.0	50	70	1.08×4.63	335	3.50	3.18

Table 5.3: Characteristics of the simulated HIFU source used in this chapter.

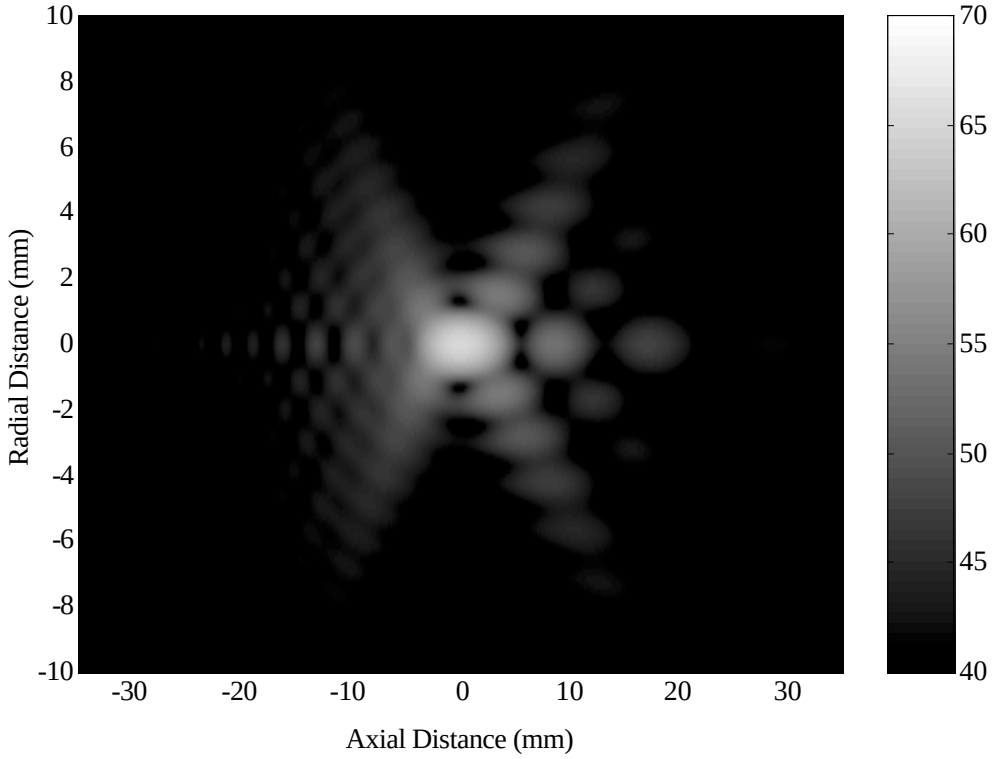

Figure 5.1: The acoustic intensity profile of the simulated HIFU beam plotted in *log* scale (*10logI*). Both the axial and radial distances are measured from the focus, and the source is projecting from left to right.

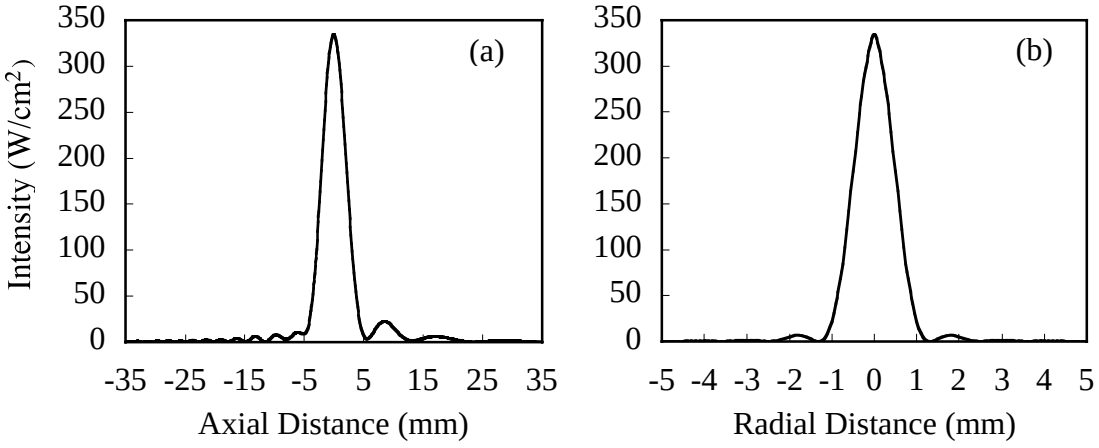

Figure 5.2: The acoustic intensity as a function of axial and radial distance for the simulated HIFU beam: (a) axial beam intensity profile; (b) radial beam intensity profile in the focal plane.

5.1.4 Insonation Geometries

For a fixed flow direction, we have simulated the heating for 5 different insonation orientations, as sketched in Fig. 5.3. Figure 5.3(f) denotes the flow direction. The shaded areas in (a)-(e) approximate the focal zone of the HIFU beam, and the arrows show the direction of beam propagation. The degree indications denote the angle between the beam axis and the flow axis. The focal spot is located at the same place for these five cases.

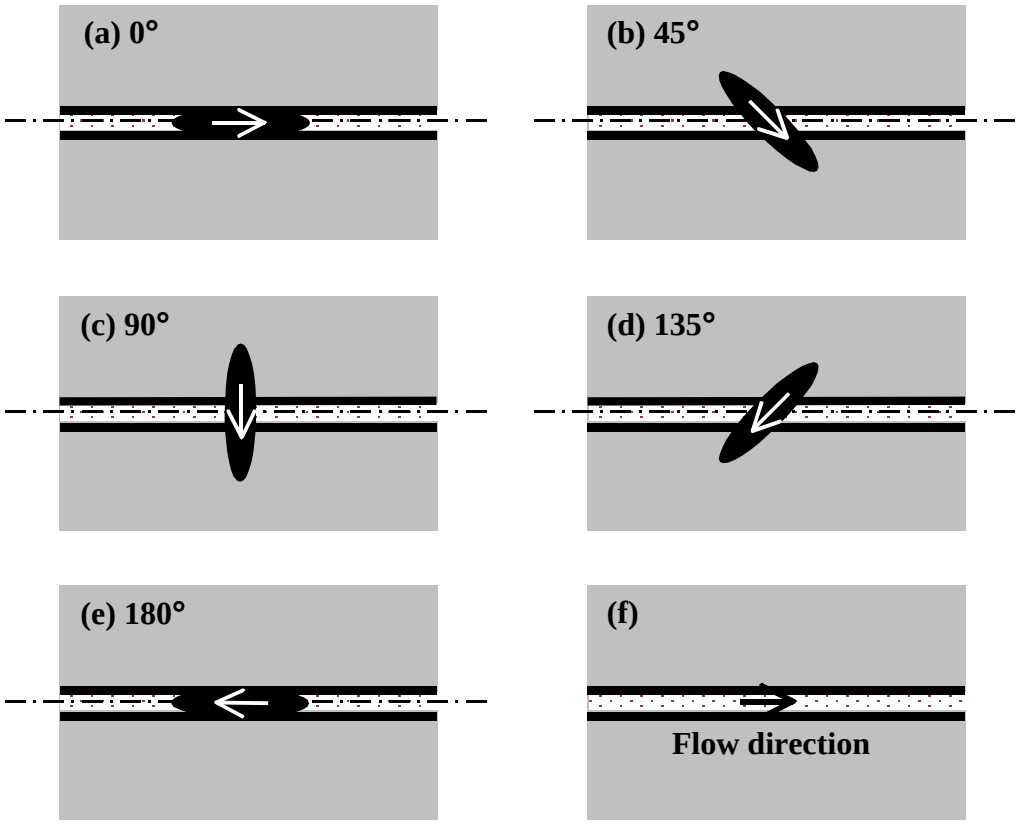

Figure 5.3: A schematic diagram showing five different insonation geometries investigated in this chapter. The shaded areas in (a)-(e) indicate the focal zone of the HIFU beam, and the arrows show the direction of beam propagation. The degrees denote the angle between the beam axis and the flow axis.

5.2 Blood Vessel Wall Sealing

Vaezy *et al.* have reported on the use of HIFU to stop hemorrhage of punctured blood vessels in pigs [110]. In their *in vivo* experiments, major blood vessels (2-10 mm in diameter) were punctured with needles and treated inter-operatively with HIFU. Complete hemostasis was achieved in most blood vessels; the vessel walls were sealed yet the vessels remained patent. The implication is that the heating is somehow limited to the vicinity of the wall; the blood itself never achieves a sufficiently elevated temperature to coagulate and seal the vessel. Indeed, gross examination of the HIFU-treated vessels showed a consistent hardening of the soft tissue surrounding the blood vessels, providing a seal for the puncture hole. Figure 5.4 is a schematic drawing of their HIFU application to a bleeding vessel. The focal spot of the transducer was directly on the puncture.

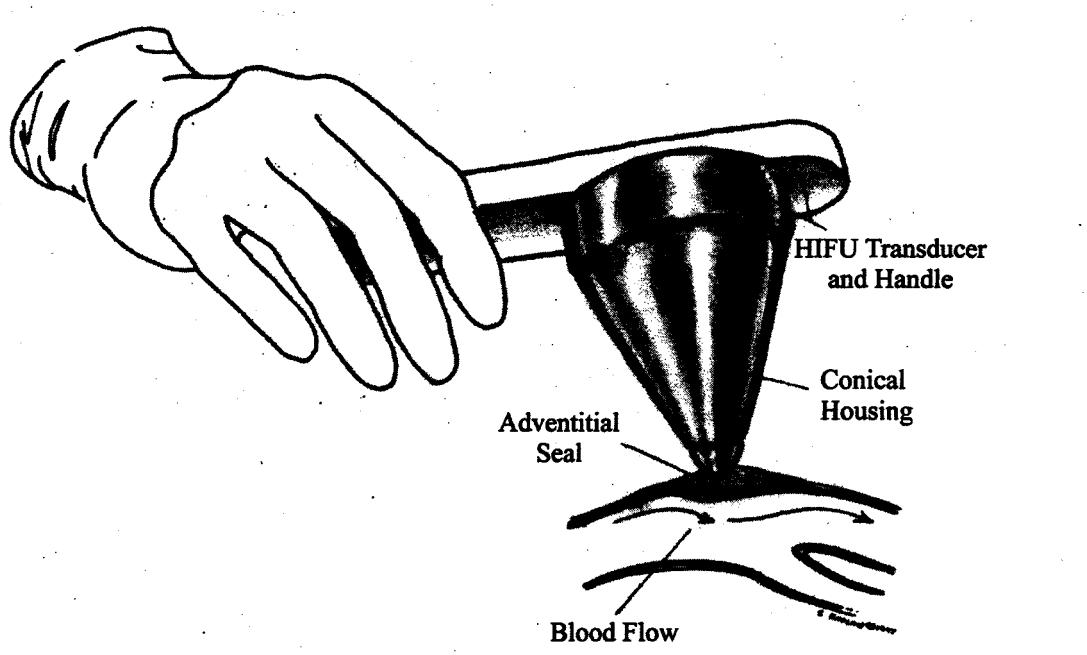

Figure 5.4: Schematic drawing of HIFU application to a bleeding vessel (Vaezy *et al.* [110])[i]. The focal spot of the transducer was directly on the puncture.

In addition to the complete control of bleeding, they reported two other important and interesting observations. First, as indicated above, HIFU has the potential to induce hemostasis of punctured blood vessels without complete blockage of the vessel. All animals were alive at the end of the experiment. Second, the jet of blood shooting out of the puncture hole was, in most cases, immediately stopped when the HIFU was turned on, due to the forcing of the exiting blood back into the vessel by either acoustic streaming or radiation stress. They observed that it was easier to produce hemostasis when the blood was "pushed" back into the vessel by streaming, and it was more difficult when it was not abated due to misalignment of the HIFU focus and the puncture hole. They explained that this was because the flow of blood out of the vessel carried away much of the heat being produced by HIFU, and cooled the vessel wall in the process.

To investigate how the temperature field develops in and around a blood vessel when the focus is positioned at the vessel wall, and how the acoustic streaming may serve to produce enhanced heating, we have conducted simulations of Vaezy *et al.*'s insonation geometry. Other insonation geometries are also investigated and the results are presented for comparison. For most of the simulations presented in this section, we employ what we term blood vessel model BV2 (inner diameter of 2 mm and wall thickness of 0.6 mm) with flow velocity of 10 cm/s; this corresponds to a typical major artery. Results assuming a reduced flow velocity (consistent with veins) are also shown at the end of this Section.

The computational domain for the simulations is sketched in Fig. 5.5. The maximum lengths in the x, y and z directions are 20 mm, 20 mm and 70 mm,

respectively. The focus is placed at x= 10 mm, y=10 mm and z=35 mm, and the beam is always positioned in the yz plane, and thus is symmetric in x direction. Therefore the computational domain is only shown in the yz plane (at x=10 mm) to promote better visualization. The flow is in the positive z direction, and the flow axis is at y=10 mm. The three observation points (A, B, and C) denoted in Fig. 5.5 are all in the vessel region, and at z=35 mm. A is at the inner side of the vessel wall (y=11 mm), B is at the middle of the vessel wall (y=11.3 mm), and C is at the outer side of the vessel wall (y=11.6 mm). The focus of the HIFU beam is placed at point B for all insonation geometries. The spatial grids used for the simulations are: dx=dy=0.1 mm, dz=0.2 mm. The time step used for temperature field and acoustic streaming simulations are 0.05 ms and 0.5 s, respectively.

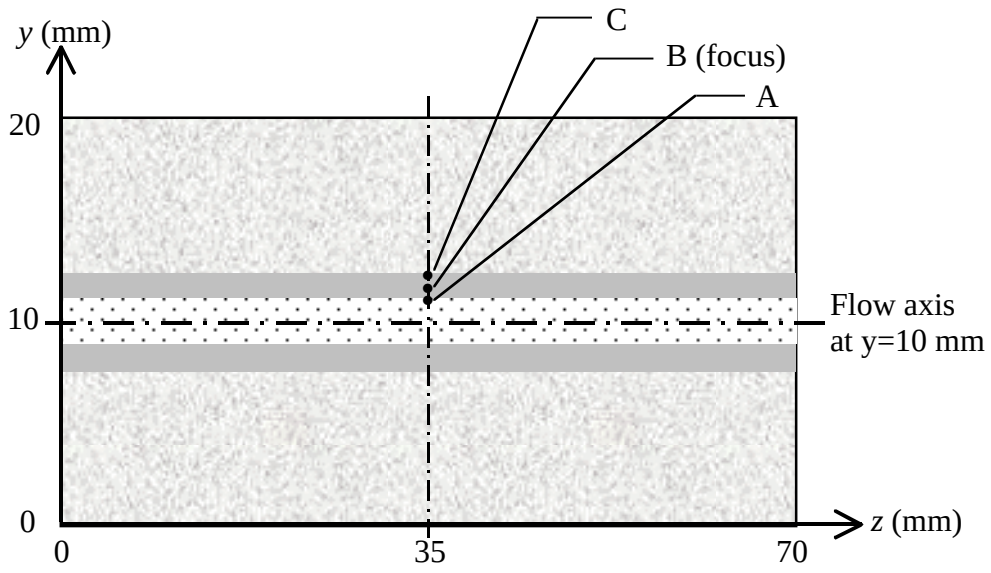

Figure 5.5: The computational domain in yz plane (at x=10 mm) for heating at the vessel wall. The inner diameter of the vessel is 2 mm. The vessel wall thickness is 0.6 mm. The three observation points (A, B, and C) are on the plane of z=35 mm: A is at the inner side of the vessel wall (y=11 mm), B is at the middle of the vessel wall (y=11.3 mm), and C is at the outer side of the vessel wall (y=11.6 mm). The focus is at point B for all insonation geometries.

5.2.1 Perpendicular Insonation

Vaezy *et al.*'s insonation geometry is closest to what we ascribe as perpendicular insonation, *i.e.*, the acoustic axis is perpendicular to the flow axis (see Fig. 5.3(c)) and the transducer focus is positioned on the vessel wall. We will present the results for this insonation geometry first. Figures 5.6 and 5.7 show the spatial temperature profiles in the *yz* (at x=10 mm) and the *xy* (at z=35 mm) planes as a function of time for a 1-sec insonation. The temperatures are all plotted in *log* scale (*10logT*). The two bright lines in Fig. 5.6 indicate the location of the inner surface of the blood vessel. We can see that when carrying normal blood flow, the artery acts as a cooling pipe and as such the blood temperature is much lower than the surrounding tissue. The temperature at the vessel wall and in the tissue increases with time during insonation while the temperature in the blood stays at a low level.

To better illustrate this characteristic, the temperature rise along acoustic axis (y direction) as a function of time is plotted in Fig. 5.8. Since the acoustic focus is on the vessel wall, the maximum temperature rise is in and near the vessel wall proximal to the transducer (the large peak to the right of the vessel boundaries indicated in this figure). There is relatively little heating on the distal side of the vessel, which suggests that for vessels of this size it is possible to selectively heat one portion of the vessel and not the other. This places additional demands on one's ability to target the bleeding site. Good targeting means effective treatment with little collateral damage whereas poor targeting could mean completely ineffective treatment. Also, note that the maximum temperature

rise in the tissue reaches 7°C after 1 second, while the temperature rise at the flow center is only 0.007 °C! Convective cooling dominates the process inside the vessel.

There is another interesting feature to note in Fig. 5.6. Note that there *is* a small region of elevated temperature in the blood immediately adjacent to the inner vessel wall proximal to the transducer (the “upper” wall as viewed in the figure). This small region of heated blood is then convected downstream and rapidly cools, forming what appears to be a “boundary layer” of heated blood that remains attached to the wall as it flows downstream. This comes as no surprise. What is intriguing, however, is that you see a similar boundary region of elevated temperature in the tissue as well, despite the fact that there is no flow in the tissue phase. It appears that heat transfer from the blood to the tissue results in a thin region of hot tissue along the outer vessel wall that tracks the flow downstream.

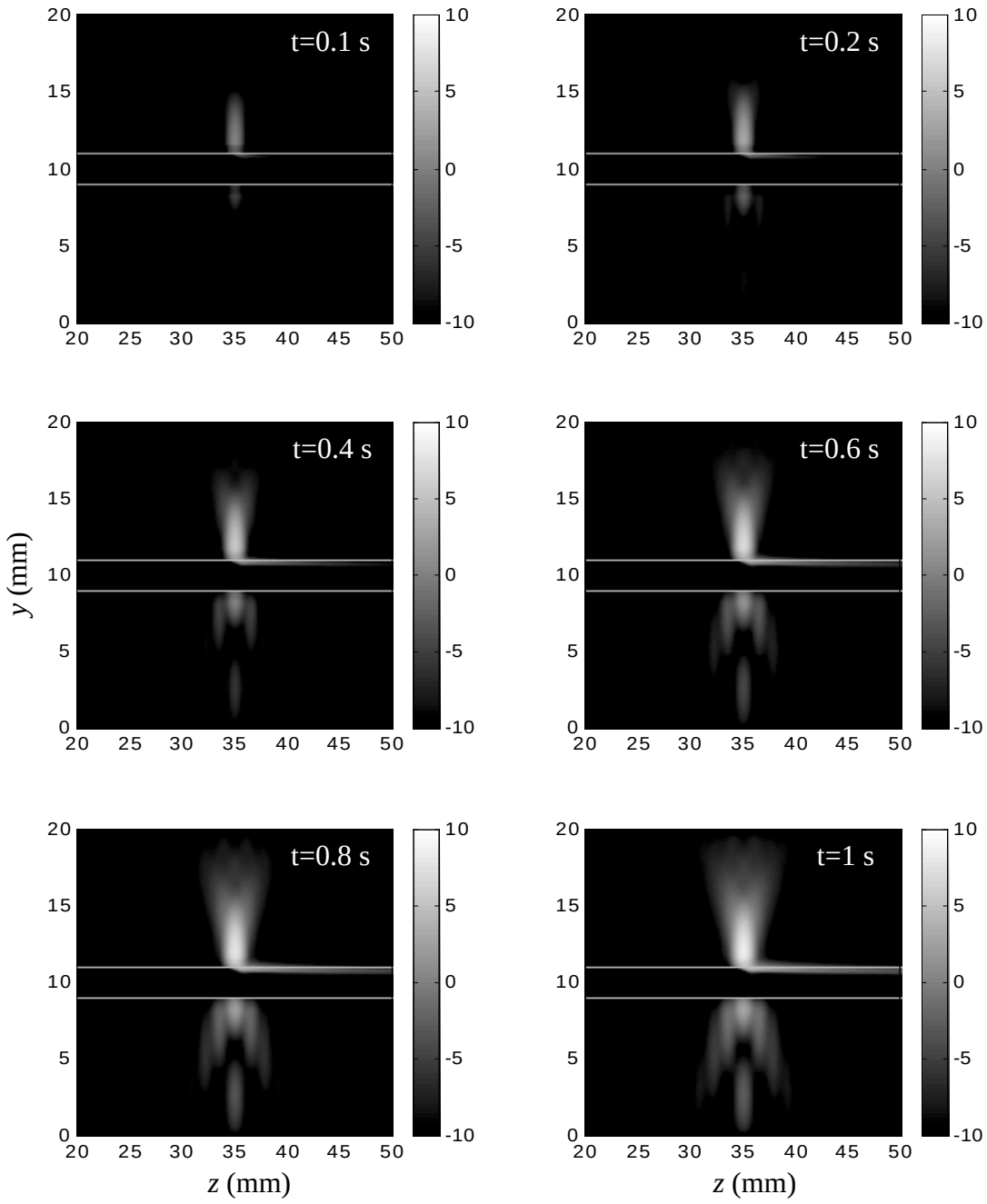

Figure 5.6: Spatial temperature profiles in *yz* plane at *x*=10 mm as a function of time for a 1 second exposure time and perpendicular insonation. The two bright lines indicate the inner side of the vessel wall. The flow velocity is 10 cm/sec (non-pulsatile) and the temperature is plotted in *log* scale (*10logT*). The acoustic source is projecting downwards from the top of each figure. The source condition for this simulation is summarized in Table 5.3.

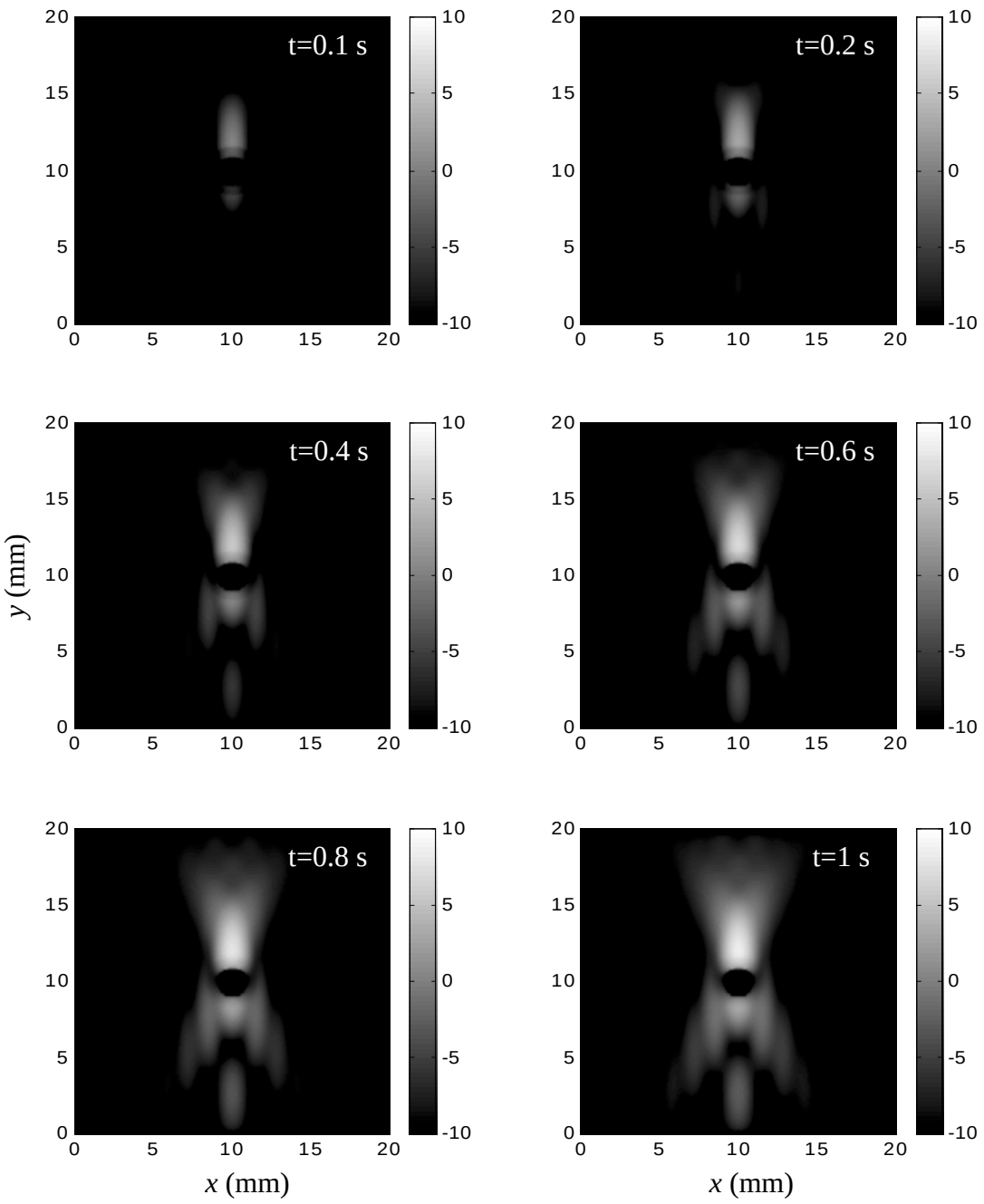

Figure 5.7: Spatial temperature profiles in *xy* plane at *z*=35 mm (focal plane) as a function of time for a 1 second exposure time and perpendicular insonation. The vessel wall is not indicated. The flow velocity is 10 cm/sec (non-pulsatile) and the temperature is plotted in *log* scale (*10logT*). The acoustic source is projecting downwards from the top of each figure. The source condition for this simulation is summarized in Table 5.3.

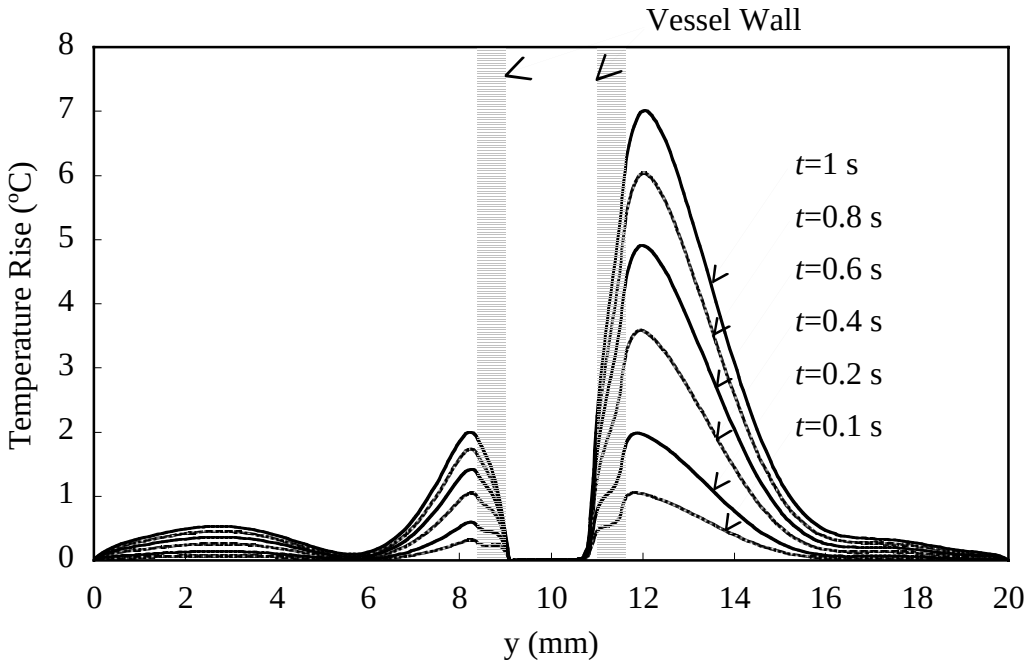

Figure 5.8: Temperature rise along acoustic axis (*y* direction) as a function of exposure time for perpendicular insonation. The flow velocity is 10 cm/sec (non-pulsatile) and the source is projecting from right to left (corresponding to the downward direction in Fig. 5.6). The source condition for this simulation is summarized in Table 5.3.

Figure 5.9 show the steady-state spatial streaming profile in blood region induced by HIFU exposure. As the HIFU beam propagates from above, the blood is pushed downward and circulates locally. The maximum downward velocity is 5.45 cm/s. Figure 5.10 shows the buildup profiles of the streaming on the acoustic axis (z=35 mm). The two observation points are 0 (y=10 mm) and 0.5 mm (y=10.5 mm) to the flow axis. The streaming at both points builds up very quickly and attains a steady state velocity within 0.1 s. In the case of a puncture wound, this streaming field can help force the leaking blood jet back into the vessel and thus minimize convective cooling of the punctured region of the vessel. The net effect is vessel wall heating is promoted and hemostasis can result. Finally, note that the presence of this streaming field has little impact on the

temperature profiles (see Figs. 5.6-5.8). As indicated earlier, for a vessel of this size and blood flow rates this large, forced convection down the vessel dominates the thermal transport process in the blood domain.

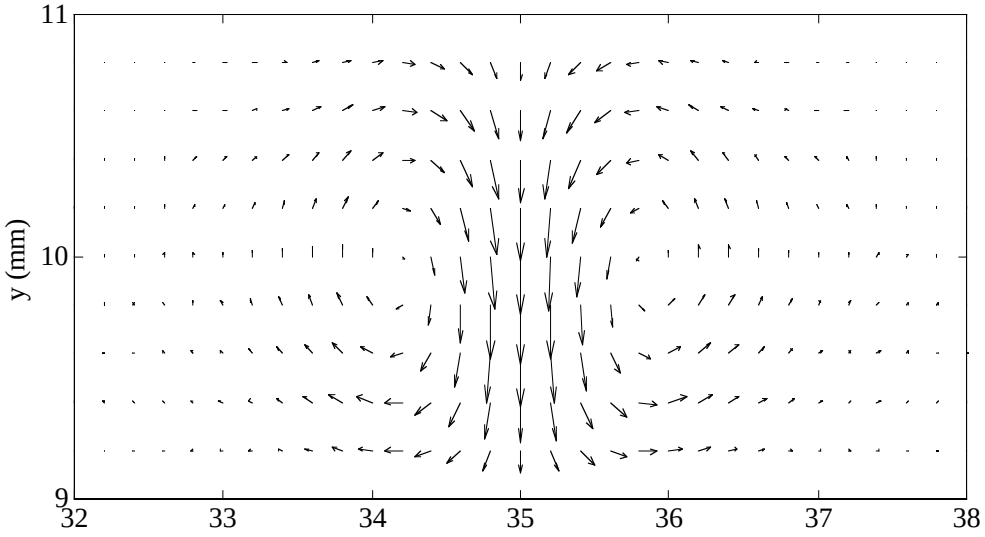

Figure 5.9: Steady-state spatial streaming profile in blood region induced by HIFU exposure for perpendicular insonation. The maximum downward velocity is 5.45 cm/s. The acoustic source is projecting downwards from the top of the figure.

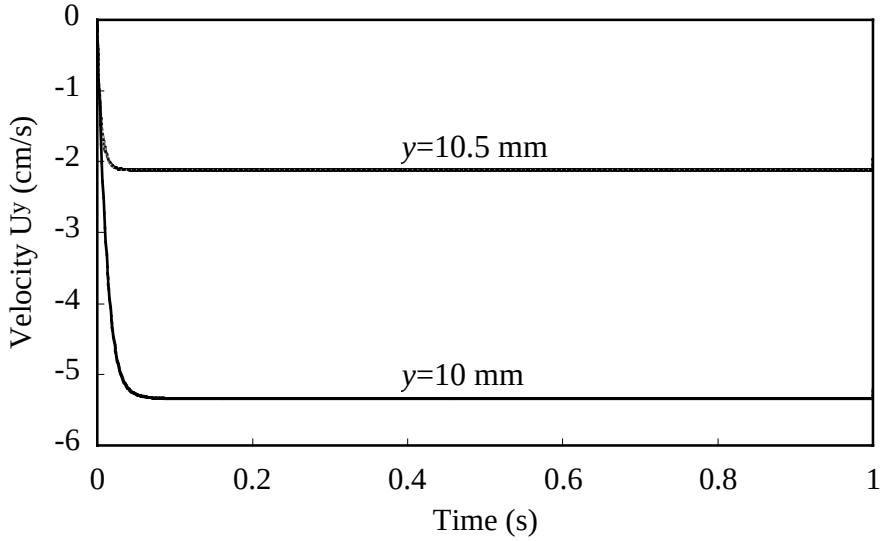

Figure 5.10: Buildup profiles of the streaming on the acoustic axis (z=35 mm). The two observation points are 0 (y=10 mm) and 0.5 mm (y=10.5 mm) to the flow axis.

5.2.2 Other Insonation Geometries

Now we present results obtained for other insonation geometries, as shown in Fig. 5.11. Once again, the acoustic focus is positioned on the vessel wall (location "B" in Fig. 5.5). The result for perpendicular insonation is also shown for comparison. These data correspond to computed temperature fields in the *yz* plane (at x=10 mm) after a 1-sec insonation; results are plotted in *log* scale (*10logT*). Again, the two bright lines indicate the location of the inner surface of the blood vessel. We can see that the spatial dependence of the temperature fields follow the acoustic intensity profiles, and once again the artery acts as a cooling pipe for all insonation geometries. The maximum temperature rises for parallel insonations (0° and 180°) are relatively small compared to other three geometries. This can be illustrated better in Fig. 5.12, which shows the temperature rises across the vessel (along y direction) at z=35 mm after 1-sec exposure for five angle insonations. This is because the acoustic axis for the parallel insonations lies along the vessel wall, a larger percentage of the heated volume lies within the vessel and is thus cooled by convective heat transport.

Figure 5.13 plots the steady state streaming fields associated with these five geometries. The streaming fields all display circulation patters, with the primary jet in the direction of HIFU beam propagation. Depending on the relative orientation of the streaming and bulk flows, acoustic streaming can either accelerate or retard the flow and this might have thermal consequences depending on the relative flow velocities. For example, for blood flow in the positive z direction and acoustic propagation in the negative z direction (an insonation angle of 180˚), streaming will serve to retard the blood

flow locally and could promote enhanced heat deposition at the vessel wall. This is precisely what we observe in the simulations. Figure 5.14 is a comparison of the simulated temperature rise as a function of time at the three observation points (A, B, and C; see Fig. 5.5) in the vessel wall for 0° and 180° insonation angles. We can see that the temperature rises for 180° insonation are higher than those for 0° insonation at all three points. The effect is more profound if we compare the results for 45° and 135° insonation angles, as shown in Fig. 5.15. The temperature rise at the inner side of the vessel wall (point A) for 135° insonation is almost twice that computed for 45° insonation. This is because the streaming velocity in *z* direction for 45° and 135° insonation (maximum 4.42 cm/s) is higher than that for 0° and 180° insonation (maximum 3.15 cm/s), which results in a greater counter-flow effect when insonating at 135º. In fact, if we compare the temperature rise at the inner vessel wall (point A) after a 1 second insonation for all five insonation geometries (Table 5.4), we find that acoustic streaming will enhance the blood cooling effect if it is induced in the same direction as blood flow (0º and 45º), and it will inhibit the blood cooling effect if it is induced in the opposite direction to blood flow (135º and 180º). For scenarios that we simulate in this section, 135º insonation provides the greatest temperature rise at the vessel wall. Insonation geometry does matter, another factor that serves to stress the importance of targeting in HIFU hemostasis of large vessels.

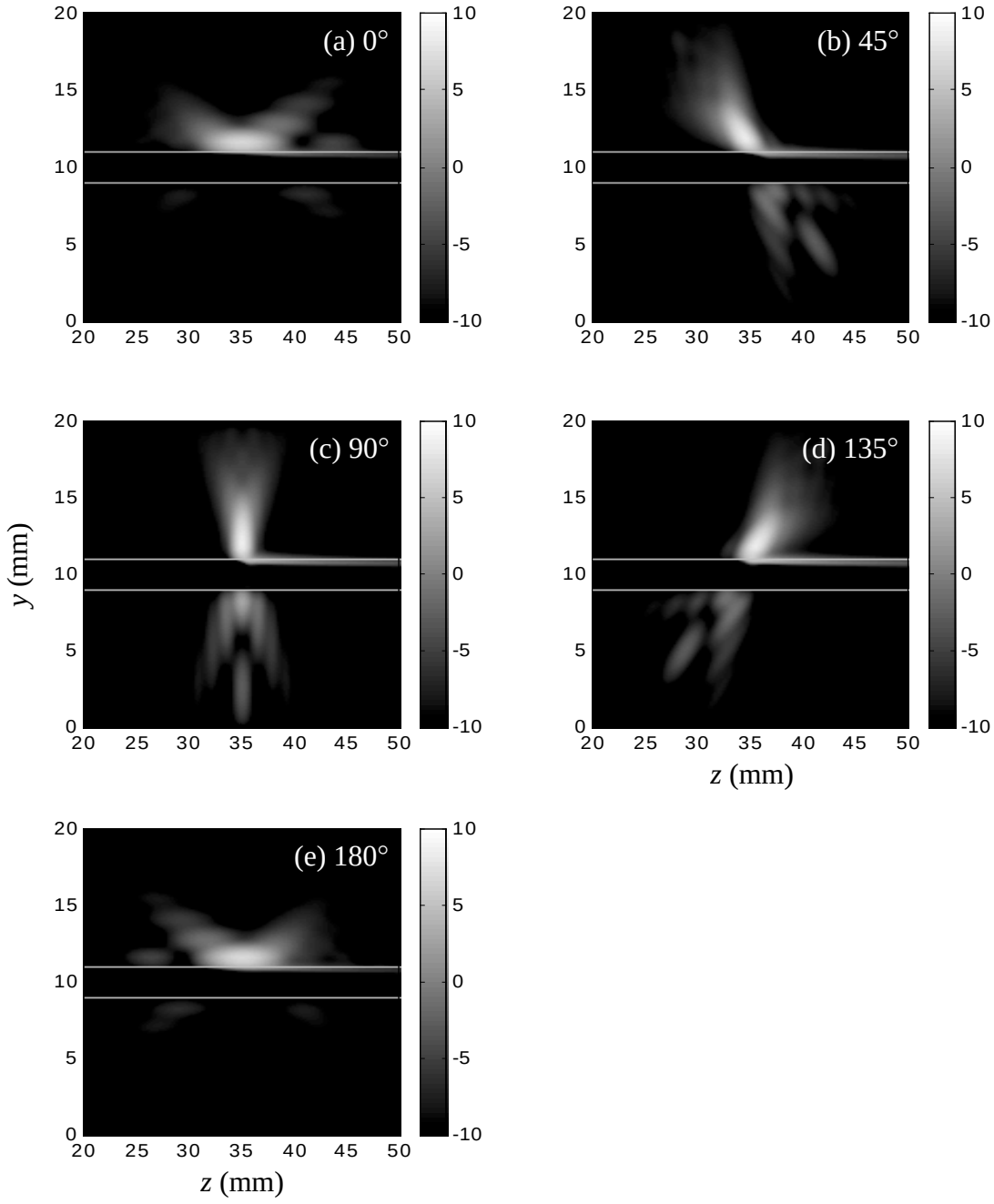

Figure 5.11: Spatial temperature profiles in *yz* plane after a 1 second exposure and for five different insonation geometries. The two bright lines indicate the inner surface of the vessel wall. The flow velocity is 10 cm/sec (non-pulsatile) and the temperature is plotted in *log* scale (*10logT*). At 0˚ the acoustic source is projecting from left to right and the angle of the source relative to the flow rotates clockwise (in subsequent plots) from there.

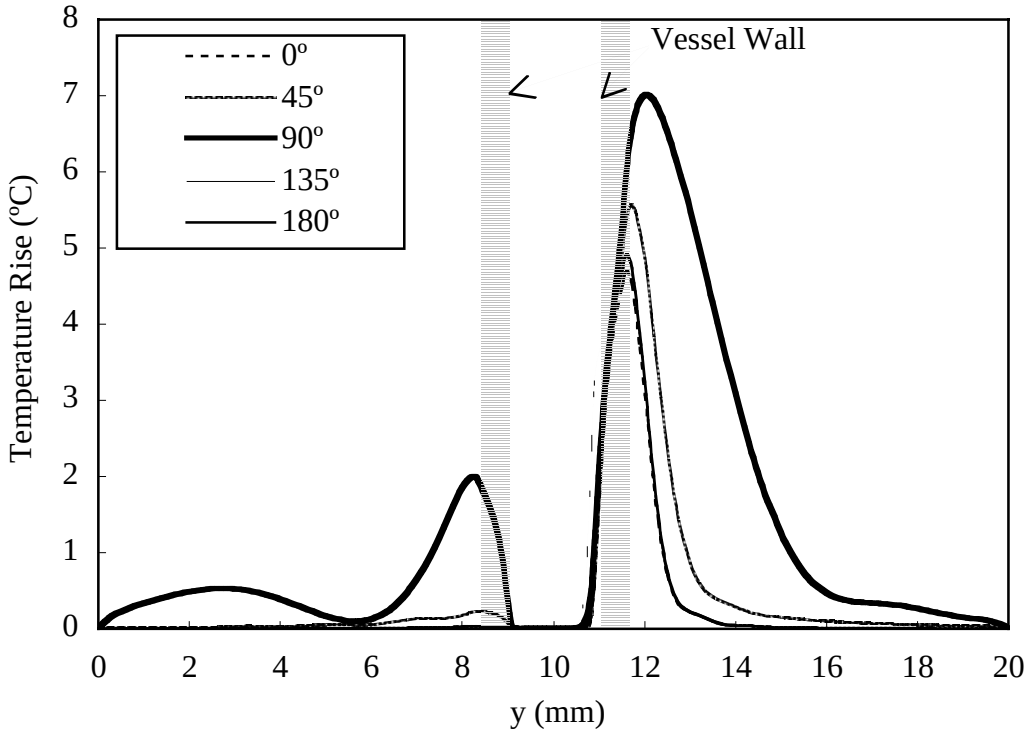

Figure 5.12: Temperature rise along *y* direction at *z*=35 mm after 1-sec exposure for five different insonation geometries. The flow velocity is 10 cm/sec (non-pulsatile). At 0˚ the acoustic source is projecting downwards from the top of the figure and the angle of the source relative to the flow rotates clockwise (in subsequent curves) from there.

Insonation Angle	0º	45º	90º	135º	180º
Temperature Rise (ºC)	1.73	2.11	2.25	3.65	2.30

Table 5.4: Temperature rise at the inner vessel wall (point A) after a 1 second insonation for five insonation geometries (mean flow velocity of 10 cm/s).

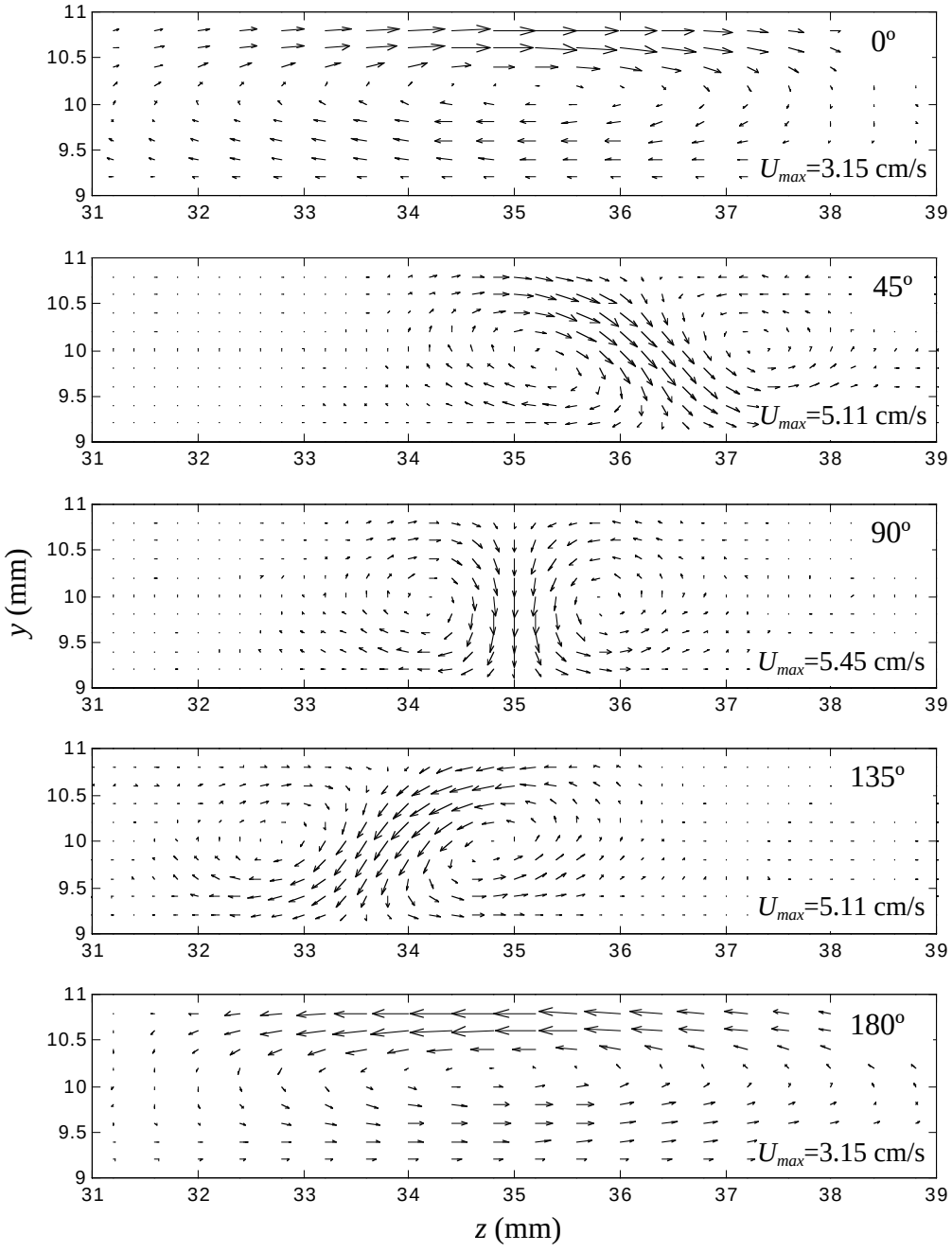

Figure 5.13: Spatial acoustic streaming profiles in steady state for five different insonation geometries. At 0˚ the acoustic source is projecting from left to right and the angle of the source relative to the flow rotates clockwise (in subsequent plots) from there. The streaming velocity is normalized to its respective maximum velocity (U_{max}) for each insonation geometry.

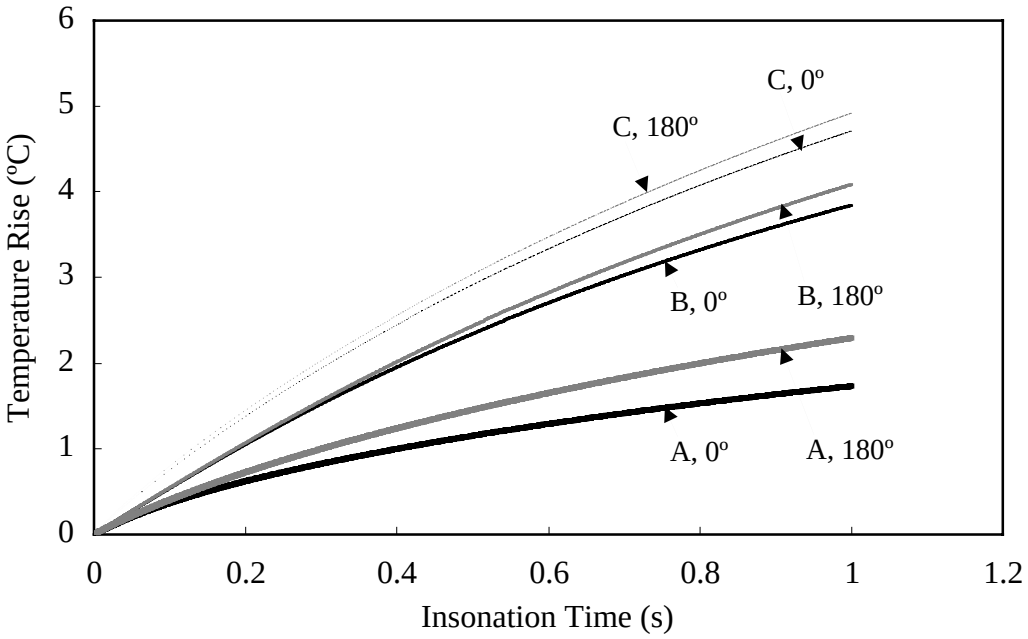

Figure 5.14: Temperature rise as a function of time at three observation points in the blood vessel wall for 0° and 180° insonation angles. The spatial mean flow velocity is 10 cm/sec (non-pulsatile) and the observation points are indicated in Fig. 5.5.

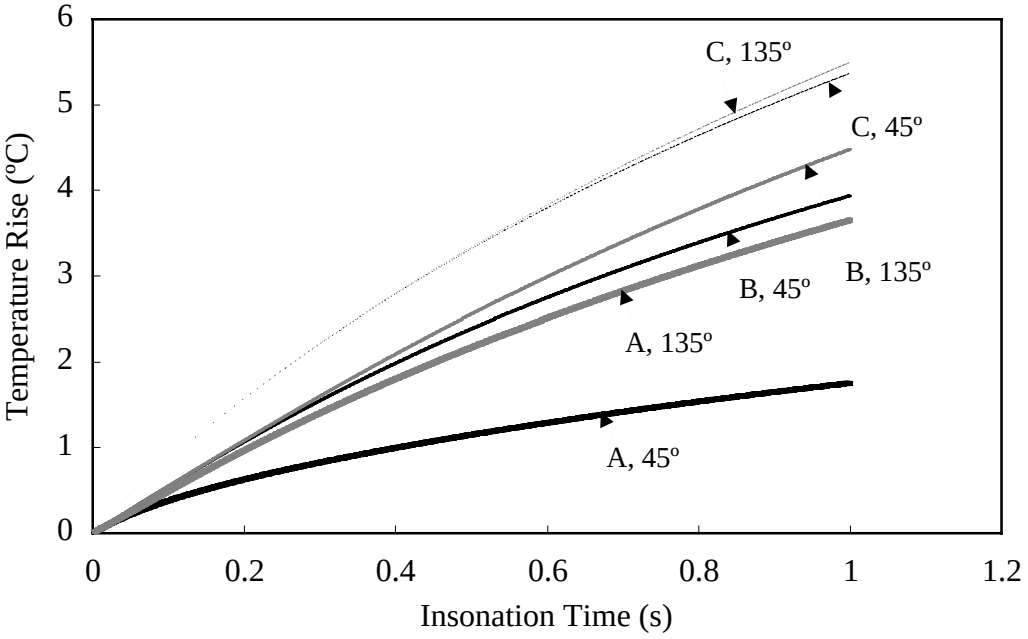

Figure 5.15: Temperature rise as a function of time at three observation points in the blood vessel wall for 45° and 135° insonation angles. The spatial mean flow velocity is 10 cm/sec (non-pulsatile) and the observation points are indicated in Fig. 5.5.

5.2.3 Results for a Reduced Flow Rate

The study described in the previous two sections focused on the artery. Now we consider the case of bleeding from a vein, where the mean flow rates are much lower. To investigate the effect of flow rate, we have repeated the simulations in Section 5.2.2 for the same insonation geometries but for a much lower flow velocity of 1cm/s. Spatial temperature profiles in the *yz* plane after 1 second of exposure are shown in Fig. 5.16. We now see a much more pronounced temperature rise in blood domain, especially for 90º and 135º insonation angles. Note the heated blood that is convected downstream and note the influence of the acoustic streaming jet. In particular, at 45˚, 90˚ and 135˚ there appears to be a thermal "plume" that is projected primarily downward, and in the 180˚ case you actually have heating upstream of the focus. Acoustic streaming definitely impacts the characteristics of the spatial temperature distribution in these slow-flow conditions.

Figure 5.17 shows the temperature profile in the *yz* plane as a function of time for a 135º insonation angle. The maximum temperature rise in the blood domain reaches 3.35ºC after a 1 second insonation. The maximum temperature rise in tissue is about 6.6ºC. This suggests that when the flow rate is small enough, the blood can be heated and coagulation or even vessel occlusion is thus possible given higher intensity and/or longer insonation times. If this is undesired, a 0º insonation angle might be preferable, for this will result in minimal temperature rise within blood. However, a longer treatment will also be required because 0º insonation also induces the lowest amount of temperature rise in the vessel wall (Table 5.5).

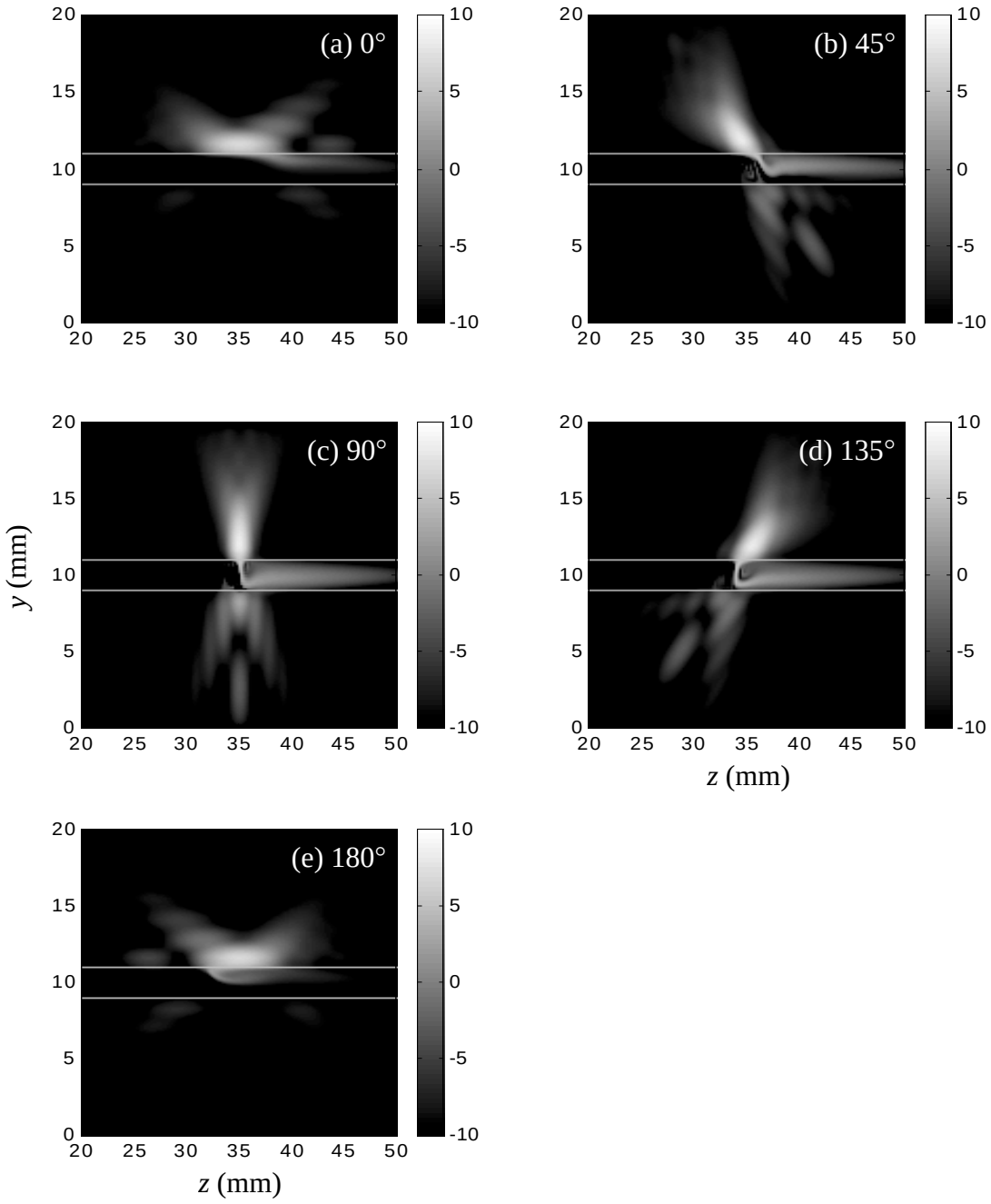

Figure 5.16: Spatial temperature profiles in the *yz* plane after a 1-sec exposure for five different insonation geometries. The two bright lines indicate the inner side of the vessel wall. The flow velocity is 1 cm/sec (non-pulsatile) and the temperature is plotted in *log* scale (*10logT*). At 0˚ the acoustic source is projecting from left to right and the angle of the source relative to the flow rotates clockwise (in subsequent plots) from there.

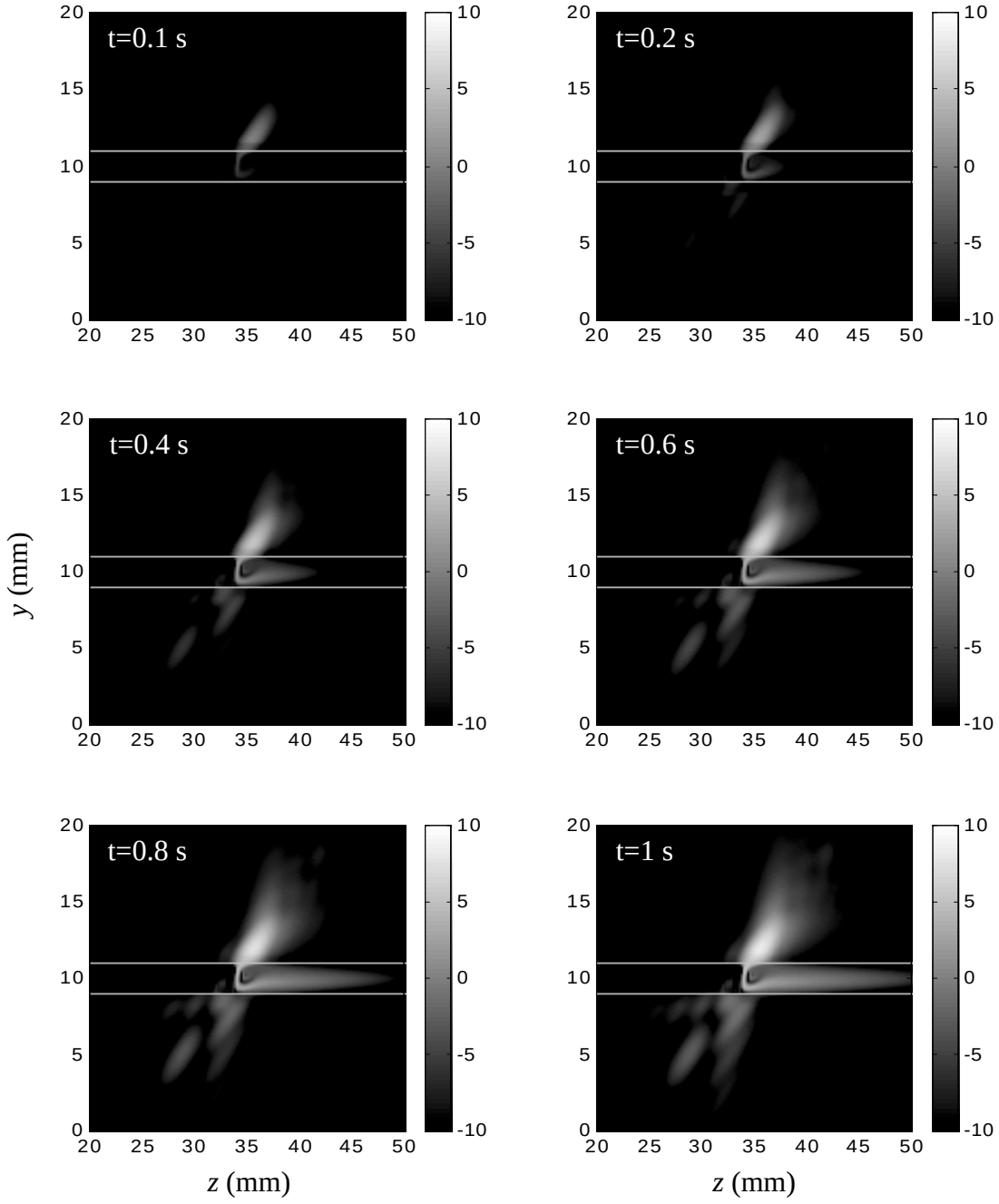

Figure 5.17: Spatial temperature profile in the *yz* plane as a function of time for a 1 second total exposure time and a 135˚ insonation angle. The two bright lines indicate the inner side of the vessel wall. The flow velocity is 1 cm/sec (non-pulsatile) and the temperature is plotted in *log* scale (*10logT*). The acoustic source is projecting from the top-right corner of each figure.

Insonation Angle	0º	45º	90º	135º	180º
Temperature Rise (ºC)	2.10	2.31	3.62	2.79	2.34

Table 5.5: Temperature rise at the inner vessel wall (point A) after a 1-sec insonation for five insonation geometries. The spatial mean flow velocity is 1 cm/s.

5.2.4 Section Summary: Blood Vessel Wall Sealing

We have shown in this Section that for a major artery carrying normal blood flow, HIFU can raise the temperature at the vessel wall while keep the blood cool. Spatial temperature profiles follow the characteristics of acoustic intensity distribution, and the primary jet of acoustic streaming induced in blood region is in the direction of HIFU beam propagation. The patterns of heat deposition at the vessel wall are different for different beam orientations. When positioning properly, acoustic streaming can reduce the local blood flow velocity, which will mediate the blood cooling effect and promote enhanced heating at the vessel wall. In addition the streaming jet and/or radiation stress can serve inhibit the outflow of blood from a puncture wound and thus limit this means for convective cooling. HIFU exposure with insonation angles between 90º and 180º may be able to do both, and thus should be considered when attempting to seal a larger artery that has experienced a puncture wound.

When the mean flow rate is much lower, as is the case for veins, the bulk of the blood can be heated even when the focus is localized to the vessel wall. If one seeks to thermally seal a vessel wall without significantly heating the blood, then a 0º insonation

angle (or as small an angle as possible) should be employed, for in this case the acoustic streaming flow enhances the convective mass transfer which helps to keep the blood cool.

5.3 Small Vessel Occlusion

As we discussed earlier, in some scenarios the permanent occlusion of blood vessel may be the desired endpoint of HIFU treatment. It has been shown that HIFU is capable of causing vessel occlusion *in vivo*. Due to the blood-flow cooling effect, however, successfully occluded blood vessels are limited to small veins (< 1.5 mm in diameter) and arteries (< 0.7 mm in diameter). In most of these *in vivo* experiments, an array of HIFU exposures was used. Hynynen *et al*. employed a novel two-step procedure to overcome the blood flow cooling effect [40]. First, exposures at a high spatial-peak intensity (6500 W/cm^2) and short pulse duration (1 s) were targeted at and around an artery. These brief, high intensity sonications (with accompanying transient cavitation) induced prompt constriction of the artery that served to temporarily reduce or even halt the flow of blood. Next, a second series of exposures at a lower intensity level (2800 W/cm^2) and a longer insonation time (10 s) were applied to the same area, resulting a thermal blood coagulation and vessel occlusion. In essence, the higher-power exposures stemmed the blood flow and the lower-power exposures produced thermal coagulation.

In general, blood-flow cooling is the most important factor that restricts the effectiveness of using HIFU to achieve blood vessel occlusion. All means for reducing this effect should be considered when designing HIFU hemostasis treatment protocols. The simulations reported in this section focus on the differences in the heat deposition

patterns and levels in the blood region for different insonation geometries, and on the possibility of making use of acoustic streaming to reduce blood cooling effect and thus promote enhanced heating. In all the simulations, blood vessel model BV1 (inner diameter of 0.6 mm and wall thickness of 0.3 mm) with flow velocity of 6 cm/s is employed; this simulates as a small artery. Results for a reduced flow velocity of 0.5 mm/s are also presented. The focus of these simulations is the assessment of heating in the blood domain as opposed to the vessel wall.

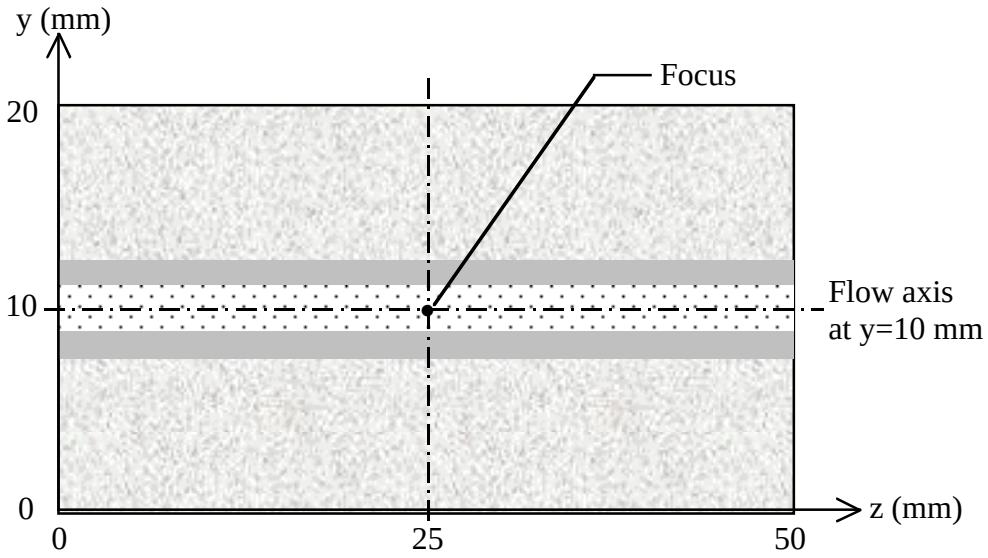

Figure 5.18: The computational domain (*yz* plane) for simulations in this section. It is symmetric in *x* direction. The inner diameter of the vessel is 0.6 mm. The vessel wall thickness is 0.3 mm. The focus is placed on the flow axis and at *z*=25 mm for all insonation geometries.

The computational domain for the simulations presented in this section is sketched in Fig. 5.18. The maximum lengthes in the *x*, *y* and *z* direction are 20 mm, 20 mm and 50 mm, respectively. The focus is placed at *x*= 10mm, *y*=10 mm and *z*=25 mm, and the

beam is always positioned in the yz plane, and thus is symmetric in *x* direction. The domain is only shown in the *yz* plane (at *x*=10 mm) for better visualization. The flow is in positive *z* direction, and the flow axis is at *y*=10 mm. The focus of the HIFU beam is placed on the flow axis and at *z*=25 mm for all insonation geometries considered. The spatial grids used for the simulations are: $dx=dy=dz$=0.1 mm. The time step used for temperature field and acoustic streaming simulations are 0.05 ms and 0.2 ms, respectively.

5.3.1 Results for a "Normal" Flow Rate

In this section we present the results for what we consider to be a "normal" flow rate, the flow is non-pulsatile and the spatial mean flow velocity of 6 cm/s. Figure 5.19 (a)-(e) shows the temperature fields computed after a 1 second exposure and for five insonation geometries. We see similar characteristics to those evident in Fig. 5.11. At this flow velocity, the artery still acts as a cooling pipe even for small vessels and it is difficult to accumulate heat energy in the blood domain. The temperature rise along flow axis as a function of insonation time for a 0º insonation angle is plotted in Fig. 5.20, clearly indicating how the generated heat is convected downstream. To show the differences in the maximum temperature rise attained in blood for these five insonation geometries, the temperature profiles along the flow axis are plotted in Fig. 5.21. Higher temperature rise in blood is achieved for the two parallel insonations compared to other insonation geometries. This may be because a greater percentage of the heated volume resides in the blood domain for the parallel insonations. Note also that the results for both 0˚ and 180˚ are quite similar, which suggests that acoustic streaming plays a minor role.

Similarly, results obtained at 45˚ and 135˚ are comparable and slightly better than that obtained at 90˚. Once again, this could be because a larger fraction of the heated region is in the blood and the impact of acoustic streaming is minor. Keep in mind that 6 cm/sec is not a trivially small flow velocity and *z* component of the streaming velocity induced in the small vessel is reduced due to the fact that the flow region is more confined. The steady state streaming fields within the small vessel for these five insonation geometries are shown in Fig. 5.22. The *z* and *y* components of the steady state streaming velocities at the focus are listed in Table 5.6. Note that all the tabulated values are much smaller than the bulk flow velocity of 6 cm/sec.

Insonation Angle	0º	45º	90º	135º	180º
U_y (mm/s)	0	-4.9	-7.0	-4.9	0
U_z (mm/s)	1.1	4.0	0	-4.0	-1.1

Table 5.6: Steady state acoustic streaming velocity at the focus for five insonation geometries. The bulk mean flow velocity is 6 cm/s.

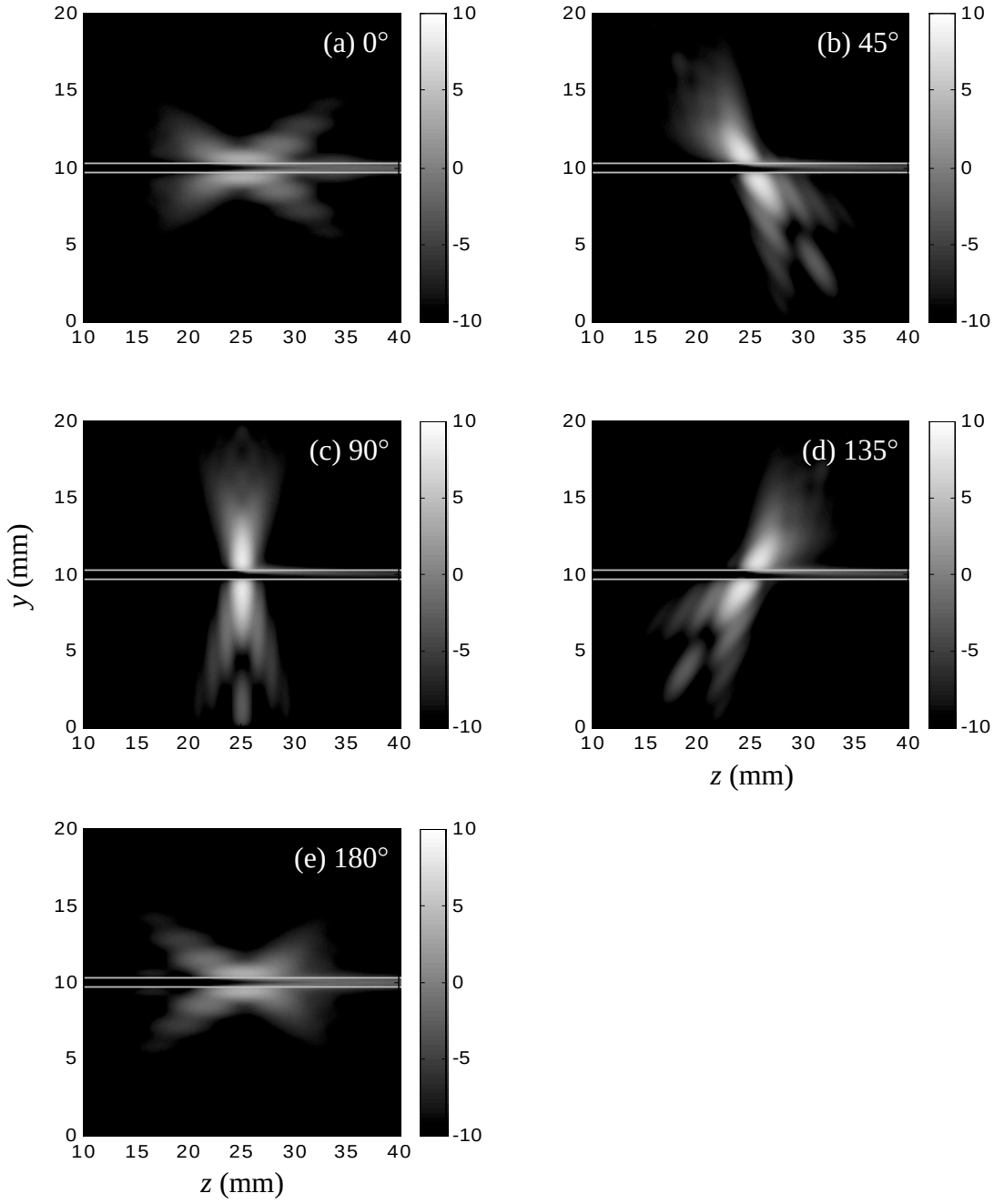

Figure 5.19: Spatial temperature profiles after a 1 second exposure for five different insonation geometries. The acoustic focus is positioned in the center of the vessel. The two bright lines indicate the inner side of the vessel wall. The flow velocity is 6 cm/sec (non-pulsatile) and the temperature is plotted in *log* scale (*10logT*). At 0˚ the acoustic source is projecting from left to right and the angle of the source relative to the flow rotates clockwise (in subsequent plots) from there.

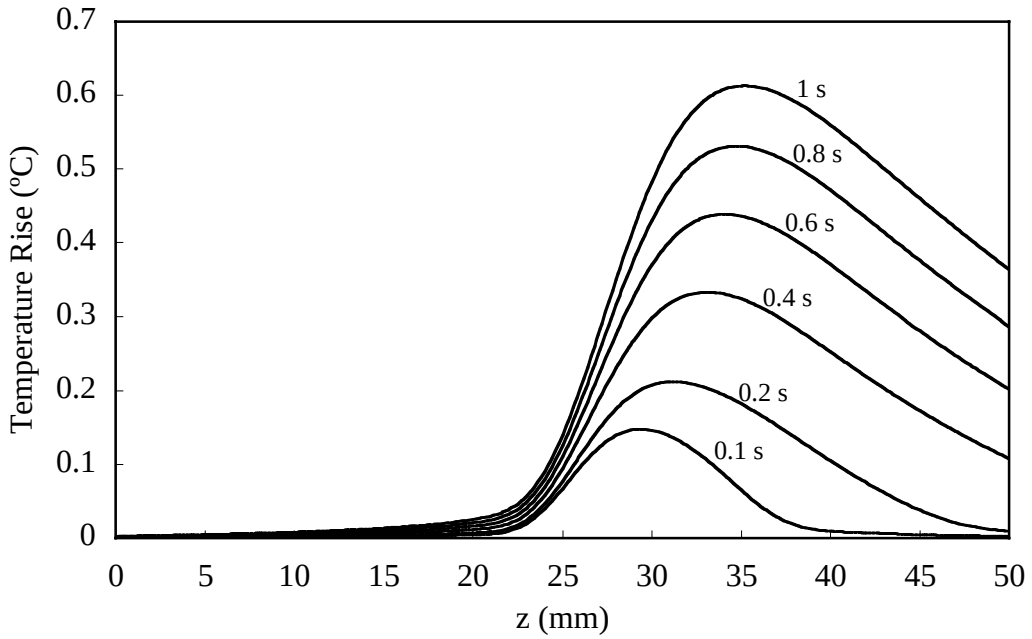

Figure 5.20: Temperature rise along the flow axis as a function of time for a 0º insonation angle. The mean flow velocity is 6 cm/sec (non-pulsatile).

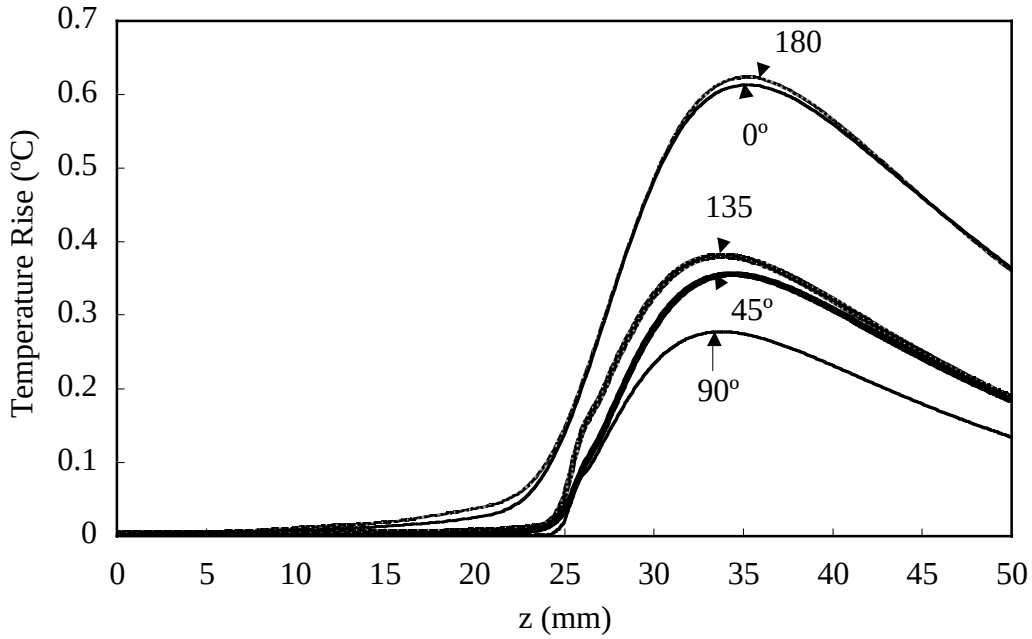

Figure 5.21: Temperature rise along the flow axis after 1-sec exposure for five insonation geometries. The flow velocity is 6 cm/sec (non-pulsatile).

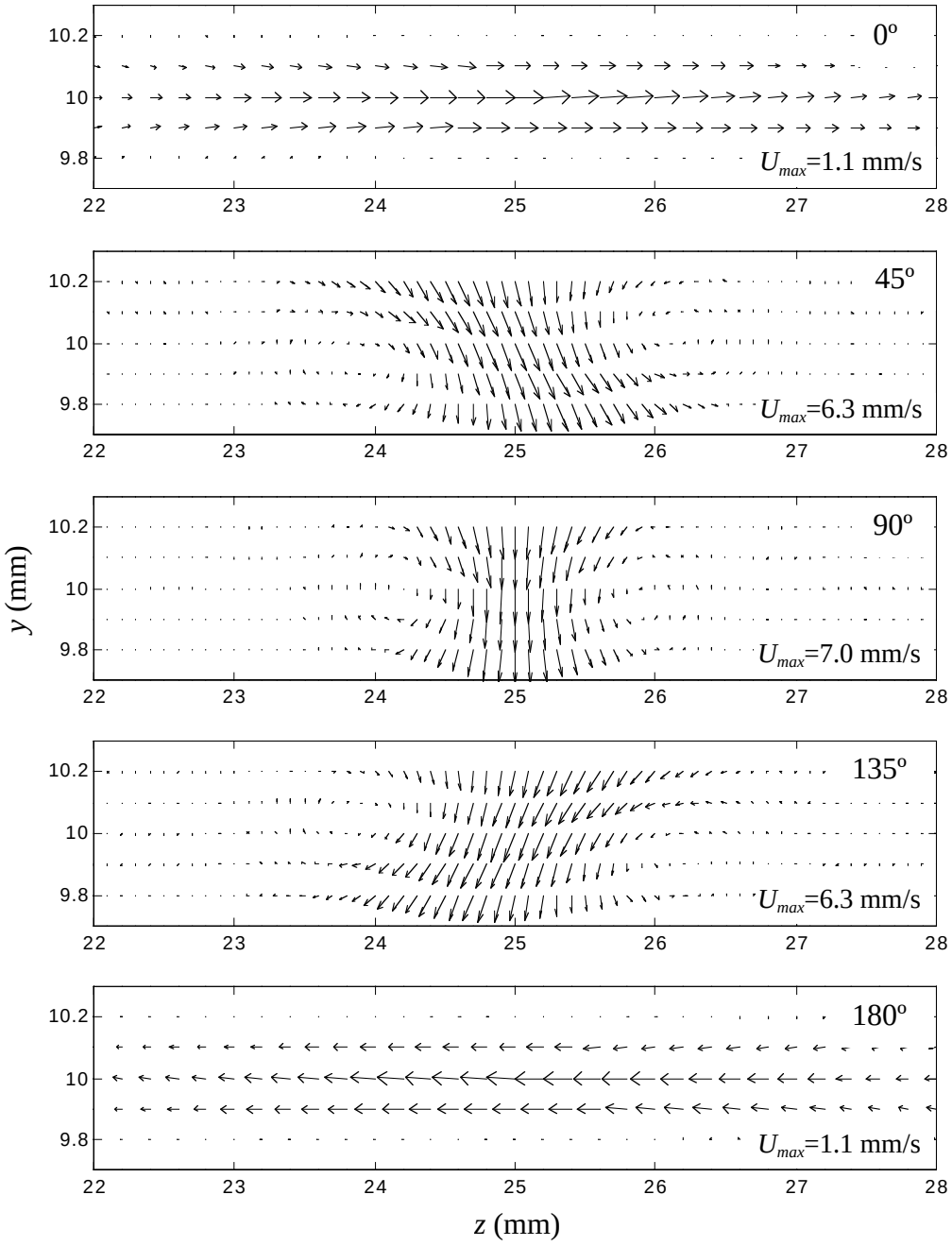

Figure 5.22: Spatial acoustic streaming profiles in steady state for five different insonation geometries. At 0˚ the acoustic source is projecting from left to right and the angle of the source relative to the flow rotates clockwise (in subsequent plots) from there. The streaming velocity has been normalized to its respective maximum velocity (U_{max}) for each insonation geometry.

5.3.2 Results for a Reduced Flow Rate

Results for small arteries with a normal flow rate confirm the necessity to take additional measures to temporarily impede the flow in order to occlude the vessel, as suggested by Hynynen *et al*. We now consider a case where the flow rate is greatly reduced. Figure 5.23 shows the temperature profiles after a 1 second exposure for a spatial mean (non-pulsatile) flow velocity of 5 mm/s. The heating within the blood is much more uniform and localized to the focal region for all insonation geometries. Temperature profiles along the flow axis for five insonation geometries are plotted in Fig. 5.24. The greatest temperature rise is found at the 135º insonation angle for this slow flow condition, rather than at for 0º & 180˚ insonation for the fast flow situation. This is because the *z*-component of the acoustic streaming velocity induced inside the vessel is now comparable to the mean bulk flow rate and its effect is more pronounced when compared to fast flow situation (see Table 5.6). Indeed, the streaming velocity in *z* direction (U_z) at the focus for 45º and 135º (4.9 mm/s) is a near match to the mean flow velocity and greater than that generated for the parallel insonations (1.1 mm/s). When insonating at 135º, the acoustic streaming field can almost hold the flow in stasis, and thus heating in the blood domain is greatly enhanced and localized to the focal spot.

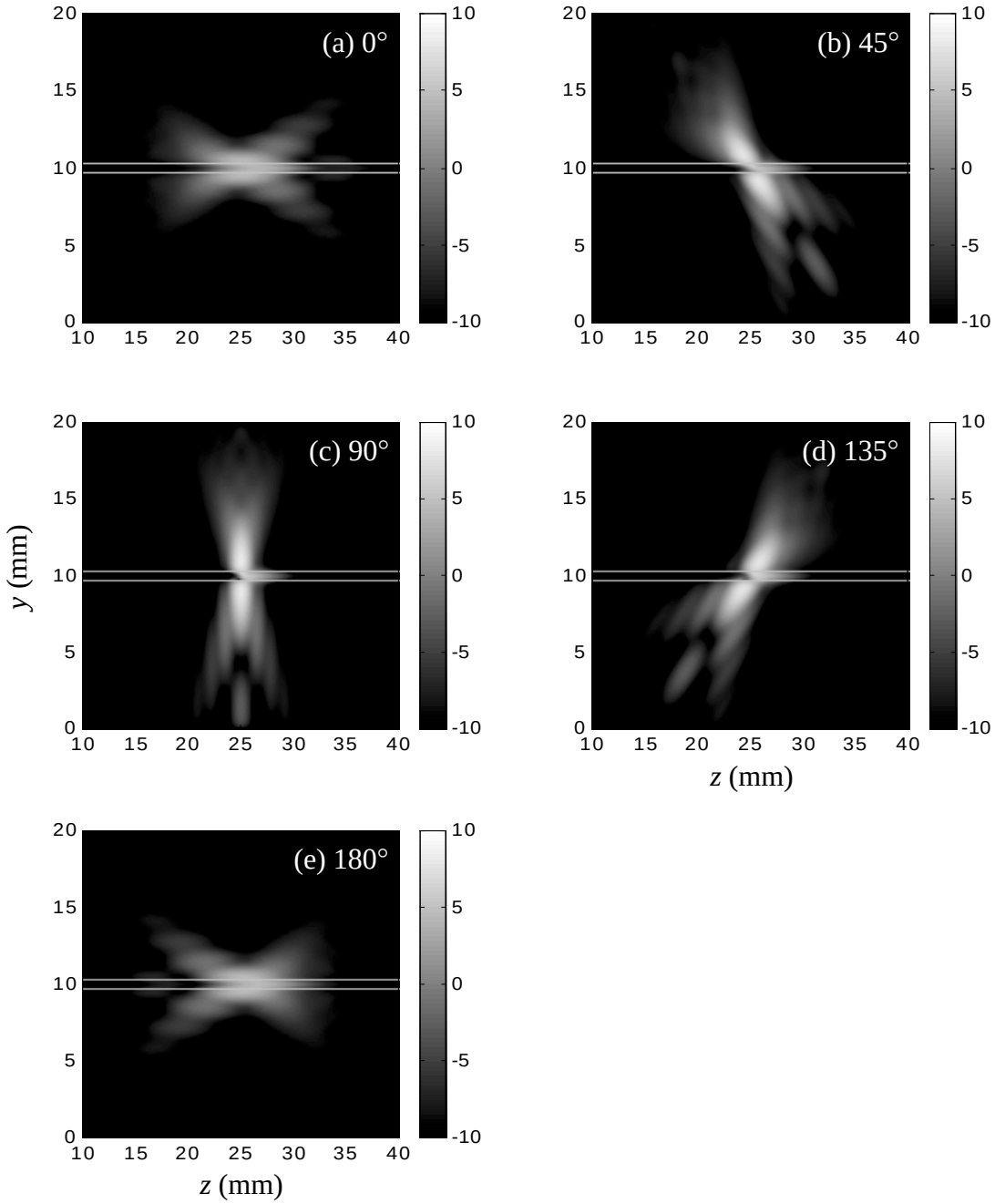

Figure 5.23: Spatial temperature profiles after a 1 second exposure for five different insonation geometries. The acoustic focus is positioned in the center of the vessel. The two bright lines indicate the inner side of the vessel wall. The flow velocity is 5 mm/sec (non-pulsatile) and the temperature is plotted in *log* scale (*10logT*). At 0˚ the acoustic source is projecting from left to right and the angle of the source relative to the flow rotates clockwise (in subsequent plots) from there.

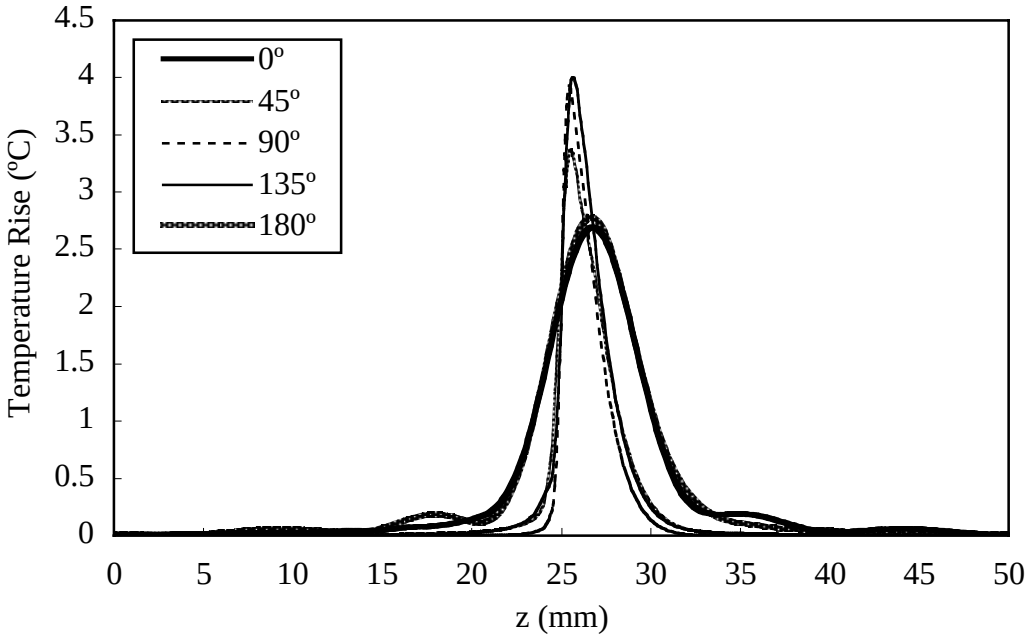

Figure 5.24: Temperature rise along the flow axis after 1-sec exposure for five insonation geometries. The flow velocity is 5 mm/sec (non-pulsatile).

5.3.3 Section Summary: Small Vessel Occlusion

We have shown that HIFU can be used to occlude a small (0.6 mm ID) vessel provided the mean flow velocity inside the vessel is not too great. Results obtained with a 6 cm/sec flow rate and an acoustic focus position in the center of the vessel do not suggest that significant heating of the blood volume is likely unless some other means is employed to constrain flow; convective cooling still dominates inside the blood domain. Many of the features of the temperature fields generated in this higher flow rate mimic those observed with the larger vessel studied earlier. On the other hand, if conditions are such that the flow velocity is significantly reduced, then reasonably uniform heating of the blood is achieved and occlusion becomes much more likely. In this scenario, it was

demonstrated that acoustic streaming can play a significant role in the heating process, and an optimum insonation angle (135˚) exists.

[i] Reprinted by permission of Elsevier Science from "Hemostasis of punctured blood vessels using high intensity focused ultrasound", by S. Vaezy, R. Martin, H. Yaziji, P. Kaczkowski, G. Keilman, S.Carter, M. Caps, E. Y. Chi, M. Bailey and L. Crum, Ultrasound in Medicine and Biology, Vol 24, No 6, pp 903-910, 1998 by World Federation of Ultrasound in Medicine and Biology.

Chapter 6

Summary, Conclusions, and Suggestions for Further Study

6.1 Summary and Conclusions

In this dissertation we addressed the problem of HIFU induced heating in vascularized tissue and flow-through tissue phantoms. The study followed a 3-step process:

1. A model was developed that employed numerical simulations of the pressure field coupled to a FDTD solution for the temperature field.

2. The model was verified through comparison with experiments run in a uniform tissue phantom instrumented for *in situ* pressure and temperature measurement and in an instrumented phantom equipped with a flow channel to simulate a wall-less blood vessel. Relevant physical properties were independently measured.

3. Thus verified, the model was used to investigate HIFU-induced heating patters in and around human blood vessels of varying size and blood flow velocity and for 5 different insonation geometries.

Important factors that were found to prominently affect the heating of tissue with vascular structure during HIFU exposures were discussed. These included direct linear heating due to sound absorption, the role of heat conduction, nonlinear propagation, blood cooling and acoustic streaming.

As indicated above, in order to better understand the heating process in tissues with vascular structure we have developed models that couple ultrasound propagation,

acoustic streaming, ultrasound heating and blood cooling in Newtonian viscous media. Our acoustic propagation model was based on an inhomogeneous wave equation that was derived from the basic equations of fluid mechanics and thermodynamics for a thermoviscous fluid, keeping terms up to second order; it is thus appropriate for simulating the propagation of finite amplitude sound in inhomogeneous biological tissue. The equation accounts for the combined effects of diffraction, absorption, inhomogeneity, and nonlinearity.

The temperature field in tissue domain was modeled by the widely used Pennes bioheat transfer equation. The localized cooling by thermally significant vessels was modeled by a forced convection term in the region of blood flow. In the blood domain, the flow velocity consisted of the sum of two components: the first was the flow profile before HIFU was turned on which was assumed to be a parabolic profiles as in laminar Pouiseille flow, the second was the imposed flow profile due to acoustic streaming. The continuity equation and the Navier-Stokes equation in a viscous incompressible fluid were used to model the HIFU-induced acoustic streaming in blood domain. The model also captured hydrodynamic nonlinearity, which has been found to play an essential role on the generation of acoustic streaming in an ultrasonic beam, in particular, from a strongly focusing source.

The model equations were numerically solved via a finite difference method imposing appropriate initial and boundary conditions. The result was a 3-D numerical simulation of the temperature field (in both the tissue and blood domain) coupled to a 2-D nonlinear acoustic propagation model and a 3-D acoustic streaming model. So long as

the tissue structures did not present significant impedance mismatches (such as bone and lung) that could alter the sound field, we assumed for the purpose of simulations that all tissue inhomogeneity was weak and that pressure calculations could be run in 2-D. The 2-D pressure field and the assumed vascular flow field were then coupled to the 3-D temperature/streaming code, which yielded a 3-D solution to the temperature field in space and time. This allowed us to predict the space- and time-dependent temperature field resulting from HIFU insonation of media with arbitrary variability and with prescribed convective flow.

In order to verify the model, we undertook a series of *in vitro* experiments in a uniform tissue phantom, in blood mimicking fluid, and in a non-uniform flow-through tissue phantom. These experiments were designed to provide a ground truth verification of the model predictions. Care was taken to avoid cavitation, for once bubbles are produced the temperature field cannot be predicted on the basis of simple conventional visco-thermal absorption due to the introduction of heating mechanisms unique to bubbles. Temperature changes were measured using thermocouples and an *ad hoc* thermocouple artifact correction was employed. Good agreement between experimental data and model predictions were found over a range of values for acoustic pressure, insonation time, and flow rate. The results also showed that acoustic streaming might play an important role, especially for the heating at the “blood” region when there was no external applied flow or when the flow rate was relatively small. The flow promoted a cooling effect on the heating generated at and near the “vessel” wall, while no significant cooling was found for heating in the tissue region removed from the vessel.

We then conducted a series of simulations that address two limiting problems of interest: the occlusion of a “small” blood vessel and the sealing of a puncture in the wall of a “large” vessel. We employed realistic human tissue properties and considered more complex geometries: a realistic vessel wall is included; and the beam axis can be positioned at any angle relative to the flow axis. Results show that the heating pattern in and around a blood vessel is different for different vessel sizes, flow rates and for varying beam orientations relative to the flow axis. The results may be summarized in the following conclusions:

1. Spatial temperature profiles follow the characteristics of acoustic intensity distribution, and the primary jet of acoustic streaming induced in blood region is in the direction of HIFU beam propagation.

2. The patterns of heat deposition in and around blood vessels are different for different beam orientations. When positioned properly, acoustic streaming can reduce the local blood flow velocity, which will mediate the blood cooling effect and promote enhanced heating at the vessel wall or/and in blood.

3. For a major artery carrying normal blood flow, HIFU can raise the temperature at the vessel wall while keep the blood cool.

4. When the mean flow rate is much lower, as is the case for veins, the bulk of the blood can be heated even when the focus is localized to the vessel wall.

5. HIFU exposure with insonation angles between 90^{o} and 180^{o} should be considered when attempting to seal a larger artery that has experienced a puncture wound, for in this case the acoustic streaming can serve to not only reduce the local blood velocity but also inhibit the outflow of blood from the wound. Both effects lead to enhanced heating at the vessel wall.

6. If one seeks to thermally seal a vessel wall without significantly heating the blood, then a 0^{o} insonation angle (or as small a angle as possible) should be employed, for in this case the acoustic streaming flow enhances the convective mass transfer which helps to keep the blood cool.

7. At a “normal” flow rate, the artery acts as a cooling pipe even for small vessels and it is difficult to accumulate heat energy in the blood domain. It is necessary to

take additional measures to temporarily impede the flow in order to occlude the vessel.

8. In conditions such that the flow velocity is significantly reduced, reasonably uniform heating of the blood is achieved and occlusion becomes much more likely. In this scenario, acoustic streaming can play a significant role in the heating process, and an optimum insonation angle (between 90º and 180º) exists.

Therefore, Complete occlusion and wall-puncture sealing are both possible depending on the exposure conditions. These results concur with prior clinical observations and may prove useful for planning of a more effective procedure in HIFU treatments.

6.2 Suggestions for Further Study

6.2.1 Modeling

Many more simulations could be performed based on the current numerical model. For example, a blood pool can develop outside a vessel puncture wound. Such a pool can be a target for heating and can support acoustic streaming. This pool could be included in the simulation and would constitute a better model to describe heating in the vicinity of an arterial puncture wound. Of course, care must be taken to apply appropriate boundary conditions for this special case. The two-stage procedure of Hynynen *et al*.'s *in vivo* experiment [40] could also be simulated using the same source condition and tissue properties that they specified in their paper.

There are several components to the model, each of which may be individually improved. One concern is that our time domain acoustic simulation assumes a classical thermoviscous medium in which the absorption increases as the frequency squared,

though for tissues (and also true for tissue phantoms) the power law for absorption is closer to $f^{1.1}$. Although this has not introduced significant error in the prediction of our *in vitro* experiments because the maximum pressures we applied were relatively small (*i.e.* the acoustic propagation was approximately linear; see Appendix A). However, this might serve overestimate the heating in the case of strongly nonlinear waves. To accurately account for the enhanced heating due to nonlinearity, a pressure solution in frequency domain is required.

An additional consideration is the possible change in material properties as the temperature changes. Again, this was not essential in our *in vitro* experiments because the maximum temperature change induced in tissue phantoms are relatively small due to the relatively small pressure we have used. However, much higher temperature rises are usually induced in *in vivo* applications. Therefore, the implementation of the model could be modified to iteratively allow for temperature dependent changes in material properties. This would require that both the solution to the pressure equation and the bioheat transfer equation be solved simultaneously.

Care must also be taken to improve the boundary conditions that we incorporated in the pressure calculations in acoustic streaming simulations. A continuous boundary condition should be defined along the curved tube wall, which provides a better model for acoustic streaming induced in a confined tube.

6.2.2 Experiment

A qualitative look at the steady-state spatial acoustic streaming profile induced inside the "blood vessel" for different insonation geometries could be achieved experimentally by using clear acrylamide gel we described in Section 3.2.1. The streaming velocity may be quantitatively measured at some observation points (*e.g*. focus, flow center) using particle-tracing methods. These measurements would provide useful experimental data to further test the validity of our model in simulations of complex geometries.

Our numerical simulations have demonstrated enhanced heating at the vessel wall and in the bulk of the blood for counter-flow beam orientations. *In vitro* experiments may be conducted to show the different heating pattern in and around a blood vessel for insonations both in line with and counter to the mean bulk flow. This would serve to demonstrate the practical utility of acoustic streaming in assisting HIFU heating.

We have focused our experimental investigations on the impact of thermally significant large vessels. One might construct a phantom to mimic a capillary bed type and associated blood perfusion. We believe this would be a much better model for highly perfused tissues such as kidneys and livers. The most difficult part would be fabrication. In-line degassers employ very fine tubes of "GORTEX" material that can be spread out to form fan-like array of flow-bearing tubes. But the highly absorptive tube walls may introduce thermal artifact similar to those discussed in Section 3.2.3. A possibility is that one may use the degassers to cast the phantoms and then pull the tubes out after the fact.

Different insonation geometries and perfusion rates could be studied, and the measurements compared to model predictions once the perfusion rates are estimated.

Appendix A

Error Analysis

Any comparison of model predictions with measurements requires an assessment of error with which to bound the comparison. For the purposes of this discussion, we take the term "error" to refer to any form of generic uncertainty, be it systematic or statistical. Error exists in the experimental measurements due to the finite precision and accuracy of the apparatus, and error is present in the simulations due to simplifying model assumptions (affects accuracy) and uncertainty in the input parameters (affects accuracy and precision). In this appendix, we consider the sources of error in both the experiments and the simulations, and attempt to quantify their magnitudes. With this information, we can answer the question: are the differences in simulation and measurement shown in Chapter 4 significant, or do the results in fact "agree" to within the estimated uncertainty.

Experimental Error: Precision and Accuracy

There are two basic measurements made in the process of running an experiment. First, one has to determine the peak focal pressure or intensity and then one has to measure the temperature field at discrete points using thermocouples. The temperature measurements were repeated 5 times, with the phantom allowed to cool completely between measurements. The peak temperature values plotted in Chapter 4 are the

numerical average of these five measurements. The error bars consist of the maximum deviation below and above the mean. We take this as an estimate of the precision of the average temperature measurements; typical values shown in Fig. 4.30 fall within ±0.2ºC (±4.2%).

To estimate the accuracy of the temperature measurement, one must keep in mind that what we measure is the temperature change, and not the absolute temperature. Thus, the error will depend on the accuracy of the slope of the measuring apparatus's calibration curve. If the system were perfectly accurate, then the slope of a plot of measured vs. true temperature would be unity. To assess accuracy, we measured this response using thermal "standards" and compared the measured slope to the ideal response. For standards, we employed an ice bath of mega-pure water, and the same water set to a rolling boil. In this manner, the accuracy of the temperature measurement was estimated to be 0.9%. The error associated with imprecision appears to dominate that due to inaccuracy; the latter is not reflected in the error bars plotted in Chapter 4.

Simulation Error: Analysis of Uncertainty

To estimate the error of the computed temperature field, we first perform a sensitivity analysis of the model equations in order to determine how computed results respond to parameter perturbations. This is accomplished by propagating the parameter uncertainties through the numerical calculations using a simple perturbation technique. To do this, we have to assume a set of nominal values for the various parameters. As a "representative case", we choose the same parameters values employed in the simulation

presented in Section 4.3.3 (Figure 4.27); the focal peak negative pressure is 1.45 MPa, the insonation time is 5-seconds, and the mean flow velocity is 1.87 cm/s.

Table A1 shows the percent changes in the peak temperature rise at the locations of the thermocouples (TC1-TC4) in response to one and five percent increases in the various physical parameters. Only one parameter at a time is varied. Also listed in the table (the bottom row) are the percentage changes in computer temperature due to an uncertainty of ±0.2 mm in the positions of the four thermocouples; this is what we determine as the maximum position uncertainty in experiments, based on the precision of the scanning apparatus.

Physical Parameter	ΔTC1(%)		ΔTC2(%)		ΔTC3(%)		ΔTC4(%)	
focal pressure	1.74	9.88	1.98	10.13	2.01	10.22	4.17	8.33
Tissue Phantom								
density	-1.16	-4.07	-0.31	-1.55	-1.10	-5.31	-2.08	-4.17
sound speed	-6.98	-72.09	-2.76	-21.75	-0.70	-5.07	-4.17	-18.75
attenuation coefficient	0.00	1.74	0.29	1.33	0.28	1.26	0.00	0.00
thermal conductivity	-0.58	-1.74	-0.68	-3.35	-0.09	-0.48	0.00	-2.08
specific heat	-0.58	-2.91	-0.29	-1.48	-0.89	-4.41	-2.08	-4.17
Blood Mimicking Fluid								
density	-3.49	-15.70	-1.02	-4.95	-0.79	-3.80	-4.17	-14.58
sound speed	4.07	6.40	0.49	13.31	0.55	1.58	2.08	6.25
attenuation coefficient	0.00	-0.01	-0.06	0.00	0.02	0.00	0.00	0.00
thermal conductivity	2.91	13.95	0.06	0.31	0.02	0.09	2.08	8.33
specific heat	-2.91	-12.79	-0.06	-0.32	-0.02	-0.09	-2.08	-10.42
viscosity	0.00	0.00	0.02	0.05	0.01	0.02	0.00	0.00
spatial mean flow velocity	-2.91	-12.79	-0.04	-0.24	-0.01	-0.06	-2.08	-10.42
position (±0.2 mm)	231.69		9.64		19.05		129.17	

Table A1: The percent change in the peak temperature rise at the location of the thermocouples (TC1-TC4) in response to a one (left column) and a five (right column) percent increase in the various physical parameters. The last row is the percentage change due to an uncertainty of ±0.2 mm in the position of thermocouple.

Note that in Table A1 there is a rather large percentage change in temperature due to position uncertainty for the two thermocouples (TC1 and TC4) residing in the flow region. Recall that the dynamics of the temperature rise for these thermocouples was dominated by flow cooling. The flow velocity gradient (for both the bulk Pouiseille flow and acoustic streaming) is quite high; a small change in position will result in very different flow cooling effect. However, one must also keep in mind that the temperature rises due to sound absorption at these two thermocouples are very small (only 0.02ºC for TC1 and 0.005ºC for TC4), as you will see below, the position-related temperature errors are in virtually negligible when expressed in degrees Centigrade.

The next step in the process of estimating simulation error is to come up with a set of reasonable estimates for the error associated with each various physical parameter:

- Focal pressure: From the comparison of the measured and predicted peak negative pressure at the focus in phantom as a function of source pressure (Figure 4.6 in Section 4.2.1), we estimate the error in focal pressure to be less than 5%.
- Phantom density: The density of the phantom was obtained by dividing the mass of the phantom sample by its volume. The mass was measured using a balance with resolution of 0.01 g, and the volume was measured by the water displacement in a cylinder before and after inserting the phantom. The resolution of the cylinder used is 1 ml. The typical mass and volume for the phantom sample used are 26.13 g and 25 ml. These errors are propagated through the density calculation by Taylor expanding the expression for the density to first order in the perturbed parameters. In this manner, we estimate the error of the phantom density measurement to be less than 2.0%.
- BMF density: The density of the blood mimicking fluid was measured using a Density Meter (DMA 35, Anton Paar, Austria). The accuracy and precision is

defined by the manufacture to be $\pm 1 \times 10^{-3} g/cm^3$. The measured BMF density is $1.036\ g/cm^3$, which gives an error of ±0.1%.

- Sound speed of phantom and BMF: The accuracy of our sound speed measurement is estimated based on the comparison of our measurement of castor oil (1518.32 m/s at 20ºC) with the average value of the published data (1503.97 m/s [199, 213, 214]). The error is thus estimated to be less than 0.95%.
- Attenuation coefficient of phantom and BMF: The accuracy of our attenuation coefficient measurement is also estimated based on the comparison of our measurement with castor oil (0.837 dB/cm at 20ºC and 1 MHz) with the average value of the published data (0.862 dB/cm at 20ºC and 1 MHz [199, 213]). The error is thus estimated to be less than 2.9%.
- Thermal conductivity of phantom and BMF: The accuracy of the thermal conductivity measurement is estimated based on the comparison of our measurement on Plexiglas (0.178 W/m·k) with the published data (0.184 W/m·k [215]). The error is thus estimated to be less than 3.26%.
- Specific heat of phantom and BMF: The accuracy of the specific heat measurement is estimated based on the comparison of our measurement on the pure water (3.95 J/g·ºC) with the published data (4.18 J/g·ºC [215]). The error is thus estimated to be less than 5.5%.
- Spatial mean flow velocity: The spatial mean flow velocity of the external applied flow was obtained by measuring the total volume of liquid (typically 50 ml) collected by a cylinder during a known period of time (typically 500 sec). The time was measured by a stop-watch. The resolution of the cylinder and the stop-watch are 1ml and 0.01 sec, respectively. Errors propagate using the aforementioned perturbation analysis. The resulting estimated error in the flow velocity measurement is less than 1.0%.

- Viscosity of BMF: The viscosity of BMF was measured by a concentric cylinder viscometer (LV2000, Cannon Instrument Company, State College, PA). The accuracy and precision specified by the manufacturer is 0.1 cP. The measured viscosity of BMF was 4.2 cP, which gives a relative error of 2.38%.

Physical Parameter	Assumed Value ± error	ΔTC1 (˚C)	ΔTC2 (˚C)	ΔTC3 (˚C)	ΔTC4 (˚C)
focal pressure	1.45 ± 0.07 MPa	1.70 e-3	0.49	0.11	0.40 e-3
Tissue Phantom					
density	1045 ± 21 kg/m^3	0.33 e-3	0.03	0.02	0.12 e-3
sound speed	1551 ± 15 m/s	1.20 e-3	0.13	0.07	0.20 e-3
attenuation coefficient	10.17 ± 0.29 Np/m/MHz	0.15 e-3	0.04	0.01	0.00 e-3
thermal conductivity	0.59 ± 0.02 W/m·^{o}C	0.20 e-3	0.10	0.00	0.05 e-3
specific heat	3710 ± 204 J/kg·^{o}C	0.50 e-3	0.07	0.05	0.20 e-3
Blood Mimicking Fluid					
density	1036 ± 1 kg/m^3	0.05 e-3	0.00	0.00	0.02 e-3
sound speed	1549 ± 15 m/s	0.70 e-3	0.02	0.01	0.10 e-3
attenuation coefficient	0.46 ± 0.11 Np/m/MHz	0.00 e-3	0.00	0.00	0.00 e-3
thermal conductivity	0.57 ± 0.02 W/m·˚C	1.45 e-3	0.01	0.00	0.25 e-3
specific heat	3930 ± 216 J/kg·˚C	2.20 e-3	0.02	0.00	0.50 e-3
viscosity	0.0042 ± 0.0001 kg/s·m	0.00 e-3	0.00	0.00	0.00 e-3
spatial mean flow velocity	1.87 ± 0.02 cm/s	0.50 e-3	0.00	0.00	0.10 e-3
position	± 0.2 mm	39.85 e-3	0.47	0.20	6.20 e-3
Total error (˚C)		0.04	0.71	0.23	0.01

Table A2: The assumed values and the errors for the physical parameters, and the biases in the peak temperature rises at the thermocouples that result from the parameter errors. The total error for each thermocouple is calculated by adding the uncertainty contribution from each variable in quadrature.

The assumed values and the corresponding temperature errors for all these parameters are listed in Table A2. As before, the assumed values are the same ones used in the simulations presented in Section 4.3.3 (Fig. 4.27). For better illustration, the errors for the two thermocouples (TC1 and TC4) that reside in flow domain are expressed in exponential notation because of the small quantities. The total errors for TC1-TC4, which

are calculated by adding the uncertainty contribution from each variable in quadrature, are listed in the last row. By summing the squares of the errors, we are in effect assuming that the individual sources of error are independent of each other.

Additional biases in measurement and modeling

(1) Effect of heat conduction along the thermocouple wire

Fry and Fry [113] have developed an analysis of the effect of conduction of heat away from the junction by the thermocouple wires. This is expressed as a relationship between the temperature of the junction and the temperature of the medium (with the thermocouple absent) under similar conditions of acoustic irradiation. Input parameters include the radius of the wire, the thermal conductivity of the wire and the absorbing medium, and the spatial intensity distribution of the irradiator. Based on their model, we estimate that the temperature in our tissue phantom insonated by HIFU source H-102 could be lowered by as much as 2.3% as a result of heat conducted away by the thermocouple wire. This bias in the measurement is small, but not vanishingly so. It is not represented in the error bars for the data plotted in Chapter 4.

(2) The effect of the power law used for frequency-dependent acoustic absorption

Our time domain acoustic simulation assumes a classical thermoviscous medium in which the absorption increases as the frequency squared. However, for biological tissues and most tissue phantoms the power law for absorption is closer to $f^{1.1}$. To estimate the impact of this erroneous assumption, we have measured the harmonic

generation at the focus in our tissue phantom using a broadband hydrophone. The results are shown in Fig. A1. Based on this measurement, we have calculated the ratio of heat absorbed by the medium at the focus using both power laws for absorption. The maximum error is 1.89% given the range of the focal pressures employed in the simulations.

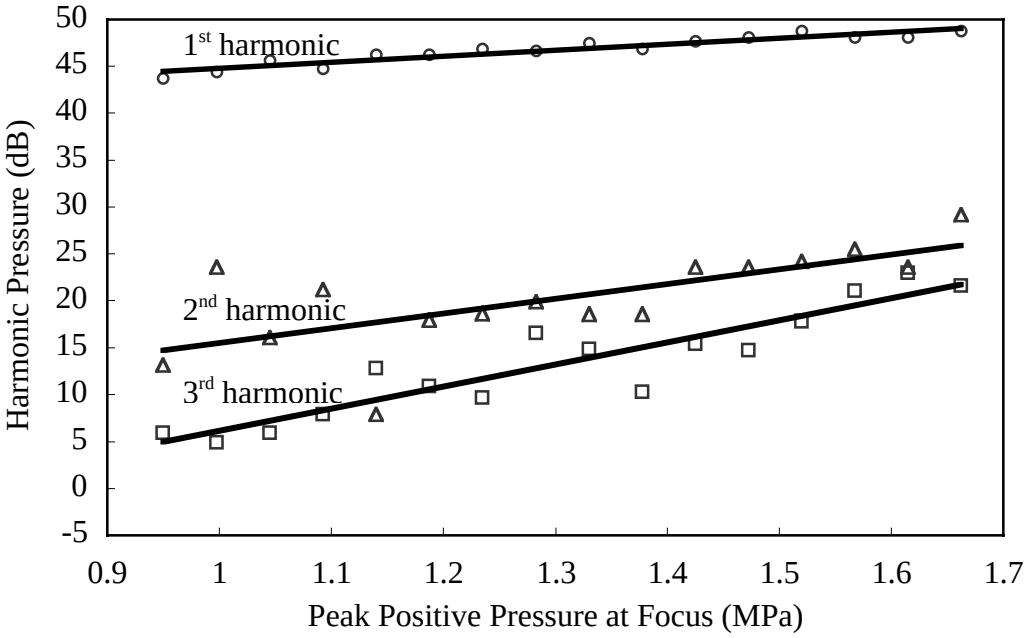

Figure A1: Harmonic generation at the focus in agar-based tissue phantom. Solid lines: least squares fits; symbols: experiment.

Appendix B

Vessel Parameters for the Human Blood Circulation

Blood Vessel Type	Internal Diameter (mm)	Wall Thickness (mm)
Aorta	10-30	2-3
Main Branches	5–22.5	≈ 2
Large arteries	4.0-5.0	≈ 1
Medium arteries	2.5-4.0	≈ 0.75
Small arteries	1.0-2.5	≈ 0.50
Tributaries	0.5-1.0	≈ 0.25
Small veins	0.6-1.1	≈ 0.25
Medium veins	1-5	≈ 0.50
Large veins	5-9	≈ 0.75

Table B1: A selection of typical blood vessel size and wall thickness for human arterial and venous systems [204].

Appendix C

Finite-Difference Time Domain Code: Pressure Solution

The following code is used to calculate the pressure field in the water-tissue domain.

```
      program pressure_nonlinear
c ********************************************************************
      implicit none
      integer Imaxp,Jmaxp,Narray,Ntrain,Nmaxp,ifocusp,jfocusp
     & ,ImaxT,JmaxT,Iskin
c ********************************************************************
      parameter(Imaxp=1201,Jmaxp=501,Narray=351,Ntrain=10001
     & ,Nmaxp=10001,ifocusp=481,jfocusp=1,ImaxT=1001
     & ,JmaxT=201,Iskin=131)
c ********************************************************************
      doubleprecision drp,dxp,dtp,t,timep(Nmaxp),cp(Imaxp,Jmaxp)
     & ,rhop(Imaxp,Jmaxp),alphap(Imaxp,Jmaxp),Betap(Imaxp,Jmaxp)
     & ,xshock,xtarget,xmaxp,rtarget,rmaxp,tmaxp,pi,period,freq,omega
     & ,kwave,lambda,tendtoend,Umax,Mach,train(Ntrain),trainmult
     & ,pnplus1(Imaxp,Jmaxp),pn(Imaxp,Jmaxp),pnminus1(Imaxp,Jmaxp)
     & ,pnminus2(Imaxp,Jmaxp),pnminus3(Imaxp,Jmaxp),q1,q2,q3,q4
     & ,cH2Op,rhoH2O,alphaH2O,BetaH2O,ctissuep,rhotissue,alphatissue
     & ,Betatissue,cbloodp,rhoblood,alphablood,Betablood,cvesselp
     & ,rhovessel,alphavessel,Betavessel
     & ,Qn,Q(ImaxT,JmaxT),Qmax,pfocusmax,pfocusmin
     & ,pxmax(Imaxp),pxmin(Imaxp),prmax(Jmaxp),prmin(Jmaxp)
c ********************************************************************
      integer i,j,n,m,itargetp,jtargetp,Nptspercycle,decimspace
     & ,decimtime,nendtoend,ielement(Narray),jelement(Narray)
     & ,xorder,Naverage,maxvalip,maxvaljp,minvalip,minvaljp
     & ,i0,j0,maxvaliQ,maxvaljQ
c ********************************************************************
      character*50 infile,trainfile,ptracefile,arrayfile,icflag,Qfile
     & ,xamplitude,ramplitude
c ********************************************************************
      data infile/'bowl_press.in'/
c ********************************************************************
      call readparams(drp,dxp,dtp,Nptspercycle,Naverage,xorder
     & ,trainmult,cH2Op,rhoH2O,alphaH2O,BetaH2O,ctissuep,rhotissue
     & ,alphatissue,Betatissue,cbloodp,rhoblood,alphablood,Betablood
     & ,cvesselp,rhovessel,alphavessel,Betavessel
     & ,decimspace,decimtime,icflag,infile,trainfile,ptracefile
     & ,arrayfile,Qfile,xamplitude,ramplitude)
c ********************************************************************
      call icfiles(cp,rhop,alphap,Betap,cH2Op,rhoH2O,alphaH2O
     & ,BetaH2O,ctissuep,rhotissue,alphatissue,Betatissue
     & ,cbloodp,rhoblood,alphablood,Betablood,cvesselp,rhovessel
```

```
     & ,alphavessel,Betavessel,Imaxp,Jmaxp,Iskin,icflag)
c ***********************************************************************
      call initialize(dtp,timep,Nmaxp,Imaxp,Jmaxp,pn,pnplus1
     & ,pnminus1,pnminus2,pnminus3,Q,ImaxT,JmaxT,pxmax,pxmin
     & ,prmax,prmin)
c ***********************************************************************
      call readtrain(train,n,Ntrain,trainfile)
c ***********************************************************************
      call cylarray(Narray,arrayfile,ielement,jelement
     & ,itargetp,jtargetp)
c ***********************************************************************
      call calcparams(rmaxp,drp,Imaxp,Jmaxp,xmaxp,dxp,tmaxp,dtp
     & ,Nmaxp,pi,period,Nptspercycle,freq,omega,lambda,kwave
     & ,tendtoend,nendtoend,trainmult,cH2Op,rhoH2O,BetaH2O
     & ,itargetp,jtargetp,rtarget,xtarget,q1,q2,q3,q4
     & ,xorder,xshock,Umax,Mach)
c ***********************************************************************
      call displayparams(drp,dxp,dtp,freq,lambda,kwave
     & ,cH2Op,rhoH2O,BetaH2O,Umax,Mach,tmaxp,tendtoend
     & ,xshock,xorder,Nptspercycle,Nmaxp,nendtoend,Imaxp,Jmaxp
     & ,decimtime,rmaxp,xmaxp,itargetp,jtargetp,rtarget,xtarget)
c ***********************************************************************
      pfocusmax=0.d0
      pfocusmin=0.d0
c ***********************************************************************
c open the ptracefile file:
      print*,'opening ',ptracefile
      open(1,file=ptracefile,form='formatted',status='unknown')
c ***********************************************************************
      print*,' ------ start time-stepping ------ '
c------ start time-stepping ------:
      t=0.d0
c ***********************************************************************
      do 11 n=1,Nmaxp
c ***********************************************************************
c use the input wave train file at array locations to drive:
      if (n.le.Ntrain) then
        do 15 m=1,Narray
          pn(ielement(m),jelement(m))=trainmult*train(n)
 15     continue
      end if
c ***********************************************************************
      call fdtd2s2t(pn,pnplus1,pnminus1,pnminus2,pnminus3
     & ,q1,q2,q3,q4,drp,dxp,dtp,Imaxp,Jmaxp
     & ,cp,rhop,alphap,Betap,omega,Narray,ielement,jelement)
c ***********************************************************************
c find pressure amplitude at the real focus at the last cycle
      if (Nmaxp-n.le.Nptspercycle)then
        if (pn(ifocusp,jfocusp).gt.pfocusmax)then
          pfocusmax=pn(ifocusp,jfocusp)
        end if
        if (pn(ifocusp,jfocusp).lt.pfocusmin)then
          pfocusmin=pn(ifocusp,jfocusp)
        end if
```

```
      end if
c ********************************************************************
c find pressure amplitude on axis at the last cycle
      if (Nmaxp-n.le.Nptspercycle)then
        do 13 i=1,Imaxp
        if (pn(i,1).gt.pxmax(i))then
          pxmax(i)=pn(i,1)
        end if
        if (pn(i,1).lt.pxmin(i))then
          pxmin(i)=pn(i,1)
        end if
 13     continue
        do 14 j=1,Jmaxp
        if (pn(ifocusp,j).gt.prmax(j))then
          prmax(j)=pn(ifocusp,j)
        end if
        if (pn(ifocusp,j).lt.prmin(j))then
          prmin(j)=pn(ifocusp,j)
        end if
 14     continue
      end if
c ********************************************************************
c output pressure at real and geometric focus
      if (MOD(n,2).eq.0)then
        write(1,110)t,pn(ifocusp,jfocusp),pn(itargetp,jtargetp)
      end if
c ********************************************************************
 110  format(3(G12.4, 1x))
c ********************************************************************
c collect intensity integral over the last ten cycles
      if (n.ge.(Nmaxp-Naverage).and.n.lt.Nmaxp)then
        do 20 j=1,JmaxT
          do 30 i=1,ImaxT
            i0=i+Iskin-1
            Qn=((3.d0*pn(i0,j)-4.d0*pnminus1(i0,j)+pnminus2(i0,j))
     &           /(2.d0*dtp))**2/(omega*omega*rhop(i0,j)*cp(i0,j))
            Q(i,j)=Q(i,j)+Qn
 30     continue
 20   continue
      end if
c ********************************************************************
      call updatep(Imaxp,Jmaxp,pn,pnplus1,pnminus1
     & ,pnminus2,pnminus3)
c ********************************************************************
      t=t+dtp
 11   continue
c ********************************************************************
      close(1)
      print*,'finish pressure calculation'
c ********************************************************************
      do 40 j=1,JmaxT
        do 45 i=1,ImaxT
          Q(i,j)=Q(i,j)/DBLE(Naverage)
 45     continue
```

```
 40   continue
c ***********************************************************************
c dump the amplitude file
      open(3,file=xamplitude,form='formatted',status='unknown')
      do 48 i=1,Imaxp
          write(3,110) (i-1)*dxp,pxmax(i),pxmin(i)
 48   continue
      close(3)
      open(4,file=ramplitude,form='formatted',status='unknown')
      do 49 j=1,Jmaxp
          write(4,110) (j-1)*drp,prmax(j),prmin(j)
 49   continue
      close(4)
c ***********************************************************************
c dump the intensity Qfile
      open(5,file=Qfile,form='formatted',status='unknown')
      do 50 j=1,JmaxT
        do 55 i=1,ImaxT
          write(5,*) Q(i,j)
 55     continue
 50   continue
      close(5)
c ***********************************************************************
c find where the maximum intensity is:
        call maxQ(Q,ImaxT,JmaxT,Qmax,maxvaliQ,maxvaljQ)
c ***********************************************************************
c display the pressure at focus
        print 111,trainmult,pfocusmax,pfocusmin
 111  format ('P0=',e14.7,' pfocusmax=',e14.7,' pfocusmin=',e14.7)
c ***********************************************************************
c display where the maximum intensity is:
        print 112,trainmult,Qmax,maxvaliQ,maxvaljQ
 112    format ('P0=',e14.7,' Qmax=',e14.7,' @ (',I4,' ',I4,')')
c ***********************************************************************
      print*,'......closed acoustic tracefile',ptracefile
      print*,'time now= ',t*1.d6,' microseconds'
c ***********************************************************************
      print*,'%%%%%%%%%%%%%%%%%%%% DONE
     &%%%%%%%%%%%%%%%%%%%%%%%%'
      end
c+++++++++++++++++++++++++++++++++++++++++++++++++++++++++++++++

c+++++++++++++++++++++++++++++++++++++++++++++++++++++++++++++++

      subroutine readparams(drp,dxp,dtp,Nptspercycle,Naverage,xorder
     & ,trainmult,cH2Op,rhoH2O,alphaH2O,BetaH2O,ctissuep,rhotissue
     & ,alphatissue,Betatissue,cbloodp,rhoblood,alphablood,Betablood
     & ,cvesselp,rhovessel,alphavessel,Betavessel
     & ,decimspace,decimtime,icflag,infile,trainfile,ptracefile
     & ,arrayfile,Qfile,xamplitude,ramplitude)
c ***********************************************************************
      implicit none
c ***********************************************************************
      doubleprecision drp,dxp,dtp,trainmult,cH2Op,rhoH2O,alphaH2O
```

```
     & ,BetaH2O,ctissuep,rhotissue,alphatissue,Betatissue
     & ,cbloodp,rhoblood,alphablood,Betablood,cvesselp,rhovessel
     & ,alphavessel,Betavessel
c ***********************************************************************
      integer Nptspercycle,xorder,decimspace,decimtime,Naverage
c ***********************************************************************
      character*50 infile,trainfile,ptracefile,arrayfile,icflag,Qfile
     & ,xamplitude,ramplitude
c ***********************************************************************
      print*,'===called SUBROUTINE READPARAMS'
c read the pressure's input parameters from input file
      open(unit=1,file=infile,status='unknown')
      print*,'opened input file ',infile
      read(1,*)drp,dxp,dtp,Nptspercycle,xorder
      read(1,*)trainfile
      read(1,*)ptracefile
      read(1,*)trainmult
      read(1,*)icflag,arrayfile
      read(1,*)cH2Op,rhoH2O,alphaH2O,BetaH2O
      read(1,*)ctissuep,rhotissue,alphatissue,Betatissue
      read(1,*)cbloodp,rhoblood,alphablood,Betablood
      read(1,*)cvesselp,rhovessel,alphavessel,Betavessel
      read(1,*)decimspace,decimtime,Naverage
      read(1,*)Qfile
      read(1,*)xamplitude
      read(1,*)ramplitude
      close(1)
      print*,'closed input file ',infile
c ***********************************************************************
      return
      end

c+++++++++++++++++++++++++++++++++++++++++++++++++++++++++++++++

c+++++++++++++++++++++++++++++++++++++++++++++++++++++++++++++++

c     SUBROUTINE ICFILES
c ***********************************************************************
      subroutine icfiles(cp,rhop,alphap,Betap,cH2Op,rhoH2O,alphaH2O
     & ,BetaH2O,ctissuep,rhotissue,alphatissue,Betatissue
     & ,cbloodp,rhoblood,alphablood,Betablood,cvesselp,rhovessel
     & ,alphavessel,Betavessel,Imaxp,Jmaxp,Iskin,icflag)
c ***********************************************************************
      implicit none
c ***********************************************************************
      doubleprecision cp(Imaxp,Jmaxp),rhop(Imaxp,Jmaxp)
     & ,alphap(Imaxp,Jmaxp),Betap(Imaxp,Jmaxp),cH2Op,rhoH2O
     & ,ctissuep,rhotissue,alphatissue,Betatissue
     & ,BetaH2O,alphaH2O,cbloodp,rhoblood,alphablood,Betablood
     & ,cvesselp,rhovessel,alphavessel,Betavessel
c ***********************************************************************
      integer i,j,Imaxp,Jmaxp,Iskin
c ***********************************************************************
      character*50 icflag
```

```
c ********************************************************************
      print*,'>>>>>>>>> beginning subroutine icfiles'
      do 10 j=1,Jmaxp
        do 20 i=1,Imaxp
          cp(i,j)=cH2Op
          rhop(i,j)=rhoH2O
          alphap(i,j)=alphaH2O
          Betap(i,j)=BetaH2O
  20    continue
  10  continue
c ********************************************************************
      if (icflag.eq.'F')then
        print*,'using homogen. H2O Ics'
      else
        print*,'using inhomogen. H2O,PPO,phantom,blood Ics'
c ********************************************************************
c... blood fill the domain: i=Iskin:Iskin+10cm, j=0:1.0mm
c... blood vessel fill the domain: i=Iskin:Iskin+10cm, j=1.0:1.6
c... tissue fill the domain: i=Iskin:Iskin+10cm, j=1.6:30
      do 30 i= Iskin,Iskin+1000
      do 40 j=1,10
          cp(i,j)=cbloodp
          rhop(i,j)=rhoblood
          alphap(i,j)=alphablood
          Betap(i,j)=Betablood
 40     continue
        do 50 j=11,16
          cp(i,j)=cvesselp
          rhop(i,j)=rhovessel
          alphap(i,j)=alphavessel
          Betap(i,j)=Betavessel
 50     continue
        do 60 j=17,301
          cp(i,j)=ctissuep
          rhop(i,j)=rhotissue
          alphap(i,j)=alphatissue
          Betap(i,j)=Betatissue
 60     continue
 30   continue
c ********************************************************************
      end if
        print*,'Properties of fluid (water):'
        print*,'     cH2O= ',cH2Op
        print*,'     rhoH2O= ',rhoH2O
        print*,'     alphaH2O= ',alphaH2O
        print*,'     BetaH2O= ',BetaH2O

      return
      end

c+++++++++++++++++++++++++++++++++++++++++++++++++++++++++++++++++++

c+++++++++++++++++++++++++++++++++++++++++++++++++++++++++++++++++++
```

```
      subroutine initialize(dtp,timep,Nmaxp,Imaxp,Jmaxp,pn,pnplus1
     & ,pnminus1,pnminus2,pnminus3,Q,ImaxT,JmaxT,pxmax,pxmin
     &,prmax,prmin)
c ********************************************************************
      implicit none
c ********************************************************************
      integer n,Nmaxp,i,j,Imaxp,Jmaxp,ImaxT,JmaxT
c ********************************************************************
      doubleprecision dtp,timep(Nmaxp),pn(Imaxp,Jmaxp)
     & ,pnplus1(Imaxp,Jmaxp),pnminus1(Imaxp,Jmaxp)
     & ,pnminus2(Imaxp,Jmaxp),pnminus3(Imaxp,Jmaxp),Q(ImaxT,JmaxT)
     & ,pxmax(Imaxp),pxmin(Imaxp),prmax(Jmaxp),prmin(Jmaxp)
c ********************************************************************
      print*,'===called SUBROUTINE INITIALIZE'
c ********************************************************************
      print*,'...initializing pressure timewise arrays'
      do 10 n=1,Nmaxp
         timep(n)=dtp*(n-1)
 10   continue
c initialize pressure field to zero everywhere:
      print*,'...initializing press. fields'
      do 20 i=1,Imaxp
         pxmax(i)=0.d0
         pxmin(i)=0.d0
         do 30 j=1,Jmaxp
            pn(i,j)=0.d0
            pnplus1(i,j)=0.d0
            pnminus1(i,j)=0.d0
            pnminus2(i,j)=0.d0
            pnminus3(i,j)=0.d0
 30     continue
 20   continue
      do 40 j=1,Jmaxp
         prmax(j)=0.d0
         prmin(j)=0.d0
 40   continue
c ********************************************************************
      do 25 j=1,JmaxT
        do 35 i=1,ImaxT
          Q(i,j)=0.d0
 35     continue
 25   continue
c ********************************************************************

      return
      end

c+++++++++++++++++++++++++++++++++++++++++++++++++++++++++++++++++++++

c+++++++++++++++++++++++++++++++++++++++++++++++++++++++++++++++++++++

      subroutine readtrain(train,n,Ntrain,trainfile)

      implicit none
```

```
      doubleprecision train(Ntrain)
      integer n,Ntrain
      character*50 trainfile

      print*,'===called SUBROUTINE READTRAIN'
c read in wave train data file:
      print*,'...reading source condition ',trainfile
      open(unit=1,file=trainfile,status='unknown')
      do 10 n=1,Ntrain
        read(1,*) train(n)
 10   continue
      close(1)
      print*,'......closed ',trainfile
      return
      end
c+++++++++++++++++++++++++++++++++++++++++++++++++++++++++++++++

c+++++++++++++++++++++++++++++++++++++++++++++++++++++++++++++++

c     SUBROUTINE cylarray
c **********************************************************************
      subroutine cylarray(Narray,arrayfile,ielement,jelement
     & ,itargetp,jtargetp)
c **********************************************************************
      implicit none
c **********************************************************************
      integer n,Narray,ielement(Narray),jelement(Narray)
     & ,itargetp,jtargetp
c **********************************************************************
      doubleprecision itargetp0,jtargetp0,ielement0,jelement0
c **********************************************************************
      character*50 arrayfile
c **********************************************************************
      print*,'>>>>>>>>>> CALLED SUBROUTINE cylarray'
c **********************************************************************
      open(1,file=arrayfile,form='formatted',status='unknown')
      read(1,*) itargetp0,jtargetp0
      itargetp = INT(itargetp0)
      jtargetp=INT(jtargetp0)
      do 20 n=1,Narray
        read(1,*) ielement0, jelement0
        ielement(n)=INT(ielement0)
        jelement(n)=INT(jelement0)
        print*,'array element:',n,ielement(n),jelement(n)
 20   continue
      close(1)
c **********************************************************************
      return
      end

c+++++++++++++++++++++++++++++++++++++++++++++++++++++++++++++++

c+++++++++++++++++++++++++++++++++++++++++++++++++++++++++++++++
```

```
      subroutine calcparams(rmaxp,drp,Imaxp,Jmaxp,xmaxp,dxp,tmaxp,dtp
     & ,Nmaxp,pi,period,Nptspercycle,freq,omega,lambda,kwave
     & ,tendtoend,nendtoend,trainmult,cH2Op,rhoH2O,BetaH2O
     & ,itargetp,jtargetp,rtarget,xtarget,q1,q2,q3,q4
     & ,xorder,xshock,Umax,Mach)
c ******************************************************************
      implicit none
c ******************************************************************
      doubleprecision rmaxp,drp,xmaxp,dxp,tmaxp,dtp,pi,period,freq
     & ,omega,lambda,kwave,tendtoend,Umax,trainmult,Mach
     & ,xshock,rtarget,xtarget,cH2Op,rhoH2O,BetaH2O
     & ,q1,q2,q3,q4
c ******************************************************************
      integer Imaxp,Jmaxp,Nmaxp,Nptspercycle,nendtoend
     &  ,itargetp,jtargetp,xorder,i,j
c ******************************************************************
      print*,'===called SUBROUTINE CALCPARAMS'
c ******************************************************************
c calculate some basic run parameters:
      rmaxp=drp*DBLE(Jmaxp-1)
      xmaxp=dxp*DBLE(Imaxp-1)
      tmaxp=dtp*DBLE(Nmaxp-1)
      pi=ACOS(-1.d0)
      period=dtp*DBLE(Nptspercycle)
      freq=1.d0/period
      omega=2.d0*pi*freq
      lambda=cH2Op*period
      kwave=omega/cH2Op
      tendtoend=xmaxp/cH2Op
      nendtoend=INT(tendtoend/dtp)
      Umax = trainmult/(rhoH2O*cH2Op)
      Mach = Umax/cH2Op
      xshock = 1.d0/(BetaH2O*Mach*kwave)
c ******************************************************************
c calculate where all the x's are at:
      xtarget=dxp*DBLE(itargetp-1)
      rtarget=drp*DBLE(jtargetp-1)
c ******************************************************************
      q1=dtp*dtp/(drp*drp)
      q2=dtp*dtp/(2.d0*drp)
      q3=dtp*dtp/(dxp*dxp)
      q4=2.d0/(omega*omega*dtp)
c ******************************************************************
      return
      end

c+++++++++++++++++++++++++++++++++++++++++++++++++++++++++++++++++++

c+++++++++++++++++++++++++++++++++++++++++++++++++++++++++++++++++++

      subroutine displayparams(drp,dxp,dtp,freq,lambda,kwave
     & ,cH2Op,rhoH2O,BetaH2O,Umax,Mach,tmaxp,tendtoend
     & ,xshock,xorder,Nptspercycle,Nmaxp,nendtoend,Imaxp,Jmaxp
     & ,decimtime,rmaxp,xmaxp,itargetp,jtargetp,rtarget,xtarget)
```

```
c ***********************************************************************
      implicit none
c ***********************************************************************
      doubleprecision drp,dxp,dtp,freq,lambda,kwave
     & ,cH2Op,rhoH2O,BetaH2O,Umax,Mach
     & ,tmaxp,tendtoend,xshock,rmaxp,xmaxp,rtarget,xtarget
c ***********************************************************************
      integer xorder,Nptspercycle,decimtime
     & ,Nmaxp,nendtoend,Imaxp,Jmaxp,itargetp,jtargetp
c ***********************************************************************
      print*,'===called SUBROUTINE DISPLAYPARAMS'
c ***********************************************************************
c put some initial info on the screen so user knows what to expect:
      print*,'### bowl_press.f RUN PARAMETERS ###:'
      print*,'-----------------------------------------------------'
      if (xorder.eq.4) then
         print*,'calculation is order dx^4'
      else
         print*,'calculation is order dx^2'
      end if
      print 10, dxp*1.d3
   10 format(' ','dx =',G12.4,' mm')
      print 15, drp*1.d3
   15 format(' ','dr =',G12.4,' mm')
      print 20, dtp*1.d6
   20 format(' ','dt =',G12.4,' microsec')
      print 40, freq/1.d6
   40 format(' ','frequency =',G12.4,' MHz')
      print 50, Nptspercycle
   50 format(' ','no. of samples/period in time =',I8)
      print 60, INT(lambda/dxp)
   60 format(' ','no. of samples/period in space =',I8)
      print 70, lambda*1.d3
   70 format(' ','wavelength in 1500 water=',G10.4,' mm')
      print 80, kwave
   80 format(' ','wave number k =',G10.4)
      print 84, cH2Op
   84 format(' ','cH2O =',G12.4,' m/sec')
      print 86, rhoH2O
   86 format(' ','rhoH2O =',G12.4,' kg/m^3')
      print 90, BetaH2O
   90 format(' ','BetaH2O =',G12.4)
      print 200, Umax
  200 format('max. particle velocity =',G12.4,' m/sec')
      print 210, Mach
  210 format('source acoustic Mach no. is about ',G12.4)
      print*,'-----------------------------------------------------'
      print 230, tendtoend*1.d6,nendtoend
  230 format('signal can go from end to end in ',F8.4,' microsec'
     &,' taking',I12,' steps')
      print 235, tmaxp*1.d6,Nmaxp
  235 format('calculation tmax is at t =',G12.4,'microsec'
     & ,' and Nmax=',I8)
      print 240, xtarget*100.d0, itargetp
```

```
  240 format('focus is at x =',G12.4,'cm and i=',I8)
      print 245, rtarget*100.d0, jtargetp
  245 format('focus is at r =',G12.4,'cm and j=',I8)
      print 250, xmaxp*100.d0,Imaxp
  250 format('calculation xmax is at x =',G12.4,'cm and i=',I8)
      print 260, rmaxp*100.d0,Jmaxp
  260 format('calculation rmax is at r =',G12.4,'cm and j=',I8)
      print 270, xshock*100.d0,INT(xshock/dxp)
  270 format('shock forms at x= ',G12.4,'cm at i=',I12)
      print 275, xshock*1.d6/cH2Op,INT((xshock/cH2Op)/dtp)
  275 format('shock forms at tshock = ',G12.4,'microsec'
     & ,' at Nshock=',I12)
      print*,'------------------------------------------------------------'
c ***************************************************************
      return
      end

c+++++++++++++++++++++++++++++++++++++++++++++++++++++++++++++++

c+++++++++++++++++++++++++++++++++++++++++++++++++++++++++++++++

      subroutine fdtd2s2t(pn,pnplus1,pnminus1,pnminus2,pnminus3
     & ,q1,q2,q3,q4,drp,dxp,dtp,Imaxp,Jmaxp
     & ,cp,rhop,alphap,Betap,omega,Narray,ielement,jelement)
c ***************************************************************
      implicit none
c ***************************************************************
      doubleprecision pn(Imaxp,Jmaxp),pnplus1(Imaxp,Jmaxp)
     & ,pnminus1(Imaxp,Jmaxp),pnminus2(Imaxp,Jmaxp)
     & ,pnminus3(Imaxp,Jmaxp),z1,z2,z3,z4,z5,z6,z7,drp,dxp,dtp
     & ,q1,q2,q3,q4,cp(Imaxp,Jmaxp),rhop(Imaxp,Jmaxp)
     & ,alphap(Imaxp,Jmaxp),Betap(Imaxp,Jmaxp),omega,r
c ***************************************************************
      integer i,j,Imaxp,Jmaxp,Narray,ielement(Narray)
     & ,jelement(Narray),I0
c ***************************************************************
c...Absorbing Mur(1) BC's at ends:
c...Put in first order Mur BC's at r=rmax, ie, j=Jmax:
      do 310 i=1,Imaxp
        pn(i,Jmaxp)=pnminus1(i,Jmaxp-1)+((cp(i,Jmaxp)*dtp-drp)/
     & (cp(i,Jmaxp)*dtp+drp))*(pn(i,Jmaxp-1)-pnminus1(i,Jmaxp))
 310    continue
c ***************************************************************
c...Put in first order Mur BC's at x=xmax, ie, i=Imax:
      do 300 j=1,Jmaxp
        pn(Imaxp,j)=pnminus1(Imaxp-1,j)+((cp(Imaxp,j)*dtp-dxp)/
     & (cp(Imaxp,j)*dtp+dxp))*(pn(Imaxp-1,j)-pnminus1(Imaxp,j))
 300    continue
c ***************************************************************
c...Put symmetric BC's at j=1, r=0, makes z2=0 and the 1/r problem
vanishes:
      do 25 i=2,Imaxp-1
      z1=2.d0*(pn(i,2)-pn(i,1))
      z3=pn(i+1,1)-2.d0*pn(i,1)+pn(i-1,1)
```

```
      z4=pn(i,1)-3.d0*pnminus1(i,1)+3.d0*pnminus2(i,1)-pnminus3(i,1)
      z5=pn(i,1)*(2.d0*pn(i,1)-5.d0*pnminus1(i,1)
     &       +4.d0*pnminus2(i,1)-pnminus3(i,1))
      z6=(3.d0*pn(i,1)-4.d0*pnminus1(i,1)+pnminus2(i,1))**2
      z7=-2.d0*pn(i,1)+pnminus1(i,1)
      pnplus1(i,1)= (cp(i,1)*cp(i,1))*(q1*z1+q3*z3)
     &      +cp(i,1)*alphap(i,1)*q4*z4+(2.d0*Betap(i,1)
     &      /(rhop(i,1)*cp(i,1)*cp(i,1)))*(z5+z6/4.d0)-z7
 25   continue
c ********************************************************************
c...Put in first order Mur BC's at i=ielement(Narray) & i=ielement(1)
      i=ielement(Narray)
      do 30 j=jelement(Narray)+1,Jmaxp-1
        pn(i,j)=pnminus1(i+1,j)+((cp(i,j)*dtp-dxp)/
     & (cp(i,j)*dtp+dxp))*(pn(i+1,j)-pnminus1(i,j))
 30   continue
c ********************************************************************
c...inside cells:
      do 10 j=2,Jmaxp-1
         r=(j-1)*drp
        if (j.lt.jelement(Narray)) then
          I0=ielement(j)+1
        else
          I0=ielement(Narray)+1
        end if
        do 20 i=I0,Imaxp-1
         z1=pn(i,j+1)-2.d0*pn(i,j)+pn(i,j-1)
         z2=pn(i,j+1)-pn(i,j-1)
         z3=pn(i+1,j)-2.d0*pn(i,j)+pn(i-1,j)
         z4=pn(i,j)-3.d0*pnminus1(i,j)+3.d0*pnminus2(i,j)-pnminus3(i,j)
         z5=pn(i,j)*(2.d0*pn(i,j)-5.d0*pnminus1(i,j)
     &       +4.d0*pnminus2(i,j)-pnminus3(i,j))
         z6=(3.d0*pn(i,j)-4.d0*pnminus1(i,j)+pnminus2(i,j))**2
         z7=-2.d0*pn(i,j)+pnminus1(i,j)
         pnplus1(i,j)=(cp(i,j)*cp(i,j))*(q1*z1+q2*z2/r+q3*z3)
     &     +cp(i,j)*alphap(i,j)*q4*z4+(2.d0*Betap(i,j)
     &      /(rhop(i,j)*cp(i,j)*cp(i,j)))*(z5+z6/4.d0)-z7
 20     continue
 10   continue
      return
      end

c+++++++++++++++++++++++++++++++++++++++++++++++++++++++++++++++++++

c+++++++++++++++++++++++++++++++++++++++++++++++++++++++++++++++++++

      subroutine updatep(Imax,Jmax,pn,pnplus1,pnminus1
     & ,pnminus2,pnminus3)
c ********************************************************************
      implicit none
c ********************************************************************
      doubleprecision pn(Imax,Jmax),pnplus1(Imax,Jmax)
     & ,pnminus1(Imax,Jmax),pnminus2(Imax,Jmax),pnminus3(Imax,Jmax)
c ********************************************************************
```

```
      integer i,j,Imax,Jmax
c *********************************************************************
c UPDATE ARRAYS IN TIME AND WRITE PRESSURE TO OUTPUT DATA FILE:
      do 10 j=1,Jmax
        do 20 i=1,Imax
         pnminus3(i,j)=pnminus2(i,j)
         pnminus2(i,j)=pnminus1(i,j)
         pnminus1(i,j)=pn(i,j)
         pn(i,j)=pnplus1(i,j)
 20     continue
 10   continue
c *********************************************************************
      return
      end

c+++++++++++++++++++++++++++++++++++++++++++++++++++++++++++++++++++++

c+++++++++++++++++++++++++++++++++++++++++++++++++++++++++++++++++++++
      subroutine maxQ(Q,Imax,Jmax,Qmax,maxvali,maxvalj)

      doubleprecision  Q(Imax,Jmax),Qmax
      integer i,j,Imax,Jmax,maxvali,maxvalj
      Qmax=Q(1,1)
      maxvalj=1
c find maximum along acoustic axis
      do 10 i=1,Imax
        if(Q(i,1).gt.Qmax)then
             Qmax=Q(i,1)
             maxvali=i
        end if
 10   continue
      return
      end

c+++++++++++++++++++++++++++++++++++++++++++++++++++++++++++++++++++++

c+++++++++++++++++++++++++++++++++++++++++++++++++++++++++++++++++++++
```

Appendix D

Finite-Difference Time Domain Code: BHTE Solution

The following code is used to calculate the temperature field in the tissue and blood domain.

```
      program bioheat
c ***********************************************************************
      implicit none
      integer ImaxT,JmaxT,KmaxT,Nsonic,NmaxT,NstepT
     & ,ifocusT,jfocusT,kfocusT,itc1,jtc1,ktc1,itc2,jtc2,ktc2,itc3
     & ,jtc3,ktc3,itc4,jtc4,ktc4,itc5,jtc5,ktc5,itc6,jtc6,ktc6
     & ,itc7,jtc7,ktc7,itc8,jtc8,ktc8,ImaxQ,JmaxQ,ImaxU,JmaxU,KmaxU
     & ,IU0,JU0,itc9,jtc9,ktc9,itc10,jtc10,ktc10,itc11,jtc11,ktc11
     & ,itc12,jtc12,ktc12
c ***********************************************************************
      parameter(ImaxT=201,JmaxT=201,KmaxT=501,Nsonic=40001,NmaxT=40001
     & ,NstepT=20,ifocusT=101,jfocusT=114,kfocusT=176,itc1=101,jtc1=101
     & ,ktc1=176,itc2=101,jtc2=106,ktc2=176,itc3=101,jtc3=111,ktc3=176
     & ,itc4=101,jtc4=114,ktc4=176,itc5=101,jtc5=117,ktc5=176,itc6=101
     & ,jtc6=122,ktc6=176,itc7=101,jtc7=127,ktc7=176,itc8=101,jtc8=101
     & ,ktc8=151,itc9=101,jtc9=101,ktc9=126,itc10=101,jtc10=101
     & ,ktc10=201,itc11=101,jtc11=101,ktc11=226,itc12=101,jtc12=101
     & ,ktc12=251,ImaxQ=1001,JmaxQ=201,ImaxU=21,JmaxU=21,KmaxU=501
     & ,IU0=91,JU0=91)
c ***********************************************************************
      doubleprecision dxT,dyT,dzT,dtT,xmaxT,ymaxT,zmaxT,tmaxT
     & ,Tfocusmax,Ttcmax,Q(ImaxT,JmaxT,KmaxT),h(ImaxT,JmaxT,KmaxT)
     & ,Tn(ImaxT,JmaxT,KmaxT),Tnminus1(ImaxT,JmaxT,KmaxT)
     & ,Tnplus1(ImaxT,JmaxT,KmaxT),maxTemp,minTemp,Ta,Tb,Wblood
     & ,CtissT,Ktiss,rhotiss,alphatiss,CbloodT,Kblood,rhoblood
     & ,alphablood,Wb(ImaxT,JmaxT,KmaxT),Q2d(ImaxQ,JmaxQ)
     & ,qh1,qh2,qh3,qh4,qh5,qh6,qh7,Uavg,Ux(ImaxT,JmaxT,KmaxT)
     & ,Uy(ImaxT,JmaxT,KmaxT),Uz(ImaxT,JmaxT,KmaxT)
     & ,drQ,dzQ,rblood,rvessel,t,qt,qb,qv,af,bf,cf,xf0,yf0,zf0,r,z
     & ,pn(ImaxU,JmaxU,KmaxU),pnplus1(ImaxU,JmaxU,KmaxU)
     & ,Uxn(ImaxU,JmaxU,KmaxU),Uyn(ImaxU,JmaxU,KmaxU)
     & ,Uzn(ImaxU,JmaxU,KmaxU),Uze(ImaxT,JmaxT,KmaxT)
     & ,Uxnplus1(ImaxU,JmaxU,KmaxU),Uynplus1(ImaxU,JmaxU,KmaxU)
     & ,Uznplus1(ImaxU,JmaxU,KmaxU),Fx(ImaxU,JmaxU,KmaxU)
     & ,Fy(ImaxU,JmaxU,KmaxU),Fz(ImaxU,JmaxU,KmaxU),w,epislon
     & ,viscoblood,dviscoblood,cblood,qu1,qu2,qu3,qu4,qu5,qu6
     & ,CvesselT,Kvessel,rhovessel,alphavessel,dtU,aQ,bQ,cQ,zQf
c ***********************************************************************
      integer i,j,k,n,dumpnumber,decimspace,decimtime,iQ,jQ,NstepU
     & ,maxvaliT,maxvaljT,maxvalkT,minvaliT,minvaljT,minvalkT
c ***********************************************************************
```

```
      character*50 infile,Ttracefile1,Ttracefile2,Q2dfile,Utracefile
c ***********************************************************************
      data infile/'heat.in'/
c ***********************************************************************
      Tfocusmax=0.d0
      Ttcmax=0.d0
      maxTemp=0.d0
      minTemp=0.d0
c ***********************************************************************
      call readparams(drQ,dzQ,dxT,dyT,dzT,dtT,dtU,Wblood,Ta,Tb
     & ,Uavg,rblood,rvessel,CtissT,Ktiss,rhotiss,alphatiss,CbloodT
     & ,rhoblood,Kblood,alphablood,viscoblood,cblood,infile,Ttracefile1
     & ,Ttracefile2,Q2dfile,Utracefile,decimspace,decimtime
     & ,af,bf,cf,xf0,yf0,zf0,aQ,bQ,cQ,zQf,CvesselT,Kvessel
     & ,rhovessel,alphavessel)
c ***********************************************************************
      call calcparams(ImaxT,JmaxT,KmaxT,xmaxT,dxT,ymaxT,dyT
     & ,zmaxT,dzT,tmaxT,dtT,dtU,NmaxT,qh1,qh2,qh3,qh4,qh5,qh6,qh7
     & ,rhotiss,CtissT,rhoblood,CbloodT,qt,qb,viscoblood,dviscoblood
     & ,qv,rhovessel,CvesselT,qu1,qu2,qu3,qu4,qu5,qu6)
c ***********************************************************************
      call calh(h,dxT,dyT,dzT,xf0,yf0,zf0,af,bf,cf,ImaxT,JmaxT,KmaxT)
c ***********************************************************************
      call icfiles(ImaxT,JmaxT,KmaxT,Wb,Wblood,rblood,Uavg,Uze,h)
c ***********************************************************************
      call initializeT(ImaxT,JmaxT,KmaxT,Tn,Tnplus1,Tnminus1,Q
     & ,Ux,Uy,Uz,Uze,Ta,Q2d,ImaxQ,JmaxQ)
c ***********************************************************************
      call initializeU(ImaxU,JmaxU,KmaxU,Uxn,Uyn,Uzn,Uxnplus1
     & ,Uynplus1,Uznplus1,Fx,Fy,Fz,pn,pnplus1)
c ***********************************************************************
      call readQ(Q2d,ImaxQ,JmaxQ,Q2dfile)
c ***********************************************************************
      NstepU=int(dtU/dtT)
c ***********************************************************************
c convert the heat source Q from 2D to 3D
      call calQ3d(Q,ImaxT,JmaxT,KmaxT,dxT,dyT,dzT
     & ,Q2d,ImaxQ,JmaxQ,drQ,dzQ,aQ,bQ,cQ,zQf,ifocusT,jfocusT,kfocusT)
c ***********************************************************************
      r=sqrt(aQ*aQ+bQ*bQ+cQ*cQ)
c ***********************************************************************
c  calculate Fz from Q3d
      do 58 k=1,KmaxU
       do 60 j=1,JmaxU
      do 62 i=1,ImaxU
       Fx(i,j,k)=(2.d0*alphablood/cblood)*Q(i+IU0-1,j+JU0-1,k)*aQ/r
       Fy(i,j,k)=(2.d0*alphablood/cblood)*Q(i+IU0-1,j+JU0-1,k)*bQ/r
       Fz(i,j,k)=(2.d0*alphablood/cblood)*Q(i+IU0-1,j+JU0-1,k)*cQ/r
 62     continue
 60    continue
 58   continue
c ***********************************************************************
c calculate the heat source for bioheat eq.
      do 65 k=1,KmaxT
```

```
        do 66 j=1,JmaxT
          do 68 i=1,ImaxT
            if(h(i,j,k).lt.rblood)then
              Q(i,j,k)=2.d0*alphablood*Q(i,j,k)
            else if(h(i,j,k).lt.rvessel)then
            Q(i,j,k)=2.d0*alphavessel*Q(i,j,k)
          else
              Q(i,j,k)=2.d0*alphatiss*Q(i,j,k)
            end if
 68     continue
 66   continue
 65   continue
c ********************************************************************
      w=1.765d0
      epislon=0.5d-4
c ********************************************************************
      print*,'......begin temperature field calculation......'
c ********************************************************************
c open the Ttracefile:
      print*,'opening ',Ttracefile1
      open(1,file=Ttracefile1,form='formatted',status='unknown')
c ********************************************************************
c open the Ttracefile:
      print*,'opening ',Ttracefile2
      open(3,file=Ttracefile2,form='formatted',status='unknown')
c ********************************************************************
c open the Utracefile:
      print*,'opening ',Utracefile
      open(2,file=Utracefile,form='formatted',status='unknown')
c ********************************************************************
c------ start time-stepping ------:
      t=0.d0
c ********************************************************************
      do 13 n=1,NmaxT
c ********************************************************************
      if (n.eq.Nsonic+1) then
        do 70 k=1,KmaxT
          do 72 j=1,JmaxT
            do 75 i=1,ImaxT
              Q(i,j,k)=0.d0
 75     continue
 72   continue
 70   continue
c ********************************************************************
      do 80 k=1,KmaxU
          do 85 j=1,JmaxU
            do 90 i=1,ImaxU
              Fx(i,j,k)=0.d0
              Fy(i,j,k)=0.d0
              Fz(i,j,k)=0.d0
 90       continue
 85     continue
 80   continue
      print*,'insonation 1 second'
```

```
      end if
c ********************************************************************
      if (n.gt.1.and.MOD(n-1,NstepU).eq.0)then
        call flow2s1t_3D(ImaxU,JmaxU,KmaxU,dxT,dyT,dzT,dtU,rhoblood,w
     & ,epislon,Uxn,Uyn,Uzn,Uxnplus1,Uynplus1,Uznplus1,qu1,qu2,qu3
     & ,qu4,qu5,qu6,dviscoblood,Fx,Fy,Fz,pn,pnplus1,rblood)
c ********************************************************************
c Generate Ux,Uy,Uz from Uxnplus1,Uynplus1,Uznplus1
        do 95 k=1,KmaxU
          do 100 j=1,JmaxU
          do 105 i=1,ImaxU
            Ux(i+IU0-1,j+JU0-1,k)=Uxnplus1(i,j,k)
              Uy(i+IU0-1,j+JU0-1,k)=Uynplus1(i,j,k)
              Uz(i+IU0-1,j+JU0-1,k)=Uznplus1(i,j,k)
     &                            +Uze(i+IU0-1,j+JU0-1,k)
 105        continue
 100      continue
 95     continue
      end if
c ********************************************************************
      call heat2s1t(ImaxT,JmaxT,KmaxT,Q,Ta,Tb,dtT,Tn,Tnplus1
     & ,qh1,qh2,qh3,qh4,qh5,qh6,qh7,qt,qb,qv,Ktiss,Wb,Kblood,Kvessel
     & ,Ux,Uy,Uz,rblood,rvessel,h)
c ********************************************************************
      if (n.le.Nsonic.and.MOD(n-1,decimtime).eq.0) then
        call snapdumpT(n,t,ImaxT,JmaxT,KmaxT,Tn,Ta
     & ,decimspace,decimtime,dumpnumber,maxTemp,minTemp
     & ,maxvaliT,maxvaljT,maxvalkT,minvaliT,minvaljT,minvalkT
     & ,ifocusT,jfocusT,kfocusT)
        call snapdumpU(n,t,ImaxT,JmaxT,KmaxT,ImaxU,JmaxU,KmaxU,IU0
     & ,JU0,decimspace,decimtime,dumpnumber,Ux,Uy,Uz,itc1,jtc1,ktc1)
      end if
c ********************************************************************
      if (MOD(n-1,NstepT).eq.0)then
        write(1,114)t,Tn(itc1,jtc1,ktc1)-Tb,Tn(itc2,jtc2,ktc2)-Tb
     & ,Tn(itc3,jtc3,ktc3)-Tb,Tn(itc4,jtc4,ktc4)-Tb
     & ,Tn(itc5,jtc5,ktc5)-Tb,Tn(itc6,jtc6,ktc6)-Tb
c ********************************************************************
        write(3,114)t,Tn(itc7,jtc7,ktc7)-Tb,Tn(itc8,jtc8,ktc8)-Tb
     & ,Tn(itc9,jtc9,ktc9)-Tb,Tn(itc10,jtc10,ktc10)-Tb
     & ,Tn(itc11,jtc11,ktc11)-Tb,Tn(itc12,jtc12,ktc12)-Tb
c ********************************************************************
      write(2,113)t,Ux(itc1,jtc1,ktc1),Uy(itc1,jtc1,ktc1)
     & ,Uz(itc1,jtc1,ktc1),Ux(itc2,jtc2,ktc2),Uy(itc2,jtc2,ktc2)
     & ,Uz(itc2,jtc2,ktc2)
      end if
 112  format(6(e14.7, 1x))
 113  format(7(e14.7, 1x))
 114  format(7(e14.7, 1x))
c ********************************************************************
c find the peak temperature rise at the location of thermocouple
      if (Tn(itc1,jtc1,ktc1).gt.Ttcmax)then
          Ttcmax=Tn(itc1,jtc1,ktc1)
      end if
```

```
c ********************************************************************
c find the peak temperature rise at the focus
      if (Tn(ifocusT,jfocusT,kfocusT).gt.Tfocusmax)then
          Tfocusmax=Tn(ifocusT,jfocusT,kfocusT)
      end if
c ********************************************************************
      call updateT(ImaxT,JmaxT,KmaxT,Tn,Tnplus1,Tnminus1)
c ********************************************************************
      if (n.gt.1.and.MOD(n-1,NstepU).eq.0)then
        call updateU(ImaxU,JmaxU,KmaxU,Uxn,Uyn,Uzn,Uxnplus1,Uynplus1
     & ,Uznplus1,pn,pnplus1)
      end if
c ********************************************************************
      t=t+dtT
 13   continue
      close(1)
      close(2)
      close(3)
c ********************************************************************
c display the max temperature at TC
      print 115,Tfocusmax-Tb,Ttcmax-Tb
 115  format ('Tfocusmax=',e14.7,' Ttcmax=',e14.7)
c ********************************************************************
      print*,'......closed Ttracefile',Ttracefile1,Ttracefile2
c ********************************************************************
      print*,'%%%%%%%%%%%%%%%%%%%% DONE %%%%%%%%%%%%%%%%%%%%'
      end

c+++++++++++++++++++++++++++++++++++++++++++++++++++++++++++++++++++

c+++++++++++++++++++++++++++++++++++++++++++++++++++++++++++++++++++
      subroutine readparams(drQ,dzQ,dxT,dyT,dzT,dtT,dtU,Wblood,Ta,Tb
     & ,Uavg,rblood,rvessel,CtissT,Ktiss,rhotiss,alphatiss,CbloodT
     & ,rhoblood,Kblood,alphablood,viscoblood,cblood,infile,Ttracefile1
     & ,Ttracefile2,Q2dfile,Utracefile,decimspace,decimtime
     & ,af,bf,cf,xf0,yf0,zf0,aQ,bQ,cQ,zQf,CvesselT,Kvessel
     & ,rhovessel,alphavessel)
c ********************************************************************
      implicit none
c ********************************************************************
      doubleprecision dxT,dyT,dzT,dtT,Wblood,Ta,Tb,Uavg,CtissT,Ktiss
     & ,rhotiss,alphatiss,CbloodT,Kblood,rhoblood,alphablood,rblood,drQ
     & ,dzQ,af,bf,cf,xf0,yf0,zf0,aQ,bQ,cQ,zQf,viscoblood,cblood,rvessel
     & ,CvesselT,Kvessel,rhovessel,alphavessel,dtU
c ********************************************************************
      integer decimspace,decimtime
c ********************************************************************
      character*50 infile,Q2dfile,Ttracefile1,Ttracefile2,Utracefile
c ********************************************************************
c read the temperature's input parameters from input file
      open(unit=1,file=infile,status='unknown')
      print*,'opened input file ',infile
      read(1,*)drQ,dzQ,dxT,dyT,dzT,dtT,dtU
      read(1,*)Wblood,Ta,Tb,Uavg,rblood,rvessel
```

```
      read(1,*)CtissT,Ktiss,rhotiss,alphatiss
      read(1,*)CbloodT,Kblood,rhoblood,alphablood,viscoblood,cblood
      read(1,*)CvesselT,Kvessel,rhovessel,alphavessel
      read(1,*)decimspace,decimtime
      read(1,*)af,bf,cf,xf0,yf0,zf0
      read(1,*)aQ,bQ,cQ,zQf
      read(1,*)Ttracefile1
      read(1,*)Ttracefile2
      read(1,*)Utracefile
      read(1,*)Q2dfile
      close(1)
      print*,'closed input file ',infile
c ***********************************************************************
      return
      end
c+++++++++++++++++++++++++++++++++++++++++++++++++++++++++++++++++++++++

c+++++++++++++++++++++++++++++++++++++++++++++++++++++++++++++++++++++++
      subroutine calcparams(ImaxT,JmaxT,KmaxT,xmaxT,dxT,ymaxT,dyT
     & ,zmaxT,dzT,tmaxT,dtT,dtU,NmaxT,qh1,qh2,qh3,qh4,qh5,qh6,qh7
     & ,rhotiss,CtissT,rhoblood,CbloodT,qt,qb,viscoblood,dviscoblood
     & ,qv,rhovessel,CvesselT,qu1,qu2,qu3,qu4,qu5,qu6)
c ***********************************************************************
      implicit none
c ***********************************************************************
      doubleprecision xmaxT,dxT,ymaxT,dyT,zmaxT,dzT
     & ,tmaxT,dtT,dtU,qh1,qh2,qh3,qh4,qh5,qh6,qh7
     & ,rhotiss,CtissT,rhoblood,CbloodT,qt,qb
     & ,viscoblood,dviscoblood,qu1,qu2,qu3,qu4,qu5,qu6
     & ,rhovessel,CvesselT,qv
c ***********************************************************************
      integer ImaxT,JmaxT,KmaxT,NmaxT
c ***********************************************************************
      print*,'===called SUBROUTINE CALCPARAMS'
c ***********************************************************************
c ***********************************************************************
c calculate some basic temperature run parameters:
      xmaxT=dxT*DBLE(ImaxT-1)
      ymaxT=dyT*DBLE(JmaxT-1)
      zmaxT=dzT*DBLE(KmaxT-1)
      tmaxT=dtT*DBLE(NmaxT-1)
c ***********************************************************************
      qh1=dtT/(dxT*dxT)
      qh2=dtT/(dyT*dyT)
      qh3=dtT/(dzT*dzT)
      qh4=dtT/(2.d0*dxT)
      qh5=dtT/(2.d0*dyT)
      qh6=dtT/(2.d0*dzT)
      qh7=dtT*CbloodT
c ***********************************************************************
      qt=rhotiss*CtissT
      qb=rhoblood*CbloodT
      qv=rhovessel*CvesselT
c ***********************************************************************
```

```
      dviscoblood=viscoblood/rhoblood
      qu1=dtU/(2.d0*dxT)
      qu2=dtU/(2.d0*dyT)
      qu3=dtU/(2.d0*dzT)
      qu4=dtU/(dxT*dxT)
      qu5=dtU/(dyT*dyT)
      qu6=dtU/(dzT*dzT)
c ***********************************************************************
      return
      end
c+++++++++++++++++++++++++++++++++++++++++++++++++++++++++++++++++++++++

c+++++++++++++++++++++++++++++++++++++++++++++++++++++++++++++++++++++++
      subroutine initializeT(ImaxT,JmaxT,KmaxT,Tn,Tnplus1,Tnminus1,Q
     & ,Ux,Uy,Uz,Uze,Ta,Q2d,ImaxQ,JmaxQ)
c ***********************************************************************
      implicit none
c ***********************************************************************
      integer i,j,k,ImaxT,JmaxT,KmaxT,ImaxQ,JmaxQ
c ***********************************************************************
      doubleprecision Q(ImaxT,JmaxT,KmaxT),Ta,Tn(ImaxT,JmaxT,KmaxT)
     & ,Tnplus1(ImaxT,JmaxT,KmaxT),Tnminus1(ImaxT,JmaxT,KmaxT)
     & ,Q2d(ImaxQ,JmaxQ),Ux(ImaxT,JmaxT,KmaxT),Uy(ImaxT,JmaxT,KmaxT)
     & ,Uz(ImaxT,JmaxT,KmaxT),Uze(ImaxT,JmaxT,KmaxT)
c ***********************************************************************
c initialize temperature field to Ta everywhere:
      print*,'...initializing temp. fields'
      do 15 k=1,KmaxT
        do 25 j=1,JmaxT
          do 35 i=1,ImaxT
            Tn(i,j,k)=Ta
            Tnplus1(i,j,k)=Ta
            Tnminus1(i,j,k)=Ta
            Q(i,j,k)=0.d0
            Ux(i,j,k)=0.d0
            Uy(i,j,k)=0.d0
            Uz(i,j,k)=Uze(i,j,k)
 35       continue
 25     continue
 15   continue
       do 45 j=1,JmaxQ
         do 55 i=1,ImaxQ
           Q2d(i,j)=0.d0
 55     continue
 45   continue
c ***********************************************************************
      return
      end
c+++++++++++++++++++++++++++++++++++++++++++++++++++++++++++++++++++++++

c+++++++++++++++++++++++++++++++++++++++++++++++++++++++++++++++++++++++
      subroutine initializeU(Imax,Jmax,Kmax,Uxn,Uyn,Uzn,Uxnplus1
     & ,Uynplus1,Uznplus1,Fx,Fy,Fz,pn,pnplus1)
c ***********************************************************************
```

```
      implicit none
c ******************************************************************
      integer i,j,k,Imax,Jmax,Kmax
c ******************************************************************
      doubleprecision Uxn(Imax,Jmax,Kmax),Uyn(Imax,Jmax,Kmax)
     & ,Uzn(Imax,Jmax,Kmax),Uxnplus1(Imax,Jmax,Kmax)
     & ,Uynplus1(Imax,Jmax,Kmax),Uznplus1(Imax,Jmax,Kmax)
     & ,Fx(Imax,Jmax,Kmax),Fy(Imax,Jmax,Kmax),Fz(Imax,Jmax,Kmax)
     & ,pn(Imax,Jmax,Kmax),pnplus1(Imax,Jmax,Kmax)
c ******************************************************************
c initialize flow field to 0 everywhere:
      print*,'...initializing flow fields'
      do 25 k=1,Kmax
        do 35 j=1,Jmax
          do 45 i=1,Imax
            Uxn(i,j,k)=0.d0
            Uyn(i,j,k)=0.d0
            Uzn(i,j,k)=0.d0
            Uxnplus1(i,j,k)=0.d0
            Uynplus1(i,j,k)=0.d0
            Uznplus1(i,j,k)=0.d0
            Fx(i,j,k)=0.d0
            Fy(i,j,k)=0.d0
            Fz(i,j,k)=0.d0
            pn(i,j,k)=0.d0
            pnplus1(i,j,k)=0.d0
 45       continue
 35     continue
 25   continue
c ******************************************************************
      return
      end
c+++++++++++++++++++++++++++++++++++++++++++++++++++++++++++++++++++

c+++++++++++++++++++++++++++++++++++++++++++++++++++++++++++++++++++
c     SUBROUTINE ICFILES
c ******************************************************************
      subroutine icfiles(ImaxT,JmaxT,KmaxT,Wb,Wblood,rblood,Uavg,Uze,h)
c ******************************************************************
      implicit none
c ******************************************************************
      doubleprecision Wb(ImaxT,JmaxT,KmaxT),Wblood,rblood
     & ,Uavg,Uze(ImaxT,JmaxT,KmaxT),h(ImaxT,JmaxT,KmaxT)
c ******************************************************************
      integer i,j,k,ImaxT,JmaxT,KmaxT
c ******************************************************************
c ******************************************************************
      print*,'>>>>>>>>> beginning subroutine icfiles'
      do 5 k=1,KmaxT
        do 15 j=1,JmaxT
          do 25 i=1,ImaxT
            Wb(i,j,k)=Wblood
          if(h(i,j,k).le.rblood)then
            Uze(i,j,k)=2*Uavg*(1-(h(i,j,k)/rblood)**2)
```

```
          else
            Uze(i,j,k)=0.d0
          end if
  25      continue
  15    continue
  5    continue
c ********************************************************************
      return
      end
c+++++++++++++++++++++++++++++++++++++++++++++++++++++++++++++++++++++

c+++++++++++++++++++++++++++++++++++++++++++++++++++++++++++++++++++++
      subroutine readQ(Q2d,ImaxQ,JmaxQ,Q2dfile)

      implicit none
      integer i,j,ImaxQ,JmaxQ
      doubleprecision Q2d(ImaxQ,JmaxQ)
      character*50 Q2dfile

      print*,'===called SUBROUTINE READQ'
      open(4,file=Q2dfile,form='formatted',status='unknown')
      do 50 j=1,JmaxQ
        do 55 i=1,ImaxQ
          read(4,*) Q2d(i,j)
 55     continue
 50   continue
      close(4)
      print*,'......closed ',Q2dfile
      return
      end
c+++++++++++++++++++++++++++++++++++++++++++++++++++++++++++++++++++++

c+++++++++++++++++++++++++++++++++++++++++++++++++++++++++++++++++++++
      subroutine heat2s1t(ImaxT,JmaxT,KmaxT,Q,Ta,Tb,dtT,Tn,Tnplus1
     & ,qh1,qh2,qh3,qh4,qh5,qh6,qh7,qt,qb,qv,Ktiss,Wb,Kblood,Kvessel
     & ,Ux,Uy,Uz,rblood,rvessel,h)

      implicit none
c ********************************************************************
      doubleprecision Q(ImaxT,JmaxT,kmaxT),Tn(ImaxT,JmaxT,KmaxT)
     & ,Tnplus1(ImaxT,JmaxT,KmaxT),h(ImaxT,JmaxT,KmaxT)
     & ,Ux(ImaxT,JmaxT,KmaxT),Uy(ImaxT,JmaxT,KmaxT)
     & ,Uz(ImaxT,JmaxT,KmaxT),Wb(ImaxT,JmaxT,KmaxT)
     & ,Ktiss,Kblood,Ta,Tb,z1,z2,z3,z4,z5,z6,z7
     & ,rblood,dtT,qh1,qh2,qh3,qh4,qh5,qh6,qh7,qt,qb,qv,Kvessel,rvessel
c ********************************************************************
      integer i,j,k,ImaxT,JmaxT,KmaxT
c ********************************************************************
c...x=0, i=1 and x=xmax, i=Imax, T=Ta
      do 120 k=1,KmaxT
        do 130 j=1,JmaxT
        Tnplus1(1,j,k)=Ta
          Tnplus1(ImaxT,j,k)=Ta
 130     continue
```

```
 120  continue
c ***********************************************************************
c...y=0,j=1 and y=ymax, j=Jmax row using T=Ta:
      do 140 k=1,KmaxT
        do 150 i=1,ImaxT
         Tnplus1(i,1,k)=Ta
         Tnplus1(i,JmaxT,k)=Ta
 150     continue
 140  continue
c ***********************************************************************
c...z=0,k=1 and z=zmax, k=Kmax row using T=Ta:
      do 160 j=1,JmaxT
        do 170 i=1,ImaxT
         Tnplus1(i,j,1)=Tn(i,j,2)
         Tnplus1(i,j,KmaxT)=Tn(i,j,KmaxT-1)
 170     continue
 160  continue
c ***********************************************************************
c inside cells:
      do 60 k=2,KmaxT-1
        do 62 j=2,JmaxT-1
          do 63 i=2,ImaxT-1
            if(h(i,j,k).lt.rblood)then
c in blood domain:
              z1=Tn(i+1,j,k)-2.d0*Tn(i,j,k)+Tn(i-1,j,k)
              z2=Tn(i,j+1,k)-2.d0*Tn(i,j,k)+Tn(i,j-1,k)
              z3=Tn(i,j,k+1)-2.d0*Tn(i,j,k)+Tn(i,j,k-1)
              z4=Tn(i+1,j,k)-Tn(i-1,j,k)
              z5=Tn(i,j+1,k)-Tn(i,j-1,k)
              z6=Tn(i,j,k+1)-Tn(i,j,k-1)
              Tnplus1(i,j,k)=Tn(i,j,k)+(Kblood/qb)*(qh1*z1+qh2*z2
     &                    +qh3*z3)-Ux(i,j,k)*qh4*z4-Uy(i,j,k)*qh5*z5
     &                    -Uz(i,j,k)*qh6*z6+dtT*Q(i,j,k)/qb
            else if(h(i,j,k).lt.rvessel)then
c in vessel domain
              z1=Tn(i+1,j,k)-2.d0*Tn(i,j,k)+Tn(i-1,j,k)
              z2=Tn(i,j+1,k)-2.d0*Tn(i,j,k)+Tn(i,j-1,k)
              z3=Tn(i,j,k+1)-2.d0*Tn(i,j,k)+Tn(i,j,k-1)
              z7=Tn(i,j,k)-Tb
              Tnplus1(i,j,k)=Tn(i,j,k)+(Kvessel/qv)*(qh1*z1+qh2*z2
     &            +qh3*z3)+dtT*Q(i,j,k)/qv
            else
c in phantom domain:
              z1=Tn(i+1,j,k)-2.d0*Tn(i,j,k)+Tn(i-1,j,k)
              z2=Tn(i,j+1,k)-2.d0*Tn(i,j,k)+Tn(i,j-1,k)
              z3=Tn(i,j,k+1)-2.d0*Tn(i,j,k)+Tn(i,j,k-1)
              z7=Tn(i,j,k)-Tb
              Tnplus1(i,j,k)=Tn(i,j,k)+(Ktiss/qt)*(qh1*z1+qh2*z2
     &            +qh3*z3)-(Wb(i,j,k)/qt)*qh7*z7+dtT*Q(i,j,k)/qt
            end if
 63       continue
 62     continue
 60    continue
      return
```

```
      end

c+++++++++++++++++++++++++++++++++++++++++++++++++++++++++++++++

c+++++++++++++++++++++++++++++++++++++++++++++++++++++++++++++++
      subroutine snapdumpT(n,t,ImaxT,JmaxT,KmaxT,Tn,Ta
     & ,decimspace,decimtime,dumpnumber,maxTemp,minTemp
     & ,maxvaliT,maxvaljT,maxvalkT,minvaliT,minvaljT,minvalkT
     & ,ifocus,jfocus,kfocus)
c ******************************************************************
      implicit none
c ******************************************************************
      doubleprecision Tn(ImaxT,JmaxT,KmaxT),Ta,maxTemp,minTemp,t
c ******************************************************************
      integer n,ImaxT,JmaxT,KmaxT,decimspace,decimtime,i,j,k
     & ,dumpnumber,maxvaliT,maxvaljT,maxvalkT,minvaliT,minvaljT
     & ,minvalkT,ifocus,jfocus,kfocus
c ******************************************************************
      character*37 Txydumpname,Txzdumpname,Tyzdumpname
c ******************************************************************
      call minmax3d(Tn,ImaxT,JmaxT,KmaxT,maxTemp,minTemp
     & ,maxvaliT,maxvaljT,maxvalkT,minvaliT,minvaljT,minvalkT)
c ******************************************************************
      print 114,minTemp-Ta,minvaliT,minvaljT,minvalkT
      print 115,maxTemp-Ta,maxvaliT,maxvaljT,maxvalkT
 114  format ('minTemp=',e14.7,' @ (',I4,' ',I4,' ',I4,')')
 115  format ('maxTemp=',e14.7,' @ (',I4,' ',I4,' ',I4,')')
c ******************************************************************
      dumpnumber=INT((n-1)/decimtime)+99
c ******************************************************************
      write(Txydumpname,118) '/hal01/scratch/jinlan1/Txy',
     &  dumpnumber,'.dat'
      write(Txzdumpname,118) '/hal01/scratch/jinlan1/Txz',
     &  dumpnumber,'.dat'
      write(Tyzdumpname,118) '/hal01/scratch/jinlan1/Tyz',
     &  dumpnumber,'.dat'
 118  format(a26,i3,a4)
c ******************************************************************
      print*,'Writing at t= ',t,'into ',Txydumpname
      open(4,file=Txydumpname,form='formatted',status='unknown')
        do 5 j=1,JmaxT
          do 6 i=1,ImaxT
            write(4,*)Tn(i,j,kfocus)-Ta
 6     continue
 5    continue
      close(4)
      print*,'......closed ',Txydumpname
c ******************************************************************
      print*,'Writing at t= ',t,'into ',Txzdumpname
      open(5,file=Txzdumpname,form='formatted',status='unknown')
        do 15 k=1,KmaxT
          do 16 i=1,ImaxT
            write(5,*)Tn(i,jfocus,k)-Ta
 16     continue
```

```
 15    continue
       close(5)
       print*,'......closed ',Txzdumpname
c ********************************************************************
       print*,'Writing at t= ',t,'into ',Tyzdumpname
       open(6,file=Tyzdumpname,form='formatted',status='unknown')
         do 25 k=1,KmaxT
           do 26 j=1,JmaxT
             write(6,*)Tn(ifocus,j,k)-Ta
 26      continue
 25     continue
       close(6)
       print*,'......closed ',Tyzdumpname
c ********************************************************************
       return
       end

c+++++++++++++++++++++++++++++++++++++++++++++++++++++++++++++++++++++

c+++++++++++++++++++++++++++++++++++++++++++++++++++++++++++++++++++++
       subroutine snapdumpU(n,t,ImaxT,JmaxT,KmaxT,ImaxU,JmaxU,KmaxU,IU0
      & ,JU0,decimspace,decimtime,dumpnumber,Ux,Uy,Uz,itc,jtc,ktc)
c ********************************************************************
       implicit none
c ********************************************************************
       doubleprecision t,Uz(ImaxT,JmaxT,KmaxT),Ux(ImaxT,JmaxT,KmaxT)
      & ,Uy(ImaxT,JmaxT,KmaxT)
c ********************************************************************
       integer n,ImaxT,JmaxT,KmaxT,decimspace,decimtime,i,j,k
      & ,dumpnumber,itc,jtc,ktc,ImaxU,JmaxU,KmaxU,IU0,JU0
c ********************************************************************
       character*37 Uzxydumpname,Uzxzdumpname,Uzyzdumpname,Uxxydumpname
      & ,Uxxzdumpname,Uxyzdumpname,Uyxydumpname,Uyxzdumpname
      & ,Uyyzdumpname
c ********************************************************************
       dumpnumber=INT((n-1)/decimtime)+99
c ********************************************************************
       write(Uzxydumpname,116) '/hal01/scratch/jinlan1/Uzxy',
      &  dumpnumber,'.dat'
       write(Uzxzdumpname,116) '/hal01/scratch/jinlan1/Uzxz',
      &  dumpnumber,'.dat'
       write(Uzyzdumpname,116) '/hal01/scratch/jinlan1/Uzyz',
      &  dumpnumber,'.dat'
       write(Uxxydumpname,116) '/hal01/scratch/jinlan1/Uxxy',
      &  dumpnumber,'.dat'
       write(Uxxzdumpname,116) '/hal01/scratch/jinlan1/Uxxz',
      &  dumpnumber,'.dat'
       write(Uxyzdumpname,116) '/hal01/scratch/jinlan1/Uxyz',
      &  dumpnumber,'.dat'
       write(Uyxydumpname,116) '/hal01/scratch/jinlan1/Uyxy',
      &  dumpnumber,'.dat'
       write(Uyxzdumpname,116) '/hal01/scratch/jinlan1/Uyxz',
      &  dumpnumber,'.dat'
       write(Uyyzdumpname,116) '/hal01/scratch/jinlan1/Uyyz',
```

```
     &  dumpnumber,'.dat'
 116  format(a27,i3,a4)
c ***********************************************************************
      open(7,file=Uzxydumpname,form='formatted',status='unknown')
      do 35 j=1,JmaxU
        do 36 i=1,ImaxU
          write(7,*)Uz(i+IU0-1,j+JU0-1,ktc)
 36     continue
 35   continue
      close(7)
c ***********************************************************************
      open(8,file=Uzxzdumpname,form='formatted',status='unknown')
      do 45 k=1,KmaxU
        do 46 i=1,ImaxU
          write(8,*)Uz(i+IU0-1,jtc,k)
 46     continue
 45   continue
      close(8)
c ***********************************************************************
      open(9,file=Uzyzdumpname,form='formatted',status='unknown')
      do 55 k=1,KmaxU
        do 56 j=1,JmaxU
          write(9,*)Uz(itc,j+JU0-1,k)
 56     continue
 55   continue
      close(9)
c ***********************************************************************
      open(10,file=Uxxydumpname,form='formatted',status='unknown')
      do 65 j=1,JmaxU
        do 66 i=1,ImaxU
          write(10,*)Ux(i+IU0-1,j+JU0-1,ktc)
 66     continue
 65   continue
      close(10)
c ***********************************************************************
      open(11,file=Uxxzdumpname,form='formatted',status='unknown')
      do 75 k=1,KmaxU
        do 76 i=1,ImaxU
          write(11,*)Ux(i+IU0-1,jtc,k)
 76     continue
 75   continue
      close(11)
c ***********************************************************************
      open(12,file=Uxyzdumpname,form='formatted',status='unknown')
      do 85 k=1,KmaxU
        do 86 j=1,JmaxU
          write(12,*)Ux(itc,j+JU0-1,k)
 86     continue
 85   continue
      close(12)
c ***********************************************************************
      open(13,file=Uyxydumpname,form='formatted',status='unknown')
      do 95 j=1,JmaxU
        do 96 i=1,ImaxU
```

```
          write(13,*)Uy(i+IU0-1,j+JU0-1,ktc)
 96     continue
 95   continue
      close(13)
c ********************************************************************
      open(14,file=Uyxzdumpname,form='formatted',status='unknown')
      do 105 k=1,KmaxU
        do 106 i=1,ImaxU
          write(14,*)Uy(i+IU0-1,jtc,k)
 106     continue
 105   continue
      close(14)
c ********************************************************************
      open(15,file=Uyyzdumpname,form='formatted',status='unknown')
      do 107 k=1,KmaxU
        do 108 j=1,JmaxU
          write(15,*)Uy(itc,j+JU0-1,k)
 108     continue
 107   continue
      close(15)
c ********************************************************************
      return
      end

c+++++++++++++++++++++++++++++++++++++++++++++++++++++++++++++++++++++

c+++++++++++++++++++++++++++++++++++++++++++++++++++++++++++++++++++++
      subroutine updateT(ImaxT,JmaxT,KmaxT,Tn,Tnplus1,Tnminus1)
c ********************************************************************
      implicit none
c ********************************************************************
      doubleprecision Tn(ImaxT,JmaxT,KmaxT)
     & ,Tnplus1(ImaxT,JmaxT,KmaxT),Tnminus1(ImaxT,JmaxT,KmaxT)
c ********************************************************************
      integer i,j,k,ImaxT,JmaxT,KmaxT
c ********************************************************************
c UPDATE ARRAYS IN TIME AND WRITE TEMP TO OUTPUT DATA FILE:
      do 10 k=1,KmaxT
        do 20 j=1,JmaxT
          do 30 i=1,ImaxT
            Tnminus1(i,j,k)=Tn(i,j,k)
            Tn(i,j,k)=Tnplus1(i,j,k)
 30       continue
 20     continue
 10   continue
c ********************************************************************
      return
      end

c+++++++++++++++++++++++++++++++++++++++++++++++++++++++++++++++++++++

c+++++++++++++++++++++++++++++++++++++++++++++++++++++++++++++++++++++
      subroutine minmax3d(pn,Imax,Jmax,Kmax,pmax,pmin
     & ,maxvali,maxvalj,maxvalk,minvali,minvalj,minvalk)
```

```
      doubleprecision  pn(Imax,Jmax,Kmax),pmin,pmax
      integer i,j,k,Imax,Jmax,Kmax,minvali,minvalj,minvalk
     & ,maxvali,maxvalj,maxvalk
      pmax=pn(1,1,1)
      pmin=pn(1,1,1)
c find minimum/maximum along slices through itarget,jtarget of an array
      do 10 i=1,Imax
        do 20 j=1,Jmax
          do 30 k=1,Kmax
            if(pn(i,j,k).gt.pmax)then
              pmax=pn(i,j,k)
              maxvali=i
              maxvalj=j
              maxvalk=k
            end if
            if(pn(i,j,k).lt.pmin)then
              pmin=pn(i,j,k)
              minvali=i
              minvalj=j
              minvalk=k
           end if
 30       continue
 20     continue
 10   continue
      return
      end
c+++++++++++++++++++++++++++++++++++++++++++++++++++++++++++++++

c+++++++++++++++++++++++++++++++++++++++++++++++++++++++++++++++
      subroutine calh(h,dx,dy,dz,x0,y0,z0,a,b,c,Imax,Jmax,Kmax)
      implicit none
      integer Imax,Jmax,Kmax,i,j,k
      doubleprecision h(Imax,Jmax,Kmax),x,y,z,x0,y0,z0,a,b,c
     & ,dx,dy,dz,xp,yp,zp,r
c ********************************************************************
      r=a*a+b*b+c*c
      do 10 k=1,Kmax
        z=(k-1)*dz
        do 20 j=1,Jmax
        y=(j-1)*dy
          do 30 i=1,Imax
          x=(i-1)*dx
          xp=((b*b+c*c)*x0+a*a*x+a*b*(y-y0)+a*c*(z-z0))/r
          yp=((a*a+c*c)*y0+b*b*y+a*b*(x-x0)+b*c*(z-z0))/r
          zp=((a*a+b*b)*z0+c*c*z+a*c*(x-x0)+b*c*(y-y0))/r
          h(i,j,k)=sqrt((xp-x)*(xp-x)+(yp-y)*(yp-y)+(zp-z)*(zp-z))
 30       continue
 20     continue
 10   continue
c ********************************************************************
      return
      end
c+++++++++++++++++++++++++++++++++++++++++++++++++++++++++++++++
```

```
c+++++++++++++++++++++++++++++++++++++++++++++++++++++++++++++++
      subroutine flow2s1t_3D(Imax,Jmax,Kmax,dx,dy,dz,dt,rho,w
     & ,epislon,Uxn,Uyn,Uzn,Uxnplus1,Uynplus1,Uznplus1,qu1,qu2,qu3
     & ,qu4,qu5,qu6,dvisco,Fx,Fy,Fz,pn,pnplus1,rblood)
c ***************************************************************
      implicit none
c ***************************************************************
      integer i,j,k,Imax,Jmax,Kmax,IUcenter,JUcenter
c ***************************************************************
      doubleprecision Uxn(Imax,Jmax,Kmax),Uyn(Imax,Jmax,Kmax)
     & ,Uzn(Imax,Jmax,Kmax),Uxnplus1(Imax,Jmax,Kmax)
     & ,Uynplus1(Imax,Jmax,Kmax),Uznplus1(Imax,Jmax,Kmax)
     & ,Fx(Imax,Jmax,Kmax),Fy(Imax,Jmax,Kmax),Fz(Imax,Jmax,Kmax)
     & ,Uxs(Imax,Jmax,Kmax),Uys(Imax,Jmax,Kmax),Uzs(Imax,Jmax,Kmax)
     & ,pnplus1(Imax,Jmax,Kmax),pn(Imax,Jmax,Kmax),dx,dy,dz,dt,rho,w
     & ,epislon,qu1,qu2,qu3,qu4,qu5,qu6,dvisco,zx1,zx2,zx3,zx4,zx5,zx6
     & ,zy1,zy2,zy3,zy4,zy5,zy6,zz1,zz2,zz3,zz4,zz5,zz6,rblood,r
c ***************************************************************
      IUcenter=int((Imax-1)/2+1)
      JUcenter=int((Jmax-1)/2+1)
c ***************************************************************
c set boundary conditions:
c at the wall, x=0,i=1 and x=xmax,i=Imax: Uxn=0,Uyn=0,Uzn=0
      do 5 k=1,Kmax
      do 6 j=1,Jmax
        Uxs(1,j,k)=dvisco*qu4*Uxn(2,j,k)+(dt/rho)*Fx(1,j,k)
        Uys(1,j,k)=dvisco*qu4*Uyn(2,j,k)+(dt/rho)*Fy(1,j,k)
        Uzs(1,j,k)=dvisco*qu4*Uzn(2,j,k)+(dt/rho)*Fz(1,j,k)
      Uxs(Imax,j,k)=dvisco*qu4*Uxn(Imax-1,j,k)+(dt/rho)*Fx(Imax,j,k)
        Uys(Imax,j,k)=dvisco*qu4*Uyn(Imax-1,j,k)+(dt/rho)*Fy(Imax,j,k)
        Uzs(Imax,j,k)=dvisco*qu4*Uzn(Imax-1,j,k)+(dt/rho)*Fz(Imax,j,k)
 6      continue
 5    continue
c at the wall, y=0,j=1 and y=ymax,j=Jmax: Uxn=0,Uyn=0,Uzn=0
      do 10 k=1,Kmax
      do 15 i=1,Imax
        Uxs(i,1,k)=dvisco*qu5*Uxn(i,2,k)+(dt/rho)*Fx(i,1,k)
        Uys(i,1,k)=dvisco*qu5*Uyn(i,2,k)+(dt/rho)*Fy(i,1,k)
        Uzs(i,1,k)=dvisco*qu5*Uzn(i,2,k)+(dt/rho)*Fz(i,1,k)
      Uxs(i,Jmax,k)=dvisco*qu5*Uxn(i,Jmax-1,k)+(dt/rho)*Fx(i,Jmax,k)
        Uys(i,Jmax,k)=dvisco*qu5*Uyn(i,Jmax-1,k)+(dt/rho)*Fy(i,Jmax,k)
        Uzs(i,Jmax,k)=dvisco*qu5*Uzn(i,Jmax-1,k)+(dt/rho)*Fz(i,Jmax,k)
 15     continue
 10   continue
c ***************************************************************
c at inlet and outlet, z=0,k=1 and z=zmax, k=Kmax: dU/dz=0
      do 20 j=2,Jmax-1
        do 25 i=2,Imax-1
        zx1=Uxn(i,j,1)*(Uxn(i+1,j,1)-Uxn(i-1,j,1))
          zx2=Uyn(i,j,1)*(Uxn(i,j+1,1)-Uxn(i,j-1,1))
          zx4=Uxn(i+1,j,1)+Uxn(i-1,j,1)-2.d0*Uxn(i,j,1)
          zx5=Uxn(i,j+1,1)+Uxn(i,j-1,1)-2.d0*Uxn(i,j,1)
        zx6=2.d0*(Uxn(i,j,2)-Uxn(i,j,1))
```

```
          Uxs(i,j,1)=Uxn(i,j,1)-qu1*zx1-qu2*zx2
     &         +dvisco*(qu4*zx4+qu5*zx5+qu6*zx6)+(dt/rho)*Fx(i,j,1)
c ***************************************************************
          zy1=Uxn(i,j,1)*(Uyn(i+1,j,1)-Uyn(i-1,j,1))
          zy2=Uyn(i,j,1)*(Uyn(i,j+1,1)-Uyn(i,j-1,1))
          zy4=Uyn(i+1,j,1)+Uyn(i-1,j,1)-2.d0*Uyn(i,j,1)
          zy5=Uyn(i,j+1,1)+Uyn(i,j-1,1)-2.d0*Uyn(i,j,1)
        zy6=2.d0*(Uyn(i,j,2)-Uyn(i,j,1))
          Uys(i,j,1)=Uyn(i,j,1)-qu1*zy1-qu2*zy2
     &         +dvisco*(qu4*zy4+qu5*zy5+qu6*zy6)+(dt/rho)*Fy(i,j,1)
c ***************************************************************
          zz1=Uxn(i,j,1)*(Uzn(i+1,j,1)-Uzn(i-1,j,1))
          zz2=Uyn(i,j,1)*(Uzn(i,j+1,1)-Uzn(i,j-1,1))
          zz4=Uzn(i+1,j,1)+Uzn(i-1,j,1)-2.d0*Uzn(i,j,1)
          zz5=Uzn(i,j+1,1)+Uzn(i,j-1,1)-2.d0*Uzn(i,j,1)
        zz6=2.d0*(Uzn(i,j,2)-Uzn(i,j,1))
          Uzs(i,j,1)=Uzn(i,j,1)-qu1*zz1-qu2*zz2
     &         +dvisco*(qu4*zz4+qu5*zz5+qu6*zz6)+(dt/rho)*Fz(i,j,1)
c ***************************************************************
        zx1=Uxn(i,j,Kmax)*(Uxn(i+1,j,kmax)-Uxn(i-1,j,kmax))
          zx2=Uyn(i,j,Kmax)*(Uxn(i,j+1,Kmax)-Uxn(i,j-1,Kmax))
          zx4=Uxn(i+1,j,Kmax)+Uxn(i-1,j,Kmax)-2.d0*Uxn(i,j,Kmax)
          zx5=Uxn(i,j+1,Kmax)+Uxn(i,j-1,Kmax)-2.d0*Uxn(i,j,Kmax)
        zx6=2.d0*(Uxn(i,j,Kmax-1)-Uxn(i,j,Kmax))
          Uxs(i,j,Kmax)=Uxn(i,j,Kmax)-qu1*zx1-qu2*zx2
     &        +dvisco*(qu4*zx4+qu5*zx5+qu6*zx6)+(dt/rho)*Fx(i,j,Kmax)
c ***************************************************************
          zy1=Uxn(i,j,Kmax)*(Uyn(i+1,j,Kmax)-Uyn(i-1,j,Kmax))
          zy2=Uyn(i,j,Kmax)*(Uyn(i,j+1,Kmax)-Uyn(i,j-1,Kmax))
          zy4=Uyn(i+1,j,Kmax)+Uyn(i-1,j,Kmax)-2.d0*Uyn(i,j,Kmax)
          zy5=Uyn(i,j+1,Kmax)+Uyn(i,j-1,Kmax)-2.d0*Uyn(i,j,Kmax)
        zy6=2.d0*(Uyn(i,j,Kmax-1)-Uyn(i,j,Kmax))
          Uys(i,j,Kmax)=Uyn(i,j,Kmax)-qu1*zy1-qu2*zy2
     &        +dvisco*(qu4*zy4+qu5*zy5+qu6*zy6)+(dt/rho)*Fy(i,j,Kmax)
c ***************************************************************
          zz1=Uxn(i,j,Kmax)*(Uzn(i+1,j,Kmax)-Uzn(i-1,j,Kmax))
          zz2=Uyn(i,j,Kmax)*(Uzn(i,j+1,Kmax)-Uzn(i,j-1,Kmax))
          zz4=Uzn(i+1,j,Kmax)+Uzn(i-1,j,Kmax)-2.d0*Uzn(i,j,Kmax)
          zz5=Uzn(i,j+1,Kmax)+Uzn(i,j-1,Kmax)-2.d0*Uzn(i,j,Kmax)
        zz6=2.d0*(Uzn(i,j,Kmax-1)-Uzn(i,j,Kmax))
          Uzs(i,j,Kmax)=Uzn(i,j,Kmax)-qu1*zz1-qu2*zz2
     &        +dvisco*(qu4*zz4+qu5*zz5+qu6*zz6)+(dt/rho)*Fz(i,j,Kmax)
 25     continue
 20   continue
c ***************************************************************
c inside cell:
      do 30 k=2,Kmax-1
        do 40 j=2,Jmax-1
        do 45 i=2,Imax-1
        zx1=Uxn(i,j,k)*(Uxn(i+1,j,k)-Uxn(i-1,j,k))
          zx2=Uyn(i,j,k)*(Uxn(i,j+1,k)-Uxn(i,j-1,k))
        zx3=Uzn(i,j,k)*(Uxn(i,j,k+1)-Uxn(i,j,k-1))
          zx4=Uxn(i+1,j,k)+Uxn(i-1,j,k)-2.d0*Uxn(i,j,k)
          zx5=Uxn(i,j+1,k)+Uxn(i,j-1,k)-2.d0*Uxn(i,j,k)
```

```
        zx6=Uxn(i,j,k+1)+Uxn(i,j,k-1)-2.d0*Uxn(i,j,k)
          Uxs(i,j,k)=Uxn(i,j,k)-qu1*zx1-qu2*zx2-qu3*zx3
     &         +dvisco*(qu4*zx4+qu5*zx5+qu6*zx6)+(dt/rho)*Fx(i,j,k)
c ***************************************************************
          zy1=Uxn(i,j,k)*(Uyn(i+1,j,k)-Uyn(i-1,j,k))
          zy2=Uyn(i,j,k)*(Uyn(i,j+1,k)-Uyn(i,j-1,k))
        zy3=Uzn(i,j,k)*(Uyn(i,j,k+1)-Uyn(i,j,k-1))
          zy4=Uyn(i+1,j,k)+Uyn(i-1,j,k)-2.d0*Uyn(i,j,k)
          zy5=Uyn(i,j+1,k)+Uyn(i,j-1,k)-2.d0*Uyn(i,j,k)
        zy6=Uyn(i,j,k+1)+Uyn(i,j,k-1)-2.d0*Uyn(i,j,k)
          Uys(i,j,k)=Uyn(i,j,k)-qu1*zy1-qu2*zy2-qu3*zy3
     &         +dvisco*(qu4*zy4+qu5*zy5+qu6*zy6)+(dt/rho)*Fy(i,j,k)
c ***************************************************************
          zz1=Uxn(i,j,k)*(Uzn(i+1,j,k)-Uzn(i-1,j,k))
          zz2=Uyn(i,j,k)*(Uzn(i,j+1,k)-Uzn(i,j-1,k))
        zz3=Uzn(i,j,k)*(Uzn(i,j,k+1)-Uzn(i,j,k-1))
          zz4=Uzn(i+1,j,k)+Uzn(i-1,j,k)-2.d0*Uzn(i,j,k)
          zz5=Uzn(i,j+1,k)+Uzn(i,j-1,k)-2.d0*Uzn(i,j,k)
        zz6=Uzn(i,j,k+1)+Uzn(i,j,k-1)-2.d0*Uzn(i,j,k)
          Uzs(i,j,k)=Uzn(i,j,k)-qu1*zz1-qu2*zz2-qu3*zz3
     &         +dvisco*(qu4*zz4+qu5*zz5+qu6*zz6)+(dt/rho)*Fz(i,j,k)
 45       continue
 40     continue
 30   continue
c ***************************************************************
      call calpress(pnplus1,pn,Uxs,Uys,Uzs,rho,dx,dy,dz,dt
     & ,w,epislon,Imax,Jmax,Kmax)
c ***************************************************************
c set boundary conditions for Uxnplus1, Uynplus1 & Uznplus1
      do 50 k=1,Kmax
        do 55 j=1,Jmax
        Uxnplus1(1,j,k)=0.d0
        Uynplus1(1,j,k)=0.d0
        Uznplus1(1,j,k)=0.d0
        Uxnplus1(Imax,j,k)=0.d0
        Uynplus1(Imax,j,k)=0.d0
        Uznplus1(Imax,j,k)=0.d0
 55     continue
 50   continue
c ***************************************************************
      do 60 k=1,Kmax
        do 65 i=1,Imax
        Uxnplus1(i,1,k)=0.d0
        Uynplus1(i,1,k)=0.d0
        Uznplus1(i,1,k)=0.d0
        Uxnplus1(i,Jmax,k)=0.d0
        Uynplus1(i,Jmax,k)=0.d0
        Uznplus1(i,Jmax,k)=0.d0
 65     continue
 60   continue
c ***************************************************************
      do 70 j=2,Jmax-1
        do 75 i=2,Imax-1
        Uxnplus1(i,j,1)=Uxs(i,j,1)-(qu1/rho)
```

```
     &                  *(pnplus1(i+1,j,1)-pnplus1(i-1,j,1))
        Uynplus1(i,j,1)=Uys(i,j,1)-(qu2/rho)
     &                  *(pnplus1(i,j+1,1)-pnplus1(i,j-1,1))
          Uznplus1(i,j,1)=Uzs(i,j,1)
        Uxnplus1(i,j,Kmax)=Uxs(i,j,Kmax)
        Uynplus1(i,j,Kmax)=Uys(i,j,Kmax)
          Uznplus1(i,j,Kmax)=Uzs(i,j,Kmax)
 75     continue
 70   continue
c ********************************************************************
      do 80 k=2,Kmax-1
        do 85 j=2,Jmax-1
          do 90 i=2,Imax-1
            r=sqrt((i-IUcenter)*dx*(i-IUcenter)*dx
     &        +(j-JUcenter)*dy*(j-JUcenter)*dy)
            if (r.ge.rblood)then
            Uxnplus1(i,j,k)=0.d0
            Uynplus1(i,j,k)=0.d0
            Uznplus1(i,j,k)=0.d0
            else
          Uxnplus1(i,j,k)=Uxs(i,j,k)-(qu1/rho)
     &                  *(pnplus1(i+1,j,k)-pnplus1(i-1,j,k))
            Uynplus1(i,j,k)=Uys(i,j,k)-(qu2/rho)
     &                  *(pnplus1(i,j+1,k)-pnplus1(i,j-1,k))
            Uznplus1(i,j,k)=Uzs(i,j,k)-(qu3/rho)
     &                  *(pnplus1(i,j,k+1)-pnplus1(i,j,k-1))
            end if
 90       continue
 85     continue
 80   continue
c ********************************************************************
      RETURN
      END

c+++++++++++++++++++++++++++++++++++++++++++++++++++++++++++++++++++++

c+++++++++++++++++++++++++++++++++++++++++++++++++++++++++++++++++++++
      subroutine calpress(pnplus1,pn,Uxs,Uys,Uzs,rho,dx,dy,dz,dt
     & ,w,epislon,Imax,Jmax,Kmax)
c ********************************************************************
c dx,dy,dz not equal
      implicit none
c ********************************************************************
      integer i,j,k,Imax,Jmax,Kmax
c ********************************************************************
      doubleprecision pn(Imax,Jmax,Kmax),pnplus1(Imax,Jmax,Kmax)
     & ,pm(Imax,Jmax,Kmax),pmplus1(Imax,Jmax,Kmax)
     & ,Uxs(Imax,Jmax,Kmax),Uys(Imax,Jmax,Kmax),Uzs(Imax,Jmax,Kmax)
     & ,b(Imax,Jmax,Kmax),rho,dx,dy,dz,dt,w,epislon,dpmax,qp1,qp2,qp3
     & ,qp4,qp5
c ********************************************************************
      qp1=dx*dx*dy*dy*dz*dz*rho/dt
      qp2=dy*dy*dz*dz
      qp3=dx*dx*dz*dz
```

```
      qp4=dx*dx*dy*dy
      qp5=2*(qp2+qp3+qp4)
c ***********************************************************************
c initialize b,pm,pmplus1
      do 2 k=1,Kmax
        do 3 j=1,Jmax
          do 4 i=1,Imax
          b(i,j,k)=0.d0
          pm(i,j,k)=pn(i,j,k)
          pmplus1(i,j,k)=0.d0
 4        continue
 3      continue
 2    continue
c ***********************************************************************
c calculate b(i,j,k):
      do 15 k=2,Kmax-1
        do 20 j=2,Jmax-1
          do 25 i=2,Imax-1
          b(i,j,k)=qp1*((Uxs(i+1,j,k)-Uxs(i-1,j,k))/(2*dx)
     &       +(Uys(i,j+1,k)-Uys(i,j-1,k))/(2*dy)
     &       +(Uzs(i,j,k+1)-Uzs(i,j,k-1))/(2*dz))
 25       continue
 20     continue
 15   continue
c ***********************************************************************
c set boundary conditions:
c at y=0, y=ymax: dp/dy=0; at z=0: dp/dz=0; at z=zmax: p=0
 200  do 30 j=1,Jmax
        do 35 i=1,Imax
          pmplus1(i,j,1)=pm(i,j,2)
          pmplus1(i,j,Kmax)=0.d0
 35     continue
 30   continue
      do 40 k=1,Kmax
        do 45 i=1,Imax
          pmplus1(i,1,k)=pm(i,2,k)
          pmplus1(i,Jmax,k)=pm(i,Jmax-1,k)
 45     continue
 40   continue
      do 46 k=1,Kmax
        do 48 j=1,Jmax
          pmplus1(1,j,k)=pm(2,j,k)
          pmplus1(Imax,j,k)=pm(Imax-1,j,k)
 48     continue
 46   continue
c ***********************************************************************
c inside the cell
      dpmax=0.d0
      do 50 k=2,Kmax-1
          do 60 j=2,Jmax-1
            do 65 i=2,Imax-1
            pmplus1(i,j,k)=(1-w)*pm(i,j,k)+(w/qp5)*(qp2*(pm(i+1,j,k)
     &          +pmplus1(i-1,j,k))+qp3*(pm(i,j+1,k)+pmplus1(i,j-1,k))
     &          +qp4*(pm(i,j,k+1)+pmplus1(i,j,k-1))-b(i,j,k))
```

```
            dpmax=Max(dpmax,ABS(pmplus1(i,j,k)-pm(i,j,k)))
 65       continue
 60     continue
 50   continue
      if(dpmax.gt.epislon)then
          do 70 k=1,Kmax
            do 80 j=1,Jmax
              do 85 i=1,Imax
                pm(i,j,k)=pmplus1(i,j,k)
 85      continue
 80     continue
 70     continue
        go to 200
      else
          do 90 k=1,Kmax
            do 100 j=1,Jmax
              do 105 i=1,Imax
                pnplus1(i,j,k)=pmplus1(i,j,k)
 105        continue
 100      continue
 90     continue
      end if

      RETURN
      END
c+++++++++++++++++++++++++++++++++++++++++++++++++++++++++++++++

c+++++++++++++++++++++++++++++++++++++++++++++++++++++++++++++++
      subroutine updateU(Imax,Jmax,Kmax,Uxn,Uyn,Uzn,Uxnplus1,Uynplus1
     & ,Uznplus1,pn,pnplus1)
c ****************************************************************
      implicit none
c ****************************************************************
      integer i,j,k,Imax,Jmax,Kmax
c ****************************************************************
      doubleprecision Uxn(Imax,Jmax,Kmax),Uyn(Imax,Jmax,Kmax)
     & ,Uzn(Imax,Jmax,Kmax),Uxnplus1(Imax,Jmax,Kmax)
     & ,Uynplus1(Imax,Jmax,Kmax),Uznplus1(Imax,Jmax,Kmax)
     & ,pn(Imax,Jmax,Kmax),pnplus1(Imax,Jmax,Kmax)
c ****************************************************************
c UPDATE ARRAYS IN TIME AND WRITE TEMP TO OUTPUT DATA FILE:
      do 10 k=1,Kmax
        do 20 j=1,Jmax
          do 30 i=1,Imax
            Uxn(i,j,k)=Uxnplus1(i,j,k)
            Uyn(i,j,k)=Uynplus1(i,j,k)
            Uzn(i,j,k)=Uznplus1(i,j,k)
            pn(i,j,k)=pnplus1(i,j,k)
 30       continue
 20     continue
 10   continue
c ****************************************************************
      return
      end
```

```
c+++++++++++++++++++++++++++++++++++++++++++++++++++++++++++++++

c+++++++++++++++++++++++++++++++++++++++++++++++++++++++++++++++
      subroutine calQ3d(Q,ImaxT,JmaxT,KmaxT,dxT,dyT,dzT
     & ,Q2d,ImaxQ,JmaxQ,drQ,dzQ,aQ,bQ,cQ,zQf,ifocusT,jfocusT,kfocusT)
c **********************************************************************
      implicit none
      integer ImaxT,JmaxT,KmaxT,ImaxQ,JmaxQ,ifocusT,jfocusT,kfocusT
     & ,i,j,k,iQ,jQ
      doubleprecision Q(ImaxT,JmaxT,KmaxT),hQ(ImaxT,JmaxT,KmaxT)
     & ,Q2d(ImaxQ,JmaxQ),dxT,dyT,dzT,drQ,dzQ,aQ,bQ,cQ,x,y,z,xf,yf,zf
     & ,r,zQ,zQf
c **********************************************************************
c  calculate the coordinate of the focus
      xf=(ifocusT-1)*dxT
      yf=(jfocusT-1)*dyT
      zf=(kfocusT-1)*dzT
c **********************************************************************
c  calculate the distance from (i,j,k) to acoustic axis
      call calh(hQ,dxT,dyT,dzT,xf,yf,zf,aQ,bQ,cQ,ImaxT,JmaxT,KmaxT)
c **********************************************************************
c convert the heat source Q from 2D to 3D
      r=sqrt(aQ*aQ+bQ*bQ+cQ*cQ)
      do 10 k=1,KmaxT
        z=(k-1)*dzT
         do 20 j=1,JmaxT
         y=(j-1)*dyT
            do 30 i=1,ImaxT
            x=(i-1)*dxT
            zQ=(aQ*(x-xf)+bQ*(y-yf)+cQ*(z-zf))/r
            iQ=int((zQf+zQ)/dzQ)+1
              jQ=int(hQ(i,j,k)/drQ)+1
               if(iQ.gt.0.and.iQ.le.ImaxQ.and.jQ.le.JmaxQ)then
                 Q(i,j,k)=Q2d(iQ,jQ)
               else
                 Q(i,j,k)=0.d0
               end if
 30       continue
 20     continue
 10   continue
c **********************************************************************
      return
      end
c+++++++++++++++++++++++++++++++++++++++++++++++++++++++++++++++

c+++++++++++++++++++++++++++++++++++++++++++++++++++++++++++++++
```

Bibliography

[1] R. W. Wood, and A. L. Loomis. The physical and biological effects of high frequency sound waves of great intensity. *The London, Edinburgh, and Dublin Philosophical Magazine and Journal of Science*, 4: 417-436, 1927.

[2] F. O. Schmitt, C. H. Johnson, and A. R. Olson. Oxidations promoted by ultrasonic radiation. *Journal of the American Chemical Society*, 51: 370-375, 1929.

[3] C. H. Johnson. The lethal effects of ultrasonic radiation. *The Journal of Physiology*, 67: 356-359, 1929.

[4] E. N. Harvey. Biological aspects of ultrasonic waves, a general survey. *The Biological Bulletin*, 59: 306-325, 1930.

[5] J. G. Lynn, R. L. Zwemer, A. J. Chick, and A. E. Miller. A new method for the generation and use of focused ultrasound in experimental biology. *The Journal of General Physiology*, 26: 179-193, 1942.

[6] J. G. Lynn and T. J. Putnam. Histology of cerebral lesions produced by focused ultrasound. *The American Journal of Pathology*, 20: 637-643, 1944.

[7] W. J. Fry, W. H. Mosberg, Jr., J. W. Barnard, and F. J. Fry. Production of focal destructive lesions in the central nervous system with ultrasound. *Journal of Neurosurgery*, 11: 471-478, 1954.

[8] W. J. Fry, J. W. Barnard, F. J. Fry, R. F. Krumins, and J. F. Brennan. Ultrasonic lesions in the mammalian central nervous system. *Science*, 122: 517-518, 1955.

[9] W. J. Fry. Intense ultrasound in investigations of the central nervous system. In: C. A. Tobias, and J. H. Lawrence, editors, *Advances in biological and medical physics*, 281-348, New York: Academic Press, 1958.

[10] T. F. Hueter, H. T. Ballantine Jr., and W. C. Cotter. Production of lesions in the central nervous system with focused ultrasound: A study of dosage factors. *The Journal of the Acoustical Society of America*, 28: 92-201, 1956.

[11] P. P. Lele. A simple method for the production of trackless focal lesions with focused ultrasound: Physical factors. *The Journal of Physiology*, 160: 494-512, 1962.

[12] L. Basauri, and P. P. Lele. A simple method for the production of trackless focal lesions with focused ultrasound. *The Journal of Physiology*, 160: 513-534, 1962.

[13] P. N. T. Wells. Biological effects. In: *Biomedical Ultrasonics*, Chapter 9, New York: Academic Press, 1977.

[14] J. Driller, and F. L. Lizzi. Therapeutic applications of ultrasound: A review. *IEEE Engineering in Medicine and Biology Magazine*, 6: 33-40, 1987.

[15] G. ter Haar. Biological effects of ultrasound in clinical applications. In: K. S. Suslick, editor, *Ultrasound: Its Chemical, Physical, and Biological Effects*, Chapter 8, New York: VCH Publishers, 1988.

[16] W. L. Nyborg. Biological effects of ultrasound: development of safety guidelines. Part II: General Review. *Ultrasound in Medicine and Biology*, 27(3), 301-333, 2001.

[17] M. H. Repacholi, M. Grandolfo, and A. Rindi. *Ultrasound: Medical Applications, Biological Effects, and Hazard Potential*, New York: Plenum Press, 1985.

[18] G. ter Haar. Ultrasound focal beam surgery. *Ultrasound in Medicine and Biology*, 21(9): 1089-1100, 1995.

[19] R. Warwick, and J. B. Pond. Trackless lesions in nervous tissues produced by high intensity ultrasound (high frequency mechanical waves). *Journal of Anatomy*, 102: 387-405, 1968.

[20] F. J. Fry, S. A. Goss, and J. T. Patrick. Transkull focal lesions in cat brain produced by ultrasound. *Journal of Neurosurgery*, 54(5): 659-663, 1981.

[21] F. L. Lizzi, D. J. Coleman, J. Driller, L. A. Franzen, and F. A. Jacobiec. Experimentally, ultrasonically induced lesions in the retina, choroids and sclera. *Investigative Ophthalmology*, 17: 350-360, 1978.

[22] F. L. Lizzi, D. J. Coleman, J. Driller, L. A. Franzen, and M. Leopold. Effects of pulsed ultrasound on ocular tissue. *Ultrasound in Medicine and Biology*, 7: 245-252, 1981.

[23] F. L. Lizzi, D. J. Coleman, J. Driller, M. Ostromogilsky, S. Chang, and P. Greenall. Ultrasonic hyperthermia for ophthalmic surgery. *IEEE Transactions on Sonics and Ultrasonics*, SU-31: 473-480, 1984.

[24] D. J. Coleman, F. L. Lizzi, J. Driller, A. L. Rosado, S. Chang, T. Iwamoto, and D. Rosenthal. Therapeutic ultrasound in the treatment of glaucoma – I. Experimental model. *Ophthalmology*, 92: 339-346, 1985.

[25] D. J. Coleman, F. L. Lizzi, J. Driller, A. L. Rosado, S. E. P. Burgess, J. H. Torpey, M. E. Smith, R. H. Silverman, M. E. Yablonski, S. Chang, and M. J. Rondeau. Therapeutic ultrasound in the treatment of glaucoma – II. Clinical applications. *Ophthalmology*, 92: 347-353, 1985.

[26] D. J. Coleman, F. L. Lizzi, J. H. Torpey, S. E. P. Burgess, J. Driller, A. L. Rosado, and H. T. Nguyen. Treatment of experimental lens capsular tears with intense focused ultrasound. *British Journal of Ophthalmology*, 69: 645-649, 1985.

[27] J. J. Angell. Clinical aspects of the surgical treatment of Menière's disease with ultrasound. *Ultrasonics*, 5: 102-104, 1967.

[28] H. Sorensen, and M. S. Andersen. Long term results of ultrasonic irradiation in Menière's disease. *Clinical Otolaryngology and Allied Sciences*, 4: 125-129, 1979.

[29] K. Hynynen, W. R. Freund, H. E. Cline, A. H. Chung, R. D. Watkins, J. P. Vetro, and F. A. Jolesz. A clinical noninvasive MRI monitored ultrasound surgery method. *RadioGraphics*, 16(1): 185-195, 1996.

[30] K. Hynynen, O. Pomeroy, D. N. Smith, P. E. Huber, N. J. McDannold, J. Kettenbach, J. Baum, S. Singer, and F. A. Jolesz. MR imaging-guided focused ultrasound surgery of fibroadenomas in the breast: a feasibility study. *Radiology*, 219(1): 176-185, 2001.

[31] G. Vallancien, M. Harouni, B. Veillon, A. Mombet, D. Prapotnich, J. M. Bisset, and J. Bougaran. Focused extracorporeal pyrotherapy: Feasibility study in man. *Journal of Endourology*, 6: 173-180, 1992.

[32] G. ter Haar, I. H. Rivens, E. Moskovic, R. Huddart, and A. Visioli. Phase 1 clinical trial of the use of focused ultrasound surgery for the treatment of soft tissue tumors. In: T. P. Ryan, editor, *Surgical Applications of Energy, Proceedings of the International Society for Optical Engineering*, 3249: 246-256, 1998.

[33] R. Bihrle, R. S. Foster, N. T. Sanghvi, J. P. Donohue, and P. J. Hood. High intensity focused ultrasound for the treatment of benign prostatic hyperplasia: early united states clinical experiences. *The Journal of Urology*, 151: 1271-1275, 1994.

[34] S. Maderbbacher, M. Pedevilla, L. Vingers, M. Susani, and M. Marberger. Effect of high intensity focused ultrasound on human prostate cancer *in vivo*. *Cancer Research*, 55: 3346-3351, 1995.

[35] A. Gelet, J. Y. Chapelon, R. Bouvier, R. Souchon, C. Pangaud, A. F. Abdelrahim, D. Cathignol, and J. M. Dubernard. Treatment of prostate cancer with transrectal focused ultrasound: early clinical experience. *European Urology*, 29: 174-183, 1996.

[36] J. Y. Chapelon, A. Gelet, R. Souchon, C. Pangaud, and E. Blanc. Therapy using ultrasound: application to localized prostate cancer. *J. Echogr. Med. Ultrason*. 19: 260-264, 1998.

[37] G. Vallancien, M. Harouni, B. Guillonneau, B. Veillon, and J. Bougaran. Ablation of superficial bladder tumors with focused extracorporeal pyrotherapy. *Urology*, 47(2): 204-207, 1996.

[38] C. Delon-Martin, C. Vogt, E. Chignier, C. Guers, J. Y. Chapelon, and D. Cathingnol. Venous thrombosis generation by means of High-Intensity Focused Ultrasound. *Ultrasound in Medicine and Biology*, 21(1): 113-119, 1995.

[39] K. Hynynen, A. H. Chung, V. Colucci, and F. A. Jolesz. Potential adverse effects of HIFU exposure on blood vessels *in vivo*. *Ultrasound in Medicine and Biology*, 22(2): 193-201, 1996.

[40] K. Hynynen, V. Colucci, A. H. Chung, and F. A. Jolesz. Noninvasive arterial occlusion using MRI-guided focused ultrasound. *Ultrasound in Medicine and Biology*, 22(8): 1071-1077, 1996.

[41] G. ter Haar, I. Rivens, I. Rowland, M. Denbow, N. Fisk, and M. Leach. Occlusion of blood flow by high-intensity focused ultrasound. *Proc. Acoust. Soc. Am.* 2: 1063-1064, 1998.

[42] I. Rivens, I. Rowland, M. Denbow, N. Fisk, M. Leach, and G. ter Haar. Focused ultrasound surgery induced vascular occlusion in fetal medicine. In: T. P. Ryan, editor, *Surgical Applications of Energy, Proceedings of the International Society for Optical Engineering*, 3249: 260-266, 1998.

[43] S. Vaezy, R. Martin, P. Mourad, and L. Crum. Review Hemostasis using high intensity focused ultrasound. *European Journal of Ultrasound*, 9: 79-87, 1999.

[44] S. Vaezy, R. Martin, and P. Kaczkowski. Use of high intensity focused ultrasound to control bleeding. *Journal of Vascular Surgery*, 29(3): 533-542, 1999.

[45] N. T. Sanghvi, K. Hynynen, and F. L. Lizzi. New developments in therapeutic ultrasound. *IEEE Engineering in Medicine and Biology*, 15(6): 83-92, 1996.

[46] G. ter Haar, D. Sinnett, and I. Rivens. High intensity focused ultrasound - a surgical technique for the treatment of discrete liver tumors. *Physics in Medicine & Biolology*, 34(11): 1743-1750, 1989.

[47] R. W. Martin, S. Vaezy, P. Kaczkowski, G. Keilman, S. Carter, M. Caps, K. Beach, M. Plett, and L. Crum. Hemostasis of punctured vessels using doppler-guided high-intensity ultrasound. *Ultrasound in Medicine and Biology*, 25(6), 985-990, 1999.

[48] S. Vaezy, X. Shi, R. W. Martin, E. Chi, P. I. Nelson, M. R. Bailey, and L. A. Crum. Real-time visualization of high-intensity focused ultrasound treatment using ultrasound imaging. *Ultrasound in Medicine and Biology,* 27(1), 33-42, 2001.

[49] K. Hynynen, A. Darkazanli, E. Unger, and J. F. Schenck. MRI-guided noninvasive ultrasound surgery. *Medical Physics*, 20: 107-115, 1993.

[50] I. J. Rowland, I. Rivens, L. Chen, C. H. Lebozer, D. J. Collins, G. ter Haar, and M. O. Leach. MRI study of hepatic tumors following high intensity focused ultrasound surgery. *The British Journal of Radiology*, 70: 144-153, 1997.

[51] K. J. Parker. The thermal pulse decay technique for measuring ultrasonic absorption coefficients. *The Journal of the Acoustical Society of America*, 74(5): 1356-1361, 1983.

[52] R. L. Clarke, and G. ter Haar. Temperature rise recorded during lesion formation by high intensity focused ultrasound. *Ultrasound in Medicine and Biology,* 23(2): 299-306, 1997.

[53] K. Hynynen, D. DeYoung, M. Hundrat, and E. Moros. The effect of blood perfusion rate on the temperature distributions induced by multiple, scanned and focused ultrasonic beams in dogs' kidneys *in vivo*. *International Journal of Hyperthermia*, 5: 485-497, 1989.

[54] J. B. Pond. The role of heat in the production of ultrasonic focal lesions. *The Journal of the Acoustical Society of America*, 47: 1607-1611, 1970.

[55] F. J. Fry, G. Kossoff, R. C. Eggleton, and F. Dunn. Threshold ultrasound dosages for structural changes in the mammalian brain. *The Journal of the Acoustical Society of America,* 48: 1413-1417, 1970.

[56] F. Dunn, and F. Fry. Ultrasonic threshold dosages for mammalian central nervous system. *IEEE Transactions on Biomedical Engineering*, BME-18(4): 253-356, 1971.

[57] F. Dunn, J. Lohnes, and F. Fry. Frequency dependence of threshold ultrasonic dosages for irreversible structural changes in mammalian brain. *The Journal of the Acoustical Society of America,* 58: 512-514, 1975.

[58] L. A. Frizzell, C. A. Linke, E. L. Carstensen, and C. W. Fridd. Thresholds for focal ultrasonic lesions in rabbit kidney, liver, and testicle. *IEEE Transactions on Biomedical Engineering*, BME-24: 393-396, 1977.

[59] L. A. Frizzell. Threshold dosages for damage to mammalian liver by high intensity focused ultrasound. *IEEE Transactions on Ultrasonics, Ferroelectrics, and Frequency Control*, 35: 578-581, 1988.

[60] T. Robinson, and P. Lele. An analysis of lesion development in the brain and in plastics by high-intensity focused ultrasound at low-megahertz frequencies. *The Journal of the Acoustical Society of America*, 51: 1333-1351, 1969.

[61] C. Damianou, and K. Hynynen. The effect of various physical parameters on the size and shape of necrosed tissue volume during ultrasound surgery. *The Journal of the Acoustical Society of America,* 95(3): 1641-1649, 1994.

[62] A. Meshorer, S. Prionas, L. Fajardo, J. Meyer, G. Hahn, and A. Martinez. The effects of hyperthermia on normal mesenchymal tissues. *Archives of Pathology and Laboratory Medicine,* 107: 328-334, 1983.

[63] J. Horst. A generalized concept for cell killing by heat. *Radiation Research,* 106: 56-72, 1986.

[64] B. Lyons, W. Obana, J. Borcich, R. Kleinman, D. Singh, and R. Britt. Chronic histological effects of ultrasonic hyperthermia on normal feline brain tissue. *Radiation Research*, 106: 234-251, 1986.

[65] M. Borrelli, L. Thompson, C. Cain, and W. Dewey. Time temperature analysis of cell killing of BHK cells heated at temperatures in the range of 43.5°C and 57°C. *International Journal of Radiation Oncology, Biology and Physics*, 19: 389-399, 1990.

[66] W. Jansen, and J. Haverman. Histological changes in the skin and subcutaneous tissues of mouse legs after treatment with hyperthermia. *Pathology, Research and Practice*, 186: 247-253, 1990.

[67] T. G. Wang, and C. P. Lee. Radiation pressure and acoustic levitation. In: M. F. Hamilton and D. T. Blackstock, editors, *Nonlinear Acoustics*, Chapter 6, Academic Press, 1997.

[68] G. ter Haar. Interaction mechanisms: non-thermal, non-cavitational effects. In: M. H. Repacholi, M. Grandolfo, and A. Rindi, editors, *Ultrasound: Medical Applications, biological effects, and Hazard Potential*, New York: Plenum Press, 105-116, 1985.

[69] M. Dyson, J. B. Pond, B. Woodward, and J. Broadbent. The production of blood cell stasis and endothelial damage in the blood vessels of chick embryos treated with ultrasound in a stationary wave field. *Ultrasound in Medicine and Biology*, 1: 133, 1974.

[70] G. ter Haar, M. Dyson, and S. P. Smith. Ultrastructural changes in the mouse uterus brought about by ultrasonic irradiation at therapeutic intensities in standing wave fields. *Ultrasound in Medicine and Biology*, 5:167, 1979.

[71] E. A. Neppiras. Acoustic cavitation: an introduction. *Ultrasonics*, 22: 25-28, 1984.

[72] R. E. Apfel. Acoustic cavitation inception. *Ultrasonics*, 22: 167-173, 1984.

[73] E. A. Neppiras. Acoustic cavitation. *Physical Letters*, 61(3): 160-251, 1980.

[74] T. G. Leighton. *The Acoustic Bubble*, Academic press, San Diego, California, 1994.

[75] A. I. Eller. Growth of bubbles by rectified diffusion. *The Journal of the Acoustical Society of America*, 46: 1246-1250, 1969.

[76] L. A. Crum. Rectified diffusion. *Ultrasonics*, 22: 215-223, 1984.

[77] H. G. Flynn. Generation of transient cavities in liquids by micro-second pulses of ultrasound. *The Journal of the Acoustical Society of America*, 72: 1926-1932, 1982.

[78] R. E. Apfel. Acoustic cavitation: A possible consequence of biomedical use of ultrasound. *British Journal of Cancer*, 45(Suppl. V): 140-146, 1982.

[79] P. D. Edmonds, and K. M. Sancier. Evidence for free radical production by ultrasonic cavitation in biological media. *Ultrasound in Medicine and Biology*, 9: 635-639, 1983.

[80] K. S. Suslick. Homogeneous sonochemistry. In: K. S. Suslick, editor, *Ultrasound: Its Chemical, Physical, and Biological Effects*, New York: VCH Publishers, Chapter 4, 1988.

[81] A. B. Kane. Mechanisms of cell and tissue injury. In: A. E. Sirica, editor, *Cellular and Molecular Pathogenesis*, Philadelphia: Lippincott-Raven, 1996.

[82] W. L. Nyborg. Acoustic streaming. In: W. P. Mason, editor, *Physical Acoustics*, Vol 2, Part B, New York: Academic Press, 265-285, 1965.

[83] D. L. Miller. A review of the ultrasonic bioeffects of microsonation, gas-body activation, and related cavitation-like phenomena. *Ultrasound in Medicine and Biology,* 13(8):443-470, 1987.

[84] W. J. Fry, V. J. Wulff, D. Tucker and F. J. Fry. Physical factors involved in ultrasonically-induced changes in the mammalian brain. *The Journal of the Acoustical Society of America,* 22(6): 867-876, 1950.

[85] J. F. Lehmann, and J. F. Herrich. Biological reactions to cavitation, a consideration for ultrasonic therapy. *Archives of Physical Medicine and Rehabilitation*, 34: 86-98, 1953.

[86] F. J. Fry, N. T. Sanghvi, R. S. Foster, R. Bihrle, and C. Hennige. Ultrasound and Microbubbles: Their generation, detection and potential utilization in tissue and organ therapy – experimental. *Ultrasound in Medicine and Biology,* 21(9): 1227-1237, 1995.

[87] P. P. Lele. Thresholds and mechanisms of ultrasonic damage to organized animal tissues. In: D. G. Hazzard, and M. L. Litz, editors, *Symposium on Biological Effects and Characterizations of Ultrasound Sources*, DHEW Publ. FDA 78-8048, Washington DC:DHEW, 224-239, 1977.

[88] P. P. Lele. Effects of ultrasound on 'solid' mammalian tissues and tumors *in vivo*. In M. H. Repacholi, M. Grandolfo, and A. Rindi, editors, *Ultrasound: Medical Applications, Biological Effects, and Hazard Potential*, Plenum Press, New York, 275-306, 1987.

[89] K. Hynynen. The threshold for thermally significant cavitation in dog's thigh muscle *in vivo*. *Ultrasound in Medicine and Biology*, 17(2), 157-169, 1991.

[90] P. P. Lele and A. D. Pierce. The thermal hypothesis of the mechanism of ultrasonic focal destruction in organised tissues. *Interaction of ultrasound and biological tissues*, Anonymous FDA 73-8008 BRH/DBE, Bureau of Radiological Health, Washington, DC, 121-128, 1973.

[91] L. Chen, I. Rivens, G. ter Haar, S. Riddler, C. R. Hill, and J. P. M. Bensted. Histological changes in rat liver tumors treated with high-intensity focused ultrasound. *Ultrasound in Medicine and Biology,* 19: 67-74, 1993.

[92] J. Y. Chapelon, F. Dupenloup, H. Cohen, and P. Lenz. Reduction of cavitation using pseudo-random signals. *IEEE Transactions on Ultrasonics, Ferroelectrics, and Frequency Control*, 43(4): 623-625, 1996.

[93] R. G. Holt, and R. A. Roy. Measurements of bubble-enhanced heating from focused, MHz-frequency ultrasound in a tissue-mimicking material. *Ultrasound in Medicine and Biology*, 27(10): 1399-1412, 2001.

[94] G. ter Haar. Acoustic surgery. *Physics Today*, 54(12): 29-34, 2001.

[95] J. Patterson, and R. Strang. The role of blood flow in hyperthermia. *International Journal of Radiation Oncology, Biology and Physics*, 5: 235-241, 1979.

[96] K. Hynynen, D. DeYoung, M. Hundrat, and E. Moros. The effect of blood perfusion rate on the temperature distributions induced by multiple, scanned and focused ultrasonic beams in dogs' kidneys *in vivo*. *International Journal of Hyperthermia*, 5: 485-497, 1989.

[97] L. Chen, G. ter Haar, C. R. Hill, M. Dworkin, P. Carnochan, H. Young, and J. P. M. Bensted. Effect of blood perfusion on the ablation of liver parenchyma with High-intensity focused ultrasound. *Physics in Medicine and Biology*, 38: 1661-1673, 1993.

[98] R. B. Roemer. Optimal power deposition in hyperthermia. I. The treatment goal: The ideal temperature distribution: The role of large blood vessels. *International Journal of Hyperthermia*, 7: 317-341, 1991.

[99] J. Crezee, and J. J. W.Lagendijk. Temperature uniformity during hyperthermia: the impact of large vessels. *Physics in Medicine and Biology*, 37: 1321-1337, 1992.

[100] L. N. Dorr, and K. Hynynen. The effect of tissue heterogeneities and large blood vessels on the thermal exposure induced by short high power ultrasound pulses. *International Journal of Hyperthermia*, 8: 45-59, 1992.

[101] M. C. Kolios, M. D. Sherar and J. W. Hunt. Blood flow cooling and ultrasonic lesion formation. *Medical Physics*, 23: 1287-1298, 1996.

[102] W. L. Lin, R. B. Roemer, and K. Hynynen. Theoretical and experimental evaluation of a temperature controller for scanned focussed ultrasound hyperthermia. *Medical Physics*, 17: 615-625, 1990.

[103] B. E. Billard, K. Hynynen, and R. B. Roemer. Effects of physical parameters on high temperature ultrasound hyperthermia. *Ultrasound in Medicine and Biology*, 16: 409-420, 1990.

[104] J. W. Hunt, R. Lalonde, H. Ginsberg, S. Urchuk, and A. Worthington. Rapid heating: critical theoretical assessment of thermal gradients found in hyperthermia treatments. *International Journal of Hyperthermia,* 7: 703-718, 1991.

[105] C. J. Diederich, and K. Hynynen. Ultrasound technology for hyperthermia. *Ultrasound in Medicine and Biology,* 25(6): 871-887, 1999.

[106] R. Yang, C. R. Reilly, F. J. Rescorla, P. R. Faught, N. T. Sanghvi, F. J. Fry, T. D. Franklin, Jr., L. Lumeng, and J. L. Grosfeld. High intensity focused ultrasound in the treatment of experimental liver cancer. *Archives of Surgery*, 126: 1002-1010, 1991.

[107] G. ter Haar, and D. Robertson. Tissue destruction with focused ultrasound *in vivo*. *European Urology,* 23 Supplement 1: 8-11, 1993.

[108] S. Vaezy, R. Martin, U. Schmiedl, M. Caps, S. Taylor, K. Beach, S. Carter, P. Kaczkowski, G. Keilman, S. Helton, W. Chandler, P. Mourad, M. Rice, R. Roy, and L. Crum. Liver hemostasis using High-Intensity Focused Ultrasound. *Ultrasound in Medicine and Biology,* 23(9): 1413-1420, 1997.

[109] S. Vaezy, R. Martin, and P. Kaczkowski. Control of Splenic Bleeding using High Intensity Ultrasound. *The Journal of Trauma,* 47(3): 521-525, 1999.

[110] S. Vaezy, R. Martin, H. Yaziji, P. Kaczkowski, G. Keilman, S. Carter, M. Caps, E. Y. Chi, M. Bailey and L. Crum. Hemostasis of punctured blood vessels using high intensity focused ultrasound. *Ultrasound in Medicine and Biology,* 24(6): 903-910, 1998.

[111] F. P. Curra, P. D. Mourd, V. A. Khokhlova, R. O. Cleveland, and L. A. Crum. Numerical simulations of heating patterns and tissue temperature response due to high-intensity focused ultrasound. *IEEE Transactions on Ultrasonics, Ferroelectrics, and Frequency Control*, 47(4): 1077-1088, 2000.

[112] P. Edson, R. G. Holt, and R. A. Roy. On the role of acoustic cavitation in enhancing hyperthermia from high-intensity focused ultrasound. *The Journal of the Acoustical Society of America,* 106(4): 2230, 1999.

[113] W. J. Fry, and R. B. Fry. Determination of absolute sound levels and acoustic absorption coefficients by thermocouple probes – theory. *The Journal of the Acoustical Society of America,* 26(3): 311-317, 1950.

[114] W. J. Fry, and R. B. Fry. Determination of absolute sound levels and acoustic absorption coefficients by thermocouple probes – experiment. *The Journal of the Acoustical Society of America,* 26(3): 294-310, 1950.

[115] K. J. Parker. The thermal pulse decay technique for measuring ultrasonic absorption coefficients. *The Journal of the Acoustical Society of America*, 74(5): 1356-1361, 1983.

[116] K. J. Parker. Effects of heat conduction and sample size on ultrasonic absorption measurements. *The Journal of the Acoustical Society of America*, 77(2): 719-725, 1985.

[117] T. G. Muir, and E. L. Carstensen. Prediction of nonlinear acoustic effects at biomedical frequencies and intensities. *Ultrasound in Medicine and Biology,* 6(4): 345-357, 1980.

[118] E. L. Carstensen, W. K. Law, and N. D. McKay. Demonstration of nonlinear acoustic effects at biomedical frequencies and intensities. *Ultrasound in Medicine and Biology*, 6(4): 359-368, 1980.

[119] F. A. Duck. *Physical properties of tissue*, Academic Press, 1990.

[120] S. A. Goss, and F. J. Fry. Nonlinear acoustic behavior in focused ultrasonic fields: observation of intensity dependent absorption in biological tissue. *IEEE Transactions on Sonics and Ultrasonics*, SU-28(1): 21-26, 1981.

[121] W. Swindell. A theoretical study of nonlinear effects with focused ultrasound in tissues: an "Acoustic Bragg Peak". *Ultrasound in Medicine and Biology*, 11(1): 121-130, 1985.

[122] K. Hynynen. Demonstration of enhanced temperature elevation due to nonlinear propagation of focused ultrasound in dog's thigh *in vivo*. *Ultrasound in Medicine and Biology,* 13(2): 85-91, 1987.

[123] D. R. Bacon, and E. L. Carstensen. Increased heating by diagnostic ultrasound due to nonlinear propagation. *The Journal of the Acoustical Society of America,* 88(1): 26-34, 1990.

[124] M. M. Chen, and K. R. Holmes. Microvascular contributions in tissue heat transfer. *Annals New York Academy of Sciences*, 137-150, 1980.

[125] J. W. Baish. Formulation of a statistical model of heat transfer in perfused tissue. In: J. J. McGrath, Editor, *Advances in Biological heat and mass transfer*, HTD-231, New York: ASME, 135-140, 1992.

[126] W. L. Nyborg. Solutions of the bio-heat transfer equation. *Physics in Medicine and Biology*, 33: 785-792, 1998.

[127] H. H. Pennes. Analysis of tissue and arterial blood temperatures in the resting human forearm. *Journal of Applied Physiology*, 2: 93-122, 1948.

[128] S. Weinbaum, L. M. Jiji, and D. E. Lemons. Theory and experiment for the effect of vascular microstructure on surface heat transfer – part I: Anatomical foundation and model conceptualization. *Journal of Biomedical Engineering*, 106: 321-330, 1984.

[129] J. J. W. Lagendijk. Thermal models: principles and implementation. In: S. B Field, and J. W. Hand, editors, *Introduction to the clinical aspects of clinical hyperthermia*, Taylor and Francis, Bristol, PA, 478-511, 1990.

[130] H. Arkin, L. X. Xu, and K. R. Holmes. Recent developments in modeling heat transfer in blood perfused tissues. *IEEE Transaction on Biomedical Engineering*, 41: 97-107, 1994.

[131] J. Crezee, and J. J. Lagendijk. Experimental verification of bio heat transfer theories: measurement of temperature profiles around large artificial vessels in perfused tissue. *Physics in Medicine & Biology*, 35: 905-923, 1990.

[132] E. G. Moros, A. W. Dutton, R. B. Roemer, M. Burton, and K. Hynynen. Experimental evaluation of two simple thermal models using hyperthermia *in vivo*. *International Journal of Hyperthermia*, 9: 581-598, 1993.

[133] C. A. Damianou, K. Hynynen, and X. Fan. Evaluation of accuracy of a theoretical model for predicting the necrosed tissue volume during focused ultrasound surgery. *IEEE Transaction on Ultrasonics, Ferroelectrics, and Frequency Control*, 42(2): 182-187, 1995.

[134] V. Sorrentino. *Experimental Evaluation of a Simple Field Equation Model for Prediction of Temperature Distribution in Focused Ultrasound Surgery*. M. S. dissertation, Boston University, 1998.

[135] E. H. Wissler. Pennes' 1948 paper revisited. *Journal of Applied Physiology*, 85: 35-41, 1998.

[136] C. Eckart. Vortices and streams caused by sound waves. *Physical Review*, 73:68-76, 1948.

[137] H. Mitome. Effects of attenuation of ultrasound as a source of driving force of acoustic streaming. In: H. Hobæk, editor, *Advances in Nonlinear Acoustics, Proceedings of the 13th International Symposium on Nonlinear Acoustics*, 589-594, 1993.

[138] T. C. Robinson, and P. P. Lele. An analysis of lesion development in the brain and in plastics by high-intensity focused ultrasound at low-megahertz frequencies. *The Journal of the Acoustical Society of America,* 51(2): 1333-1351, 1972.

[139] E. L. Carstensen, M. W. Miller, and C. A. Linke. Biological effects of ultrasound. *Journal of Biological Physics,* 2: 173-192, 1974.

[140] E. L. Carstensen, S. A. Becroft, W. K. Law, and D. B. Barbee. Finite amplitude effects on the thresholds for lesion production in tissues by unfocused ultrasound. *The Journal of the Acoustical Society of America,* 70(2): 302-312, 1981.

[141] W. L. Nyborg. Heat generation by ultrasound in a relaxing medium. *The Journal of the Acoustical Society of America,* 70: 310-312, 1981.

[142] W. L. Nyborg, and R. B. Steele. Temperature elevation in a beam of ultrasound. *Ultrasound in Medicine and Biology,* 9: 611-620, 1983.

[143] K. Beissner. On the plane-wave approximation of acoustic intensity. *The Journal of the Acoustical Society of America,* 71(6): 1406-1411, 1982.

[144] T. J. Cavicchi, and W. D. O'Brien Jr.. Heat generated by ultrasound in an absorbing medium. *The Journal of the Acoustical Society of America,* 76: 1244-1245, 1984.

[145] H. D. Mair, D. A. Hutchins, and P. A. Puhach. Intensity fields of continuous-wave axisymmetric transducers. *The Journal of the Acoustical Society of America,* 81(2): 328-334, 1987.

[146] F. L. Lizzi, J. Driller, and M. Ostromogilsky. Thermal model for ultrasound treatment of glaucoma. *Ultrasound in Medicine and Biology,* 10(3): 289-298, 1984.

[147] F. L. Lizzi, J. Driller, B. Lunzer, A. Kalisz, and D. J. Coleman. Computer model of ultrasound hyperthermia and ablation of tissue volumes using high intensity focused ultrasound. *Ultrasound in Medicine and Biology,* 18(1): 59-73, 1992.

[148] C. R. Hill, I. H. Rivens, M. G. Vaughan, and G. ter Haar. Lesion development in focused ultrasound surgery: a general model. *Ultrasound in Medicine and Biology,* 20(3): 259-269, 1994.

[149] J. Wu, and G. Du. Temperature elevation generated by a focused Gaussian beam of ultrasound. *Ultrasound in Medicine and Biology,* 16(5): 489-498, 1990.

[150] J. Wu, J. D. Chase, Z. Zhu, and T. P. Holzapfel. Temperature rise in a tissue-mimicking material generated by unfocused and focused ultrasonic transducers. *Ultrasound in Medicine and Biology*, 18(5): 495-512, 1992.

[151] H. Wan, P. VanBaren, E. S. Ebbini, and C. A. Cain. Ultrasound surgery: comparison of strategies using gphased array systems. *IEEE Transactions on Ultrasounics, Ferroelectrics, and Frequency Control*, 43(6): 1085-1098, 1996.

[152] P. M. Meaney, R. L. Clarke, G. R. ter Haar, and I. H. Rivens. A 3-D finite-element model for computation of temperature profiles and regions of thermal damage during focused ultrasound surgery exposures. *Ultrasound in Medicine and Biology*, 24(9): 1489-1499, 1998.

[153] I. M. Hallaj. *Nonlinear Acoustics in Underwater and Biomedical Applications: Array Performance Degradation and Time Reversal Invariance*, Ph. D. Dissertation, University of Washington, 1999.

[154] M. F. Hamilton, and C. L. Morfey. Model equations. In: M. F. Hamilton, and D. T. Blackstock, editors, *Nonlinear Acoustics*, Chapter 3, Academic Press, 1998.

[155] R. T. Beyer. The parameter B/A. In: M. K. Hamilton, and D. T. Blackstock, editors, *Nonlinear Acoustics*, Chapter 2, Academic Press, 1998.

[156] A. D. Pierce. *Acoustics, An introduction to its physical principles and applications*, Chap 10, McGraw-Hill Book Company, 1981.

[157] O. V. Rudenko, and S. I. Soluyan. *Theoretical Foundations of Nonlinear Acoustics*, Chap 8, Plenum, New York, 1977.

[158] W. L. Nyborg. Acoustic streaming. In: M. F. Hamilton, and D. T. Blackstock, editors, *Nonlinear Acoustics*, Chapter 7, Academic Press, 1998.

[159] R. T. Beyer. *Non-linear acoustics*, Washington DC: U.S. Naval Sea Systems, U.S. Government Printing Office, 239-268, 1974.

[160] J. Lighthill. Acoustic streaming. *Journal of Sound and Vibration*, 61: 391-418, 1978.

[161] V. E. Gusev, and O. V. Rudenko. Nonsteady quasi-one-dimensional acoustic streaming in unbounded volumes with hydrodynamic nonlinearity. *Soviet Physical Acoustics*, 25: 493-497, 1979.

[162] S. Tjøtta, and J. Naze Tjøtta. Acoustic streaming in ultrasound beams. In: H. Hobæk, editor, *Advances in Nonlinear Acoustics, Proceedings of the 13th International Symposium on Nonlinear Acoustics*, 601-606, 1993.

[163] J. Wu, and G. Du. Acoustic streaming generated by a focused Gaussian beam and finite amplitude tonrbursts. *Ultrasound in Medicine and Biology*, 19(2): 167-176, 1993.

[164] H. Mitome. Acoustic streaming and nonlinear acoustics research activities in Japan. In: H. Hobæk, editor, *Advances in Nonlinear Acoustics, Proceedings of the 13th International Symposium on Nonlinear Acoustics*, 43-54, 1993.

[165] T. Kamakura, M. Matsuda, Y. Kumamoto, and M. A. Breazeale. Acoustic streaming induced in focused Gaussian beams. *The Journal of the Acoustical Society of America*, 97: 2740-2746, 1995.

[166] M. F. Hamilton, Yu. A. Il'inskii, and E. A. Zabolotskaya. Acoustic streaming at high Reynolds numbers in focused sound beams, *The Journal of the Acoustical Society of America*, 97: 3376, 1995.

[167] X. Shi, R. W. Martin, S. Vaezy, and L. A. Crum. Quantitative investigation of acoustic streaming in blood. *The Journal of the Acoustical Society of America*, 111(2): 1110-1121, 2002.

[168] H. C. Starritt, F. A. Duck, and, V. F. Humphrey. An experimental investigation of streaming in pulsed diagnostic ultrasound beams. *Ultrasound in Medicine and Biology*, 15(4): 363-373, 1989.

[169] K. Matsuda, T. Kamakura, and Y. Kumamoto. Buildup of acoustic streaming in focused beams. *Ultrasonics*, 34: 763-765, 1996.

[170] C. A. J. Fletcher. *Computational Techniques for Fluid Dynamics*, Vol. 1 of Springer series in computational physics, Spring-Verlag, Berlin, 2nd edition, 1991.

[171] J. L. Buchanan, and P. R. Turner. *Numerical Methods and Analysis. International series in pure and applied mathematics*. McGraw Hill, Inc., New York, 1992.

[172] G. Mur. Absorbing boundary conditions for the finite-difference approximation of the time-domain electromagnetic-field equations. *IEEE Transactions on Electromagnetic Compatibility*, EMC-23(4): 377-382, 1981.

[173] G. D. Smith. *Numerical Solution of Partial Differential Equations: Finite Difference Methods*, Chapter 5, Oxford U.P., New York, 1987.

[174] H. T. O'Neil. Theory of focusing radiators. *The Journal of the Acoustical Society of America*, 21(5): 516-526, 1949.

[175] B. G. Lucas, and T. G. Muir. The field of a focusing source. *The Journal of the Acoustical Society of America*, 72(4): 1289-1296, 1982.

[176] F. A. Duck, *Physical properties of tissue*, Academic Press, 1990.

[177] M. M. Burlew, E. L. Madsen, J. A. Zagzebski, R. A. Banjavic, and S. W. Sum. A new ultrasound tissue-equivalent material. *Radiation Physics*, 134: 517-520, 1980.

[178] S. Bloch. *Ultrasonic tissue characterization: Towards high-intensity focused ultrasound treatment monitoring*, M. S. Thesis, University of Washington, 1998.

[179] T. Tanaka. Gels. *Scientific American*, 244: 110-123, 1981.

[180] K. K. Shung, and R. A. Sigelmann. Scattering of ultrasound by blood. *IEEE Transactions on Biomedical Engieering*, BME-23(6): 460-467, 1976.

[181] Y. F. Law, K. W. Johnston, H. F. Routh, and R. S. C. Cobbold. On the design and evaluation of a steady flow model for doppler ultrasound studies. *Ultrasound in Medicine and Biology*, 15(5): 505-516, 1989.

[182] J. Petrick, M. Zomack, and R. Schlief. An investigation of the relationship between ultrasound echo enhancement and doppler frequency shift using a pulsatile arterial flow phantom. *Investigative radiology*, 32(4): 225-235, 1997.

[183] B. Lavandier, D. Cathignol, R. Muchada, B. B. Xuan, and J. Motin. Noninvasive aortic blood flow measurement using an intraesophageal probe. *Ultrasound in Medicine and Biology*, 11(3): 451-460, 1985.

[184] W. N. McDicken. A versatile test-object for the calibration of ultrasonic doppler flow instruments. *Ultrasound in Medicine and Biology*, 12(3): 245-249, 1986.

[185] V. L. Newhouse, R. S. Nathan, and L. W. Hertzler. A proposed standard target for ultrasound doppler gain calibration. *Ultrasound in Medicine and Biology*, 8(3): 313-316, 1982.

[186] K. V. Ramnarine, D. K. Nassiri, P. R. Hoskins, and J. Lubbers. Validation of a new blood-mimicking fluid for use in Doppler flow test objects. *Ultrasound in Medicine and Biology*, 24(3): 451-459, 1998.

[187] J. Lubbers. Application of a new blood-mimicking fluid in a flow Doppler test objects. *European Journal of Ultrasound*, 9: 267-276, 1999.

[188] D. W. Ricky, P. A. Picot, D. A. Christopher, and A. Fenster. A wall-less vessel phantom for doppler ultrasound studies. *Ultrasound in Medicine and Biology*, 21(9): 1163-1176, 1995.

[189] R. L. Whitmore. *Rheology of the Circulation*, Oxford: Pergamon, 90-108, 1968.

[190] D. C. Wilcox. *Basic Fluid Mechanics*, DCW Industries, Inc., California, 1997.

[191] W. J. Fry, and R. B. Fry. Determination of absolute sound levels and acoustic absorption coefficients by thermocouple probes – theory. *The Journal of the Acoustical Society of America*, 26(3): 294-310, 1954.

[192] W. J. Fry, and R. B. Fry. Determination of absolute sound levels and acoustic absorption coefficients by thermocouple probes – experiment. *The Journal of the Acoustical Society of America*, 26(3): 311-317, 1954.

[193] S. A. Goss, J. W. Cobb, and L. A. Frizzell. Effect of beam width and thermocouple size on the measurement of ultrasonic absorption using the thermoelectric technique. *IEEE Ultrasonic Symposium Proceedings*, Cat. No 77CH1264-1SU, 206-211, 1977.

[194] K. Hynynen, C. J. Martin, D. J. Watmough, and J. R. Mallard. Errors in temperature measurement by thermocouple probes during ultrasound induced hyperthermia. *The British Journal of Radiology*, 56: 968, 1983.

[195] K. Hynynen, and D. K. Edwards. Temperature measurements during ultrasound hyperthermia. *Medical Physics*, 16(4): 618-626, 1989.

[196] E. X. Wu, M. M. Goodsitt, and E. L. Madsen. Microscopic mechanism of attenuation of compressional ultrasonic waves in tissue-mimicking phantom materials. *Ultrasonic Imaging*, 14: 121-133, 1992.

[197] K. D. Maglic, A. Cezairliyan, and V. E. Peletsky. *Compendium of Thermophysical Property Measurement Methods*, Plenum Press, New York, 1984.

[198] H. J. McSkimin. Ultrasonic methods of measuring the mechanical properties of liquids and solids. In: W. P. Mason, and R. N. Thurston, editors, *Physical Acoustics: Principles and Methods*, Vol. 1 – Part A, Academic Press, New York, Chapter 10, 1964.

[199] F. Dunn, P. D. Edmonds, and W. J. Fry. Absorption and dispersion of ultrasound in biological media. In: H. P. Schean, editor, *Biological Engineering*, McGraw-Hill, New York, Chapter 3, 1969.

[200] E. P. Papadakis. Ultrasonic velocity and attenuation: Measurement methods with scientific and industrial applications. In: *Physical Acoustics*, Vol. XII, edited by W. P. Mason and R. N. Thurston, Academic Press, New York, Chapter 5, 1976.

[201] E. L. Madsen, F. Dong, G. R. Frank, B. S. Garra, K. A. Wear, T. Wilson, J. A. Zagzebski, H. L. Miller, K. K. Shung, S. H. Wang, E. J. Feleppa, T. Liu, W. D. O'Brien, Jr., K. A. Topp, N. T. Sanghvi, A. V. Zaitsev, T. J. Hall, J. B. Fowlkes, O. D. Kripfgans, and J. G. Miller. Interlaboratory comparison of ultrasonic backscatter, attenuation, and speed measurements. *Journal of Ultrasound in Medicine*, 18: 615-631, 1999.

[202] V. A. Del Grosso, and C. W. Mader. Speed of sound in pure water. *The Journal of the Acoustical Society of America*, 52(5): 1442-1446, 1972.

[203] C. T. Liauh. Fast numerical scheme of computing acoustic pressure fields for planar circular ultrasound transducers. *The Journal of the Acoustical Society of America*, 105(4): 2243-2247, 1999.

[204] J. D. Bronzino. *The Biomedical Engineering Handbook*, CRC Press, 1995.

[205] P. L. Edson. *The Role of Acoustic Cavitation in Enhanced Ultrasound-Induced Heating in a Tissue-Mimicking Phantom*, PH. D. dissertation, Boston University, 2001.

[206] J. Mooibroek, and J. J. W. Lagendijk. A fast and simple algorithm for the calculation of convective heat transfer by large vessels in three-dimensional inhomogeneous tissues. *IEEE Transactions on Biomedical Engineering*, BE-38: 490-501, 1991.

[207] Z. P. Chen, and R. B. Roemer. The effects of large blood vessels on temperature distributions during hyperthermia. *Journal of Biomechanical Engineering*, 114: 473-481, 1992.

[208] E. G. Moros, W. L. Straube, and R. J. Myerson. Finite difference vascular model for 3-d cancer therapy with hyperthermia. In: *Advances in Biological and Heat and Mass Transfer*, Vol HTD-268, edited by R. B. Roemer, New York: ASME, 107-111, 1993.

[209] X. Fan, and K. Hynynen. Control of the necrosed tissue volume during noninvasive ultrasound surgery using a 16-element phased array. *Medical Physics*, 22(3): 297-306, 1995.

[210] X. Fan, and K. Hynynen. A study of various parameters of spherically curved phased arrays for noninvasive ultrasound surgery. *Physics in Medicine and Biology*, 41(4): 591-608, 1996.

[211] X. Fan, and K. Hynynen. Ultrasound surgery using multiple sonications — treatment time considerations. *Ultrasound in Medicine and Biology*, 22(4): 471-482, 1996.

[212] B. Krasovitski, and E. Kimmel. A blood vessel exposed to ultrasound: A mathematical simulation of the temperature field. *The Journal of the Acoustical Society of America*, 111(3): 1454-1459, 2002.

[213] B. Fan. *Principles and Applications of Ultrasound*, Science and Technology Press, China, 1985.

[214] E. C. Everbach. *Tissue Composition Determination via Measurement of the Acoustic Nonlinearity Parameter*, Ph. D. Dissertation, Yale University, 1989.

[215] A. Bejan. *Heat Transfer*, John Wiley & Sons, Inc., 1993.